University of Reading

DEPARTMENT OF METEOROLOGY

Quantifying Arctic Storm Risk in a Changing Climate

by

Alexander Frank Vessey

Thesis submitted for the degree of Doctor of Philosophy

July 2021

DECLARATION

I confirm that this is my own work and the use of all material from other sources has been properly and fully acknowledged.

Alexander Frank Vessey.

ACKNOWLEDGEMENTS

I would like to thank everyone who has helped me throughout my PhD. I am very grateful to all of them.

First of all, I would like to thank my supervisors: Kevin Hodges, Len Shaffrey and Jonathan Day. You have all given large amounts of your time to support me. You have provided excellent support and guidance whenever I have needed it. It has been a pleasure to work with you all and I hope to do so again in the future.

I want to also thank my monitoring committee members Suzanne Gray and Joy Singarayer. It was great to always have a fresh pair of eyes to look over my work, and to have useful discussions with you.

I am very grateful for the discussions had with my two thesis examiners, Suzanne Gray and Jennifer Catto.

I would also like to thank my sponsor, AXA XL. I was very fortunate to spend 3 months of my PhD on a secondment at the AXA XL London Office from August-November 2019. When I was there, I always felt very welcome, and it gave me a great insight into the insurance industry. I learnt a lot, and I am sure that my experiences will help me in my future career. I want to thank Tom Philp for making all of the necessary arrangements for this.

I want to also thank all of the people that I have met during my PhD at the Department of Meteorology at the University of Reading or elsewhere, who talked to me about my research and helped me to develop my ideas.

ABSTRACT

Recent reductions in sea ice extent have made the Arctic Ocean more accessible for industries including shipping, oil exploration and tourism. The Arctic has been increasingly used for shipping since 2012, and this trend will likely continue over the 21st century as sea ice extent reduces further. Thus, increasing the exposure to synoptic-scale Arctic storms, which cause hazardous weather. But Arctic storms are not fully understood. This thesis aims to further understand present-day Arctic storm statistics and development, and better evaluate changes in risk due to climate change.

The representation of present-day Arctic storm statistics is found to be consistent across the ERA5, ERA-Interim, JRA-55, MERRA-2 and NCEP-CFSR reanalyses. Arctic storm statistics are found to be more sensitive to the storm tracking variable used. Approximately twice as many storms per season were identified in ERA-Interim in winter using 850 hPa relative vorticity, rather than mean sea level pressure.

In most seasons the structure and development of Arctic storms is found to be similar to mid-latitude storms (and conceptual models e.g. Norwegian Cyclone Model). But the structure and development of Arctic summer storms is found to be different. The composite structure of Arctic summer storms shows that they typically undergo a structural transition around the time of maximum intensity, from having a baroclinic structure to an axi-symmetric cold-core structure throughout the troposphere. Arctic summer storms are also long-lived, potentially causing prolonged hazardous conditions.

Future climate RCP8.5 HadGEM3-GA3.0 simulations (2086-2110) performed at horizontal resolutions of 150 km, 60 km, and 25 km from the UPSCALE project (Mizielinski et al., 2014) show that the Arctic environment will change due to climate change. Consequently, Arctic storm track density will likely decrease over Arctic Ocean in winter and increase around Greenland in summer. This response is consistent between all projections at each resolution, adding confidence in this response.

Table of Contents

List of Tables

List of Figures

Chapter 1

Introduction

1.1 Motivation

The Arctic has undergone the greatest warming of all regions on Earth over the past few decades in response to anthropogenic climate change (Screen and Simmonds, 2010b; Smith et al., 2019). Annual surface air temperatures north of 64°N have increased by as much as 3.26 °C above the 1951-1980 average, whereas annual global surface air temperatures have only increased by as much as 1.02 °C (Lenssen et al., 2019; GISTEMP Team, 2021). As a result, Arctic sea ice extent has reduced substantially since 1979 (see Figure 1.1). Global surface temperatures are projected to increase further over the 21st century (Stocker et al., 2014), which will lead to the continued and perhaps accelerated reduction in Arctic sea ice extent (Stroeve et al., 2007, 2012).

Reduced sea ice extent has allowed for the movement of ships over the Arctic Ocean and access to the Arctic Ocean floor. Reduced sea ice extent in the Arctic has benefits to multiple industries and is encouraging more human activity in the Arctic. These include shorter shipping transits between ports in North America, Europe and Asia (Melia et al., 2016; Smith and Stephenson, 2013), access to previously inaccessible natural resources (Harsem et al., 2015), and new destinations for tourism (Maher, 2017). These have encouraged human activity in the Arctic in industries such as shipping, oil exploration and tourism. However, the hazards in the Arctic that endanger these human activities are not well understood.

The Arctic is a challenging environment for human activity. It is a place of extreme cold, and there is a lack of critical infrastructure, such as search and rescue services and ports. Sea ice can confine ships to travel over shallow coastlines on the boundaries of the Arctic Ocean, where the depth can be <100 metres. Conditions in the Arctic can be made worse by the passage of a storm. Storms are associated with high surface wind speeds and high ocean waves, leading to hazardous rough sea conditions (Thomson and Rogers, 2014; Liu et al., 2016; Waseda et al., 2018). They can also break-up sea ice, which may then become mobile and drift toward shipping lanes, creating an additional hazard (Simmonds and Keay, 2009; Asplin et al., 2012; Parkinson and Comiso, 2013; Peng et al., 2021). As the Arctic becomes increasingly used for shipping, oil exploration and tourism, the exposure of valuable assets and the risk to life from hazardous weather increases.

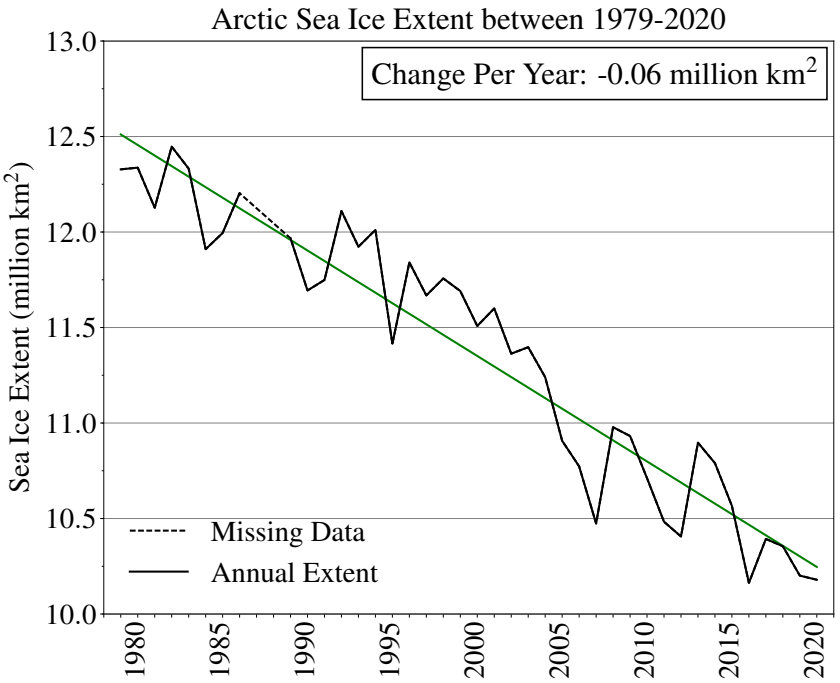

Figure 1.1: Annual Arctic sea ice extent from 1979 to 2020. The green line is the line of best fit. Data sourced from National Snow & Ice Data Centre (2020a).

Storms have been a focal point of atmospheric research over the last century because of their damaging impact on populous areas (Browning, 2004; Leckebusch et al., 2007; Pinto et al., 2012). For example, storm Lothar devastated central Europe in 1999, resulting in damages totalling €15.6 billion (Munich RE, 2021). The Arctic is expected to become increasingly used for shipping, oil exploration and tourism over the 21st century as sea ice extent continues to reduce and the Arctic Ocean becomes increasingly accessible. Thus, it is becoming increasingly important to understand the risk that Arctic storms pose to human activity, so that activities can become safer and potential financial damages can be mitigated through insurance.

The aim of this thesis is to improve the understanding of synoptic-scale Arctic storms, to raise awareness of such hazards and better evaluate the risk they pose to human activity in the Arctic.

1.2 The Arctic Environment and Potential Impacts of Climate Change

The Arctic is often defined as the region north of the Arctic Circle (north of 66.5°N), and encompasses an area of approximately 20 million km^2 (see Figure 1.2). The Arctic Ocean accounts for an area of approximately 14 million km^2, of which approximately 11.3 million km^2 is covered by sea ice annually (calculated from Figure 1.1). The Arctic is a complex environment, with areas of high elevation, and changes in surface type between land, ocean and sea ice (see Figure 1.2). It receives less thermal energy from the sun than the Tropics and mid-latitudes, and is mostly surrounded by land. The Arctic Ocean can be quite shallow in places, in particular near the coastlines of major landmasses, where it can be <100 metres deep (see Figure 1.2). In this section, the Arctic environment is described with an emphasis on phenomena that may influence Arctic storminess and the amount of human activity in the Arctic. An indication of how the Arctic environment may change in the future in response to climate change is also given.

1.2.1 Seasonal Cycle of the Arctic: The Polar Day and Polar Night

The Earth is tilted so that its equatorial plane is 23.5° from its orbital plane. This results in the North Pole being tilted toward the sun between the spring and autumn equinoxes (March - September) and tilted away from the sun between the autumn and spring equinoxes (September - March). Between September and March, the sun does not rise above the horizon and the Arctic is in shadow. The opposite occurs between March and September. This phenomenon where by the sun remains above / below the horizon for 24 hours, is referred to as the Polar Day / Night.

The cycle between Polar Day and Night changes the amount of incoming solar radiation received in the Arctic at the surface from the Sun. It drives annual changes in surface temperatures in the Arctic. This was measured by Persson et al. (2002), who measured solar radiation received at the surface and surface temperature across October 1997 - October 1998

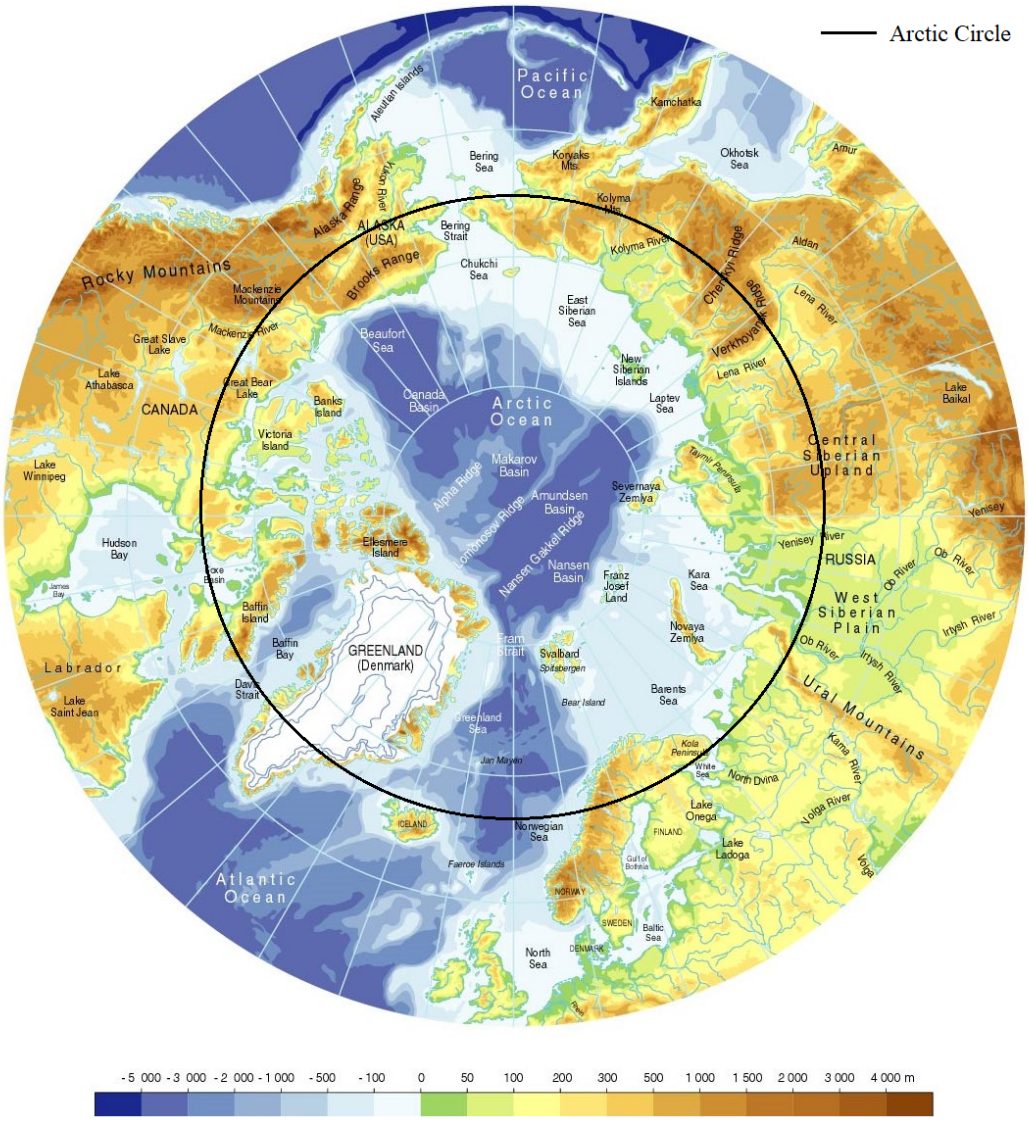

Figure 1.2: Map of the Arctic, with the elevation of land, and depth of the Arctic Ocean. Sourced from Arctic Monitoring & Assessment Programme: Working Group of the Arctic Council (2020).

at a field site, which was set up on a pack of sea ice. The field site moved with the sea ice pack between 74 - 81°N, and was part of the Surface Heat Budget of the Arctic Ocean Experiment (SHEBA). Results showed that during the Polar Night (September to March), incoming solar radiation received at the field site was near 0 Wm^{-2}, and the average surface temperature was approximately -25 °C. When the Polar Night neared its end in March, an increase in incoming solar radiation from the sun caused surface temperatures to increase to just above 0 °C in June, July and August. Surface temperatures then decreased to well below 0 °C, as the Polar Night began again (see Figures 8 and 22 in Persson et al., 2002).

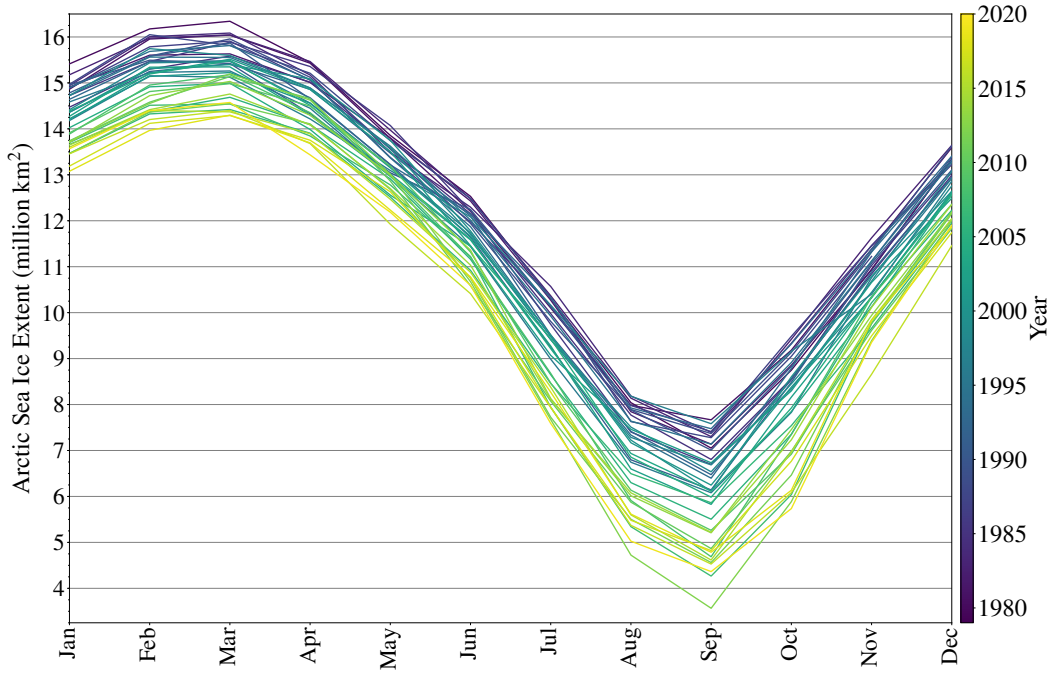

Figure 1.3: Monthly Arctic sea ice extent from 1979 to 2020. The record minimum sea ice extent occurred in September 2012. Data sourced from National Snow & Ice Data Centre (2020a).

1.2.2 Arctic Sea Ice

Surface air temperatures are often below 0 °C in many parts of the Arctic (Rigor et al., 2000), leading to ice formation on the surface of the Arctic Ocean. Sea ice prevents human activity in the Arctic, by restricting the movement of ships and access to the ocean floor. There is a distinct cycle in Arctic sea ice extent throughout the year, which coincides with the cycle from Polar Night to Polar Day (see Figure 1.3). The maximum Arctic sea ice extent typically occurs in March, just before the Polar Night ends, where surface temperatures in the Arctic then start to increase and sea ice begins to melt. The minimum sea ice extent typically occurs in September, when the Polar Day ends and ice starts to reform as Arctic surface temperatures decrease.

Arctic sea ice has a surface albedo (reflectivity of a surface to incoming solar radiation) of approximately 0.6, whereas an open ocean surface and tundra land surface have a surface albedo of approximately 0.06 and 0.2 (National Snow & Ice Data Centre, 2020c; Climate Data, 2020). As a result, sea ice reflects more solar radiation back into space than the other surface types in the Arctic, and therefore absorbs less solar radiation.

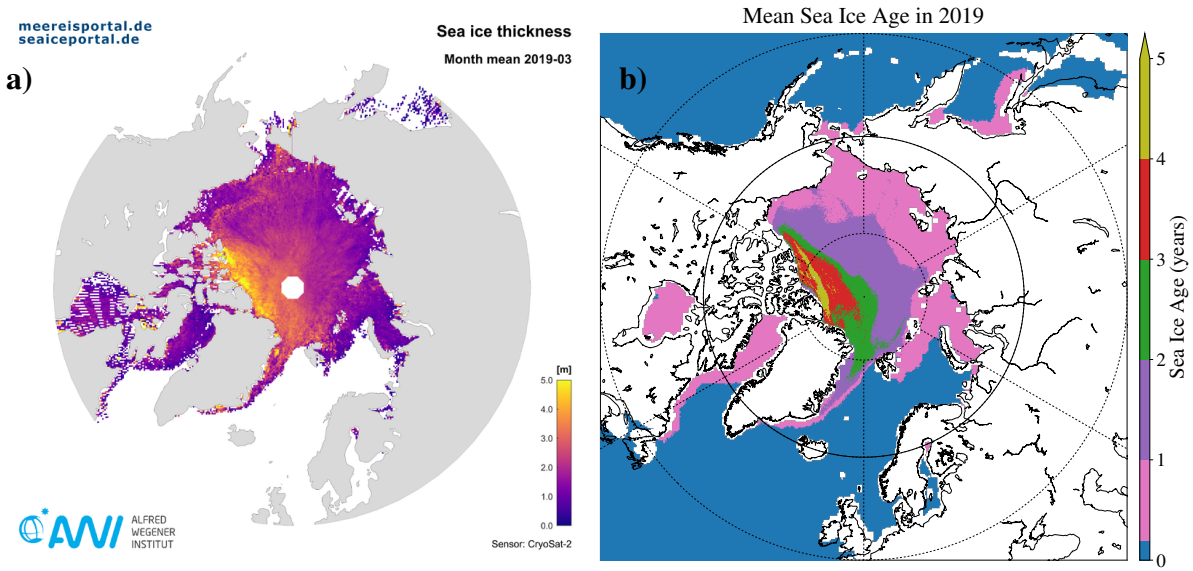

Figure 1.4: Arctic sea ice **a)** thickness and **b)** age in March 2019. **a)** is sourced from Alfred Wegener Institute (2019), and, the data for **b)** is sourced from National Snow & Ice Data Centre (2019a).

The distribution of sea ice varies annually and between regions. It determines the amount of open ocean that ships are able to travel across. Sea ice cover depends on the thickness of ice, which determines the volume of ice needed to be melted before an area becomes open ocean. Maykut (1985) subdivided Arctic sea ice into zones, which categorise it by its persistence throughout the year. The 'perennial ice zone' describes the thickest and oldest area of sea ice, which persists year-round and has an age greater than 1 year. It is largely found north of 80°N around north Greenland and the Canadian Archipelago (see Figure 1.4). The 'seasonal ice zone' describes the area of ice that melts within a year and has an age less than 1 year. It is the thinnest and youngest area of ice, and typically extends as far south as to the coastline of Eurasia, to southern Greenland and into the Hudson Bay (see Figure 1.4).

In a year, sea ice extent can change dramatically from its maximum to minimum extent in March and September. For example, in 2012, Arctic sea ice extent reduced from 15.2 million km^2 in March to 3.6 million km^2 in September (see Figure 1.5). Consequently, shipping routes along the coastline of Eurasia and through the Canadian Archipelago that join Europe and North America to Asia, are only typically open around the minimum sea ice extent in September (see Figure 1.5).

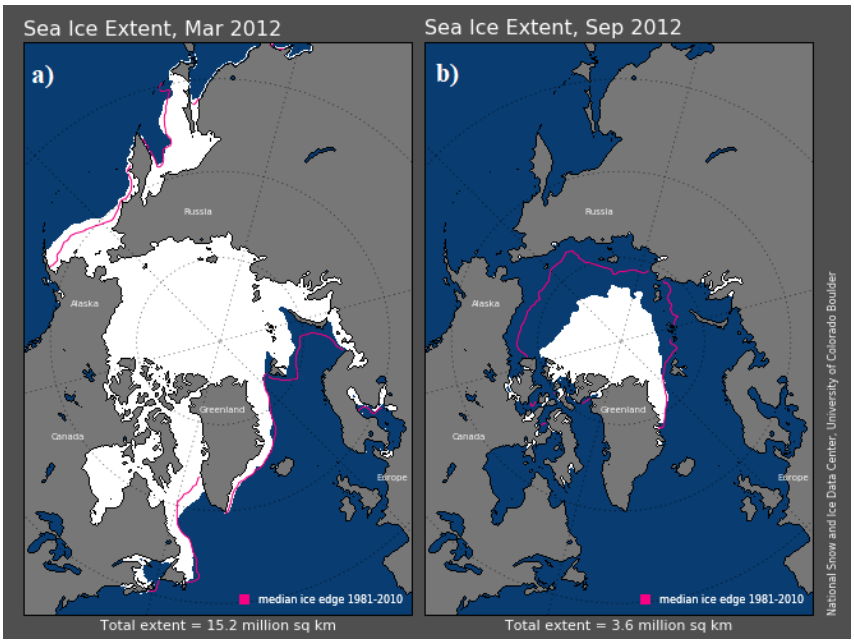

Figure 1.5: Monthly mean Arctic sea ice extent in 2012 during its **a)** maximum extent in March and **b)** minimum extent in September. Adapted from National Snow & Ice Data Centre (2020b).

The Arctic has undergone major warming over recent decades. Surface temperatures north of 64°N have increased by as much as 3.26 °C above the average surface temperature from 1951 - 1980 (Lenssen et al., 2019; GISTEMP Team, 2021). Climate change has meant that more northern areas of the Arctic experience surface temperatures above 0 °C (Zach Labe, 2021), and the length of the melting season has also increased at a rate of 5 days per decade (Stroeve et al., 2014). As a result, more sea ice has melted in the spring and summer than has grown in the autumn and winter in recent decades, resulting in a net decline in sea ice extent (see Figure 1.1 and 1.3) (Lindsay and Zhang, 2005). Sea ice extent will continue to decline over the 21st century due to climate change (Stroeve et al., 2012), making the Arctic increasingly navigable for ships.

Sea ice extent has reduced at a faster rate in September than the annual average. Annually, sea ice extent has reduced by -0.06 million km^2 per year (see Figure 1.1), but in September it has reduced at a faster rate of -0.08 million km^2 per year (see Figure 1.6). This is most likely the consequence of Arctic Amplification. This describes how warming can change the surface type in the Arctic from ice to ocean, increasing the amount of solar radiation absorbed by the surface, which leads to further warming of the atmosphere (Arrhenius, 1896; Manabe and Stouffer, 1980; Serreze and Barry, 2011). The effect of Arctic Amplification is greatest when

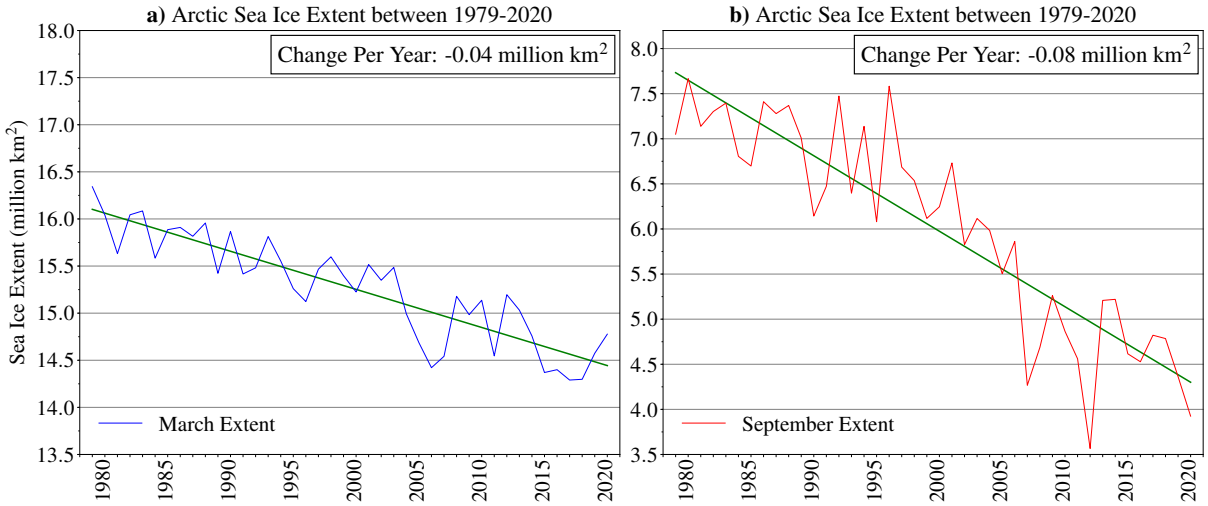

Figure 1.6: Monthly mean Arctic sea ice extent in **a)** March and **b)** September from 1979 to 2020. Data sourced from National Snow & Ice Data Centre (2020a).

the Arctic is not in shadow, during the Polar Day, likely causing faster decline in September sea ice extent. As a consequence of climate change, the Arctic Ocean will likely become ice-free (sea ice extent <1 million km^2) by the 2030s in September (Wang and Overland, 2012b), earlier than the annual decline in sea ice extent suggests (see Figure 1.1).

1.2.3 The Arctic Frontal Zone

The differences in albedo and heat capacity between surface types in the Arctic cause air temperatures over sea ice, open ocean and land to differ, creating local temperature gradients. The Arctic Frontal Zone (AFZ) has been identified as an area of local temperature gradients in the Arctic, and occurs over the boundary between the land surrounding the Arctic and the Arctic Ocean (Dzerdzeevskii, 1945; Reed and Kunkel, 1960; Crawford and Serreze, 2015) (see Figure 1.7). The AFZ was first recognised and coined by Dzerdzeevskii (1945) and was considered as a place of origin for Arctic storms (Serreze et al., 2001). Subsequent research has found the AFZ to be an area of significant storm activity (Reed and Kunkel, 1960; Serreze et al., 2001; Crawford and Serreze, 2015). The strength of temperature gradients across the AFZ are typically strongest in summer when incoming solar radiation from the sun is greatest (Crawford and Serreze, 2015).

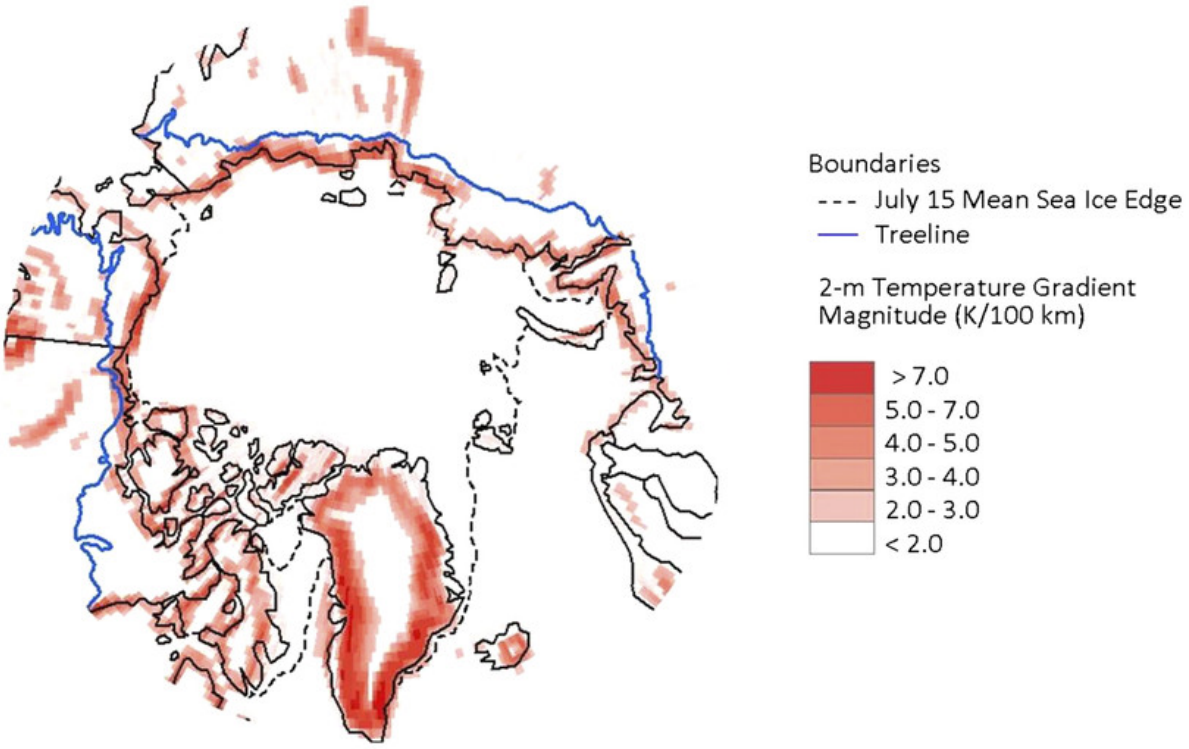

Figure 1.7: Mean July 2 metre temperature gradients between 1979 and 2012, from the ERA-Interim reanalysis dataset. Also shown is the mean treeline (blue solid line) and the mean 15 Jul sea ice edge (black dashed line) between 1979 and 2012. Figure adapted from Crawford and Serreze (2015).

1.2.4 Impact of Climate Change on the Arctic

The Arctic will undergo greater warming than other regions on Earth over the 21st century, as a consequence of Arctic Amplification (see Figure SPM.8 in Stocker et al., 2014, and also Smith et al., 2019). Warming in the Arctic over the 21st century will likely be greater in winter (DJF) than in summer (JJA) (see Figure 1.8). In winter, the greatest warming will occur over the Arctic Ocean (see Figure 1.8). Sea ice extent will be much lower in the future, allowing for more heat transfer from the ocean (Screen and Simmonds, 2010a; Boeke and Taylor, 2018). Heat that builds up during the summer, when incoming solar radiation is highest, is not immediately transferred into the atmosphere. Instead, water has a higher heat capacity than air, so that the heat is transferred over longer time-scales, and could compound warming from climate change in autumn and winter (see Figure 1.8). In summer, greater changes in surface temperature may also occur over land, as a future reduction in snow cover will lower the albedo of the land surface and cause more solar radiation to be absorbed (Crawford and Serreze, 2017).

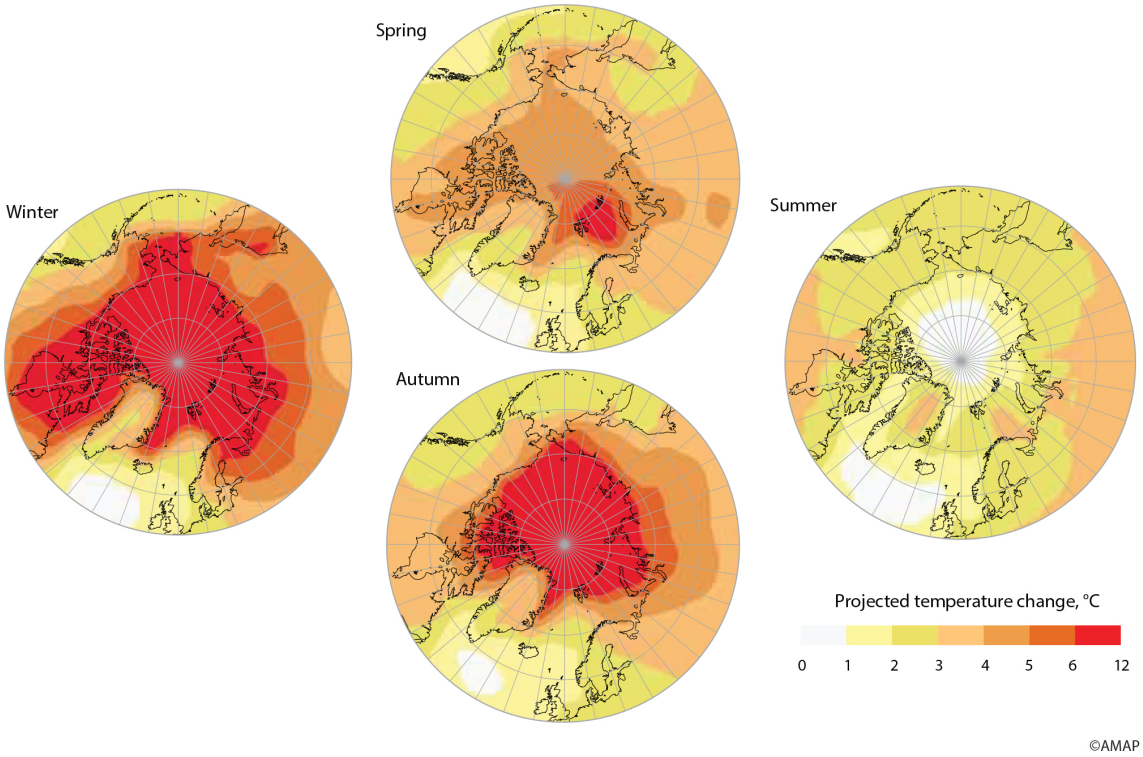

Figure 1.8: Differences in surface air temperature between the mean 2070-2090 surface temperature (following the RCP2.6 future climate scenario from the Intergovernmental Panel on Climate Change) and the mean 1960-1990 surface temperature (future minus present). Sourced from Arctic Monitoring and Assessment Programme (2012).

Arctic sea ice extent will continue to decline over the 21st century, as a consequence of climate change (Stroeve et al., 2007, 2012). Recent studies have estimated that the Arctic may become ice-free as early as the 2030s (Wang and Overland, 2009, 2012a), much sooner than previous estimates (Houghton, 2001; Arzel et al., 2006; Zhang and Walsh, 2006). Thus, the Arctic will likely become increasingly navigable and accessible, which will encourage more human activity in the Arctic and increase the exposure to hazardous weather further.

1.3 Concepts of Storm Development, Structure and Identification at Mid-Latitudes

Mid-latitude storms have been a focus of research over the last century due to their damaging impact on populous areas such as Europe (Munich RE, 2021). In this section, the current knowledge of the development, structure and identification of mid-latitude storms is described.

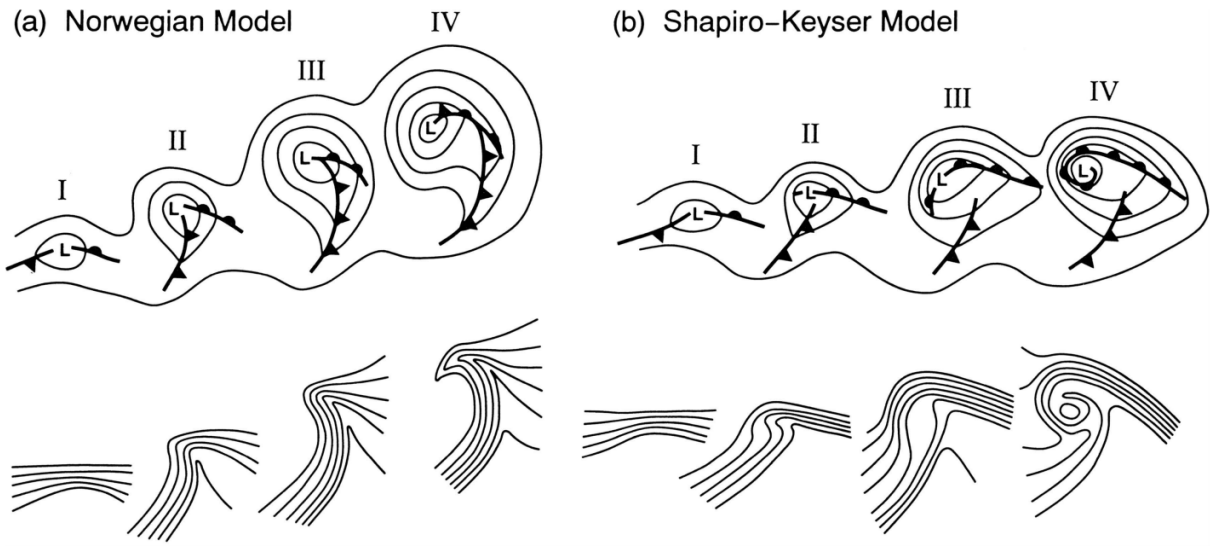

Figure 1.9: Conceptual models of cyclone evolution - the **a)** Norwegian Cyclone Model, and **b)** Shapiro-Keyser Model. Lower-tropospheric geopotential height and fronts (top), and lower-tropospheric potential temperature (bottom). **a)** Norwegian cyclone model: (I) incipient frontal cyclone, (II) and (III) narrowing warm sector, (IV) occlusion. **b)** Shapiro-Keyser cyclone model: (I) incipient frontal cyclone, (II) frontal fracture, (III) frontal T-bone and bent-back front, (IV) frontal T-bone and warm seclusion. The thick black lines with with circles indicate a warm front, and triangles indicate a cold front. Figure from Schultz et al. (1998).

1.3.1 Storm Development and Tracks

Bjerknes (1919, 1922) were among the first to describe and conceptualise the development of mid-latitude storms, through the Norwegian Cyclone Model. This model describes the stages of growth and decay that mid-latitude storms typically undergo (see Figure 1.9a). These include having genesis along the Polar Front, a boundary between a cold air mass to the north and a warm air mass to the south (see Stage I in Figure 1.9a). Occlusion then starts to take place, as the moving storm is affected by the Earth's rotation, where the cold air mass starts to wrap around the storm centre into the warm air mass, ultimately leading to the growth and eventual decay of the storm (see Stages I, II and III in Figure 1.9a). This model has been built upon in subsequent research, with case studies of storms that appear to follow the model being identified using satellite imagery (e.g. Carlson, 1980), technology that was unavailable to Bjerknes (1919, 1922).

Other studies have proposed alternative models of storm development, such as the Shapiro-Keyser Model (see Figure 1.9b) (Shapiro and Keyser, 1990). Case studies of storms

have also been identified with similar development to that described by this model (e.g. Browning, 2004). The early stages of the Shapiro-Keyser Model are similar to those of the Norwegian Cyclone Model. They both show storms to grow on the Polar Front (see Stage I in Figures 1.9a and 1.9b).

However, the description of mid-latitude storms in their mature stages differ between the models, with the Shapiro-Keyser Model describing how storms may undergo frontal fracture. During the frontal fracture process, the warm and cold fronts may separate, and the storm may develop a warm-core centre. Case studies of storms that follow the development described in each model have been identified (e.g. Carlson, 1980; Browning, 2004), and it is generally agreed that a particular storm may follow either models, or even a combination of both (Schultz et al., 1998).

The Norwegian Cyclone Model and the Shapiro-Keyser Model agree that storm genesis typically occurs along the Polar Front, an area of high baroclinicity, and where temperature gradients exist (Bjerknes, 1919, 1922; Shapiro and Keyser, 1990). The Polar Front describes the division between warm air to the south and cold air to the north, with each air mass having different buoyancy; warm air being more buoyant than cold air. A storm may develop if these different air masses were to advect into each other and occlude. Fronts define the boundaries between these air masses and are a typically regions of ascent, and are typically associated with high precipitation (Bjerknes, 1919, 1922).

Baroclinic environments typically have high vertical wind shear, where the wind speed changes with height. Thermal Wind Balance describes that areas of high horizontal temperature gradient typically have high vertical wind shear. There may be divergence or convergence of air, which can also promote ascent of air and the growth of a storm, and the deepening in mean sea level pressure of its centre (Dacre et al., 2012).

Baroclinic environments have been shown to be areas that favour storm development, as the air masses interact and lead to the development of a storm (Charney, 1947; Eady, 1949; Holton, 2004). Eady (1949) and Charney (1947) described the growth of a storm in a baroclinic environment, and proposed methods to quantify baroclinicity. Each differ by their

representation of the Coriolis force, but each calculates similar results. The Eady Growth Rate (Eady, 1949) is often used to quantify baroclinicity and is given by Equation 1.1 (Hoskins and Valdes, 1990). It can be used to indicate the suitability of an environment for storm development, with environments of high Eady Growth Rate being more favourable for storm development (Hoskins and Valdes, 1990).

Equation 1.1 describes that the most favourable environment for storm development has a high Coriolis parameter (f), low atmospheric static stability (N), and high vertical wind shear ($\frac{\partial U}{\partial Z}$). Static stability ($N$) describes the tendency of the atmosphere to vertical displacements. A statically stable atmosphere inhibits vertical displacements of air, whereas a statically unstable atmosphere is more conducive for vertical displacements. The Coriolis force (f) describes the effect whereby an air mass is affected by the rotation of the Earth and experiences a force acting perpendicular to the direction of motion. The Coriolis force varies with latitude.

$$\text{Eady Growth Rate} = 0.31 \times \frac{f}{N} \times |\frac{\partial U}{\partial Z}| \tag{1.1}$$

where:

f is the Coriolis parameter ($f = 2 \times \Omega \times \sin(\phi)$, where Ω is Earth's Rotation Speed, ϕ is latitude)

N is the Brunt Vaisala Frequency ($N = \sqrt{\frac{g}{\theta}\frac{\partial \theta}{\partial Z}}$, where g is acceleration of gravity, θ is potential temperature, Z is altitude)

$\frac{\partial U}{\partial Z}$ is the vertical wind shear (where U is zonal wind speed and Z is altitude)

Storm development has also been described by Hoskins et al. (1985), as the interaction of a positive potential vorticity (PV) anomaly at upper levels interacting with a baroclinic environment at the surface. Storms may develop if an upper-level PV anomaly is advected over a region with high meridional temperature gradients near the surface, which may then cause warm air and cold air to interact (Hoskins et al., 1985; Holton, 2004). A positive upper-level PV anomaly typically induces a cyclonic circulation in the atmosphere below. This can interact with the surface to advect warm air northward and cold air southward, resulting in the formation of a storm (see Figure 1.10). Dacre et al. (2012) also described that the divergence

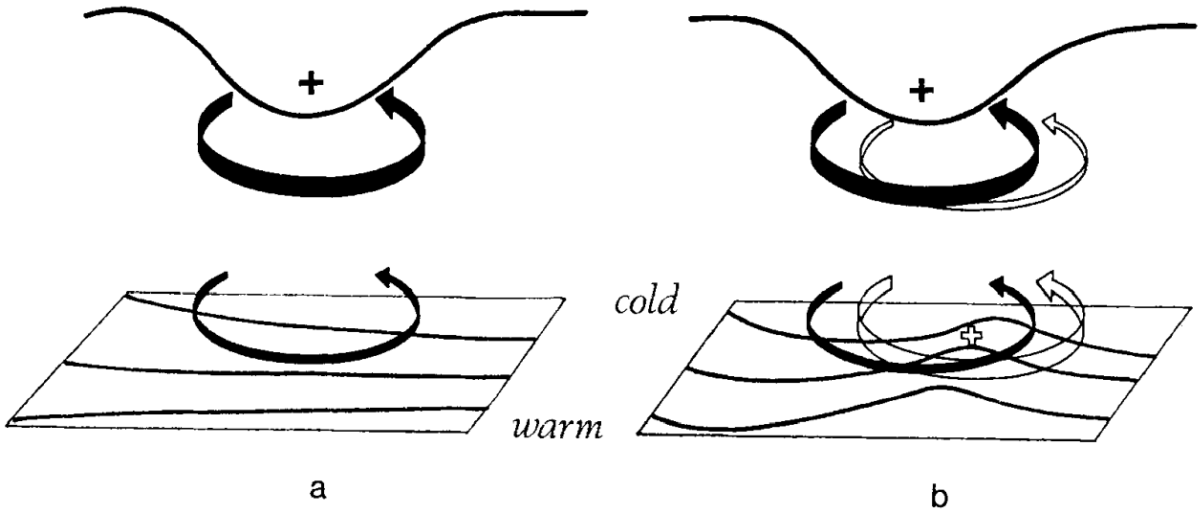

Figure 1.10: A schematic of storm genesis associated with the advection of a positive upper-level potential vorticity anomaly over a region of high temperature gradients at the surface. **a)** shows that the positive upper-level potential vorticity anomaly induces a cyclonic (anti-clockwise) circulation on the atmosphere below. **b)** Shows that this cyclonic circulation can result in the advection of warm air northward, which encourages mixing of air masses that can ultimately lead to the development of a storm. From Hoskins et al. (1985).

of air at upper levels may become aligned with the centre of the storm at the surface, leading to the ascent of air from the surface and the deepening and growth of the storm (see Figure 1.11).

Storms can also develop on the lee side of high orography. As air travels down the lee side of high orography, the column of air is stretched vertically. To conserve mass, the horizontal area of the column of air will reduce and increase in vorticity (Carlson, 1961). There are areas of high orography in the Arctic and surrounding the Arctic, which could lead to the development of Arctic storms. These include the Rockies, the Ural mountains, and other mountain ranges in north-east and central Siberia, Scandinavia, and Greenland (see Figure 1.2).

1.3.2 Arctic Storm Tracks

Previous studies have identified that the spatial distribution of Arctic storms typically depends on the season. Serreze (1995) showed that in summer, the highest density of Arctic storms occurs over the Arctic Ocean, with storms travelling northward from Eurasia and the North Atlantic Ocean. In winter, the highest density of Arctic storms tends occur over the Greenland, Norwegian and Barents Seas. Serreze et al. (2001) showed that during winter, the areas of

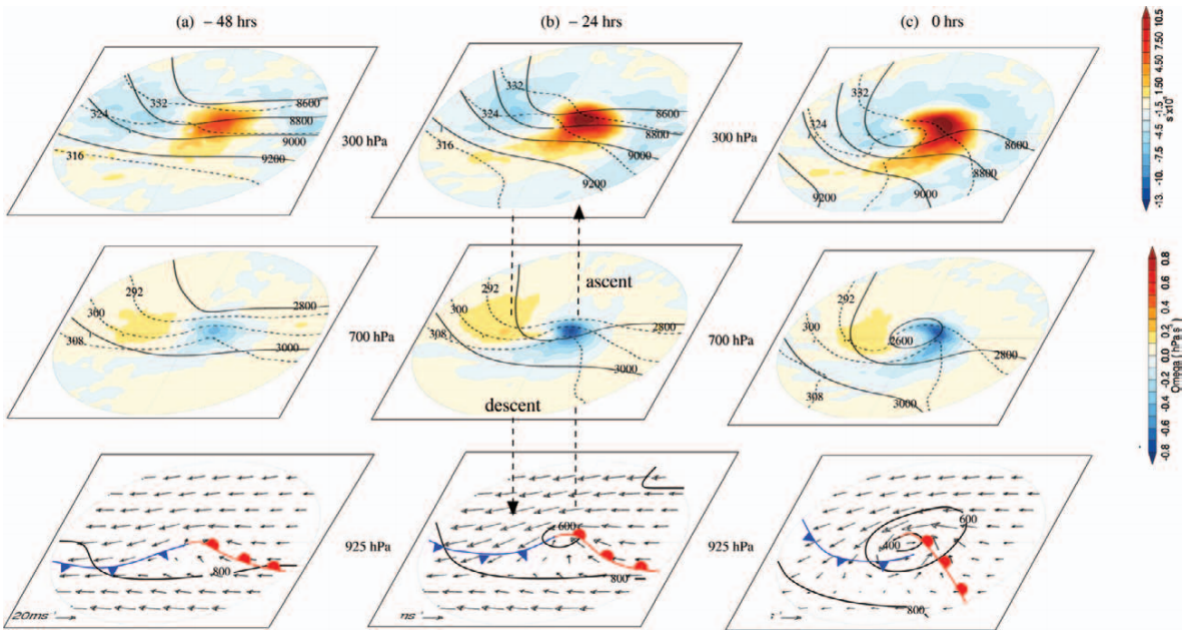

Figure 1.11: Horizontal composites at **(a)** 48 and **(b)** 24 h before the time of maximum intensity, and **(c)** at the time of maximum intensity. Bottom row: 925-hPa geopotential height (solid lines at 400, 600, and 800 m); system-relative wind vectors, and frontal positions. Middle row: 700-hPa geopotential height (solid lines at 2,800 and 3,000 m); equivalent potential temperature (θe, dashed lines at 292, 300, and 308 K) and vertical velocity (Omega, filled). Top row: 300-hPa geopotential height (solid lines at 8,600, 8,800, 9,000, and 9,200 m); θe (dashed lines at 316, 324, and 332 K) and divergence (filled). Figure and caption from Dacre et al. (2012).

greatest 850 hPa meridional temperature gradients occur over the Greenland, Norwegian and Barents Sea, but in summer the largest temperature gradients occur over AFZ. This seasonality in Arctic storm tracks has also been shown by Zhang et al. (2004), Sorteberg and Walsh (2008), Sepp and Jaagus (2011), Tilinina et al. (2013), Zahn et al. (2018).

The AFZ is an area of high baroclinicity, and typically occurs in summer (Crawford and Serreze, 2015). In summer, baroclinicity over the Greenland, Norwegian and Barents Seas is lower than it is in winter (Serreze et al., 2001), as the Arctic warms and meridional temperature gradients (and baroclinicity) decrease. The AFZ forms due to different heating of the atmosphere between air over land and the Arctic Ocean, and more storms are typically generated over the AFZ than over the Greenland, Norwegian and Barents Seas (Serreze, 1995; Crawford and Serreze, 2015, 2016; Day and Hodges, 2018). The exact role of the AFZ in storm evolution is currently open to debate, with a new line of research from Crawford and Serreze (2016) suggesting that the AFZ is more of a storm intensifier than a region of high storm genesis, and that there is higher storm genesis over inland Eurasia than the AFZ.

There is disagreement between studies to whether the total number of Arctic storms per season is similar between winter and summer. Some studies show Arctic storm number to be highest in summer (e.g. Serreze, 1995; Serreze et al., 2001; Tilinina et al., 2014; Zahn et al., 2018), whereas, Simmonds et al. (2008) found that Arctic storm number is higher in winter than in summer. There is also disagreement as to whether the total number of Arctic storms per year has changed in response to recent reductions in Arctic sea ice extent (see Figure 1.3). Earlier studies (e.g. Sorteberg and Walsh, 2008; Sepp and Jaagus, 2011) showed that Arctic storm number has increased over the past decades. Whereas, more recent studies have shown no trend in storm number (Tilinina et al., 2014; Zahn et al., 2018). There is a need to further assess Arctic storms in the present climate to better understand current Arctic storm statistics.

1.3.3 Storm Structure

The structure of mid-latitude storms in their mature phase is characterised by weather fronts, which show the boundaries between warm and cold air (see Figure 1.9a and Figure 1.9b). Storms typically have a radius greater than 1,000 km (Catto et al., 2010; Martínez-Alvarado et al., 2014). Browning (1997) described that storms typically contain conveyor belts within their horizontal and vertical extent. These are distinct air flows that arise from temperature and pressure gradients within the storm, giving rise to the movement of air (i.e. wind) (Browning, 1997). A storm may contain a Warm Conveyor Belt (WCB), an air flow ahead of the warm front that ascends northward, a Cold Conveyor Belt (CCB), an air flow ahead of the cold front that can wrap westward around the storm centre or eastward, and a Dry Intrusion that is a descending air flow toward the cold front that typically occurs south of the storm centre (see Figure 1.12). The description from Browning (1997) was based on an example storm that followed a Norwegian Cyclone Model type of development. More case studies of storms that have a similar structure to that described by Browning (1997) have been identified since using satellite imagery (e.g. see Figure 2 from Catto et al., 2010).

Martínez-Alvarado et al. (2014) described the structure of storms that typically evolve in a similar way to that described by the Shapiro–Keyser Model. These storms can have similar

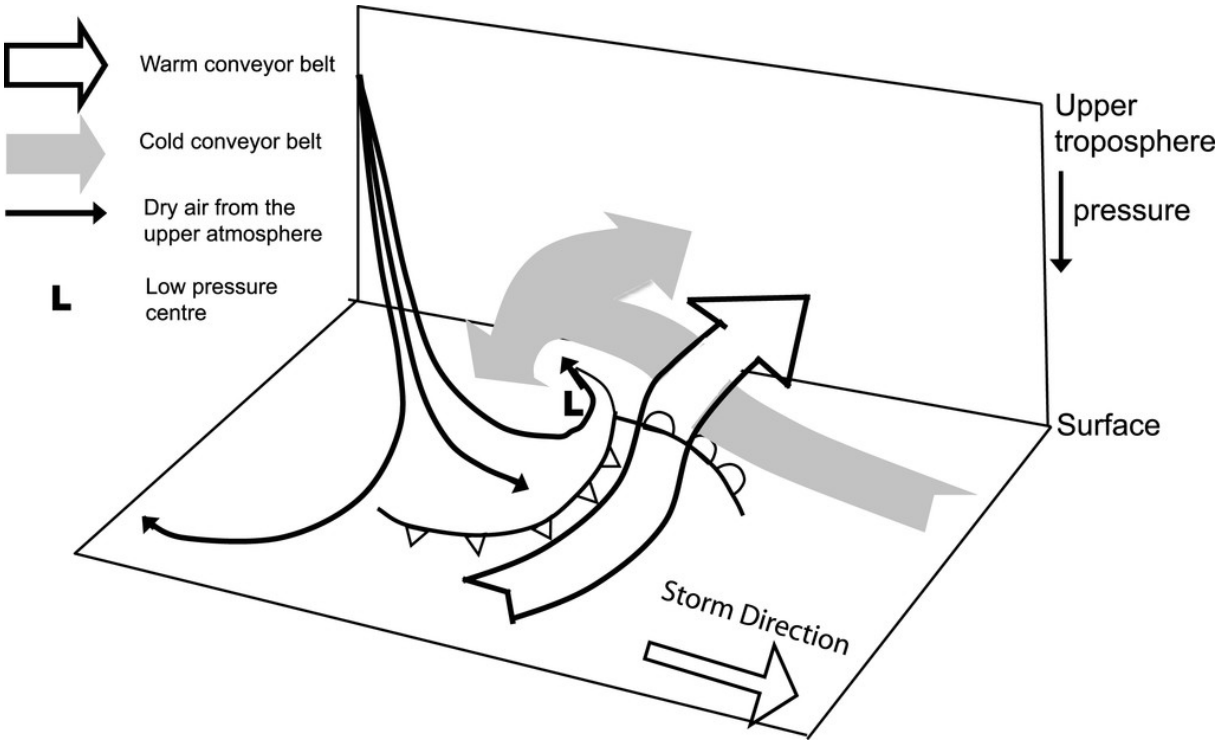

Figure 1.12: Schematic of the structure of mid-latitude storms, showing the Warm Conveyor Belt, Cold Conveyor Belt and Dry Intrusion. Figure from Catto et al. (2010), which was adapted from Browning (1997).

features to that described by Browning (1997). But may include frontal fracture and a sting jet (SJ). A sting jet is a region of very intense low-level wind speeds behind the cold front (Martínez-Alvarado et al., 2014; Browning, 2004).

1.3.4 Arctic Storm Structure

The typical structure of Arctic storms is unclear. It is currently unclear whether Arctic storms typically have a structure similar to that described by the conceptual models of Browning (1997) and Martínez-Alvarado et al. (2014), which are based on the analysis of mid-latitude storms. This is because individual case studies of Arctic storms have been identified that have a different structure to these conceptual models based on mid-latitude storms.

The Great Arctic Storm of 2012 has been the subject of previous research (e.g. Simmonds and Rudeva, 2012; Parkinson and Comiso, 2013; Aizawa and Tanaka, 2016). This storm may have contributed to the record sea ice extent minimum in September 2012 (see Figure 1.6b), by

causing the separation of a large area of sea ice due to high surface winds and waves, making it more susceptible to melting (Parkinson and Comiso, 2013). The storm reached a minimum sea level pressure of 966 hPa, which was found to be the among the most extreme summer Arctic storms in the past few decades, leading it to be referred to as "Great" (Simmonds and Rudeva, 2012).

Aizawa and Tanaka (2016) showed that around the time of maximum intensity, the Great Arctic Storm of 2012 had a deep barotropic and axi-symmetric cold-core structure throughout the troposphere without fronts, which is different to the typical structure of mid-latitude storms (see Figure 1.12). This distinct structure was also found in one other past Arctic storm case-study that occurred in June 2008 (Aizawa and Tanaka, 2016). Tao et al. (2017) also showed this in a case-study of a past Arctic storm occurring in September 2012. Aizawa and Tanaka (2016) and Tao et al. (2017) called for further research to understand the typical structure of Arctic storms.

1.3.5 Identifying and Characterising Storms using Objective Storm Tracking Algorithms

Storm tracking algorithms have been developed to identify storms within large amounts of meteorological data in a time efficient and automated way. There are currently many storm tracking algorithms available, which may identify a different number of storms from the same dataset depending on factors such as the atmospheric field and identification criteria used. For example, Neu et al. (2013) showed that the average number of winter (DJF) and summer (JJA) storms identified in the Northern Hemisphere (30° – 90°N) from 1989-2009 based on the ERA-Interim reanalysis dataset varied greatly between 70 - 214 storms and 51 - 285 storms per season respectively, using 15 different storm tracking algorithms (see Table 2 in Neu et al., 2013). Neu et al. (2013) highlighted the choice of atmospheric field used for storm tracking to be one of the main reasons why storm statistics may differ between multiple storm tracking algorithms. There are two parts of these algorithms: identification and tracking.

Storms can be identified as minima in the mean sea level pressure (MSLP) field (e.g. Serreze et al., 1993; Serreze, 1995), or as maxima in a lower tropospheric relative vorticity field as

an area of significant rotation (e.g. Hodges, 1994, 1995, 1999). Typically, more smaller-scale storms are identified by algorithms based on the relative vorticity field (Hoskins and Hodges, 2002). The number of storms identified by storm tracking algorithms can also be affected by other factors, such as different methods to filter storms after they have been identified. These filters may exclude storms under a certain intensity threshold, and storms that occur over high orography where the atmospheric field used for tracking may have been extrapolated from the surface (e.g. mean sea level pressure field). The atmospheric field may also have been filtered prior to tracking.

In addition to differing methods to identify storms, there are also multiple schemes that track systems between time steps. For example, a nearest neighbour or optimisation tracking method may be used (Serreze, 1995). There are many ways in which these algorithms may differ, which can impact the number of storms identified in a dataset (Hoskins and Hodges, 2002). The impact of the storm tracking identification variable (i.e. MSLP or relative vorticity) on the number of Arctic storms identified has not yet been evaluated.

There are other methods to quantify storm characteristics other than objective storm tracking algorithms. For example, Blackmon (1976) used a Eulerian 2–6-day band-pass filtered variance analysis to infer the main storm track regions, identifying the North Atlantic Ocean and North Pacific Ocean as regions of high storm activity. These regions have similarly been found to be areas of high storm activity using storm tracking algorithm methods (e.g. Hoskins and Hodges, 2002). Although the regions of highest storm track density are similar between these methods, the band-pass method generally gives less detail, making it harder to look at characteristics of a single storm, as the method gives an integrated interpretation of storms over long periods of time, The band-pass method may also be influenced by the development of anti-cyclones, as the methods does not isolate cyclones and anti-cyclones. More detail of a storm is given using an objective storm tracking algorithm, as the method is able to identify the track of an individual the storm, which can then be used to give additional information about the storm's life-cycle.

1.4 Impacts of Arctic Storms

Storms have long been associated with hazardous weather. They can cause high wind speeds and high precipitation, which can damage populous areas (Leckebusch et al., 2007; Hawcroft et al., 2012). For example storm Lothar, one of the most devastating storms to impact central Europe, resulted in damages totalling €15.6 billion, costing the insurance industry €8.6 billion (Munich RE, 2021). In the Arctic, storms may result in additional hazards such as high ocean waves (Thomson and Rogers, 2014; Khon et al., 2014; Liu et al., 2016; Waseda et al., 2018) and enhanced break-up of sea ice, which may become mobile and drift toward shipping lanes (Simmonds and Keay, 2009; Asplin et al., 2012; Parkinson and Comiso, 2013).

Without storms, the Arctic is already a fairly dangerous environment for human activity. It is cold, and sea ice can restrict ships to travel close to coastlines, where it is shallow (see Figure 1.2). The combination of these conditions and the passage of a storm can make the Arctic an even more dangerous environment for human activity.

As Arctic sea ice extent reduces, hazardous ocean conditions could become more severe. Wave height is determined by wind speed and fetch (the area to which wind travels over the ocean surface). Ocean wave heights have increased in the Arctic over the last few decades, as the amount of open ocean has increased (Liu et al., 2016; Waseda et al., 2018). As sea ice extent reduces over the 21st century, fetch will increase further, likely leading to taller and more hazardous ocean waves (Khon et al., 2014; Casas-Prat and Wang, 2020). Thus, the Arctic may become even more hazardous in the future.

The Arctic is being increasingly used for shipping, oil extraction and tourism (Arctic Council, 2018; Harsem et al., 2015; Maher, 2017), increasing the potential for a disaster. A well-studied case-study of a shipping disaster is the 1989 Exxon Valdez oil spill (Lyon and Weiss, 2010). The Exxon Valdez oil tanker ran aground near the coast of Tatitlek in Alaska, causing 10.8 million US gallons of crude oil to leak and pollute the local environment. The cost of this singular disaster is estimated to exceed $7 billion (Lyon and Weiss, 2010). The Arctic is also being used by cargo ships, which if damaged, may also incur substantial financial loss. For example, in

2017, the Mediterranean Shipping Company Napoli container ship was severely damaged as a result of hazardous weather in the English Channel, where wave heights exceeded 9 metres and played a role in causing the ship to run aground (Lloyds of London, 2013). The cost of the wreck removal is estimated as $135 million alone, with additional costs including the loss of cargo (Lloyds of London, 2013). These examples show that a costly disaster could occur in the Arctic.

1.5 Future Arctic Storm Tracks

The Arctic will undergo further warming over the 21st century, as a consequence of climate change (Smith et al., 2019). However, as highlighted in Section 1.2.4, warming may not be uniform across the whole Arctic and the same in all seasons. This raises the question; how will Arctic storms change in a future climate in response to climate change?

Future climate projections are typically made using atmospheric models with an added climate forcing, to simulate possible future atmospheric conditions. The Inter-Governmental Panel on Climate Change (IPCC) has devised future climate scenarios, including the Representative Concentration Pathways (RCPs), which describe how much additional carbon dioxide there may be in a future atmosphere following different future emission scenarios. There are four main possible RCPs described by the IPCC: RCP2.6, RCP4.5, RCP6.0 and RCP8.5 (Pachauri et al., 2014). Each differ by the amount of extra carbon dioxide there may be in the atmosphere, with RCP8.5 having the greatest increase in future carbon dioxide levels (see Table SPM.1 in Pachauri et al., 2014).

Results from previous studies show that the spatial distribution of Arctic storms will likely change in response to climate change (e.g. Orsolini and Sorteberg, 2009; Akperov et al., 2015; Nishii et al., 2015; Crawford and Serreze, 2017; Day et al., 2018). Orsolini and Sorteberg (2009) showed that the number and intensity of summer storms that travel over the Arctic Ocean may increase in response to climate change. Similar results are shown by Akperov et al. (2015) and Nishii et al. (2015). Crawford and Serreze (2017) and Day et al. (2018) showed that the

change in summer Arctic storm frequency may be more regional. These recent studies found that Arctic storm density will likely increase over the Canadian Archipelago, but decrease over Eurasia. This suggests that the risk to human activity from storms may increase or decrease in different regions across the Arctic in response to climate change.

A main focus of previous research has been to determine the future response of Arctic storms in summertime, as this is when exposure of human activity to storms is highest. Akperov et al. (2015) found the number of Arctic storms in the cold season (October-March) will decrease in the future. Moreover, Day et al. (2018) showed that in winter (DJF) there may be a decrease in Arctic storm track density around Greenland and the Arctic Ocean. In addition, future winter Arctic storms that travel over the Arctic Ocean may be less intense than those in the present climate (Day et al., 2018). More work is needed to assess the change in Arctic storm track density in all seasons.

Nishii et al. (2015) also highlighted that there is uncertainty in these changes when comparing multiple future atmospheric projections from models in the Coupled Model Inter-Comparison Project Phase 5 (CMIP5) ensemble, and called for a further investigation of the inter-model spread in the future response of Arctic storms to climate change. In particular, Nishii et al. (2015) highlighted that horizontal resolution may affect the response of Arctic storms to climate change shown by different models. Both Crawford and Serreze (2017) and Day et al. (2018) used future projections made by the Community Earth System Model Ensemble, therefore, one would expect their results to be fairly similar.

This calls for further investigation of Arctic storms in the future climate using other models, to validate previous results. This will lead to a better understanding in the range of possible responses of Arctic storms to climate change. Moreover, future work is needed to understand why future climate projections made using different models may differ, to understand the sources of uncertainty in these simulations. This may lead to greater confidence in how Arctic storms may change in response to climate change.

1.6 Human Activity in the Arctic

1.6.1 Arctic Shipping

The Arctic Ocean has only just become navigable in recent decades for Arctic voyages, as sea ice extent has sufficiently declined. In 2007, the largest reduction from the previous year in the minimum Arctic sea ice extent in September occurred (see Figure 1.3), and was the first time sea ice extent was below 5 million km^2 (see Figure 1.6). Sea ice extent decreased from 5.86 million km^2 in 2006 to 4.27 million km^2 in 2007, a reduction of 1.59 million km^2 (see Figure 1.6). The year of 2008 was the first year where the shipping lanes connecting North America and Europe to Asia were open simultaneously, due to sea ice retreating northward from the Eurasian coastline and the Canadian Archipelago (European Space Agency, 2008). This feat was next achieved in 2011 (European Space Agency, 2011). In 2012, Arctic sea ice extent reduced to a new record minimum extent of 3.6 million km^2 (see Figure 1.6). These landmark events between 2007 and 2012 raised awareness that North America, Europe and Asia could be connected by shipping routes in the Arctic Ocean and has since encouraged ships to travel through the Arctic.

The first large commercial vessel to complete a transit from Asia to Europe following the coastline of Eurasia was the Yong Sheng, in 2013 (Financial Times, 2013). In the same year, the Nordic Orion was the first large commercial vessel to travel through the west Arctic Ocean, as it completed its journey from Vancouver, through the Canadian Archipelago, to Finland (US Dept. of Defense, 2020). The first cargo vessel to complete a transit through the Arctic without the assistance of an Icebreaker (a ship that cuts a path through sea ice for other ships to follow - see Figure 1.13) occurred in 2014 (BBC, 2018).

The establishment of the Polar Code in 2014 by the International Maritime Organization showed that the number of ships in the Arctic was expected by regulatory authorities to increase in the following years. The Polar Code sets out regulations for ships that travel through the Polar Code Area, in ordered to ensure safety in Arctic shipping (International Maritime Organization, 2016). Since these pioneering transits first showed that travel through the Arctic Ocean was

Figure 1.13: The Icebreakers Andrey Vilkitsky (foreground) and Alexander Sannikov (left background) providing year-round support to shipping in the Northern Sea Route (see Figure 1.14) in June 2019. Sourced from Gazprom Neft (2020).

possible, Arctic shipping has been encouraged by further reductions in sea ice extent and has since increased (Arctic Council, 2018).

Arctic shipping is currently limited by sea ice extent. At the time of maximum sea ice extent typically in March, it is only the Greenland, Norwegian and Barents Seas that are not covered by sea ice (see Figure 1.5). This is likely because the Gulf Stream transports warm water toward the Barents Sea region, heating the ocean and preventing sea ice formation. At the time of minimum sea ice extent typically in September, sea ice retreats northward, and two shipping routes that connect Baffin Bay and the Barents Sea to the the Bering Strait open and become navigable; the North-West Passage and Northern Sea Route (see Figure 1.14). Each shipping route follows the coastline of North America and Eurasia respectively, and connect North America and Europe to Asia (see Figure 1.14). Arctic sea ice is expected to reduce further in the near-future (Stroeve et al., 2007, 2012), which may enable ships to travel more closely to the North Pole, along the Trans-Arctic sea route (Melia et al., 2016) (see Figure 1.14).

The main benefit of travelling through the Arctic is that it offers shorter routes to destinations between continents than traditional mid-latitude routes. Traditionally, ships that travel between

Figure 1.14: Map showing the main Arctic shipping routes of the North-West Passage (through the Canadian Archipelago), the Northern Sea Route (along the coastline of Eurasia), and Trans-Arctic Sea Route (over the North Pole). Hypothetical sea ice cover is shown in white. Adapted from BBC (2016).

Europe and Asia travel through the Suez Canal, through the Mediterranean and Red Sea. Ports on the east coast of North America are connected to Asia through the Panama Canal, which runs by Panama City. Distances along Arctic shipping routes are shorter than these traditional mid-latitude shipping routes between Europe and North America to Asia (see Table 1.1). Moreover, these mid-latitude shipping routes also include the passage through busy, long and narrow straits, which can be subject to potential delays and disruption for shipping (e.g. the blockage of the Suez Canal by the Ever Given ship in March 2021 - BBC, 2021).

The distance between the Port of Rotterdam and Tokyo along the Northern Sea Route is 4,300 nautical miles shorter than along the Suez Canal shipping route (see Table 1.1). If the speed of a ship is assumed to be 10 knots (approximately 11.5 miles per hour), this means that the journey between these destinations would be approximately 15.5 days shorter when using the

Table 1.1: Distances between major ports in Europe and North America to major ports in Asia when using Arctic routes, or mid-latitude routes (the Suez Canal Route between Europe and Asia, and the Panama Canal Route between North America and Asia). The distances have been calculated on Google Earth (Google, 2021), and are given to the nearest hundred nautical miles (nm).

Departure Port	Destination Port	Distance Using Mid-Latitude Route	Distance Using Arctic Route (1979-2020 mean Sept. Arctic Sea Ice extent)	Arctic Minus Mid-Latitude Route (1979-2020 Sept. Arctic Sea Ice extent)
Rotterdam	Tokyo	11,300 nm	7,000 nm	**-4,300 nm**
Rotterdam	Shanghai	10,500 nm	7,900 nm	**-2,600 nm**
New York and New Jersey	Tokyo	9,700 nm	7,400 nm	**-2,300 nm**
New York and New Jersey	Shanghai	10,700 nm	8,300 nm	**-2,400 nm**

Arctic route. This would lead to fuel savings, and reduced time for travel between destinations, allowing ships to be used for additional journeys throughout the year. Thus, using the Arctic for shipping could increase revenue for shipping companies.

Distances along Arctic routes will be even short in the future and ships are able to use the more direct Trans-Arctic route, as sea ice extent reduces further. This will give even more incentive to use the Arctic for shipping. As the number of ships in the Arctic increases, so does the exposure of valuable assets and risk to life from hazards such as Arctic storms. Thus, it is becoming increasingly important to understand Arctic storms and better evaluate the risk they pose to human activity (e.g. shipping), so that activities can become safer and potential financial damages can be mitigated through insurance.

1.6.2 Other Human Activity in the Arctic

The Arctic is also being increasingly used for tourism and oil exploration. The Crystal Serenity became the first cruise liner to travel through the North-West Passage in 2016 (National Geographic, 2016). This has encouraged more tourism activities in the Arctic since (Maher, 2017; Lasserre, 2019), and there are now multiple Arctic cruises in a year (Têtu et al., 2019).

Recent reductions in Arctic sea ice extent have allowed for access to the Arctic Ocean floor, which has encouraged the search for natural resources in the Arctic Ocean (Bird et al., 2008; The Arctic Institute, 2013; Harsem et al., 2015). This search and extraction of natural resources has brought valuable assets such as oil rigs, support infrastructure and people, into the Arctic. As a result, the value of assets exposed to hazardous weather has increased. It has also increased the chances of an extremely costly environmental disaster such as an oil spill.

1.7 Current Knowledge Gaps

1.7.1 Present Climate Arctic Storm Characteristics

The choice of reanalysis dataset and storm tracking algorithm identification variable has been shown to contribute to differences in the present-day climatology of Northern Hemisphere storms (e.g. Hodges et al. 2011; Neu et al. 2013), which introduces uncertainty about present-day climate Arctic storm statistics. The impacts of the choice of global reanalysis dataset and of storm tracking identification variable on present-day climate Arctic storm statistics are unclear. Furthermore, there are still questions as to the seasonality of present-day climate Arctic storms and whether recent reductions in Arctic sea ice extent have led to changes in the number of storms. A more comprehensive evaluation of Arctic storms in global reanalysis datasets using different storm tracking identification variables is needed to clarify present-day climate characteristics of Arctic storms.

1.7.2 Arctic Storm Development and Structure

The structure and development of mid-latitude storms has been a focal point of research over the past 100 years. But, storms that occur in mid-latitude regions (30°N - 65°N) have been the primary focus, likely due to their impact on populous areas such as Europe. Subsequently, conceptual models of mid-latitude storms have been developed (e.g. the Norwegian Cyclone Model and the Shapiro Keyser Cyclone Model - see Figure 1.9), and their general structure is fairly well understood (see Figure 1.12).

Analysis on the structure and development of Arctic storms is limited to a few individual case studies, particularly of storms occurring in summertime. These studies show that some Arctic storms have a different structure to typical mid-latitude storms and to that of conceptual models (e.g. Norwegian Cyclone Model and Shapiro-Keyser Model) (Tanaka et al., 2012; Aizawa and Tanaka, 2016; Tao et al., 2017). Based on just two case studies, Aizawa and Tanaka (2016) proposed a model of the structure of Arctic summer storms. However, Aizawa and Tanaka (2016) could not find their model to be typical of most Arctic summer storms due to their focus on just two case studies, and called for further studies to test the models generality by performing a more systematic structural investigation involving a larger sample of Arctic storms. Moreover, some past Arctic storms have been identified that have exceptionally long lifetimes (Simmonds and Rudeva, 2012; Yamagami et al., 2017). For example, Yamagami et al. (2017) described an Arctic storm that occurred in summer 2016, that had a lifetime greater than a month. This raises the questions, what is the general structure of Arctic storms? Does this vary seasonally? Why do some Arctic storms have such long lifetimes?

1.7.3 Future Climate Arctic Storm Characteristics

Over the 21st century, the Arctic will undergo the most warming of any other region on Earth, due to Arctic Amplification (Smith et al., 2019). The future response of Arctic storms to climate change has only been described in few studies such as Orsolini and Sorteberg (2009), Akperov et al. (2015), Nishii et al. (2015), Crawford and Serreze (2017) and Day et al. (2018). There is a continual need to assess how Arctic storms may change in the future in response to climate change to determine the range and uncertainty in possible responses. There is also a need to understand why future projections from different models may differ, which introduce uncertainty in the response of Arctic storms to climate change.

One way in which climate models can differ is their horizontal resolution. Climate models have undergone rapid refinement over recent decades due to great improvements in computational resources. Thus, there are currently many climate models with differing horizontal resolution

that are used to project the future atmosphere. The Arctic is a region of complex orography, and, sharp temperature gradients that result from the distinct changes in surface type (between land, ocean and sea ice). One of the key questions that has not been investigated is how the horizontal resolution of the climate model impacts the future projection. Does it influence the projected response of Arctic storms to climate change?

1.7.4 The Risk of Storms to Arctic Shipping

Presently, the number of ships in the Arctic that are impacted by the passage of a storm has not been quantified. Though, there have been studies that have quantified the number of ships that operate in the Arctic. For example, Eguiluz et al. (2016) described the spatial and seasonal distribution of ships that operated in the Arctic from 2010-2014. In addition, in a report from the Arctic Council in 2018 highlighted that the number of ships travelling through the Arctic from 2013-2019 has increased (Arctic Council, 2018). However, no study has yet combined historic Arctic storm tracks with historic shipping transits in the Arctic, in order to quantify the number of ships that have been impacted by past Arctic storms.

1.8 Research Questions and Thesis Outline

The overall aim of this thesis is to **improve the understanding of present and future risk associated with synoptic-scale Arctic storms and the mechanisms that lead to their development**. In order to fulfil this aim, research questions (RQ) have been devised to address the knowledge gaps identified in Section 1.7, which are investigated in Chapters 3 - 6. These include:

RQ1: What are the present-day climate characteristics of Arctic storms, and, what is the uncertainty associated with the choice of reanalysis dataset and storm tracking identification variable?

RQ2: What is the typical development and structure of Arctic storms, and how does this differ to that of mid-latitude storms and existing conceptual models?

RQ3: How might Arctic storms change in response to climate change? In particular, does the horizontal resolution of the climate model impact the response of Arctic storms to climate change?

RQ4: How can we best use information on Arctic storms and shipping activity to assess storm risk in the Arctic?

The remainder of this thesis is structured as follows:

Chapter 2: Data and Methods

In this chapter, a description of the main datasets used in this thesis is given. A description of the storm identification and tracking method is also given, as well as a description the analysis techniques.

Chapter 3: An Inter-Comparison of Arctic Synoptic Scale Storms between Four Global Reanalysis Datasets

This chapter identifies the climatology of Arctic storms from 1980-2017, using data from modern reanalysis datasets. Moreover, Arctic storms statistics identified using a storm tracking algorithm based on 850 hPa relative vorticity and mean sea level pressure are compared. This chapter was published in full in the Journal of *Climate Dynamics* as Vessey et al. (2020). In addition to Vessey et al. (2020), the climatology of Arctic storms identified in a new reanalysis dataset, ERA-5, which was released after the submission of Vessey et al. (2020), is given.

Chapter 4: Arctic Storm Development and Structure

The structure and development of some past Arctic storms has been shown to be different to that of mid-latitude storms, and to that described by existing conceptual models of mid-latitude storm development (e.g. the Norwegian Cyclone Development Model from Bjerknes, 1919, 1922) and of mid-latitude storm structure (e.g. Browning, 1997). In this chapter, the typical structure and development of a large sample of past Arctic storms per season is investigated using storm compositing methodology. The structure of Arctic

storms per season is also compared to that storms that occur over the North Atlantic Ocean.

Chapter 5: Response of Arctic Storms to Climate Change: Sensitivity to Model Horizontal Resolution

The Arctic will undergo substantial warming over the 21st century in response to climate change. This chapter describes how Arctic storms may change in a future climate by analysing and evaluating future climate simulations of the atmosphere. Furthermore, the impact of model horizontal resolution on these future climate simulations and the response of Arctic storms to climate change is assessed.

Chapter 6: The Risk of Arctic Storms to Shipping

This chapter describes the changes in shipping across the Arctic in recent years. Arctic shipping data is then combined with historical Arctic storm tracks to assess the current exposure of ships to Arctic storms.

Chapter 7: Discussion and Conclusions

Finally, the main conclusions of this thesis are summarised and discussed. The limitations of this thesis are also summarised, and ideas for future work are proposed.

Chapter 2

Data and Methods

In this chapter, an overview of the datasets and methods used to examine Arctic storms and answer the research questions outlined in Section 1.8 is given. Firstly, the datasets that are used to assess the present-day climate characteristics of Arctic storms are described in Section 2.1. Secondly, a description of the future climate simulations analysed to determine the response of Arctic storms to climate change is given in Section 2.2. Thirdly, the dataset used to examine current Arctic shipping activities is discussed in Section 2.3. Finally, the objective storm identification tracking method used to identify Arctic storms within the datasets is described in Section 2.4, along with a description of the analysis techniques used to determine storm statistics and composite structure.

2.1 Reanalysis Datasets

2.1.1 What is a Reanalysis Dataset?

To assess historical Arctic storm activity over the past few decades, the most suitable data to use is a spatially and temporally homogeneous gridded dataset. Such data are available in the form of reanalysis datasets. Reanalysis datasets have been developed over recent decades and provide the most-suitable 4-dimensional representation of past atmospheric conditions. They are created by assimilating historical observations from a range of sources into state-of-the-art Numerical Weather Prediction (NWP) models. NWP models use super-computers to solve equations that describe the state of the atmosphere quickly. The Arctic is typically poorly observed, with more limited surface observations compared to other regions, due to its remoteness (Jung et al., 2016). Data from satellites became available from 1979, which greatly increased the availability of atmospheric data in the Arctic. Thus, most reanalysis datasets include atmospheric data from 1979.

The version of the NWP model and data assimilation scheme used to produce reanalysis data are kept constant to ensure homogeneity of the data created. Data are typically available at regular 6-hour intervals (i.e. 00:00 UTC, 06:00 UTC, 12:00 UTC and 18:00 UTC), though in the most recent reanalysis dataset, ERA5, data are output at 1-hour intervals (see Table 2.1). Data are output onto a grid, with horizontal resolution denoting the horizontal area of each grid-cell, and the vertical resolution denoting the vertical extent of each grid-cell throughout the depth of the atmosphere. Typically, reanalysis datasets have a global domain, however, some modern reanalysis datasets, such as the Arctic System Reanalysis, have a regional domain, allowing them to be run at a higher spatial resolution (Bromwich et al., 2018). Regional reanalysis datasets allow for higher resolution of the region, at the same computational cost as a lower resolution global reanalysis dataset. However, this also brings with it disadvantages, such as reduced influence of the atmosphere outside of the regional domain. The Arctic System Reanalysis also only includes data from only 2000-2010, limiting its use to identify long-term present-day climate statistics of Arctic storms. This thesis aims to

analyse Arctic storms that have genesis outside of the Arctic as well as those with genesis inside the Arctic, therefore global reanalysis datasets are most suitable.

2.1.2 Reanalysis Datasets used in this Thesis

Multiple global reanalysis datasets have been produced over the last few decades, with multiple meteorological institutes producing their own dataset or an updated dataset, using modern NWP models and data assimilation methods. The global reanalysis datasets used in this thesis are listed below, and a description of the specifications of each dataset is given in Table 2.1.

- **ERA-Interim** from the European Centre for Medium-Range Weather Forecasts (ECMWF) (Dee et al., 2011)
- **ERA5** from the European Centre for Medium-Range Weather Forecasts (ECMWF) (Hersbach et al., 2020)
- **JRA-55** from the Japanese Meteorological Society (JMA) (Kobayashi et al., 2015)
- **MERRA-2** from the National Aeronautics Space Association (NASA) (Gelaro et al., 2017)
- **NCEP-CFSR** from the National Centers for Environmental Prediction and National Center for Atmospheric Research (NCEP and NCAR) (Saha et al., 2014)

2.1.3 Differences between the Reanalysis Datasets

Each of the reanalysis datasets have been created using a different atmospheric model that may have a different dynamical cores (how mathematical equations of the atmosphere are solved), data assimilation methods, and horizontal and vertical resolution (see Table 2.1). Many more differences may also exist. These may all impact the data simulated of the past atmosphere, and lead to differences in past storm statistics (e.g. Hoskins and Hodges, 2002).

Table 2.1: Key differences between the ERA-Interim, ERA5, JRA-55, MERRA-2, NCEP-CFSR reanalysis datasets.

Reanalysis Name	Institution	Time Period	Model Used	Model Type	Horizontal Vertical Resolution	Temporal Resolution	Data Assimilation Method	Sea Ice Concentration	Land Surface Model
ERA5	ECMWF	1950-present	ECMWF IFS (41r2)	Spectral	TL639 (0.25° × 0.25°) / 137 levels up to 0.01hPa	1-hourly	4D-Var	HadISST2.0.0.0 (1950-1978), OSI SAF (1979-present)	HTESSEL Scheme
ERA-Interim	ECMWF	1979-2019	ECMWF IFS (Cy31r2)	Spectral	TL255 (0.75° × 0.75°) / 60 levels up to 0.1hPa	6-hourly	4D-Var	OSTIA	TESSEL Scheme
JRA-55	JMA	1958-present	JMA's Global Spectral Model (GSM)	Spectral	T319L60 (0.55° × 0.55°) / 60 levels up to 0.1hPa	6-hourly	4D-Var	COBE-SST	Simple Biosphere (SiB)
MERRA-2	NASA	1980-present	NASA GEOS	Grid Point	0.5° × 0.625° / 72 levels up to 0.01hPa	6-hourly	3D-Var	OSTIA	Catchment Model
NCEP-CFSR	NCEP & NCAR	1979-present	NCEP CFS	Spectral Coupled Atmosphere-Ocean-Land	0.5° × 0.5° / 64 levels up to 0.3hPa	6-hourly	4D-Var	GFDL Sea Ice Simulator	NASA LSM

Note: ECMWF = European Centre for Medium Range Forecasts, JMA = Japanese Meteorological Association, NASA = National Aeronautics Space Association, NCEP = National Centers for Environmental Prediction, NCAR = National Center for Atmospheric Research. Sourcesof information include (Dee et al., 2011; Hersbach et al., 2020; Kobayashi et al., 2015; Gelaro et al., 2017; Saha et al., 2014).

Data assimilation describes the way that historical observations are incorporated into the atmospheric model to produce the analysis or "best guess" of the past atmospheric state. During this process the model background state (the models "first guess" of past atmospheric conditions) is nudged towards the historical observations. This produces the best estimate of past atmospheric conditions that is more consistent with the observations than the model background state. However, this is not a simple process, and methods can differ. Table 2.1 shows that MERRA-2 is created using a 3D-Var data assimilation scheme, whereas the other datasets are created using a 4D-Var data assimilation scheme. Observations are also quality controlled during the data assimilation process, where observations that are too different to the background state can be rejected, to ensure numerical stability of the atmospheric model. Methods of achieving this may differ between the reanalysis datasets.

Horizontal resolution has been shown to impact the number of storms captured in a dataset. Jung et al. (2006) showed that the number of storms captured by the same NWP model nearly doubled when the resolution was increased from T95L60 to T255L60. Horizontal resolution may also affect the representation of storm intensity, with reanalysis datasets with higher horizontal resolution having more intense storms (Hersbach, 2019). The reanalysis dataset used in this thesis with the highest horizontal and vertical resolution is ERA5, where data are output at a spectral resolution of TL639, which is equivalent to 0.25° x 0.25° on a longitude and latitude grid, with 137 levels up to 0.01hPa. The reanalysis dataset with the lowest horizontal resolution is ERA-Interim, which has a spectral resolution of TL255 that is equivalent to 0.75° x 0.75° on a longitude and latitude grid, with 60 levels up to 0.1hPa.

Overall, it is evident that there are numerous differences in the methods used to create each reanalysis dataset. They are used in a range of applications across meteorological and weather-related hazard research. They are often used as "the truth" even though they are a simulation, and it is often not considered how results may differ by using a different reanalysis dataset. The same is true when they are used for the evaluation of other atmospheric models e.g. General Circulation Models. Differences in the methods of creating a reanalysis dataset (i.e. horizontal resolution, data assimilation method, model used, use of observations) can impact the accuracy of the data created compared to the true past state of the atmosphere.

Thus, it is imperative to understand the differences between each reanalysis dataset as they are essentially approximations, not perfect representations of past atmospheric conditions.

2.2 HadGEM3-GA3.0 Future Climate Simulations

2.2.1 How are Future Climate Simulations Made?

General Circulation Models (GCMs) are often used to simulate future atmospheric conditions and determine the change between present-day climate conditions and future climate conditions. They use atmospheric computer models to simulate the atmosphere as well as other land processes (e.g. vegetation processes), but by adding a climate forcing (e.g. by increasing the amount of carbon dioxide in the atmosphere). These forcings are typically based on the Representative Concentration Pathways (RCPs) devised by the Inter-Governmental Panel on Climate Change (IPCC) (Van Vuuren et al., 2011). Though, in the latest generation of GCMs (e.g. the CMIP-6 ensemble), these RCP future climate scenarios have been updated and are referred to as Shared Socioeconomic Pathways (SSP) (Carbon Brief, 2019). These future climate scenarios describe multiple possible future scenarios of how human activity may react to climate change and influence the atmosphere, leading to a range of possible future scenarios with varying magnitudes of climate change (i.e. further temperature changes). For example, RCP8.5 is often referred to as the worst-case future climate scenario, with the greatest warming by the end of the century of all RCPs. It describes a continual increase in carbon dioxide levels until 2100, resulting in an additional 8.5 Wm^{-2} radiative forcing by 2100 (see Figure 9 in Van Vuuren et al. 2011).

Like reanalysis datasets, there are multiple GCMs available, and each is different. GCMs are used for both climate simulations and weather forecasts, but climate simulations tend to be run at a lower resolution due to the required simulation length, which is typically to the end of the century. One main difference between GCMs is whether they simulate only the atmosphere (atmosphere-only) or the atmosphere and ocean (coupled). In coupled models, the ocean and atmosphere can evolve and interact, whereas in atmosphere-only models, the state of boundary

conditions to the atmosphere e.g. sea surface temperature and sea ice extent, are determined by an external dataset. These models can also differ by the underlying atmospheric model that is used to solve mathematical equations of the atmosphere, and each model's horizontal and vertical resolution. Differences between models can impact the simulation of the future atmosphere that they make, and this can lead to uncertainty in the response of the atmosphere to climate change.

2.2.2 HadGEM3-GA3.0 Simulations

An ensemble of future climate simulations is analysed in this thesis, which was created by the United Kingdom on Partnership for Advanced Computing in Europe (PRACE): Weather-Resolving Simulations of Climate for Global Environmental Risk (UPSCALE) project (Mizielinski et al., 2014). These simulations have been made using the atmosphere-only Hadley Centre Global Environmental Model (version 3) Global Atmosphere 3.0 (HadGEM3-GA3.0) (Walters and Coauthors, 2011), at different horizontal resolutions, whilst all other configurations of the model are the same between each simulation. This allows for the analysis of how Arctic storms may change in the future in response to climate change, but also for the assessment of how horizontal resolution may affect the simulated response of Arctic storms to climate change.

The ensemble contains simulations of the present-day climate from 1986-2011 and additionally of the end of the 21st century future climate from 2086-2111 (following the RCP8.5 future climate scenario). The present-day climate simulations have been made using 5, 3 and 5 ensemble members at horizontal resolutions of N512, N216 and N96 respectively. The future climate simulations have been made using 3 ensemble members at each horizontal resolution of N512, N216 and N96. At 50° latitude, the horizontal resolution of N512, N216 and N96 simulations are equivalent to grid cells with an area of approximately 25 km, 60 km and 135 km (see Figure 2.1). The vertical resolution is constant across all simulations, with 85 vertical levels up to an altitude of 85 km (Mizielinski et al., 2014). Other settings of the HadGEM3-GA3.0 model have been kept the same between all simulations (Mizielinski et al.,

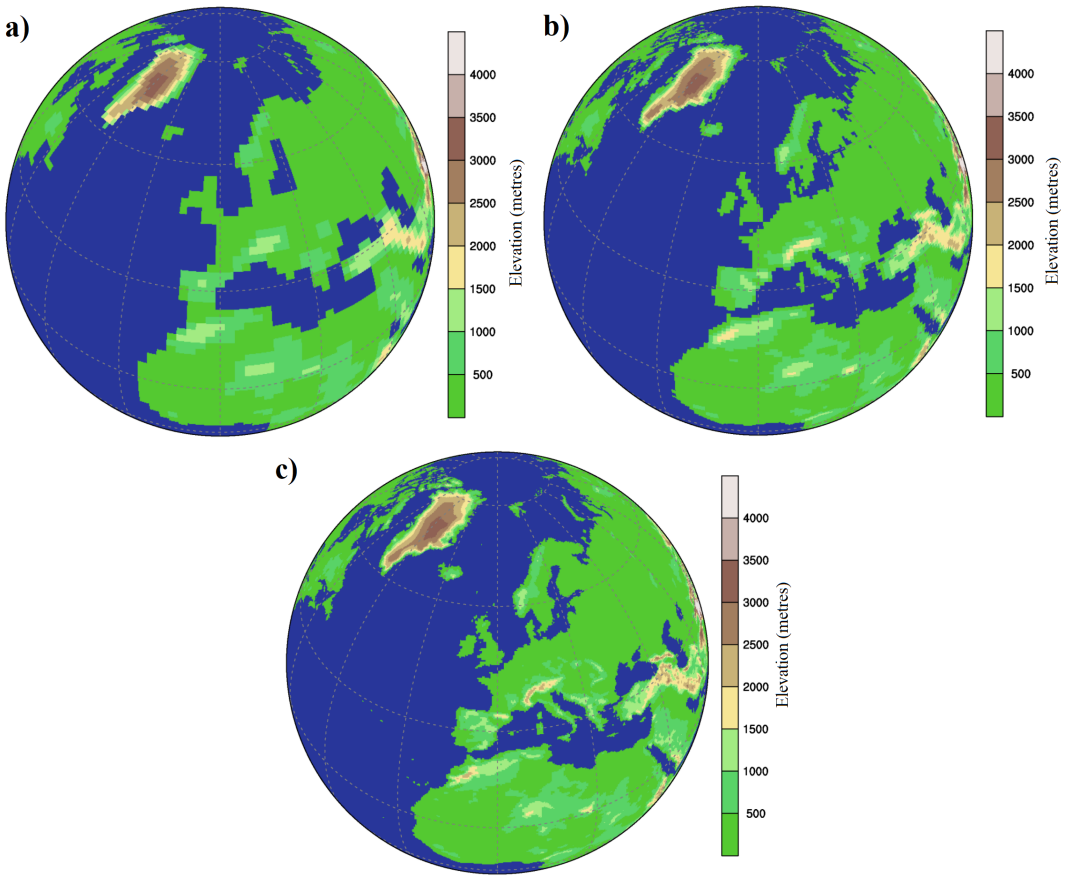

Figure 2.1: A schematic illustrating the differences in the representation of the Earth's surface and topography in an atmospheric model with a horizontal resolution of **a)** N96 (130 km), **b)** N216 (60 km), and **c)** N512 (25 km). From UPSCALE (2021).

2014). Thus, the impact of horizontal resolution on the present-day and future climate simulations can be isolated and assessed.

In the present-day climate simulations, sea surface temperatures (SSTs) and sea ice extent were prescribed in the HadGEM3-GA3.0 model using the Operational Sea Surface Temperature and Sea Ice Analysis (OSTIA) dataset (Donlon et al., 2012), which were regridded to each of the N512, N216 and N96 resolutions. This dataset is based on satellite observations from 1985 and provides daily SST and sea ice data (Donlon et al., 2012).

The end of century (2086-2110) future atmosphere has been simulated using the HadGEM3-GA3.0 model at each horizontal resolution, following the RCP8.5 future emission scenario (Mizielinski et al., 2014). Following this pathway, carbon dioxide emissions continue to increase throughout the 21st century and there is an additional 8.5 Wm^{-2} radiative forcing by 2100 (see Figure 9 in Van Vuuren et al. 2011).

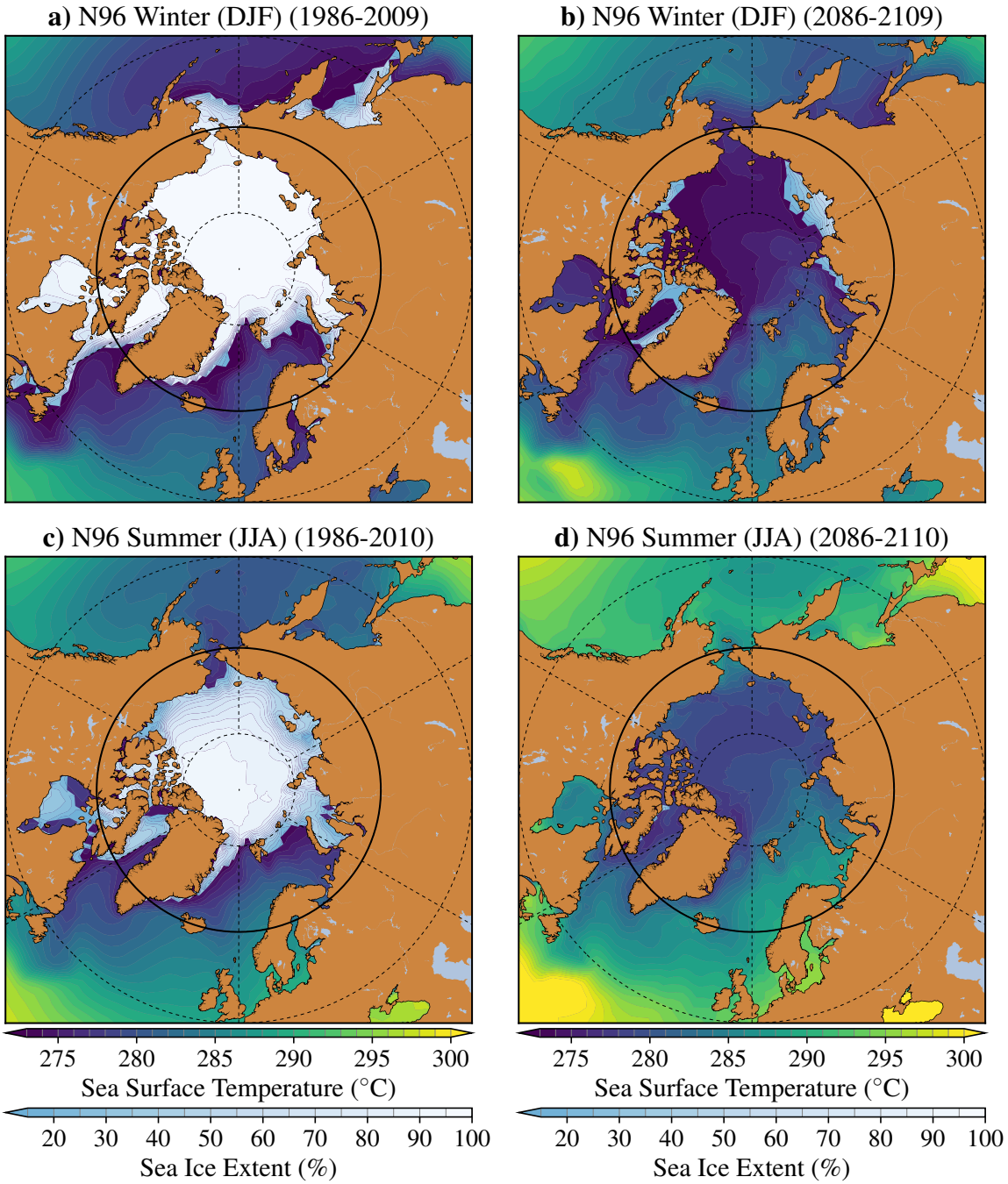

Figure 2.2: Mean sea surface temperature (SST) and sea ice extent in the HadGEM3-GA3.0 N96 present-day climate simulations (1986-2010) and RCP8.5 future climate simulations (2086-2110) in winter (DJF) (**a and b**) summer (JJA) (**c and e**). **a) and c)** are of the present-day climate simulations (1986-2010), and **b) and d)** are of the RCP8.5 future climate simulations (2086-2110).

Sea surface temperatures and sea ice extent were prescribed using the SSTs from the present-day climate plus the change in SST between 1990-2010 and 2090-2110 per month, as derived from simulations using the HadGEM2 Earth System following RCP8.5 future climate scenario (Collins et al., 2011). These HadGEM2 simulations were made following SST and sea ice changes based on Atmospheric Model Inter-comparison Project (AMIP I) (Gates et al.,

1999). Likewise, future sea ice extent was prescribed from the same HadGEM2 Earth System simulations using the RCP8.5 scenario. Future changes in SST and sea ice extent were interpolated from monthly to daily frequencies. To account for the day-to-day variability, this monthly change is added to the daily OSTIA data that is used in the present-day climate simulations (Mizielinski et al., 2014). For regions that lose sea ice coverage in the RCP8.5 future climate, SST values from the HadGEM2 Earth System simulations were used.

Figure 2.2 shows the changes in SST and sea ice extent in winter (DJF) and summer (JJA) between the present-day and RCP8.5 future climate N96 HadGEM3-GA3.0 simulations. In summer, future sea ice extent is much reduced over the Arctic Ocean, with ice only remaining over land and a very small region west of Greenland (see Figure 2.2). In winter, sea ice remains in the Canadian Archipelago and north of the Eurasian coastline in the future climate simulations.

However, these sea ice amounts do seem rather low when compared to other studies. For example, Figure 12.29 in Collins et al. (2013) shows a higher sea ice concentration between 2081 and 2100 following the RCP8.5 future climate scenario using the multi-model mean of CMIP-5 models, particularly in winter. Collins et al. (2013) shows that in CMIP-5 models in February, sea ice covers most of the Arctic Ocean in a RCP8.5 future climate, with the highest concentrations occurring around Greenland and the Eurasian Coastline, whereas in HadGEM3-GA3.0, sea ice cover is much less over the Arctic Ocean (see Figure 2.2). A like-for-like comparison between the HadGEM3-GA3.0 simulations and Figure 12.29 from Collins et al. (2013) is given in Figure A.1 in Appendix A.

By analysing the future climate simulations from the UPSCALE project, the response of Arctic storms in a future climate to climate change can be determined. Moreover, the sensitivity of this response to horizontal resolution can be also assessed.

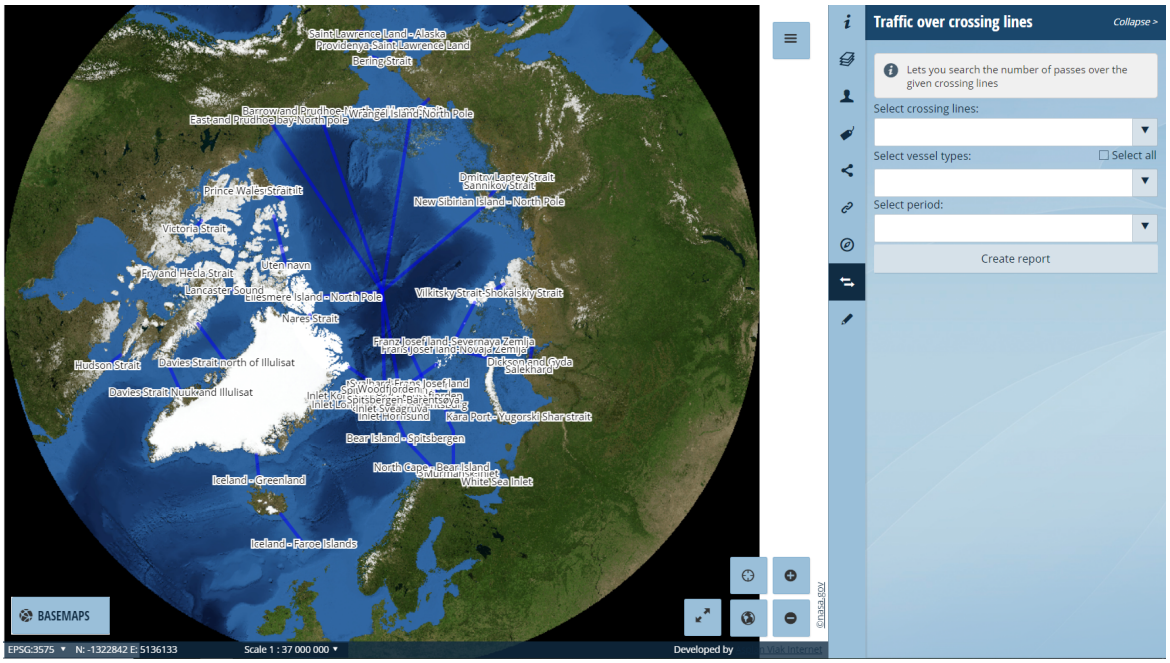

Figure 2.3: The Norwegian Coastal Administration Sea Base (Havbase) web-interface. The map shows all of the gates where ship crossings can be obtained for, and the right column shows where data can be filter to the gate, type of ship and time period. From Norwegian Coastal Administration (2021).

2.3 Arctic Shipping Database: The Norwegian Coastal Administration Sea Base (Havbase)

Not much is known of Arctic shipping activities, partly because ship track data is not open source. It became mandatory for all large ships to fit Automated Identification System (AIS) transponders in 2005, which transmit the ships position in real time (International Maritime Organization, 2019). This was revised in 2013, where is became mandatory for all ships over 18 metres to have AIS transponders fitted (International Maritime Organization, 2019). This was established to increase the safety of ships. This has allowed for the live transmission of the position of most ships, which can be viewed in real time via sources such as Marine Traffic (2021) and Vessel Finder (2021). Historical records of ship transits can also be obtained from these sources. However, such historical records are privatised, and are only available at a substantial price.

Alternatively, a record of Arctic shipping transits can be obtained from the Norwegian Coastal Administration Sea Base (Kystverket Havbase) (Norwegian Coastal Administration, 2021) -

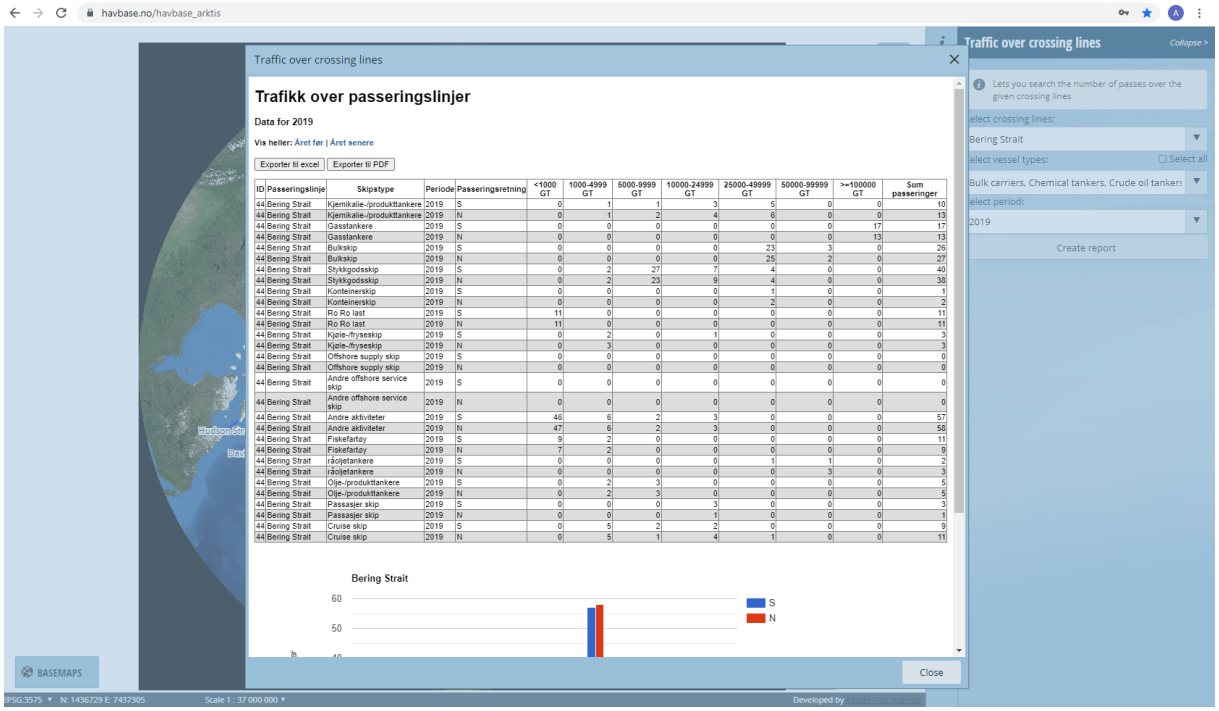

Figure 2.4: An example output from the Norwegian Coastal Administration Sea Base (Havbase) web-interface, after filtering ship passages to those that cross the Bering Strait, selecting all ship types, and filtering to those passages that occurred in all months of 2019. The total number of gate crossings by ships is given in column 13. From Norwegian Coastal Administration (2021).

hereafter "Havbase". The Havbase database contains information of ship transits travelling between regions in the Arctic and can be accessed via: *https://havbase.no/havbase_arktis* (Norwegian Coastal Administration, 2021). It is used in this thesis, as it is the most informative and freely available historical record of past shipping transits in the Arctic.

Figure 2.3 shows the web interface of the Havbase database. It contains data on the number of ships that have travelled between regions in the Arctic, and more specifically, the number of ships that travel through gates over the Arctic in each month from 2012 to 2019. These gates are shown in Figure 2.3. Gate crossings by ships are also categorised into ship type (see the third column of Figure 2.4). This can be used to indicate the primary ship type that operate in each region of the Arctic. The number of gate crossings by ships is based on data from AIS devices, but output in the format of the Havbase interface. Within this period, it became mandatory for fishing ships over 18 metres and 15 metres to have AIS transponders fitted in May 2013 and May 2014 respectively. This may increase the number of ships reporting their position from 2013 and 2014.

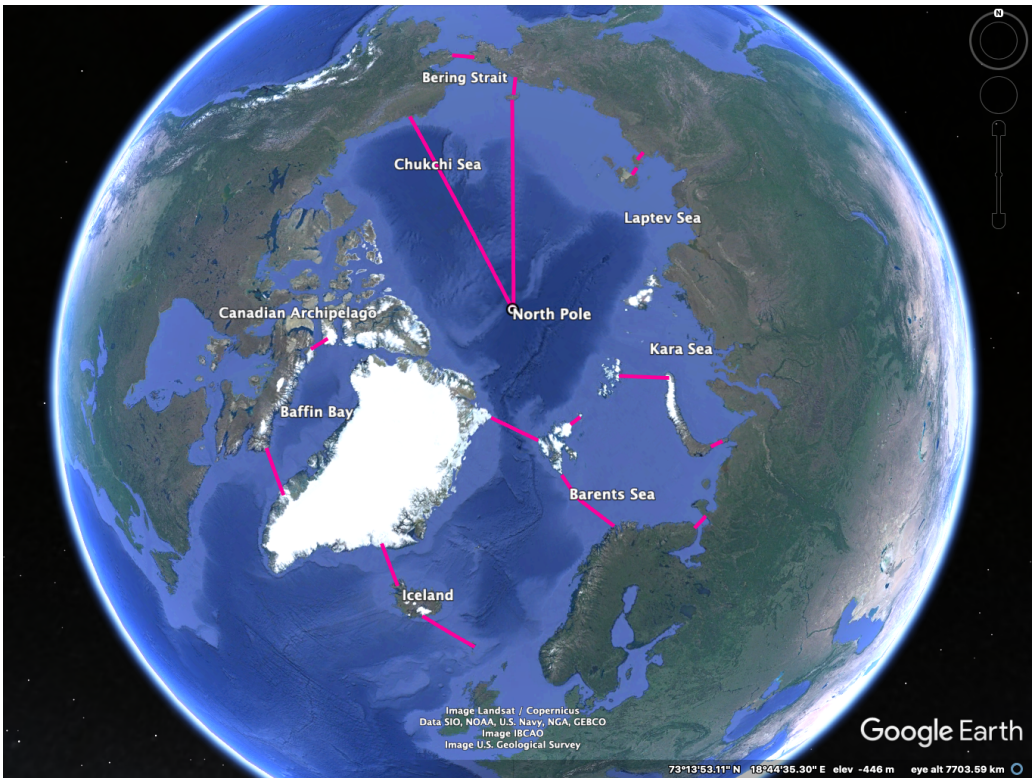

Figure 2.5: The gates from the Havbase database that are analysed in this Thesis. Based on Norwegian Coastal Administration (2021), and made using Google Earth (Google, 2021).

The data available details how many ships crossed each gate over the time period, after selecting the gate, type of ship and the time period on the right-hand side of the Havbase Web-Interface (see Figures 2.3 and 2.4). Information is also given for the direction at which the ship crossed the gate (i.e. the direction the ship was travelling - see the fifth column of Figure 2.4). The Havbase database gives the number of gate crossings by ships over 47 gates across the Arctic in total. It is shown in Figure 2.3 that many of these gates are in close proximity to each other (especially in the Barents Sea). So, one ship may be responsible for gate crossings over multiple gates. In this thesis, the number of these gates is reduced to 16 gates across the whole Arctic, which are shown in Figure 2.5.

Shipping data from Havbase gives information about current Arctic shipping activities and can be used to simulate past ship transits across the Arctic per month. These ship transits can then be combined with past Arctic storm tracks to quantify how many ships in the Arctic have been impacted by past storms. Thus giving an indication of the exposure of ships to Arctic storms, which can help to determine the risk to such hazards.

2.4 Identifying Cyclone Tracks

2.4.1 Cyclone Tracking

Storms have been identified in the reanalysis datasets and the HadGEM3-GA3.0 simulations using TRACK (Hodges, 1994, 1995, 1999). This is an automated storm tracking algorithm, which can process through the gridded datasets and identify cyclone tracks. This cyclone tracking method has been widely used in other studies to identify cyclone characteristics (e.g. Hoskins and Hodges, 2002; Zappa et al., 2013; Day et al., 2018), and has also been shown to agree well with storm statistics identified by other storm tracking methods (e.g. Raible et al., 2008; Pinto et al., 2016).

One of the primary differences between cyclone tracking algorithms, is whether storms are identified in the field of mean sea level pressure (MSLP) or 850 hPa relative vorticity (Neu et al., 2013). Using the 850 hPa relative vorticity field has been shown to generally identify more smaller scale storms than using the MSLP field at the same resolution (Hoskins and Hodges, 2002; Neu et al., 2013). In addition, the MSLP field is an extrapolated field over land regions, whereas the 850 hPa relative vorticity field is only extrapolated over the highest orography. The number of Arctic storms and their lifecycles identified by the two methods may differ, potentially leading to a different representation of Arctic storm statistics. This thesis uses both fields to identify Arctic storms, to determine the impact of storm tracking variable on Arctic storm statistics.

The first stage of the cyclone tracking process is to spectrally truncate the 850 hPa relative vorticity and MSLP fields to a horizontal resolution of T42 and T63 respectively. Higher resolution filters are typically used to analyse meso-scale phenomena such as polar lows (Zappa et al., 2014; Tous et al., 2016), however in this study T42 is used for 850 hPa relative vorticity and T63 is used for MSLP, which focus on synoptic-scale storms. Filters of different resolution are used because the MSLP field is generally a smoother field than 850 hPa relative vorticity, thus requiring a higher resolution filter to identify synoptic-scale storm feature points

in the data. During this stage, planetary scales with total wavenumbers less than or equal to 5 are removed, ensuring that large spatial scales are removed, and synoptic-scale features are focused on (Hoskins and Hodges, 2002).

Features are then identified within the chosen atmospheric field at each time-step. Cyclonic features are identified as MSLP minima, and in the vorticity field as a relative vorticity maxima, which are typical characteristics of cyclones (Hodges, 1994). The features from each field are identified on a polar stereographic grid, with the features that occur off-grid being found using a B-spline interpolation and steepest ascent / descent optimisation (Hodges, 1995). These feature location points are then projected back onto a sphere for the next step (Hodges, 1995).

The second stage of the cyclone tracking process is to group the identified features into storm tracks. This is accomplished by first initialising a set of tracks using a nearest-neighbour approach that links feature points in consecutive time-steps. The tracks are then refined by minimising a cost-function to produce the smoothest set of tracks subject to adaptive constraints of track smoothness and displacement distance in consecutive time-steps. This cost-function depends on the storm propagation speed and direction (Hodges, 1999).

Once the storm tracks have been identified, they are filtered to retain storms that last more than 2 days and travel more than 1000 km. This ensures that mobile synoptic-scale storms are the main focus. If these thresholds are relaxed, then more weak and semi-stationary storms are identified (see Figure 2.6). After the tracking process is complete, other atmospheric fields can be attached to the storm tracks, such as wind maxima, which can give an alternative measure of storm intensity than the initial storm tracking variable. The full resolution atmospheric fields of 925 hPa wind speed, 10 metre wind speed and significant wave height have been attached to the tracks from each dataset. This is achieved by searching for the maximum grid point values within a 6° radius of the storm centre per time-step. The MSLP minima have also been attached to the cyclone tracks, by searching for the MSLP minima within a 5° radius of the storm centre using B-spline interpolation and steepest descent minimisation.

To compare Arctic storm statistics between datasets, the cyclone tracks identified in each dataset are then filtered to those that travel north of 65°N (referred to as Arctic storms). Arctic storms

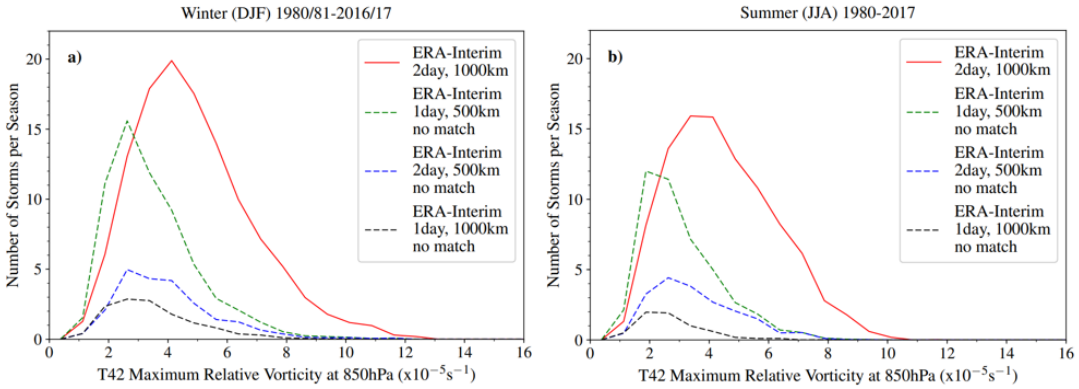

Figure 2.6: Intensity distribution of **a)** winter (DJF) and **b)** summer (JJA) Arctic storms identified in ERA-Interim using varying thresholds of minimum storm propagation distance and lifetime. Bin widths are 0.75x10^{-5}s^{-1}. Red solid line denotes storms identified after filtering out storms that travel <1,000 km and have lifetimes >2 days. Dashed lines denote the additional ("no match") storms identified by relaxing these criteria.

are also filtered for those that have genesis (i.e. their first feature point) north of 65°N (referred to as Arctic genesis), and those that have genesis south of 65°N and then travel north of 65°N (referred to as mid-latitude genesis). Mid-latitude cyclones are also considered for some parts of this thesis to contrast with the Arctic storms. In Chapter 3, Arctic storms are compared to mid-latitude storms, which are defined as storms that have genesis between 35°N and 65°N. In Chapter 4, Arctic storms are compared to mid-latitude storms that occur over the North Atlantic Ocean, which have 60% of their storm track points between -53°E to 20°E and 30°N - 65°N.

2.4.2 Storm Statistics

To compare Arctic storms between the reanalysis datasets and the UPSCALE simulations, storm statistics have been calculated. The frequency/number of Arctic storms is determined by counting the number of all Arctic storms that enter the Arctic at any time during their track. The spatial distribution (track density and genesis density) of Arctic storms is computed using the spherical kernel approach (Hodges, 1996), to allow for the analysis of the geographical distribution of Arctic storms. Track density describes the number of storm tracks that travel over a region and genesis density describes the number of storm tracks that start in a region. These statistics have units of number of storms per season per unit area, where the unit area is equivalent to a 5° spherical cap (approximately 10^6 km^2).

The statistical significance of differences in storm track and genesis density between two samples of storm tracks can be tested. The null hypothesis that is tested being that there is no difference between the two samples. This is achieved using a permutation method that uses a Monte Carlo approach (Hodges, 2008). This method pools the two storm track samples, which are then re-sampled without replacement 2,000 times into new pairs of storm track datasets, which have the same size as the original sample. Storm statistics (e.g. track and genesis density) are then computed for each newly paired samples. Differences in these storm statistics are taken from a sampling distribution and the p-value that determines statistical significance is obtained by comparing with the original difference statistic.

To directly compare the Arctic storm tracks between the reanalysis datasets, a storm matching analysis has also been performed (Hodges et al., 2011). Storms are matched between two reanalysis datasets by finding the storm tracks that have a minimum mean separation distance of less than 4° (geodesic), and that overlap in time by at least 50% of the points in their life cycles.

2.4.3 Composite Structure Analysis

The structure of Arctic storms is studied using a system centred composite method described in Bengtsson et al. (2007, 2009) and Catto et al. (2010). The composite method has three steps, which include storm selection, lifetime positioning and storm rotation (see Figure 2.7) (Catto et al., 2010). A composite method is able to identify the general structure of a group of storms, by taking an average of atmospheric fields across a space centred on the storm centre. The composite structure is an average over multiple storms, therefore, small scale features can be smoothed out by the method and are more difficult to identify within the composite. But the general structure of a group of storms can be determined. Atmospheric fields are plotted on a 20° longitude-latitude grid centred on the storm's centre (the location of minimum mean sea level pressure at the surface), so to determine the horizontal composite structure. This grid is initially setup centred on the equator, ensuring a fair comparison between storms that occur at different latitudes.

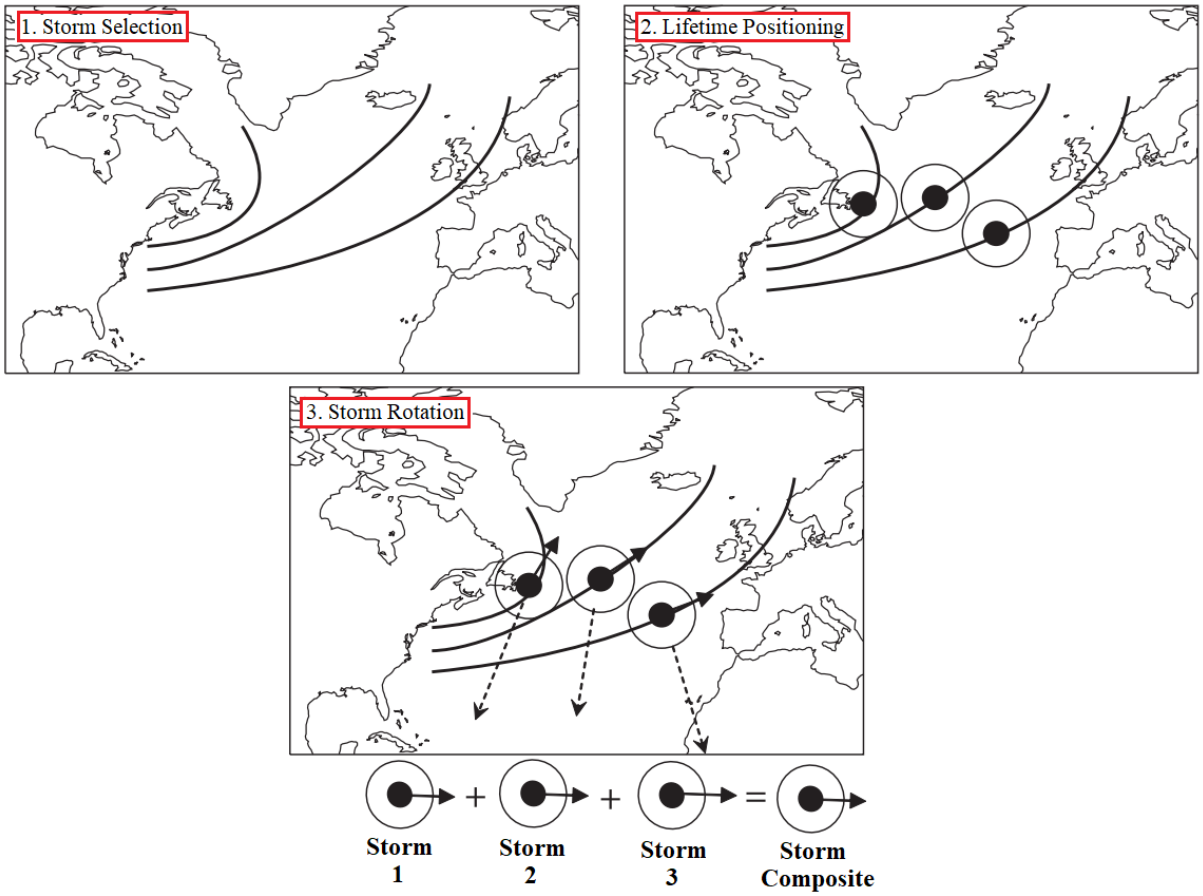

Figure 2.7: An illustration of the storm composite method. 1. Storm Selection: selecting the set of storm tracks to perform the composite for. 2. Lifetime Positioning: the position through the storms lifetime to perform the composite e.g. at the time of maximum intensity. 3. Storm Rotation: ensure that each storm has the same orientation e.g. the direction of propagation. Adapted from Catto et al. (2010).

The first step of the composite method is to select the storm tracks for the analysis (storm selection) (see Figure 2.7.1). In this thesis, storm tracks have been determined for Arctic storms with mid-latitude and Arctic genesis. However, storms that only have one timestep north of 65°N can be included. To exclude these storms, the storm tracks are further filtered to only include storms that have their maximum intensity in the Arctic (north of 65°N), and have 60% of their points within the Arctic region. In addition, storms have been filtered further to the 100 most intense storms per season (based on storms with the lowest MSLP minima), so that the composite structure of most impactful storms is analysed, which is not affected by the structure of weaker or smaller-scale storms. The composite structure of Arctic storms is contrasted with that of mid-latitude storms, which have 60% of their points over the North Atlantic Ocean, between -53 to 20°E and 30 - 65°N.

The second step in creating a storm composite is to determine the point in the storm's life-cycle to average the atmospheric field over the storms centre and to create the composite (lifetime positioning) (see Figure 2.7.2). In this study, the composite structure is determined at the point of maximum intensity, the time that they reach their MSLP minima. This is to determine the structure of storms when they are at their most hazardous. To determine the development of storms, the composite structure is also determined at time-steps 48 hours before and up to 192 hours after the time-step that they reach their MSLP minima.

The third step and final step before averaging is to rotate storms to a common direction (storm rotation) (see Figure 2.7.3). This ensures storms are averaged with a common orientation and allows for system-relative winds to be computed for the composite, in addition to Earth-relative winds. Earth-relative winds describe the wind speed relative to the Earth surface and includes the propagation speed of the storm. System-relative winds describe the wind speeds within a storm, with the propagation speed of the storm subtracted from the wind field.

In this thesis, the storm composites have been performed using mean sea level pressure data, and temperature and wind data across 9 pressure levels (925 hPa, 850 hPa, 700 hPa, 600 hPa, 500 hPa, 400 hPa, 300 hPa, 200 hPa, 100 hPa) from the ERA5 reanalysis dataset. A temperature anomaly is calculated by subtracting the temperature value at each point from the mean temperature across the horizontal 20° longitude-latitude domain. Composite vertical cross sections of these atmospheric fields are analysed. Cross sections have been made along transects that intersect the composite storm centre from west to east, and south to north (see Figure 2.6).

2.4.3.1 Rotated and Non-Rotated Storm Composites

Storm composites can be created by either rotating each storm to a common direction e.g. direction of propagation, or by not rotating them and keeping the geographical orientation of each storm, before averaging. By rotating each storm to their direction of propagation, differences in the orientation of each storm may be minimised, and the clarity of features within the composite may improve (Catto et al., 2010).

However, previous research has shown that a number of Arctic storms, especially in summer, can stagnate over the Arctic (e.g. Simmonds and Rudeva, 2012; Yamagami et al., 2017). This means that the direction of these storms may be less well defined. Consequently, orientating all storms to their direction of propagation may not ensure that all storms that contribute to the composite have a similar orientation, which may impact the clarity of the composite.

An alternative to rotating each storm to the direction of propagation is to keep the storms geographical orientation before averaging. For these non-rotated storms, their geographical orientation is kept as north, east, south, and west. Typically, in the Northern Hemisphere, cold air is located to the north towards the poles and warm air is located to the south towards the Equator. By keeping the geographical orientation of each storm, this large-scale feature of the atmosphere may be better maintained in the non-rotated storm composite than if the storms were rotated before averaging. Hence, the composite may show stronger temperature gradients.

There is not a preferred way of creating storm composites when considering whether to or not to rotate storms before averaging. This is shown by the varied approaches of previous research, with some studies deciding to rotate storms before averaging (e.g. Bengtsson et al., 2007, 2009; Catto et al., 2010), and other studies deciding not to rotate storms before averaging (e.g. Wang and Rogers, 2001; Bauer and Del Genio, 2006). To thoroughly examine the composite structure of Arctic storms in this thesis, storm composites are produced by both rotating and not rotating storms before averaging.

Chapter 3

An Inter-Comparison of Arctic Synoptic Scale Storms between Four Global Reanalysis Datasets

This chapter aims to quantify present-day climate Arctic storm statistics and the associated uncertainty, by contrasting Arctic storm statistics from different reanalysis datasets and storm tracking methods. This addresses the first research question of this thesis:

RQ1: What are the present-day climate characteristics of Arctic storms, and, what is the uncertainty associated with the choice of reanalysis dataset and storm tracking identification variable?

The text and figures that follow have been published in the Journal of *Climate Dynamics*: Vessey et al. (2020). The author of this thesis (A.F. Vessey) is the first author of the paper, and completed all of the analysis, creation of figures and writing of text. Other authors helped to read through and check the material, and to develop ideas.

Citation:

Vessey, A.F., Hodges, K.I., Shaffrey, L.C. and Day, J.J., 2020. An inter-comparison of Arctic synoptic scale storms between four global reanalysis datasets. Climate Dynamics, **54(5)**, 2777-2795.

Supplementary material for this paper can be found in Appendix B.

Since this paper was published, a new reanalysis dataset became available, ERA5. The subsequent figures and storm statistics identified in the ERA5 reanalysis dataset in winter (DJF) and summer (JJA) can be found in Appendix C.

This paper focuses on Arctic storm statistics in winter (DJF) and summer (JJA), but the subsequent figures and storm statistics for the frequency, spatial distribution and intensity of spring (MAM) and autumn (SON) Arctic storms can be found in Appendix D.

3.1 Abstract

The Arctic is becoming more accessible as sea ice extent continues to decline, resulting in higher human exposure to Arctic storms. This study compares Arctic storm characteristics between the ECMWF-Interim Reanalysis, 55-year Japanese Reanalysis, NASA-Modern Era Retrospective Analysis for Research and Applications Version 2 and NCEP-Climate Forecast System Reanalysis datasets from 1980-2017, in winter (DJF) and summer (JJA). It is shown that Arctic storm characteristics are sensitive to the variable used for storm tracking. The Arctic storm frequency is found to be similar in summer and winter when using sea level pressure minima to track Arctic storms, whereas the storm frequency is found to be higher in winter than summer when using 850 hPa relative vorticity to track storms, based on using the same storm tracking algorithm. It is also found that there are no significant trends in Arctic storm characteristics from 1980-2017. Given the sparsity of observations in the Arctic, it might be expected that there are large differences in Arctic storm characteristics between the reanalysis datasets. Though, some similar Arctic storm characteristics are found between the reanalysis datasets, it is found that the differences in Arctic storm characteristics between the reanalysis datasets are generally higher in winter than in summer. Overall, the results show that there are differences in Arctic storm characteristics between reanalysis datasets, but even larger differences can arise between using 850 hPa relative vorticity or mean sea level pressure as the storm tracking variable, which adds to the uncertainty associated with current Arctic storm characteristics.

3.2 Introduction

The Arctic is currently undergoing rapid change. Arctic sea ice extent has reduced dramatically over recent decades in both its maximum and minimum extent (National Snow & Ice Data Centre, 2019b). Climate model projections indicate that sea ice extent will continue to reduce in summer and winter, with a sea ice-free Arctic expected to occur in summer in the near future (Wang and Overland, 2012a; Flake, 2013; Petrick et al., 2017). As a consequence of the decline in sea ice, human activity in the Arctic (such as oil exploration, shipping and

tourism) is increasing (Melia et al., 2016). Increased human activity will also result in an increase in exposure to hazardous weather conditions, such as the strong winds and waves associated with Arctic synoptic-scale storms. To assess the risks associated with increased exposure it is therefore important to determine the characteristics of Arctic storms. One way to assess Arctic storm risk is to use atmospheric reanalyses, which are created by assimilating observations into numerical atmospheric models. Reanalyses provide both spatial and temporal homogeneous datasets, which is particularly important in the poorly observed Arctic. However, the sparseness of conventional observations, conservative use of lower tropospheric satellite data over sea ice, snow and low-level cloud covered areas, and high background model error in polar regions, could lead to large differences between reanalyses in the Arctic, compared to mid-latitudes (Bauer et al., 2016a; Jung et al., 2016; Lawrence et al., 2019).

Earlier studies of Arctic storm characteristics focused on analysing individual reanalyses. For example, using the NCEP-NCAR reanalysis Zhang et al. (2004) and Sorteberg and Walsh (2008) found that Arctic storms reach a lower central mean sea level pressure (MSLP) and higher relative vorticity in winter than in summer, and that Arctic storms have longer duration in summer than in winter. Recent studies have compared multiple reanalysis datasets to assess the uncertainty of Arctic storm characteristics (Tilinina et al., 2014; Zahn et al., 2018). Tilinina et al. (2014) found that the number of Arctic storms was dependent on the resolution of the reanalysis, with the higher resolution Arctic System Reanalysis dataset (ASR) having a higher number of weaker storms or mesoscale storms than the lower resolution ECMWF Interim Reanalysis (ERA-Interim), NASA Modern Era Retrospective Analysis for Research and Applications (MERRA) and NCEP Climate Forecast System Reanalysis (NCEP-CFSR) datasets.

Differences in the trends of Arctic storm frequency have also been found in atmospheric reanalyses. Sorteberg and Walsh (2008) and Sepp and Jaagus (2011) found that Arctic storm frequency increased between 1949-2002 in the National Centre for Environmental Prediction (NCEP)-National Centre for Atmospheric Research reanalysis dataset, especially for summer. However, results using more recent reanalysis datasets such as European Centre for Medium Range Forecasting (ECMWF) 40 year Re-Analysis dataset, found that Arctic storm frequency

had not changed (Simmonds et al., 2008; Serreze and Barrett, 2008). Similarly, Zahn et al. (2018) also assessed a range of different reanalyses but did not find any substantial trends over the period studied (1981-2010). The above differences found between reanalyses highlights the continuing need to evaluate and understand the uncertainty in Arctic storm characteristics in the reanalyses, especially as they are often used as a baseline for evaluating climate models (Vavrus, 2013; Day et al., 2018).

One robust feature seen in reanalyses is that the location of Arctic storm tracks also appear to be seasonally dependent (Reed and Kunkel, 1960; Serreze et al., 2001; Simmonds et al., 2008; Crawford and Serreze, 2016). The main summer storm track tends to be strongest over Eurasia and into the central Arctic Ocean. The region of storm genesis over coastal continental Eurasia and the Arctic Ocean in summer has been referred to as the Arctic Frontal Zone, and results from the strong temperature gradient between the snow-free land and ocean (Reed and Kunkel, 1960; Serreze et al., 2001; Simmonds et al., 2008; Crawford and Serreze, 2015; Day and Hodges, 2018). In winter, the storm track predominantly occurs in the Greenland, Norwegian and Barents Seas. Synoptic-scale Arctic storms in winter often have their genesis in the mid-latitudes and travel polewards into the Arctic (Hodges et al., 2011). One key question is whether the differences between storms in the reanalyses are predominantly associated with those that have genesis in the Arctic, where reanalyses may be poorly constrained by the sparse observational network.

Another topic addressed in previous studies is the seasonal cycle of Arctic storm frequency. A number of papers using mean sea level pressure as a tracking variable found that Arctic synoptic-scale storm frequency was higher in summer than in winter (Serreze, 1995; Serreze et al., 2001; Tilinina et al., 2014; Zahn et al., 2018). In contrast, Simmonds et al. (2008) found that Arctic synoptic-scale storm frequency was higher in winter than in summer in the ERA-40, NECP1 and NCEP2 reanalysis datasets, using the laplacian of pressure (geostrophic vorticity) as the tracking variable. One possibility for these different results is the assumptions made in the storm tracking algorithm in terms of storm identification, tracking and filtering, for example the number of storms identified within reanalyses is dependent on the choice of storm tracking algorithm (Neu et al., 2013). One of the main differences between methods are whether storms

are identified using MSLP minima or lower tropospheric vorticity maxima. Hodges et al. (2011) and Jung et al. (2012) showed that the number of storms identified is higher for a storm tracking algorithm that is based 850hPa relative vorticity field rather than the MSLP. This is primarily because smaller spatial scales are present in vorticity compared to MSLP (Hoskins and Hodges, 2002). Arctic storm characteristics have typically been assessed using storm tracking algorithms based on MSLP (Serreze, 1995; Zhang et al., 2004; Simmonds et al., 2008; Tilinina et al., 2014; Crawford and Serreze, 2016; Zahn et al., 2018) which raises questions regarding the sensitivity of the choice of identification variable.

This paper aims to improve our understanding of the Arctic synoptic scale storms by assessing their characteristics in multiple global reanalyses. This will be achieved by the following objectives:

- Determine whether there are any trends in Arctic storm activity from 1980-2017 for winter (DJF) and summer (JJA) in the ERA-Interim, JRA-55, MERRA-2 and NCEP-CFSR reanalyses,
- Assess the frequency, spatial distribution and intensity of synoptic-scale Arctic storms,
- Determine whether the differences in Arctic storm characteristics between reanalyses are associated with storms that have their genesis in mid-latitude regions or the Arctic,
- Determine the sensitivity of Arctic storm characteristics to the storm tracking identification variable using relative vorticity and MSLP.

In section 2 a description of the data and methodology used to identify and compare Arctic storms in each reanalysis dataset is given. Section 3 presents the climatological and inter-annual variability in Arctic storm frequency between each reanalysis dataset. Section 4 describes the spatial distribution of Arctic storms in terms of track density and genesis density and the difference between each reanalysis dataset. Section 5 compares the intensity of Arctic storms between each reanalysis dataset. Section 6 presents results from storm track matching analysis between reanalysis datasets. Arctic storms identified using the different tracking

variables (i.e. relative vorticity or MSLP) are compared in section 7. A summary and conclusions are given in section 8.

3.3 Methodology

3.3.1 Reanalysis Datasets

This study compares Arctic storms identified in data from the ERA-Interim (Dee et al., 2011), JRA-55 (Kobayashi et al., 2015), MERRA-2 (Gelaro et al., 2017) and NCEP-CFSR (Saha et al., 2014) reanalysis datasets. A comparison is made between winter (DJF) and summer (JJA) for a common time-period, 1980-2017. In this study, data from the 6-hour analyses are used for each of the datasets. Each of the four reanalysis datasets are created by different institutions, using different numerical weather prediction (NWP) models and data assimilation systems.

a) **ERA-Interim**

ERA-Interim is produced by the European Centre for Medium Range Weather Forecasting (ECMWF). Data are created using the Integrated Forecasting System (IFS) version Cy31r2 model, which is a spectral model (Dee et al., 2011). ERA-Interim has a horizontal resolution of 0.75°x0.75° and a vertical resolution of 60 levels up to 0.1 hPa (T255 spectral resolution, L60). Historical observations are quality controlled, bias corrected, and assimilated using a 4D-Variational system, which adjusts model projections to observations both forward and backward in time.

b) **JRA-55**

JRA-55 has been produced by the Japanese Meteorological Agency (JMA) and was created using the JMA Global Spectral Model (GSM). JRA-55 has a higher horizontal resolution than ERA-Interim; 0.55°x0.55° (T319 spectral resolution), and has the same vertical resolution of 60 levels up to 0.1 hPa (L60) (Kobayashi et al., 2015). However, the relative vorticity, wind and

MSLP data are provided at a reduced horizontal resolution of 1.25°x1.25°. Like ERA-Interim, historical observations are quality controlled and bias corrected and assimilated into the JMA GSM using a 4D-Variational system.

c) **MERRA-2**

Unlike ERA-Interim and JRA-55, MERRA-2 is created using a Grid-Point model; the Goddard Earth Observing System (GOES) model from the National Aeronautics Space Association (NASA) (Gelaro et al., 2017). MERRA-2 has a higher horizontal and vertical resolution than ERA-Interim and JRA-55 of 0.625°x0.5° and 72 levels up to 0.01 hPa respectively. Past observations are assimilated using a 3D-Variational system, which only adjusts model projections forward in time.

d) **NCEP-CFSR**

Unlike the other reanalysis datasets, NCEP-CFSR was created using a coupled atmosphere-ocean model, from the National Centers for Environmental Prediction (NCEP) (Saha et al., 2010). The atmosphere component is derived from the Climate Forecast System (CFS), which is coupled to the Modular Ocean Model (MOM) version 4. Similar to ERA-Interim and JRA-55, NCEP-CFSR was created using a spectral model. NCEP-CFSR has the highest resolution of all the reanalysis datasets compared in this study, with a horizontal resolution of 0.5°x0.5° and vertical resolution of 64 levels up to 0.3 hPa (T382 spectral resolution, L64). Historical observations were assimilated into the CFS model using a 3D-Variational system, similar to MERRA-2.

3.3.2 Arctic Storm Tracking

There are many storm tracking algorithms available (Neu et al., 2013). In this study, storms were identified from the reanalysis datasets using the objective storm tracking algorithm developed by Hodges (1994, 1995, 1999). This tracking algorithm has been widely used to track storms

in climate and numerical weather prediction studies (Hodges et al., 2011; Zappa et al., 2013; Day et al., 2018). In this study, a comparison is performed between storms identified using the two different identification variables of 850 hPa relative vorticity and MSLP. Typically, tracking algorithms based on the 850 hPa relative vorticity field are able to identify smaller scale systems than is the case for MSLP at the same resolution. Vorticity based algorithms are also less influenced by the background flow than MSLP, which can mask synoptic scale systems until they develop sufficiently (Sinclair, 1994). The 850 hPa vorticity field is also not extrapolated over regions of high orography. In this study, Arctic storms are first identified based on tracking with the 850 hPa relative vorticity rather than MSLP, as storms generally have smaller radius at higher latitudes (Rudeva and Gulev, 2007), and relative vorticity based algorithms tend to identify smaller scale storms better than MSLP based algorithms (Neu et al., 2013).

The data from each reanalysis datasets is first regridded onto a similar grid to allow for a fair comparison. In this study, data from each reanalysis dataset has been interpolated onto the ERA-Interim grid, as it is the lowest resolution grid of all the reanalysis datasets (0.75°x0.75°). Before performing the tracking, the field of choice is first spectrally filtered to remove the planetary scales for total wavenumbers less than or equal to 5, to focus on systems independent of large-scale forcings. The resolution of the 850 hPa relative vorticity and MSLP fields are decreased to T42 and T63 resolution respectively, to reduce noise within the field and ensure that the tracking algorithm identifies the main circulation of storms and not small-scale features within the storm. The T42 and T63 spectral filters were chosen to focus on synoptic scale storms, whereas higher resolution filters are typically used to analyse meso-scale phenomena such as polar lows (Zappa et al., 2014; Tous et al., 2016). The different filters for vorticity and MSLP are due to MSLP being a much smoother field and more influenced by the large-scale background.

The storms are first identified at each 6 hourly time-step in each reanalysis dataset as maxima in the 850 hPa relative vorticity above a threshold of $1.0\text{x}10^{-5}$ s^{-1} and minima in MSLP. The tracks are initialised based on a nearest-neighbour method and then refined by minimising a cost function. Once the storms have been tracked in either field, the tracks are filtered to retain those

that last more than 2 days and travel more than 1,000 km, so that the focus is on the synoptic scale and mobile storms Following the tracking, additional fields are added to the tracks of the full resolution 925 hPa wind speed maxima and the MSLP minima. The additional fields are added by searching for the maximum wind speed within a 6 degree radius of the tracked centre and by identifying the closest pressure minima within a 5 degree radius. These additional fields are added to give a more relatable measure of the intensity of a storm, rather than 850 hPa relative vorticity maxima at T42 spectral resolution.

In previous studies, different domains have been used to define the Arctic. In this study, Arctic storms are defined as storms that travel north of 65°N, so that storms that have genesis over inland continental Eurasia, as identified by (Crawford and Serreze, 2016), are included. A distinction between Arctic storms with Arctic genesis (north of 65°N) and mid-latitude genesis (south of 65°N and travel north of 65°N) is also made.

3.3.3 How Arctic Storm Characteristics are Calculated

In this study, the number of storms per season, the spatial distribution, and the intensity of Arctic storms are identified and compared between the four reanalysis datasets. Arctic storm frequency is calculated by counting the number of storms per season that travel north of 65°N. The spatial distribution statistics of Arctic storms are calculated using the spherical kernel approach (Hodges, 1996). The spatial statistics of track density and genesis density are highlighted to show the geographical distribution of storms across the Arctic and how this may differ between the reanalysis datasets. The statistical significance of the spatial distribution differences between the reanalysis datasets are tested using a Monte Carlo significance test (Hodges, 2008). To calculate the inter-annual variation, the standard deviation in the spatial statistics has been calculated from the statistics of each year from 1980-2017 at each grid point. To quantify the intensity of Arctic storms, the maximum intensity distributions of Arctic storms from each reanalysis dataset have been constructed for the 925 hPa wind field and the MSLP field, to quantify the impact of Arctic storms at the surface and how this may differ between reanalysis dataset. For Arctic storms with mid-latitude genesis, the maximum

intensity has been taken once they are in the Arctic. The 925 hPa wind speed field are compared instead of the 10-metre wind speed field as they are specifically calculated by each model, whereas 10-metre wind speeds are a diagnostic extrapolated from the lowest model level. To directly compare the storm tracks between the reanalysis datasets, a storm matching analysis has been performed (Hodges et al., 2011). The same storm is matched between two reanalysis datasets by finding the storm tracks that have a minimum mean separation distance of less than 4° (geodesic), and that overlap in time by at least 50% of the points in their life cycle. To gauge how similarly Arctic storms are represented in reanalyses to mid-latitude storms, a comparison is made by matching mid-latitude storms between the datasets; mid-latitude storms are defined as storms that have genesis between 35°N and 65°N.

3.4 Arctic Storm Frequency

3.4.1 Climatological Arctic Storm Frequency

Using the storm tracking based on the T42 850 hPa relative vorticity, it has been found that Arctic storms occur with a frequency of more than 1 storm per day in both winter and summer (see Table 3.1). Storm frequency is higher in winter than in summer in every reanalysis dataset. The reanalyses show that on average, 116 storms per season occur in winter and 97 storms per season occur in summer, with the frequency per season in winter and summer being similar between the reanalyses (see Table 3.1). The percentage of Arctic storms with Arctic or mid-latitude genesis is also consistent across the reanalysis datasets (see Table 3.1). In winter and summer, approximately 50% of all Arctic storms have mid-latitude genesis. This indicates that there are a considerable amount of Arctic storms with mid-latitude genesis, which may transport air from low to high latitudes.

Overall, ERA-Interim has the highest number of Arctic storms per season in both winter (119.4) and in summer (98.3) than the other reanalyses, whereas MERRA-2 has the lowest number of storms per season in winter (113.7) and in summer (96.2) compared with the other reanalyses. The range of the differences in storm frequency per season between the reanalysis

Table 3.1: Frequency of all Arctic storms that travel north of 65°N and the percentage with Arctic (north of 65°N) or mid-latitude genesis (south of 65°N) in winter (DJF) and summer (JJA) between ERA-Interim, JRA-55, MERRA-2 and NCEP-CFSR, for the period of 1980/81-2016/17 in winter and 1980-2017 in summer.

	Winter (DJF) (1980/81-2016/17) (per season)			Summer (JJA) (1980-2017) (per season)		
	Total number of Arctic Storms	% of Total with Arctic Genesis	% of Total with Mid-latitude Genesis	Total number of Arctic Storms	% of Total with Arctic Genesis	% of Total with Mid-latitude Genesis
ERA-Interim	119.4	54.0%	46.0%	98.3	47.1%	52.9%
JRA-55	116.3	55.3%	44.7%	96.4	47.0%	53.0%
MERRA-2	113.7	53.4%	46.6%	96.2	47.6%	52.4%
NCEP-CFSR	115.6	54.9%	45.1%	96.6	47.8%	52.2%
Average	**116.3**	**54.4%**	**45.6%**	**96.9**	**47.4%**	**52.6%**

datasets is higher in winter than in summer, 5.7 and 2.1 storms per season respectively. Thus, in winter, there is less agreement in Arctic storm frequency per season between the datasets. The frequency of Arctic storms shown in Table 3.1 is lower than was found in Tilinina et al. (2014) and Zahn et al. (2018), likely due to filtering the storms to stricter criteria on lifetime and distance travelled in this study.

Arctic storm frequency is found to be higher in winter than in summer, which is contrary to previous studies (Serreze, 1995; Serreze et al., 2001; Tilinina et al., 2014; Zahn et al., 2018), that used storm tracking algorithms based on MSLP minima to identify Arctic storms within reanalysis datasets, instead of the 850 hPa relative vorticity used in this study. MSLP based storm tracking algorithms identify fewer small-scale storms than vorticity based algorithms (Neu et al., 2013). Thus Table 3.1 may include more small scale storms than were identified in previous studies. Simmonds et al. (2008) used a storm tracking algorithm based on the Laplacian of MSLP (geostrophic vorticity) rather than minima in MSLP, and also found storm frequency per season to be higher in winter than summer. Simmonds et al. (2008) found that in winter, there are more 'open strong' storms, which are not associated with a closed MSLP minima. As a result, these storms would not be identified by storm tracking algorithms based on MSLP minima.

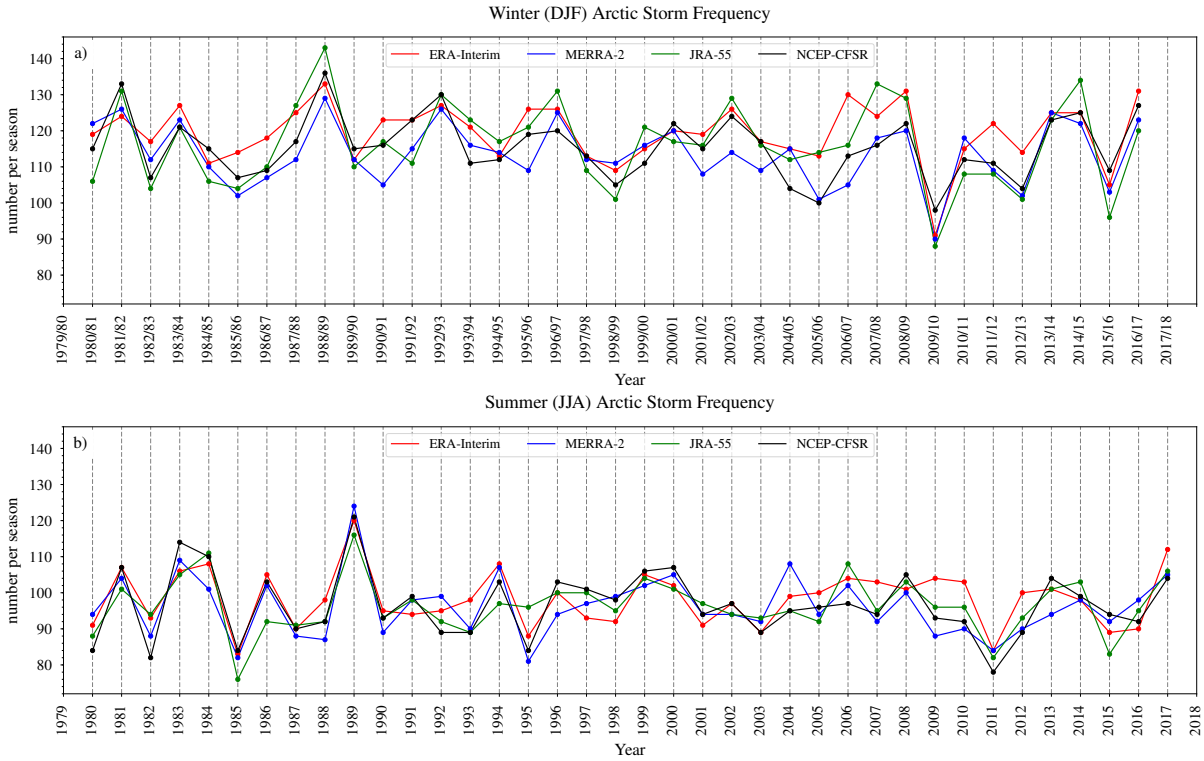

Figure 3.1: Time series of the number of Arctic storms that travel north of 65°N per season from the ERA-Interim, JRA-55, MERRA-2 and NCEP-CFSR reanalysis datasets between **a)** 1980/81-2016/17 in winter (DJF), and, **b)** 1980-2017 in summer (JJA).

3.4.2 Inter-Annual Variability and Trends in Arctic Storm Frequency

The timeseries of storm frequency from 1980-2017 in winter and summer is shown in Figure 1. Overall, all of the reanalysis datasets indicate the inter-annual range in Arctic storm frequency is approximately 9-11% in summer and 11-15% in winter of the total storm frequency per season. Although, there are seasons of notably high (winter 1988/89 and summer 1989) and low (winter 2009/10 and summer 2011) Arctic storm frequency. These periods coincide with periods of strong low and high phases of the Arctic Oscillation respectively. Figure 3.1 shows some resemblance to Figure 8 from Simmonds et al. (2008), e.g. the peaks in Arctic storm frequency in summer 1989. Simmonds et al. (2008) showed that from the ECMWF 40 year reanalysis dataset, there is some correlation between Arctic storm frequency and the Arctic Oscillation, one of the leading modes of atmospheric variability in the Arctic. Though, there are some differences between Figure 3.1 and Figure 8 from Simmonds et al. (2008), for example the increase in winter 1988/89 across all of the reanalyses.

Previous studies have reported an increasing trend of Arctic storm frequency from 1980, although these studies used previous versions of reanalysis datasets such as the NCEP - National Centre for Atmospheric Research reanalysis, NCEP - Department of Energy reanalysis and ECMWF 40 year reanalysis datasets (Zhang et al., 2004; Sorteberg and Walsh, 2008; Simmonds et al., 2008). Figure 3.1 shows that current reanalysis datasets show no significant trend in Arctic storm frequency in winter and summer, which was also found by Zahn et al. (2018). In addition, it is found in Figure S1 in the supplementary material (Figure B.1 in Appendix B) that there is no significant trend in the frequency of Arctic storms with Arctic genesis and mid-latitude genesis.

Table 3.1 shows that approximately 50% of all Arctic storms have mid-latitude genesis in both winter and summer. Figure S1 shows that the variability of storms with Arctic genesis and with mid-latitude genesis both contribute to the variability of all Arctic storms. For example, the decrease in total Arctic storm frequency in winter 2009/10 was mainly due to a low number of storms with mid-latitude genesis, whereas the increase in total Arctic storm frequency in summer 1989 was due to a high number of storms with Arctic genesis. The variation in Arctic storm frequency with Arctic and mid-latitude genesis is quite similar, with the average standard deviation of storm frequency being 6.78 and 7.82 storms in winter respectively, and 6.85 and 5.53 storms in summer respectively. This shows that variations in the frequency of Arctic storms with Arctic genesis is as important in determining the frequency of all Arctic storms, as the variations in the frequency of Arctic storms with mid-latitude genesis.

The degree of agreement in Arctic storm frequency between the reanalysis datasets can be quantified using the Pearson correlation coefficients of storm frequency from 1980-2017, and shown in Table 3.2. Overall, the correlation coefficient in storm frequency of all Arctic storms between the reanalysis datasets is lower in winter than in summer, with the average correlation between all reanalysis datasets being 0.73 in winter and 0.77 in summer (see Table 3.2). The lowest correlation coefficients are found when comparing the frequency of Arctic storms with Arctic genesis in winter, with the average correlation between all reanalysis datasets being only 0.55. In contrast, the average correlation coefficient of winter Arctic storms with mid-latitude genesis is much higher (0.84). In summer, the correlation coefficients are relatively similar

Table 3.2: Pearson correlation coefficients of the inter-annual variability in the frequency per season of all Arctic storms that travel north of 65°N, Arctic storms with Arctic genesis (north of 65°N) and Arctic storms with mid-latitude genesis (south of 65°N), between the ERA-Interim, JRA-55, MERRA-2 and NCEP-CFSR reanalysis datasets between 1980/81-2016/17 in winter (DJF) and 1980-2017 in summer (JJA).

	Winter (DJF)			Summer (JJA)		
	All Arctic Storms	Arctic Genesis	Mid-latitude Genesis	All Arctic Storms	Arctic Genesis	Mid-latitude Genesis
ERA-Interim, JRA-55	0.82	0.58	0.89	0.77	0.70	0.86
ERA-Interim, MERRA-2	0.68	0.43	0.80	0.73	0.72	0.79
ERA-Interim, NCEP-CFSR	0.76	0.43	0.80	0.79	0.79	0.82
JRA-55, MERRA-2	0.73	0.42	0.82	0.72	0.73	0.75
JRA-55, NCEP-CFSR	0.78	0.57	0.86	0.80	0.76	0.81
MERRA-2, NCEP-CFSR	0.62	0.62	0.79	0.83	0.71	0.73
Average	**0.73**	**0.55**	**0.84**	**0.77**	**0.74**	**0.79**

for storms with Arctic and mid-latitude genesis, 0.74 and 0.79 respectively. It was noted in section 3.1. that there were larger differences in the climatological Arctic storm frequency in winter than in summer between the reanalysis datasets. Table 3.2 further shows that there is less agreement in the inter-annual variability of storm frequency in winter than summer, especially for Arctic storms with Arctic genesis.

3.5 Arctic Storm Spatial Characteristics

3.5.1 ERA-Interim Climatology

To quantify the differences in the spatial distribution of Arctic storms, the genesis density and track density from the ERA-Interim reanalysis dataset are first calculated, and then the other reanalysis datasets are compared to this frame of reference.

Figure 3.2 shows the climatology of Arctic storm genesis density and track density in winter and summer from 1980-2017 for ERA-Interim. In winter, the Arctic storm track density is highest in the Greenland, Norwegian and Barents Seas (see Figure 3.2c). Storms that occur in these regions have genesis in the North Atlantic Ocean, east coast of Greenland and Scandinavia, or

have genesis over the Rockies and travel through the Canadian Archipelago and the Labrador Sea. These storms tend to propagate eastward toward the north-west coast of Eurasia. Arctic storm track density is also high over the Canadian Archipelago (see Figure 3.2c). Storms that travel into the Canadian Archipelago typically have genesis in the Rockies and around north Greenland (see Figure 3.2a). Storms that have genesis around north Greenland tend to travel westward into the Canadian Archipelago (not shown), which is not typical of high Northern Hemisphere storms, which tend to propagate eastward. Storms also travel into the Arctic Ocean in winter, which tend to have genesis over the mountainous regions over North Siberia. Previous studies identified few storms that travel into the Canadian Archipelago in winter, which is in contrast to Figure 3.2c (Zhang et al., 2004; Tilinina et al., 2014; Crawford and Serreze, 2016; Zahn et al., 2018).

In summer, the main Arctic storm track is over of the coastline of Eurasia, especially in the Barents Sea and Kara Sea, which extends into the Arctic Ocean north of Eurasia (see Figure 3.2d). This is also shown in previous studies (Zhang et al., 2004; Simmonds et al., 2008; Tilinina et al., 2014; Crawford and Serreze, 2016; Zahn et al., 2018). Storms along this storm track form along the Arctic Frontal Zone, a region of sharp temperature gradient between the Arctic Ocean and the land, creating a baroclinic environment that leads to storm genesis (Reed and Kunkel, 1960; Serreze et al., 2001; Simmonds et al., 2008; Crawford and Serreze, 2015; Day and Hodges, 2018). It is found in Figure 3.2 that storm genesis in this region tends to occur inland rather than over the coastline. This is consistent with Crawford and Serreze (2016) who found that storms in this region have genesis over the interior of coastal Eurasia and that the Arctic Frontal Zone acts to intensify these storms rather than being a region of storm genesis. In addition, storms that have genesis over the east coast of Greenland can travel into both the Eurasian coastline and the Arctic Ocean (see Figure 3.2b and 3.2d). The storm track in the Canadian Archipelago is less active in summer than in winter, with track density being 15-20 and 25-30 storms per season respectively. In winter, storms travel into the Canadian Archipelago from the Rockies and North Greenland. However, in summer, storm genesis around north Greenland is limited, suggesting they are primarily winter phenomena (see Figure 3.2a and Figure 3.2b).

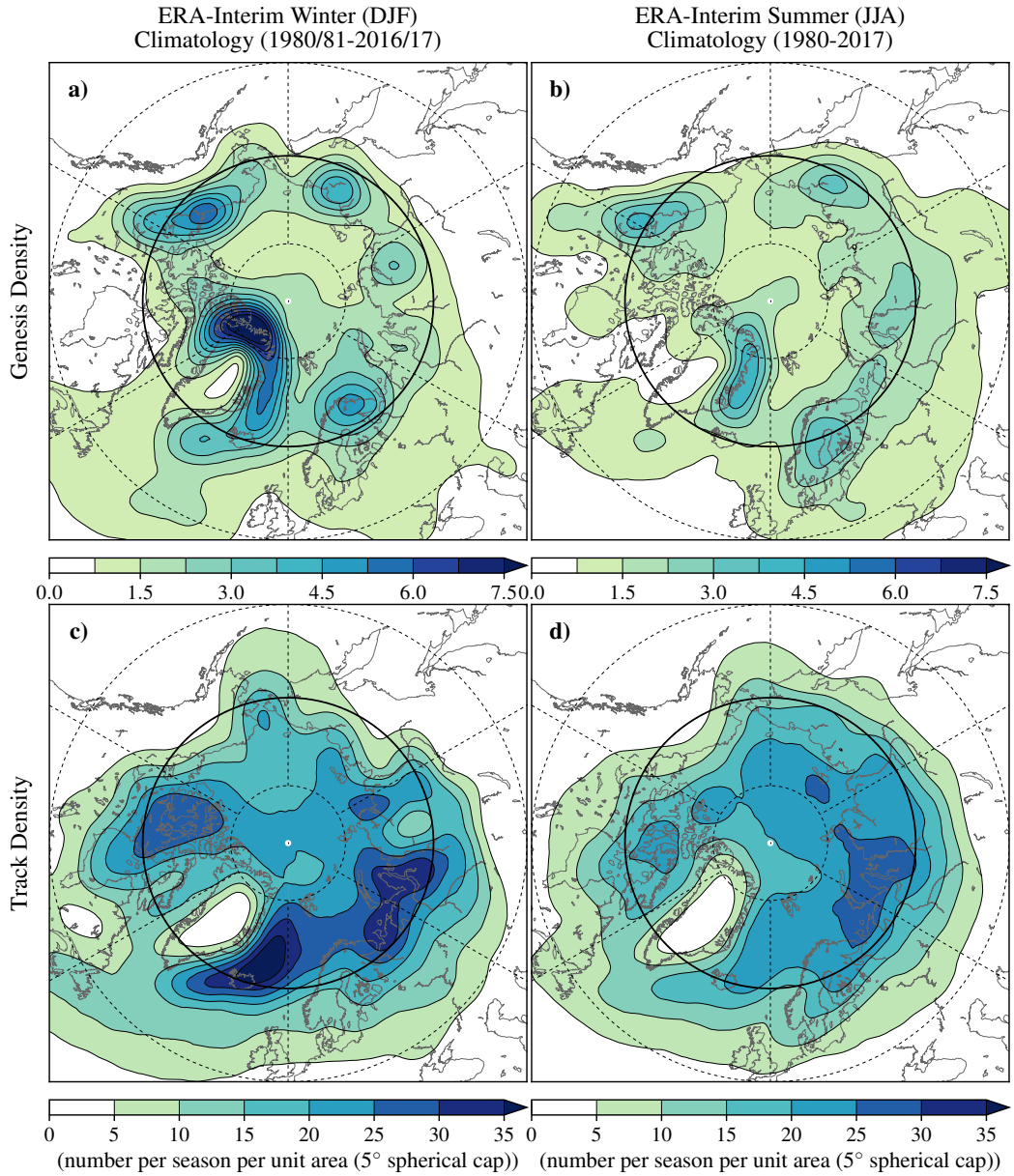

Figure 3.2: Climatological **a)** and **b)** storm genesis and c) and **d)** track density of all Arctic storms that travel north of 65°N between 1980/81-2016/17 in winter (DJF) (left panel) and 1980-2017 in summer (JJA) (right panel), based on the ERA-Interim reanalysis dataset. Densities have units of number per season per unit area (5° spherical cap, $\approx 10^6$ km^2). Longitudes are shown every 60°E, and latitudes are shown at 80°N, 65°N (bold) and 50°N.

In Section 3.1., it was identified that approximately 50% of winter and summer Arctic storms have genesis in mid-latitude regions and travel into the Arctic. Figures S2 and S3 in the supplementary material (Figures B.2 and B.3 in Appendix B) show the storm genesis and track density of Arctic storms with mid-latitude and Arctic genesis. In summer, Arctic storms with mid-latitude genesis can travel deeper into the Arctic Ocean than winter storms (see supplementary material Figure S2 - Figure B.2 in Appendix B). Storms with Arctic genesis

generally stay within the Arctic and rarely travel into mid-latitude regions (see Figure S3 in supplementary material - Figure B.3 in Appendix B).

3.5.2 Differences in Spatial Statistics between Reanalysis Datasets

Figures 3.3 and 3.4 show that ERA-Interim generally has higher Arctic storm track density and genesis density than the other reanalysis datasets. Though, these differences between the reanalysis datasets are generally not statistically significant at a 95% confidence level. This is likely due to the differences being relatively small compared to the total storm frequency per season (see Figures 3.2, 3.3 and 3.4). Although, it appears that the differences in Arctic storm track density and genesis density between ERA-Interim and the other reanalysis datasets are higher in winter than in summer.

In winter, all of the reanalysis datasets show the highest Arctic storm track density to occur over the Greenland, Norwegian and Barents Seas and Canadian Archipelago. In previous studies that used storm tracking algorithms based on MSLP minima or the Laplacian of MSLP (geostrophic vorticity), the Arctic storm track density was found to be much lower in the Canadian Archipelago than found in this study (Zhang et al., 2004; Simmonds et al., 2008; Tilinina et al., 2014; Crawford and Serreze, 2016; Zahn et al., 2018). The differences in Arctic storm track density between ERA-Interim and the other reanalysis datasets are highest in the Canadian Archipelago (see Figure 3.3a, 3.3c, 3.3e). In this region, ERA-Interim has higher track density than the other reanalysis datasets and the largest differences between ERA-Interim and MERRA-2, with the track density in MERRA-2 being 4-5 storms lower per season per unit area than ERA-Interim. The largest differences in storm genesis density occur over high terrain over north Greenland and over the Rockies (see Figure 3.4a, 3.4c, 3.4e); these storms generally travel into the Canadian Archipelago (see Figure 3.4). In addition, ERA-Interim has higher Arctic storm track density over the Greenland, Norwegian and Barents Seas than MERRA-2 and NCEP-CFSR (see Figure 3.3c and 3.3e). Storms that occur in this region tend to propagate toward the north-west coast of Eurasia, where there are also large differences in storm track density between ERA-Interim and MERRA-2, and,

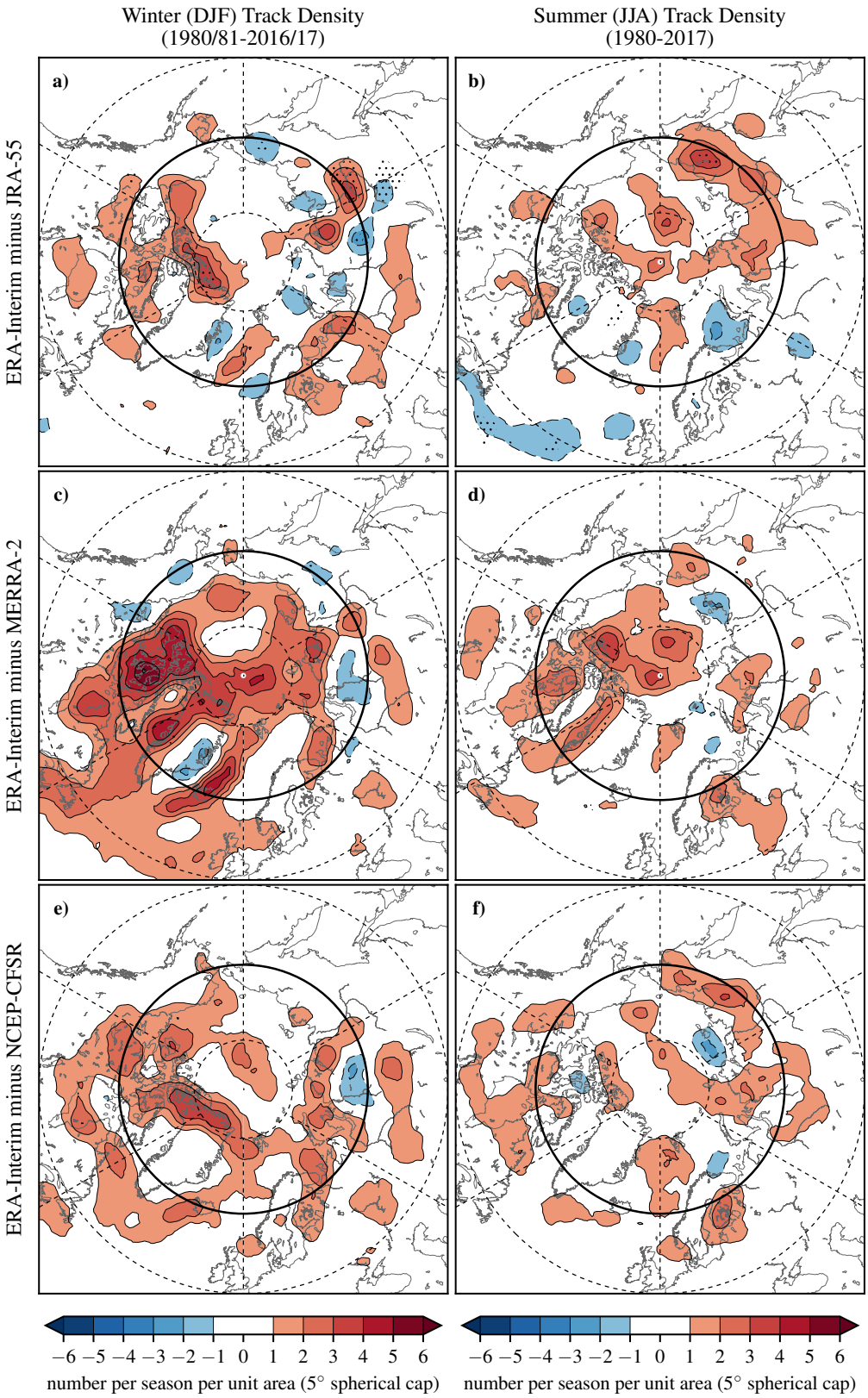

Figure 3.3: Differences in the climatological storm track density of all Arctic storms that travel north of 65°N between **a)** and **b)** ERA-Interim and JRA-55, **c)** and **d)** ERA-Interim and MERRA-2, and **e)** and **f)** ERA-Interim and NCEP-CFSR between 1980/81-2016/17 in winter (DJF) (left panel) and 1980-2017 in summer (JJA) (right panel). Densities have units of number per season per unit area (5° spherical cap, $\approx 10^6$ km^2). Longitudes are shown every 60°E, and latitudes are shown at 80°N, 65°N (bold) and 50°N. Stippling show areas where the differences are statistically significant to a 95% confidence level.

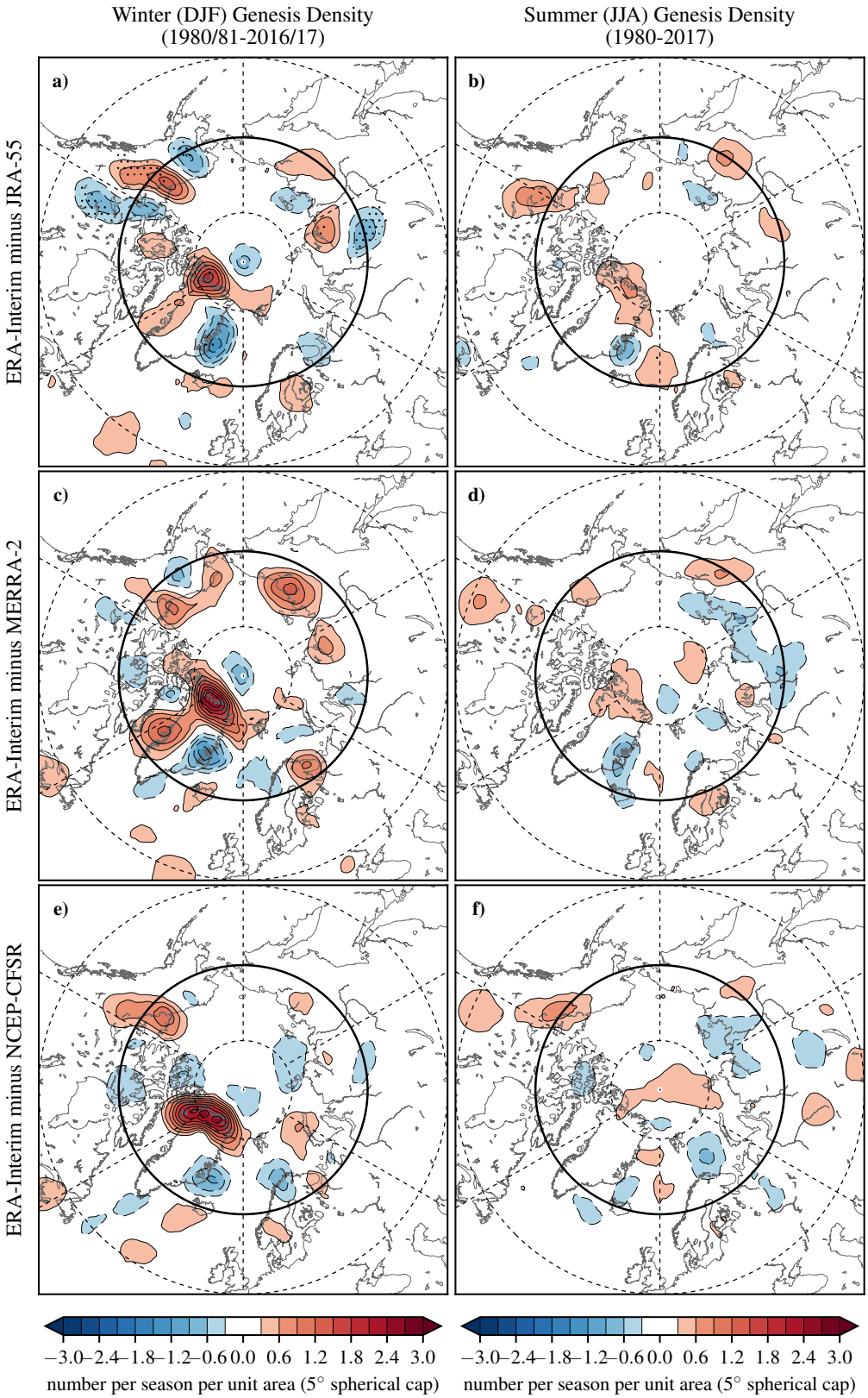

Figure 3.4: Differences in the climatological storm genesis density of all Arctic storms that travel north of 65°N between **a)** and b) ERA-Interim and JRA-55, **c)** and **d)** ERA-Interim and MERRA-2, and **e)** and **f)** ERA-Interim and NCEP-CFSR between 1980/81-2016/17 in winter (DJF) (left panel) and 1980-2017 in summer (JJA) (right panel). Densities have units of number per season per unit area (5° spherical cap, $\approx 10^6$ km^2). Longitudes are shown every 60°E, and latitudes are shown at 80°N, 65°N (bold) and 50°N. Stippling show areas where the differences are statistically significant to a 95% confidence level.

ERA-Interim and NCEP-CFSR. MERRA-2 also shows lower storm track density over the Kara and Laptev Seas and lower storm genesis density over central north Siberia.

In summer, the differences in Arctic storm track density and genesis density are smaller than in winter, with ERA-Interim generally having higher track densities than the other reanalysis datasets. In winter and summer, the largest differences in storm track density have a magnitude of ≥5 and 3-4 storms per season per unit area respectively. The differences in the storm track density, over the main summer storm track, over of the coastline of Eurasia is small, less than 2 storms per season per unit area (see Figure 3.3b, 3.3d, 3.3f). This indicates that all of the reanalysis datasets show a consistent behaviour in that the Arctic storm activity shifts from predominately over the Canadian Archipelago and the Greenland, Norwegian and Barents Seas in winter, to over the coast of the Eurasian continent (see Figure 3.3b, 3.3d, 3.3f). In summer, JRA-55 and NCEP-CFSR show lower track density over Siberia than ERA-Interim (see Figure 3.3b), whereas MERRA-2 shows lower track density over the Arctic Ocean (see Figure 3.3d). It was shown in ERA-Interim that the Arctic storm genesis occurs inland of the Arctic Frontal Zone, which is consistent with the conclusions of Crawford and Serreze (2016). The differences in genesis density are small over inland Eurasia (see Figures 3.4b, 3.4d, 3.4f), thus, in all of the reanalysis datasets, Arctic storm genesis is shown to occur inland of the Arctic Frontal Zone.

3.6 Storm Intensity

3.6.1 Climatological Arctic Storm Intensity

Figure 3.5 shows that Arctic storms are more intense in winter than in summer in terms of maximum 925 hPa wind speed and minimum MSLP (see Figure 3.5). This is consistent with previous studies (Zhang et al., 2004; Sorteberg and Walsh, 2008; Simmonds et al., 2008). The minimum MSLP distributions of Arctic storms are more consistent across the reanalysis datasets than the maximum 925 hPa wind speed (see Figure 3.5). There is more similarity in the minimum MSLP distributions of Arctic storms between the reanalysis datasets in summer than in winter, with the spread between the reanalysis datasets in the mean MSLP minimum

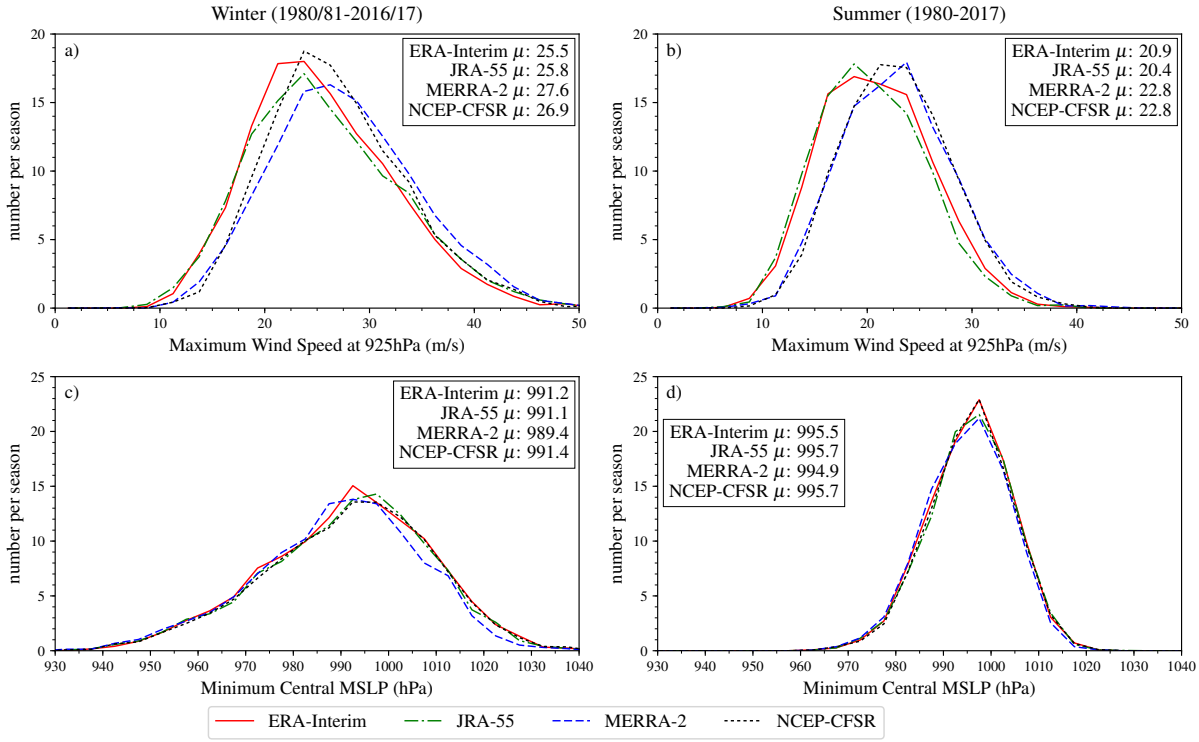

Figure 3.5: Frequency distributions of the maximum intensity of a) and b) 925 hPa wind speed, and c) and d) minimum central mean sea level pressure (MSLP) of all winter (DJF) Arctic storms between 1980/81-2016/17 (left panel) and summer (JJA) Arctic storms from 1980-2017 (right panel) from ERA-Interim, JRA-55, MERRA-2 and NCEP-CFSR. Bin widths are 2.5 ms^{-1} for 925 hPa wind speed and 5 hPa for MSLP and the mean (μ) of the distribution is given for each dataset. Intensity is taken when the storm is north of 65°N.

being 0.8 hPa and 2.0 hPa in summer and winter respectively. Though, there is good agreement in the minimum central MSLP of the most intense storms between the reanalysis datasets in both seasons. MERRA-2 shows fewer weak storms in winter whereas, ERA-Interim, JRA-55 and NCEP-CFSR have similar distributions of weak storms. Zahn et al. (2018) also compared the minimum MSLP of Arctic storms between the datasets shown in Figure 3.5, and also found that the distributions of the more intense storms are more in agreement between the datasets.

The maximum 925 hPa wind speed distributions of Arctic storms between ERA-Interim, JRA-55, MERRA-2 and NCEP-CFSR has not been considered in previous studies. In summer, ERA-Interim and JRA-55 show Arctic storms to have lower maximum 925 hPa winds speeds (with means of 20.9 and 20.4 ms^{-1} respectively) than MERRA-2 and NCEP-CFSR (with means of 22.8 and 22.8 ms^{-1} respectively) (see Figure 3.5a and 3.5b). Wind speeds at 925 hPa are produced at a lower horizontal resolution in ERA-Interim (0.75x0.75°) and JRA-55

(1.25x1.25°) than MERRA-2 (0.625x0.5°) and NCEP-CFSR (0.5x0.5°), and lower horizontal resolution tends to smooth the wind field and result in lower wind speeds. In winter, MERRA-2 and NCEP-CFSR indicate a more intense distribution of maximum 925 hPa winds speeds whereas, ERA-Interim and JRA-55 are lower. There is less consistency between MERRA-2 and NCEP-CFSR in winter than in summer, despite their similar horizontal resolution, with the means of the maximum 925 hPa wind speed distributions in winter being 27.6 and 26.9 ms^{-1} respectively.

The inter-annual variability of the maximum 925 hPa wind speed and minimum MSLP of the 10 most intense Arctic storms per season in winter and summer are shown in Figure S4 in the supplementary material (Figure B.4 in Appendix B). There is no significant trend in Arctic storm intensity from 1980-2017 in terms of maximum 925 hPa wind speed and minimum MSLP in both winter and summer. The inter-annual variability of the intensity of extreme Arctic storms is higher in winter than summer. The standard deviation in the mean winter and summer maximum wind speed and minimum MSLP of the extreme Arctic storms is shown to be less than 2.27 ms^{-1} and 1.31 ms^{-1}, and 6.22 hPa and 2.65 hPa respectively. There is higher consistency between the reanalysis datasets in the minimum central MSLP of the most intense Arctic storms, than the maximum 925 hPa wind speeds, which is also shown in Figure 3.5. It is shown that the maximum intensity of the most intense storms, in terms of the maximum 925 hPa wind speed per year, is different between the reanalysis datasets in both winter and summer.

3.7 Arctic Storm Track Matching

The reanalysis datasets attempt to capture the same atmospheric conditions between 1980 and 2017, thus, they should capture the same storms. To test this, a storm matching algorithm has been used to compare the Arctic storms identified in each reanalysis dataset (Hodges et al., 2011). A comparison is also made between Arctic and mid-latitude storms, to contrast the agreement between the reanalysis datasets in Arctic and mid-latitude regions.

Table 3.3: Percentage of Arctic storms (storms that travel and have genesis north of 65°N) and mid-Latitude Storms (storms that travel and have genesis between 35°N and 65°N) that match between the ERA-Interim, JRA-55, MERRA-2 and NCEP-CFSR reanalysis datasets in winter (DJF) between 1980/81-2016/17 and in summer (JJA) from 1980-2017. Matching criteria are that the storm tracks must have a mean separation distance less than 4° (geodesic), and overlap in time by at least 50% of the points in their life-cycle.

	Winter (DJF)		Summer (JJA)	
	Arctic Storms	Mid-Latitude Storms	Arctic Storms	Mid-Latitude Storms
ERA-Interim, JRA-55	82.4%	85.2%	83.7%	84.7%
ERA-Interim, MERRA-2	79.1%	84.2%	81.9%	83.6%
ERA-Interim, NCEP-CFSR	81.5%	84.8%	83.1%	84.1%
JRA-55, MERRA-2	78.6%	83.7%	82.2%	82.9%
JRA-55, NCEP-CFSR	82.0%	84.3%	82.9%	83.0%
MERRA-2, NCEP-CFSR	81.4%	83.6%	83.1%	83.3%
Average	**80.8%**	**84.3%**	**82.8%**	**83.6%**

Table 3.3 provides a summary of the percentage of storms that match in winter and summer between the reanalysis datasets. Overall, the percentage of Arctic storms that match between the reanalysis datasets is slightly higher in summer than in winter. The average percentage of storms between the reanalysis datasets that match in summer is 82.8% and in winter is 80.8%. The difference of 2% equates to approximately 80 storms from 1980-2017. The highest percentage of matches between the reanalysis datasets in winter and in summer is between ERA-Interim and JRA-55 whereas, the lowest percentage of Arctic storms that match in winter is between JRA-55 and MERRA-2 and in summer is between ERA-Interim and MERRA-2. The percentage of mid-latitude storms that match between the reanalysis datasets is slightly higher than that of Arctic storms in both seasons. This shows that there is more agreement in storms captured in the reanalysis datasets in mid-latitude regions than in Arctic regions, especially in winter.

Figure 3.6 shows the maximum 850 hPa T42 relative vorticity of Arctic storms from JRA-55, MERRA-2 and NCEP-CFSR that match and do not match with storms from ERA-Interim. This is found to occur between ERA-Interim and all of the other reanalysis datasets. ERA-Interim was shown in Table 3.1 to have the highest storm frequency of all of the datasets in winter and summer. Generally, the more intense Arctic storms match well between the reanalysis datasets,

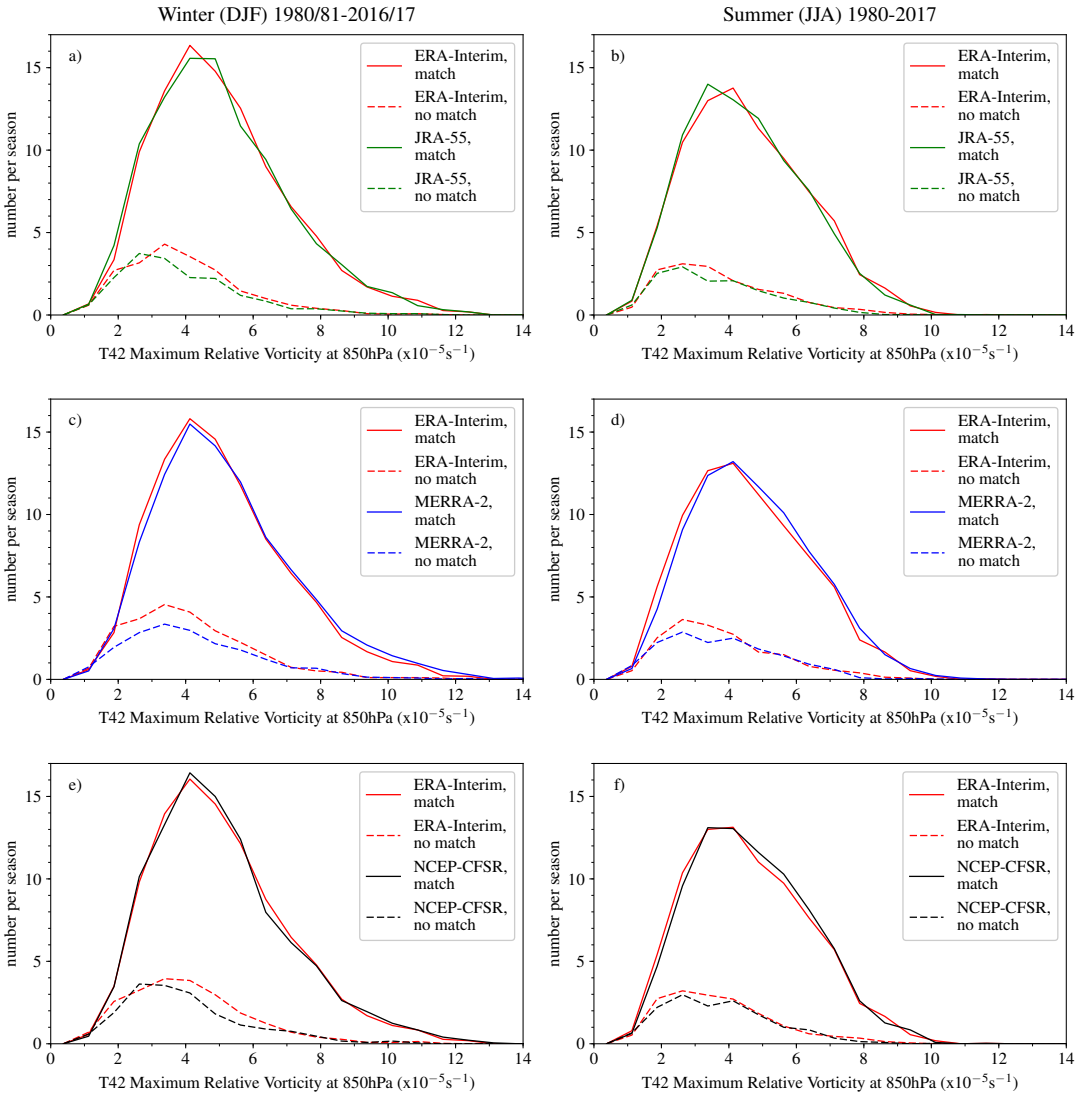

Figure 3.6: Maximum 850 hPa T42 relative vorticity distributions of Arctic storms from ERA-Interim that match with a) and b) JRA-55, c) and d) MERRA-2, and e) and f) NCEP-CFSR, between the period of 1980/81-2016/17 in winter (DJF) (left panel) and 1980-2017 in summer (JJA) (right panel). Storm tracks match if they are separated by a distance less than 4° (geodesic) and 50% of the points in the track occur at the same time. Bin widths are 0.75x10^{-5}s^{-1}. Intensity is taken when the storm is north of 65°N.

and it is the weaker Arctic storms that do not match between the reanalysis datasets.

To test the sensitivity, the analysis was also performed with stricter criteria where the storm tracks must have a mean separation distance less than 2° (geodesic), and overlap in time by at least 75% of the points in their life cycle (see Figure S5 and Table S1 in the supplementary material - Figure B.5 and Table B.1 in Appendix B). Using these stricter criteria, it is also found that generally the more intense Arctic storms still match well between the reanalysis datasets, and it is the weaker Arctic storms that do not match between the reanalysis datasets. Winter is

Table 3.4: Frequency of all Arctic storms that travel north of 65°N per season between 1980/81-2016/17 in winter (DJF) and 1980-2017 in summer (JJA) identified by the storm tracking algorithm developed by Hodges (1994, 1995, 1999) based on the 850hPa relative vorticity field (VOR850) and on the mean sea level pressure field (MSLP).

	Winter (DJF) (1980/81-2016/17) (per season)	Summer (JJA) (1980-2017) (per season)
ERA-Interim VOR850 T42	119.4	98.3
ERA-Interim MSLP T63	64.4	65.6

found to have a lower percentage of Arctic storms that match than summer, 64.3% and 68.2% respectively. In winter, the percentage of matching mid-latitude storms between the reanalysis datasets is also higher than that of Arctic storms when using these stricter criteria, 69.2% and 64.2% respectively. Though, the percentage of matching of summer storms is higher in Arctic regions than mid-latitude regions, 68.2% and 67.7% respectively. Zahn et al. (2018) showed that approximately 60% of Arctic storms match between the reanalysis datasets using similar matching criteria to the stricter matching criteria used in this study, which are similar to results found in this study. Thus, there is more certainty between the reanalysis datasets in the location and time of the most intense Arctic storms.

3.8 Mean Sea Level Pressure Field Based Versus Relative Vorticity Field Based Storm Tracking Algorithm

Results from this study have some differences from previous studies. In section 3.1., it was shown that there is higher storm frequency in winter than summer using storm tracking based on 850hPa relative vorticity, which differs from the results of Serreze (1995), Serreze et al. (2001), Tilinina et al. (2014) and Zahn et al. (2018). In section 4.1., the Canadian Archipelago was found to be an area of high storm track density in winter and summer; an area that has not been previously shown to have high storm activity (Zhang et al., 2004; Tilinina et al., 2014; Crawford and Serreze, 2016; Zahn et al., 2018). In this study, the storm tracking algorithm is based on the 850 hPa relative vorticity field, whereas most previous studies use a storm tracking algorithm based on minima in the MSLP field.

Table 3.4 shows the number of storms per season in winter and summer is different when the storm tracking is based on the 850 hPa relative vorticity field and on the MSLP field. When using the MSLP field, Arctic storm frequency in summer and winter is similar, which is in agreement with Serreze (1995), Serreze et al. (2001), Tilinina et al. (2014) and Zahn et al. (2018). In contrast, Arctic storm frequency is higher in winter than summer when basing the storm tracking algorithm on the 850hPa relative vorticity. Although Crawford and Serreze (2016) showed that 31 more storms (approximately 1 more storm per season) had occurred between 1979-2014 in winter (DJF) than in summer (JJA) when using a storm tracking algorithm based on MSLP, the differences between using 850 hPa relative vorticity and MSLP, shown in Table 3.4 for each season, are substantially higher. Table 3.1 shows that for ERA-Interim, 21 more storms per season occur in winter (DJF) than in summer (JJA) when using storm tracking based on 850hPa relative vorticity. Relative vorticity is able to represent smaller spatial scales than MSLP, thus storm tracking algorithms based on the vorticity field are able to identify more smaller scale storms than those based on MSLP (Hoskins and Hodges, 2002; Neu et al., 2013), even if the vorticity is at lower resolution than the MSLP (Jung et al., 2012).

Figure 3.7a and 3.7b show the spatial differences in Arctic storm track density in winter and summer between using the 850 hPa relative vorticity and the MSLP as the identification variable. The differences are of higher magnitude in winter than summer, with the largest differences occurring in the Canadian Archipelago in winter and in summer, with magnitudes of 22+ and 14-16 storms per season per unit area respectively. Additional storms are also identified using relative vorticity in the Greenland Sea, the Arctic Ocean and north of coastal Siberia in summer and winter. In winter, additional storms are also found over Scandinavia, inland Siberia and the Bering Strait when using relative vorticity. Although the MSLP and 850 hPa relative vorticity fields have been filtered to a spatial resolution of T63 and T42 respectively, this should in fact lead to the MSLP storm tracking to identify more storms (Blender and Schubert, 2000). In section 4.1. it was found that the track density of Arctic storms was significantly higher in the Canadian Archipelago using relative vorticity than shown previously by Zhang et al. (2004), Tilinina et al. (2014), Crawford and Serreze (2016),

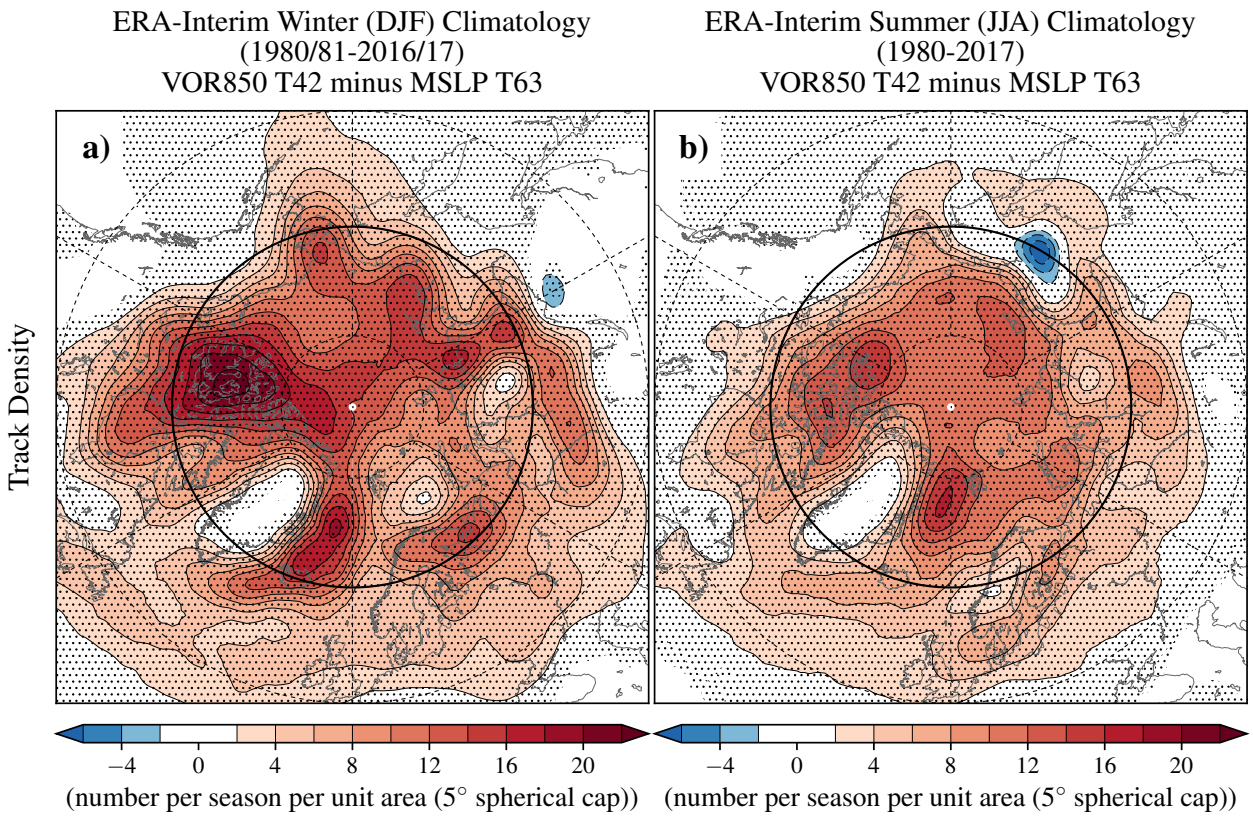

Figure 3.7: Differences in the climatological storm track density of all Arctic storms that travel north of 65°N storms identified by a storm tracking algorithm based on the 850hPa relative vorticity field (VOR850) and the mean sea level pressure field (MSLP) between a) 1980/81-2016/17 in winter (DJF) (left panel) and b) 1980-2017 in summer (JJA), based on the ERA-Interim reanalysis dataset. Stippling show areas where the differences are statistically significant to a 99% confidence level.

and Zahn et al. (2018) which all used MSLP tracking. Differences between this study and previous studies could be due to using storm tracking based on 850 hPa relative vorticity or MSLP (Neu et al., 2013). Although, the differences could also arise from a number of other reasons. One reason may be that previous studies have used a higher resolution storm tracking variable, whereas in this study, 850 hPa relative vorticity is smoothed to T42 spectral resolution (Blender and Schubert, 2000). Previous studies may also use different filtering thresholds of the intensity, lifespan and track length of the storms, and, may also filter out storms over high orography (Rudeva et al., 2014; Pinto et al., 2005). However, Table 3.4 and Figure 3.7 show the differences in Arctic storm frequency and track density between using storm tracking based on 850 hPa relative vorticity and MSLP using the same method.

It is notable that the differences in Arctic storm frequency when using 850 hPa relative vorticity and MSLP as the storm tracking variable are much higher than the differences in

Arctic storm frequency between the reanalysis datasets (see Tables 3.1 and 3.4). The highest differences in Arctic storm track density between using 850 hPa relative vorticity or MSLP for the storm tracking, shown in Figure 3.7, exceed 21 storms per season. In comparison, the highest differences in Arctic storm track density between reanalysis datasets is between 5-6 storms per season (see Figure 3.3). Furthermore, there are also more statistically significant differences between Arctic storm track density shown in Figure 3.7 than in Figure 3.3, even at a higher confidence level of 99% rather than 95%.

3.9 Summary and Conclusions

The spatial distribution, frequency and intensity of Arctic storms has been compared between the ERA-Interim, JRA-55, MERRA-2 and NCEP-CFSR reanalysis datasets. Arctic storms were identified using a tracking scheme based on the 850 hPa relative vorticity field, with the emphasis on mobile synoptic-scale storms that travel north of 65°N in winter (DJF) and summer (JJA). The objectives are to quantify the climatological and inter-annual characteristics of Arctic storms and how different these characteristics are between multiple reanalysis datasets, and also when using two different storm tracking identification variables, 850 hPa relative vorticity and mean sea level pressure (MSLP).

- There are no significant trends in Arctic storm characteristics from 1980-2017 in winter (DJF) or summer (JJA).

Despite the Arctic climate changing dramatically over the past few decades, no significant trend was found in the frequency of Arctic storms in winter and summer from 1980-2017 in all of the reanalysis datasets. This was also found by Zahn et al. (2018). In addition, Arctic storms have been separated into storms that have Arctic genesis and mid-latitude genesis in this study. It was found that there were no significant trends in the frequency of Arctic storms with Arctic genesis or mid-latitude genesis in winter and summer. Similarly, no significant trends were found for the intensity of the 10 most intense storms per season from 1980-2017.

Given that the observations assimilated in the Arctic are sparser than in mid-latitude regions, it may be expected that the differences in the Arctic storm characteristics between the reanalysis datasets may be large than in mid-latitudes. However, this study has identified some robust characteristics of Arctic storms that are consistent between the four reanalysis datasets. For example, in winter, the areas with the highest Arctic storm track density occur in the Greenland, Norwegian and Barents Seas and the Canadian Archipelago, whereas in summer, Arctic storm track density is highest over and north of continental Eurasia. In addition, the four reanalysis datasets show that approximately 50% of all Arctic storms have Arctic genesis (north of 65°N) and mid-latitude genesis (south of 65°N). Arctic storms were also found to become more intense in winter than in summer, in terms of their minimum MSLP and maximum 925 hPa wind speed. All four of the reanalysis datasets show that the inter-annual variability in Arctic storm frequency is small, approximately 15% of the total storm number (about 15-20 storms per season). Although there are similarities in Arctic storm characteristics between the reanalysis datasets, there are also differences.

- The differences in Arctic storm characteristics between the reanalysis datasets are higher in winter (DJF) than in summer (JJA).

Greater differences were found when comparing the storm track density and genesis densities of JRA-55, MERRA-2 and NCEP-CFSR with ERA-Interim in winter than in summer. The greatest differences in track density were found to occur over the Canadian Archipelago in winter, where track densities differed by as much as 5-6 storms per season per unit area (5° spherical cap). In comparison, the differences in summer Arctic storm track density did not exceed 3-4 storms per season per unit area. When comparing the inter-annual variability in the frequency of Arctic storms between the reanalysis datasets, the average Pearsons correlation coefficient for storms with Arctic genesis between the reanalysis datasets across the time-series was found to be 0.55 in winter, but 0.74 in summer. The differences between the four reanalysis datasets in Arctic storm frequency were also found to be higher in winter than in summer, differences of 5.7 and 2.1 storms per season respectively. The percentage of Arctic storms that match between the reanalysis datasets was also found to be also higher in summer than in winter across all of the

reanalysis datasets.

Arctic winter poses significant challenges for the creation of global atmospheric reanalyses. From an observational perspective there is a low density of conventional observations, and difficulties in identifying cloud and estimating emissivity over snow and ice limit the current use of infrared and microwave satellite data in the troposphere (Jung et al., 2016). From a physical perspective there is a frequent occurrence of conditions that are hard to represent in numerical models, like stable boundary layers and mixed phase clouds (Sandu et al., 2013; Pithan et al., 2016). Difficulties may also arise from a large differences between the background state of the numerical models and the observations, which may lead to the data assimilation scheme to reject some observations (Lawrence et al., 2019). It is plausible that these factors may contribute to greater differences in Arctic storm characteristics between the reanalysis datasets in winter than in summer.

- Approximately half of all Arctic storms have Arctic genesis (north of 65°N) and half of all Arctic storms have mid-latitude genesis (south of 65°N) in winter (DJF) and summer (JJA).

It was found that an average of 54.4% and 47.4% of all Arctic storms across the reanalysis datasets have genesis in the Arctic (north of 65°N) in winter and summer respectively. This shows that storms are a significant mechanism for transporting air from low to high latitudes. The differences between the reanalysis datasets are generally higher when comparing Arctic storms with Arctic genesis than comparing Arctic storms with mid-latitude genesis. This is particularly true in winter. When comparing the inter-annual variability in the frequency of Arctic winter storms between the reanalysis datasets between 1980/81-2016/17, the average Pearsons correlation coefficient for storms with Arctic genesis across the reanalysis datasets was found to be 0.55, compared to an average Pearsons correlation coefficient of 0.84 for Arctic storms with mid-latitude genesis. In comparison, the average Pearsons correlation coefficient of the frequency of summer Arctic storms with Arctic and mid-latitude genesis is 0.74 and 0.79, which is higher for Arctic storms with mid-latitude genesis. In addition, the average percentage of storms that match between the reanalysis datasets was found to be higher for

Arctic storms with mid-latitude genesis than Arctic storms with Arctic genesis. In addition, the average percentage of storms that match between the reanalysis datasets was found to be higher for mid-latitude storms than Arctic storms, 80.8% and 84.3% in winter respectively, and 82.8% and 83.6% in summer respectively. This highlights the additional challenges in producing atmospheric reanalyses in the Arctic compared to mid-latitude regions, especially in winter.

- The representation of Arctic storm characteristics identified in reanalysis datasets are dependent on the storm tracking variable.

Basic properties of the Arctic storm climatology, such as whether the total number of storms in the summer is larger or smaller than in winter, are dependent on whether one uses relative vorticity or MSLP as the storm tracking variable. Previous studies (such as Serreze (1995); Serreze et al. (2001); Tilinina et al. (2014); Zahn et al. (2018)) show that Arctic storm frequency is higher in summer than in winter. These studies identified Arctic storms in reanalysis datasets using a storm tracking algorithm based on the MSLP field, whereas in this study, Arctic storm characteristics were compared between storms identified in the ERA-Interim dataset based on MSLP and on 850 hPa relative vorticity.

Here the storm tracking applied to the MSLP field was found to identify fewer storms than the 850 hPa relative vorticity storm tracking. Different seasonal patterns of Arctic storm frequency are obtained using the two different tracking variables, with storm frequency being similar in winter and summer using MSLP (64.4 and 65.6 storms per season respectively), whereas when using 850 hPa relative vorticity the frequency of Arctic storms is higher in winter than in summer (119.4 and 98.3 storms per season respectively). The differences in Arctic storm frequency between the two identification variables was found to be higher in winter than in summer, with the highest differences occurring over the Canadian Archipelago and the North Atlantic Ocean. The differences between the 850 hPa relative vorticity and MSLP storm tracking were substantially larger than the differences found between the reanalysis datasets. In winter, Arctic storm frequency differed by 55 storms per season between the 850 hPa

relative vorticity and MSLP storm tracking, whereas between the reanalysis datasets, storm frequency in winter only differed by as much as 5.7 storms per season.

Relative vorticity in general focuses on smaller spatial scales than MSLP. Thus storm tracking algorithms based on the relative vorticity field are able identify more smaller scale storms than those based on MSLP (Hoskins and Hodges, 2002; Neu et al., 2013). It is plausible that these smaller scale storms tend to occur more in winter than in summer, as larger differences in Arctic storm characteristics has been found in winter than in summer between storm tracking based on relative vorticity and MSLP. In this study, it was found that there are larger differences in Arctic storm frequency per season and track density when identifying storms using the 850 hPa relative vorticity compared to using MSLP, than differences between the different reanalysis datasets. This shows that the decision to use 850 hPa relative vorticity or MSLP for storm tracking can be more important than the choice of reanalysis dataset.

Reanalysis datasets have many applications and are widely used as a source of data by decision makers (e.g. the insurance industry). Reanalyses are also used within the climate community, for example, to evaluate climate models (e.g. Vavrus, 2013; Day et al., 2018). However, there are multiple reanalysis datasets available that use different models and data assimilation systems. This study has found some robust characteristics of Arctic storms. Generally, there is good agreement between the reanalysis datasets in the location, time and maximum T42 relative vorticity of the most intense Arctic storms. However, there are generally greater differences between the datasets in winter than in summer, which may be associated with the lower amount of observations that are assimilated into the datasets and the occurrence of conditions that are hard to represent in numerical models in winter. These differences in Arctic storms characteristics between reanalysis datasets may be reduced by special observing periods such as the Year of Polar Prediction (Jung et al., 2016), that may increase the amount of observations available for data assimilation or may lead to the improvement in the representation of Arctic conditions in numerical models. These differences may also be reduced in future reanalysis datasets, which may use more sophisticated data assimilation schemes.

Chapter 4

Arctic Storm Development and Structure

It is unclear whether the typical development and structure of Arctic storms is similar to that described by existing conceptual models of mid-latitude storm development (e.g. the Norwegian Cyclone Development Model from Bjerknes, 1919, 1922) and of mid-latitude storm structure (e.g. Browning, 1997). Case studies of past Arctic storms have been identified, which do not follow these conceptual models (e.g. Tanaka et al., 2012; Aizawa and Tanaka, 2016; Tao et al., 2017). Moreover, other case studies have identified past Arctic storms with exceptionally long lifetimes (e.g. Yamagami et al., 2017). This chapter aims to determine the typical structure and development of Arctic storms in all seasons using a large sample of past Arctic storms. The development and structure of Arctic storms is contrasted with storms that occur over the North Atlantic Ocean, and existing conceptual models.

This chapter addresses the second research question of this Thesis:

RQ2: What is the typical development and structure of Arctic storms, and how does this differ to that of mid-latitude storms and existing conceptual models?

4.1 Introduction

The structure of mid-latitude storms has been a focal point of scientific research for over 100 years, since Bjerknes (1919) first proposed the Norwegian Cyclone Model, a conceptual model of mid-latitude storm development (Schultz et al., 1998; Dacre, 2020). It is now understood that the occurrence of hazardous weather within a storm is tied to its structure, with high precipitation typically occurring at the location of fronts (Bjerknes, 1919; Dacre, 2020), and high low-level wind speeds generally occurring at locations of low-level conveyor belts and features such as sting jets (Browning, 1997, 2004; Martínez-Alvarado et al., 2014; Schultz and Browning, 2017). The structure of storms and their features that result in hazardous weather are now better forecasted (e.g. Gray et al., 2020). However, the typical structure of Arctic storms is unclear.

It is unclear whether Arctic storms have a similar development and structure to that described in conceptual models based on mid-latitude storms (e.g. the Norwegian Cyclone Model and Shapiro-Keyser Model). In fact, previous research has shown examples of Arctic storms that have a different structure to mid-latitude storms (Tanaka et al., 2012; Aizawa and Tanaka, 2016; Tao et al., 2017). For example, Aizawa and Tanaka (2016) showed that the Great Arctic Storm of 2012 had an axi-symmetric cold core and barotropic structure, which contrasts with the baroclinic structure of mid-latitude storms (characterised by fronts between cold and warm air) (Bjerknes, 1919, 1922). This unique structure was also identified in two other Arctic storms that occurred in June 2008 (Aizawa and Tanaka, 2016) and September 2010 (Tao et al., 2017). Moreover, some Arctic storms have been found to have exceptionally long lifetimes (Simmonds et al., 2008; Yamagami et al., 2017). This would bring prolonged hazardous weather conditions in the Arctic, such as high wind speeds and waves, which are associated with the passage of a storm (Thomson and Rogers, 2014). Yamagami et al. (2017) described an Arctic storm that occurred in August 2016 with a lifetime greater than 1 month. This raises the questions; what is the typical development and structure of Arctic storms, and how does this differ to mid-latitude storms?

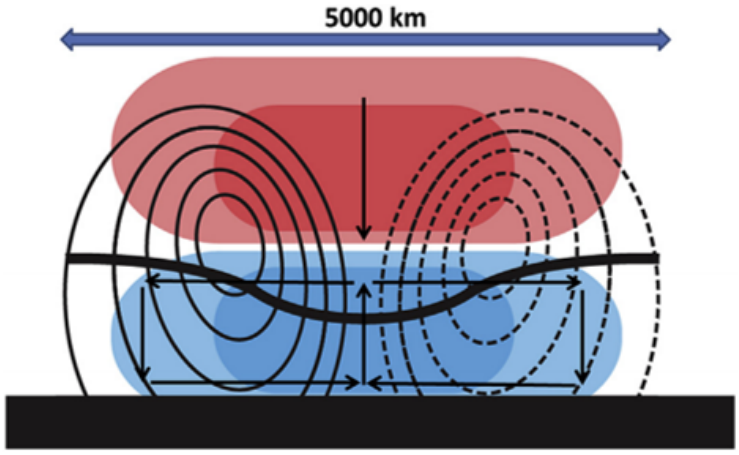

Figure 4.1: Conceptual model the structure of Arctic summer storms, based on just two Arctic storm case studies from Aizawa and Tanaka (2016). The thin solid and dashed lines indicate the tangential wind jet and the opposite tangential wind jet of the cyclonic circulation. The bold black line indicates the tropopause. The warm and cold regions are shaded in red color and blue color, respectively. Black arrows show the secondary circulation, and the lower stratospheric downdraft. From (Aizawa and Tanaka, 2016)).

Previous research on the structure and development of Arctic storms is limited to examining individual case studies of Arctic storms (Tanaka et al., 2012; Aizawa et al., 2014; Aizawa and Tanaka, 2016; Tao et al., 2017; Yamagami et al., 2017). There is a need for further research to find how typical the development and structure of these individual Arctic storm case studies are relative to a larger sample storms, as highlighted by Aizawa and Tanaka (2016) and Tao et al. (2017). It is expected that human activity (e.g shipping, oil exploration, tourism) in the Arctic will increase as Arctic sea ice extent continues to decline (Stroeve et al., 2007; Melia et al., 2016; Hansen et al., 2016; Maher, 2017). As the occurrence of hazardous weather is tied to the structure of a storm, it is imperative to understand the typical development and structure of Arctic storms. This will help to better understand the occurrence of hazardous weather associated with Arctic storms, which threatens human activities in the Arctic.

Aizawa and Tanaka (2016) proposed a conceptual model of the Arctic summer storm structure at the time of maximum intensity (see Figure 4.1). But, this study was based on just two Arctic storms: the Great Arctic Storm of 2012 and another occurring in June 2008. Aizawa and Tanaka (2016) stated that based on the two case studies, Arctic summer storms typically have a "deep barotropic cyclonic circulation, a secondary circulation in the troposphere, a downdraft at the lower stratosphere, a coupling of a warm core in the lower stratosphere and a cold core in the troposphere, and a deep tropopause fold over the cyclone center". Aizawa and Tanaka (2016)

also stated that they typically have a large horizontal extent of 5,000 km. This is in contrast to existing conceptual models of mid-latitude storm development (e.g. the Norwegian Cyclone Model - Bjerknes, 1919, 1922), which characterise storms with fronts between cold and warm air masses, which occlude as the storm decays. Occlusion is the process by which the cold front of a low-pressure system catches up the warm front, and wraps around the storm centre (Bjerknes, 1919, 1922). The question is whether the model proposed by Aizawa and Tanaka (2016) is typical of most Arctic storms.

The spatial distribution of Arctic storms changes significantly between seasons (Vessey et al., 2020). In winter, the highest track density of Arctic storms occurs over the Greenland, Norwegian and Barents seas, whereas in summer, the highest track density of Arctic storms occurs over the coastline of Eurasia and the high Arctic Ocean. Previous research on the structure and development of Arctic storms has tended to focus on case studies occurring in summer (Tanaka et al., 2012; Aizawa et al., 2014; Aizawa and Tanaka, 2016; Tao et al., 2017). The typical structure of Arctic storms in other seasons has not yet been determined and described.

This chapter aims to describe the typical development and structure of intense Arctic storms across all seasons for the first time. The general structure of Arctic storms is determined using a storm compositing methodology similar to Catto et al. (2010) and Dacre et al. (2012) (see Section 2.4.3 in Chapter 2). This will be achieved by the following objectives:

- Obtain the composite structure and life-cycles of the 100 most intense Arctic storms per season using the ERA5 reanalysis dataset,
- Compare the structure and life-cycle development of Arctic storms with mid-latitude storms occurring over the North Atlantic Ocean,
- Evaluate the model of Arctic summer storm structure from Aizawa and Tanaka (2016) against the composite structure of the 100 most intense Arctic summer storms.

In Section 4.2, the method of selecting intense Arctic and mid-latitude North Atlantic Ocean storms is described. The life-cycles of intense Arctic storms and North Atlantic Ocean storms

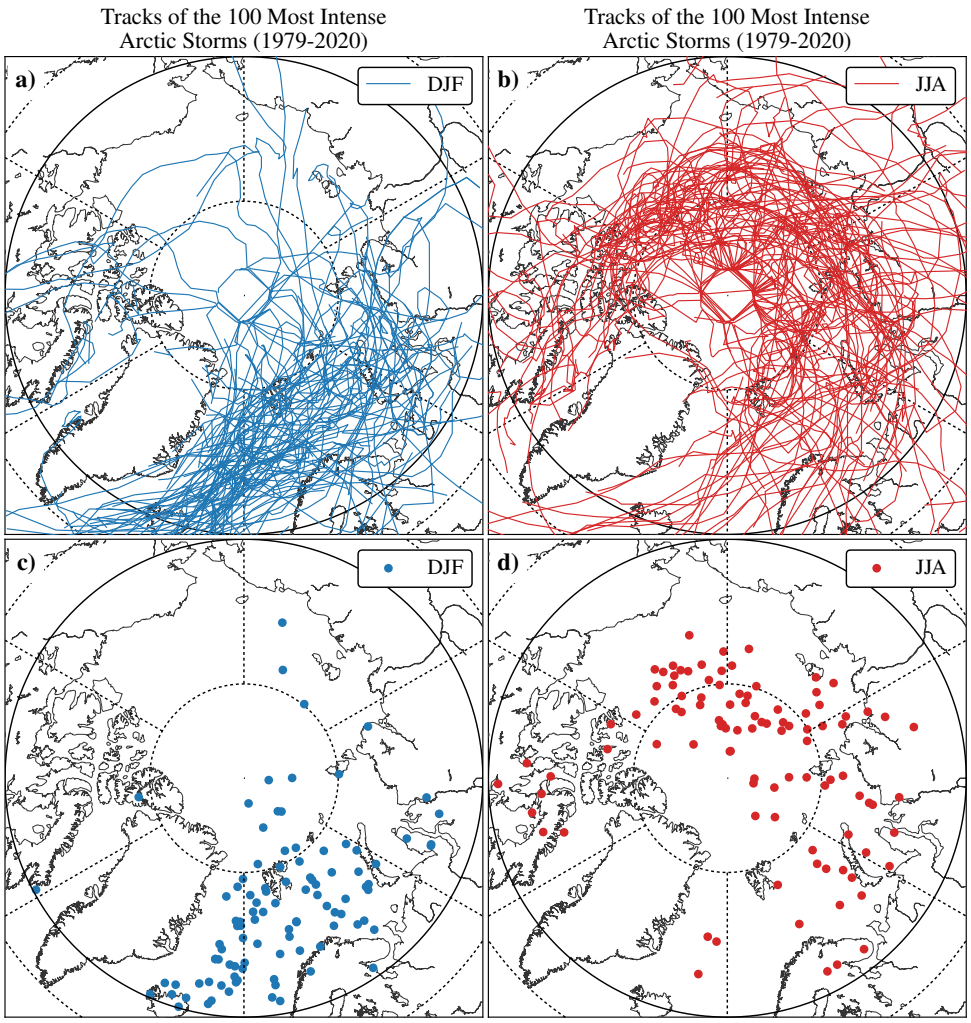

Figure 4.2: Individual tracks of the 100 most intense **a)** winter (DJF) and **b)** summer (JJA) Arctic storms, and the locations of the minimum mean sea level pressure of each **c)** winter and **d)** summer storms between 1979 and 2019 based on the ERA5 reanalysis dataset.

are compared across all seasons in Section 4.3. The composite structure of intense Arctic storms is compared with that of intense North Atlantic Ocean storms in winter (DJF) and summer (JJA) in Sections 4.4 and 4.5. Section 4.6 compares the model of Arctic summer storm structure from Aizawa and Tanaka (2016) to the composite structure of the 100 most intense Arctic summer storms. Finally, a summary and conclusions are given in Section 4.7.

4.2 Identifying Intense Arctic Storms

The 100 most intense Arctic storms, storms with the lowest mean sea level pressure (MSLP) minima, have been identified in each season between 1979 and 2019, from storm tracks

identified in the ERA5 reanalysis datasets, using TRACK (see Section 2.4 in Chapter 2). To focus on intense Arctic storms, 60% of the storm track points of each storm must be in the Arctic (north of 65°N) and their maximum intensity (i.e. minimum MSLP) must also occur in the Arctic. Arctic storms are contrasted to the 100 most intense mid-latitude storms that occur over the North Atlantic Ocean (between -53 to 20°E and 30 - 65°N), and likewise, these storms must have 60% of the storm track points and their maximum intensity in this region.

The track density of all Arctic storms has been found to be seasonally dependent (Vessey et al., 2020), which is also shown in the spatial distribution of the 100 most intense Arctic storms per season. Figure 4.2 shows the tracks of the 100 most intense winter and Arctic summer storms and the locations of the minimum MSLP of each storm. Generally, intense winter Arctic storms tend to occur over the Greenland, Norwegian and Barents Seas (see Figure 4.2). Whereas, intense Arctic summer storms tend to occur north of the Eurasia coastline and over the Arctic Ocean (see Figure 4.2). Similarly to winter, the 100 most intense spring (MAM) and autumn (SON) Arctic storms also tend to occur over the Greenland, Norwegian and Barents Seas (see E.1 in Appendix E).

4.3 Development of Arctic and North Atlantic Ocean Storms

The most intense Arctic and North Atlantic Ocean storms occur in winter, where the mean minimum MSLP of the 100 most intense storms is 953.8 hPa and 945.5 hPa respectively (see Figure 4.3). Although the mean minimum MSLP of intense Arctic summer storms is slightly lower than that of intense summer North Atlantic Ocean storms, it appears that North Atlantic Ocean storms grow and decay from and to a higher MSLP at the start and end of their life-cycle than Arctic storms. This is likely because the environmental MSLP of mid-latitude regions is higher than that of Arctic regions, as air temperatures are typically lower in the Arctic. Thus, the minimum MSLP shown in Figure 4.3 may be similar between summer Arctic and North Atlantic Ocean storms, but pressure gradients that affect wind speeds may be higher in summer North Atlantic Ocean storms.

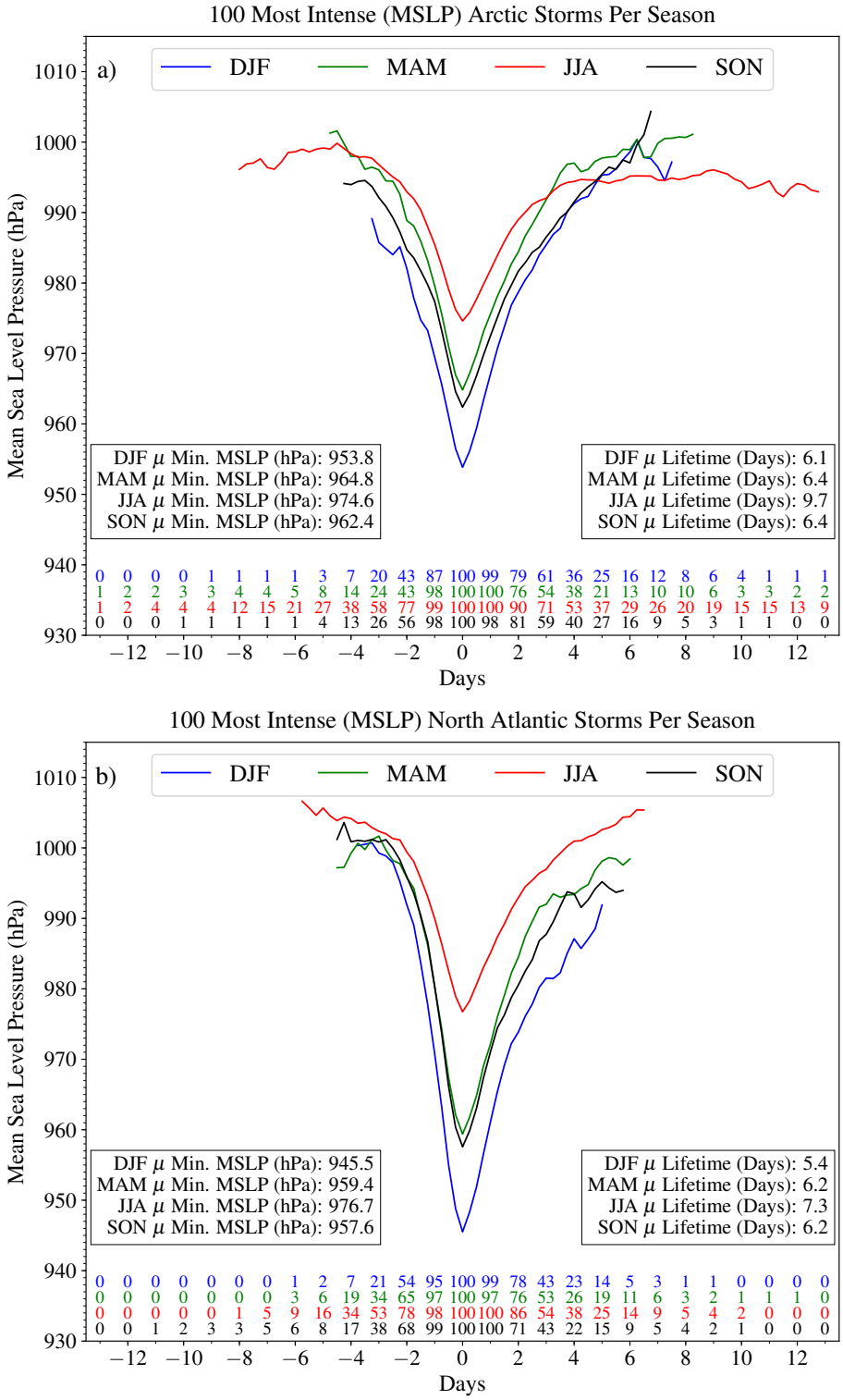

Figure 4.3: The mean life-cycles of the 100 most intense (based on minimum mean sea level pressure - MSLP) **a)** Arctic and **b)** North Atlantic Ocean storms per season between 1979 and 2019 based on the ERA5 reanalysis dataset. Storms are centred at the time of their maximum intensity (minimum MSLP), and the numbers indicate how many storms occur at each timestep. At least 10 storms must exist at each timestep. The mean (μ) minimum MSLP and lifetime of the 100 most intense storms per season is also given.

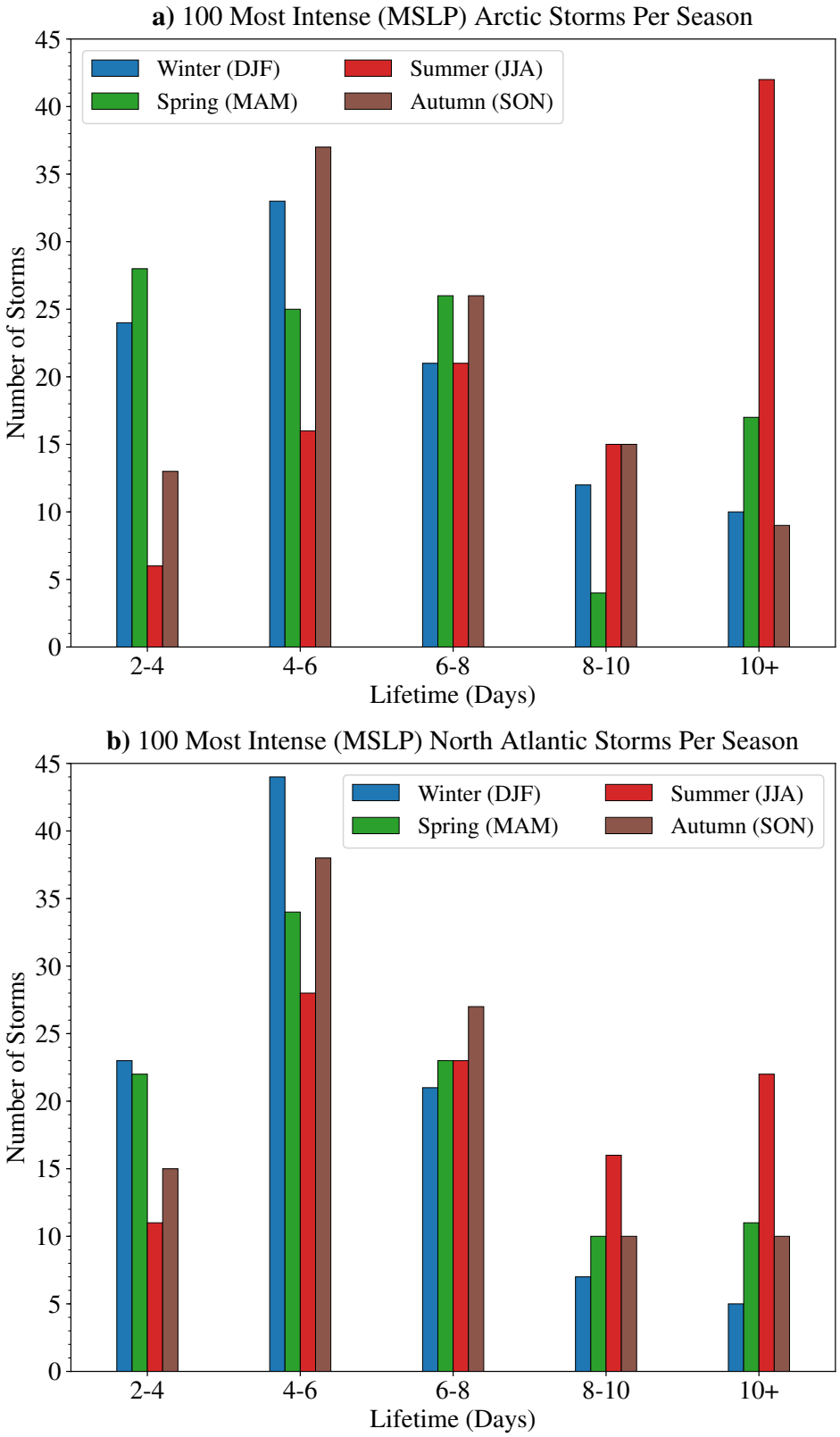

Figure 4.4: Lifetimes of the 100 most intense (based on minimum mean sea level pressure) **a)** Arctic and **b)** North Atlantic Ocean storms per season between 1979 and 2019 based on the ERA5 reanalysis dataset.

Intense Arctic summer storms typically have longer-lifetimes than that of intense Arctic storms in other seasons and North Atlantic Ocean storms in all seasons(see Figure 4.4). The modal lifetime of the 100 most intense Arctic summer storms is greater than 10 days, with 44% of storms having a lifetime greater than 10 days. This is greater than the modal lifetime for Arctic storms in other seasons, and North Atlantic Ocean storms in all seasons, which is between 4 - 6 days (see Figure 4.4). This is also shown in Figure 4.3, as the mean lifetime for intense Arctic summer storms is 2.4 days greater than that of intense summer North Atlantic Ocean storms (see Figure 4.3). Moreover, the mean lifetime of intense Arctic summer storms is more than 3 days greater than that of intense Arctic and North Atlantic Ocean storms in winter, spring and autumn (see Figure 4.3).

4.4 Composite Structure of Winter (DJF) Arctic and North Atlantic Ocean Storms

The composite structure of the 100 most intense Arctic and North Atlantic Ocean storms is shown in the following sections. Storm composites are produced by sampling atmospheric fields to a 20° x 20° longitude and latitude grid centred to a storm, which is then averaged over all storms (see Section 2.4.3 in Chapter 2). When making the composites, storms can be orientated relative to the direction of propagation before they are averaged together, or the geographical orientation (e.g. north, east, south and west) of the storm can be kept before they are averaged. By rotating the storms relative to the direction of propagation, system-relative winds can be computed in addition to earth-relative winds, which describe the wind speeds within a storm with the propagation speed of the storm deducted from the wind field. In this thesis, both rotated and non-rotated composites have been computed.

4.4.1 Surface Features

The minimum MSLP of the winter Arctic storm non-rotated composite at the time of maximum intensity is less intense than the winter North Atlantic Ocean storm composite (see Figures

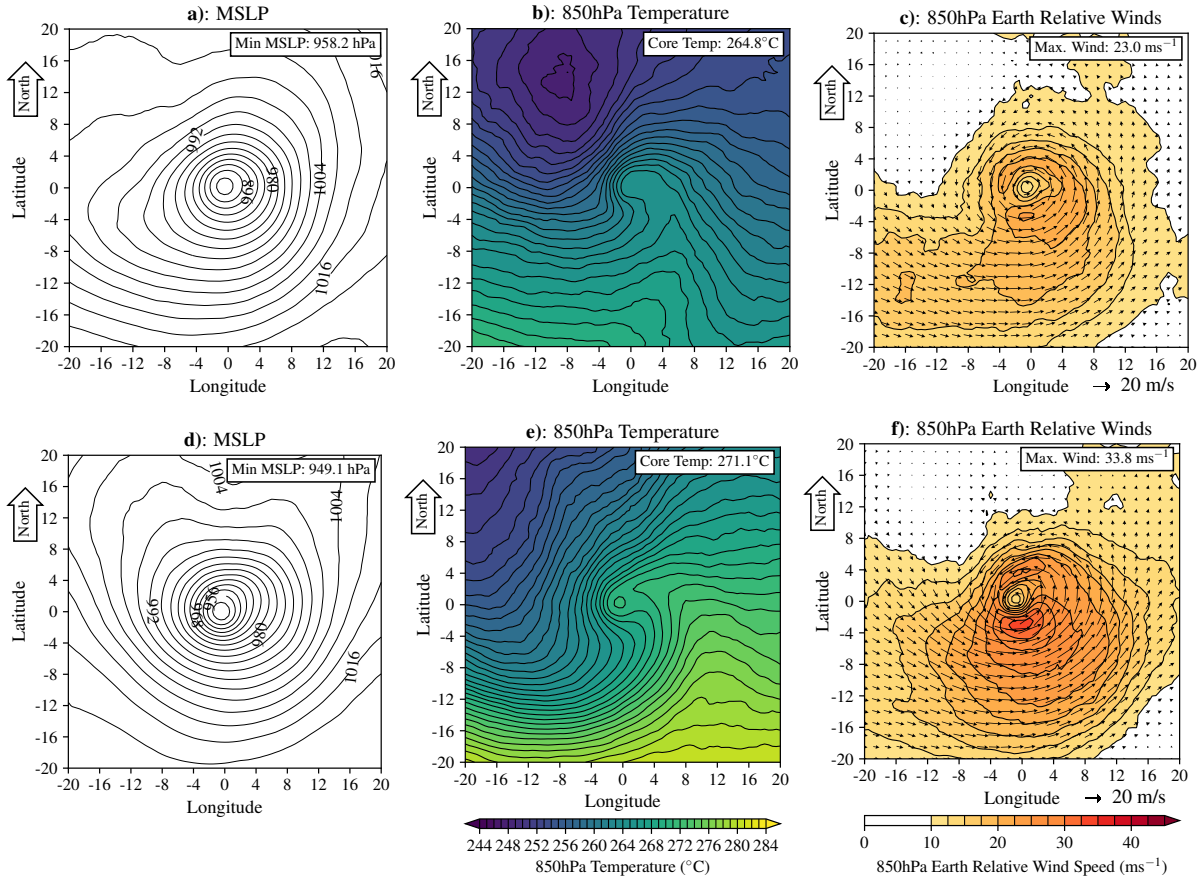

Figure 4.5: Horizontal composite structure at the time of maximum intensity (i.e. the time of minimum mean sea level pressure - MSLP) of the 100 most intense (based on minimum MSLP) winter (DJF) **a) - c)** Arctic storms and **d) - f)** North Atlantic Ocean storms between 1979 and 2019 based on the ERA5 reanalysis dataset. **a) and d)** show the composite mean sea level pressure (MSLP) structure. **b) and e)** show the composite 850 hPa temperature structure. **c) and f)** show the composite 850 hPa wind speed (contours) and direction (vectors). In producing these composites, storms have not been rotated before averaging, so that the top of each figure is north (see arrow).

4.3 and 4.5a and 4.5d). The minimum MSLP of each composite is 958.2 hPa and 949.2 hPa for Arctic and North Atlantic Ocean storms respectively (Figure 4.5a and 4.5d). The MSLP composites show deformation occurring to the west of the Arctic composite centre (see Figure 4.5a) and to the north of the North Atlantic Ocean composite centre (see Figure 4.5d). The deformation in the MSLP composite is likely a consequence of the presence of the Iceland, Greenland and Svalbard landmasses, as these tend to be to the north or west of the storms at the time of maximum intensity, and are elevated above the ocean (see Figure E.8a in Appendix E).

The 850 hPa temperature composite structure at the time of maximum intensity of intense winter Arctic and North Atlantic Ocean storms have a similar structure (see Figure 4.5b and 4.5e). In both non-rotated composites, cold air appears to have propagated southward and

wrapped around the storm centre. This shows that the composite is undergoing occlusion. Both composites have a similar structure to that described in Stage II of the Norwegian Cyclone Model (Bjerknes, 1919, 1922) (see Figure 1.9 in Chapter 1). Cold and warm fronts would be typically associated with these features, which represent the division between the cold and warm air masses. Temperature gradients in the North Atlantic Ocean storm composite appear to be stronger than in the Arctic composite (see Figure 4.5b and 4.5e).

The Earth-relative 850 hPa wind composites show that wind speeds are typically higher in North Atlantic Ocean storms than Arctic storms (see Figure 4.5c and 4.5f). The maximum 850 hPa wind speeds of the Arctic storm composite is 23.0 ms^{-1}, but 33.8 ms^{-1} for the North Atlantic Ocean storm composite (see Figure 4.5c and 4.5f). Winter North Atlantic Ocean storms typically have a lower MSLP minima than winter Arctic storms, which may result in higher wind speeds (see Figure 4.3). The maximum wind speed occurs in a similar region in both storm composites, approximately 4° south of the storm centre (see Figure 4.5c and 4.5f). The Arctic storm composite is perhaps more axi-symmetric, as high wind speeds above 20 ms^{-1} can also be found approximately 4° north and east of the storm centre (see Figure 4.5c). Generally, mid-latitude storms typically propagate eastward, which enhances the speed of westerly winds within a storm, so that the highest near-surface wind speed typically occur south of the storm centre. This is shown in composites of both storm type (see Figure 4.5c and 4.5f), and is consistent with results from other studies (e.g. Catto et al., 2010 and Dacre et al., 2012).

The equivalent composites for intense spring and autumn Arctic and North Atlantic Ocean storms are shown in Figures E.2 and E.4 in Appendix E. These show similar features to the winter composites and are similar between Arctic and North Atlantic Ocean storms. However, the magnitude of the MSLP minima, and near-surface wind speed maxima are weaker than the winter composites (see Figures E.2 and E.4 in Appendix E). For the Arctic storm composite, maximum wind speeds at 850 hPa are 20.5 ms^{-1} in spring and 21.0 ms^{-1} in autumn (see Figures E.2c and E.4c in Appendix E). The 850 hPa composite structure of spring and autumn Arctic storms also show signs of occlusion. This is similar to the North Atlantic Ocean storm composite in the same season, where the cold air appears to have advected southward and has started to wrap around the storm centre (see Figures E.2b, E.2e, E.4b and E.4e in Appendix E).

Similar storm structure characteristics are found when the composites are made by rotating the storms to their direction of propagation before averaging. The 850 hPa temperature composites of Arctic and North Atlantic Ocean storms both show cold air wrapping around the storm centre at the time of maximum intensity (i.e. occlusion) (see Figure E.9 in Appendix E). However, the temperature gradients appear stronger in the non-rotated storm composites (see Figures 4.5b and 4.5e) than the rotated storm composites (see Figures E.9b and E.9e in Appendix E). This is perhaps a consequence of general temperature structure of the atmosphere (i.e. cold air to the north and warm air to the south) being better maintained in the non-rotated composite than the rotated composite. The maximum 850 hPa wind speed occurs in a similar area of the storm (south of the storm centre), but the magnitude is slightly different compared to when the composites are made by not rotating the storms before averaging. Instead, the maximum 850 hPa wind speeds of the Arctic and North Atlantic storm composites are 24.4 and 32.3 ms^{-1} respectively.

4.4.2 Vertical Features

Storms typically contain conveyor-belts that occur in different regions of the storm and at different altitudes (see Figure 1.12 in Chapter 1) (Browning, 1997). These include a warm conveyor belt (WCB) that is typically located in front of the cold front that ascends from south to north along the front, and a cold conveyor-belt (CCB) that typically occurs at low-levels in the atmosphere and wraps around the storm centre from the north (see Figure 1.12 in Chapter 1). These features can be analysed by examining a vertical section through storms (e.g. Schultz, 2001; Catto et al., 2010; Dacre et al., 2012). To examine these features in the winter Arctic and North Atlantic Ocean storm composites, Figure 4.6 shows the cross section along the transect perpendicular to the direction of storm propagation and 4° ahead of the composite storm centre.

The WCB and CCB are present in both the winter Arctic and North Atlantic Ocean storm composites (see Figure 4.6). The CCB is shown by the low-level high magnitude zonal (U-component) wind speeds that are present approximately 4° north of the level of the composite storm centre along this transect. The magnitude of zonal winds of the CCB are

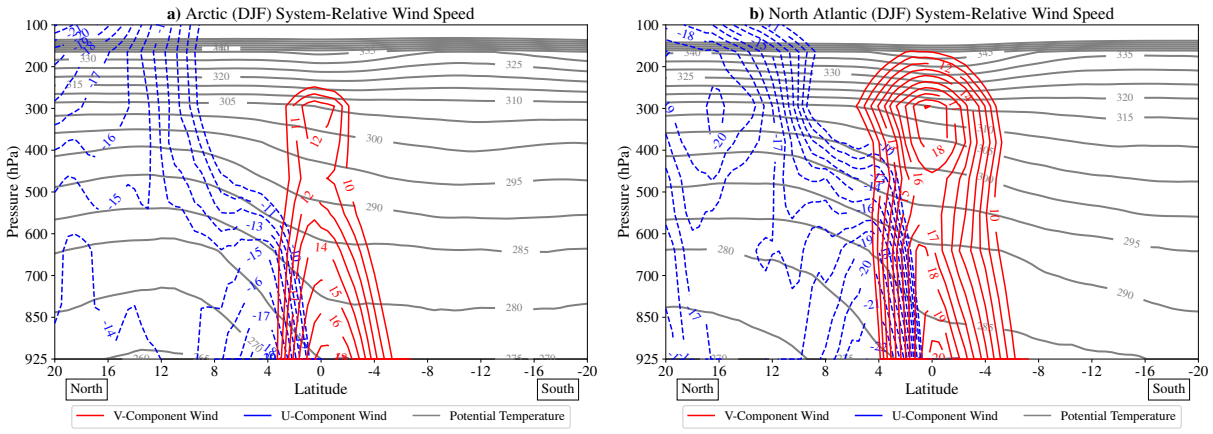

Figure 4.6: Composite vertical slices through the transect perpendicular to the direction of storm propagation and 4° ahead of the composite storm centre, in the 100 most intense winter (DJF) **a)** Arctic and **b)** North Atlantic Ocean composite based on ERA5.

lower in the Arctic storm composite (approximately 18ms^{-1}) than the North Atlantic Ocean storm composite (approximately 22ms^{-1}). The WCB is shown by the high magnitude meridional (V-component) winds within this cross section that are south of the CCB that exist between 925hPa to 600 hPa (see Figure 4.6). Like the CCB, the highest magnitude of these meridional wind speeds are lower in the Arctic composite (approximately 18ms^{-1}) than the North Atlantic Ocean composite (approximately 20ms^{-1}). The stark changes in the wind direction shown in each cross section of the composites indicates the presence of the CCB and WCB in each composite. However, there are differences between the cross sections of each composite.

The isentropes that show the potential temperature changes through this cross section differ between the composites (see Figure 4.6). For the North Atlantic Ocean composite, the isentropes through this cross section slope from 20° south to 20° north through the storm, with the steepest slope located from 0-4° north of the level of the composite storm centre along this transect. This is likely where warm air is ascending over the cold air to the north. However, in the Arctic composite, the isentropes are more gradual through this cross section, with a slope in the isentropes being present only from approximately 4°-10° of the level of the composite storm centre along this transect. This may suggest that the WCB of Arctic winter storms is not as long as in North Atlantic Ocean storms.

Furthermore, between 12° and 20° north of the level of the composite storm centre, air starts to become warmer in the Arctic composite, whereas it continues to become colder in the North Atlantic Ocean composite. The 100 most intense Arctic storms typically have their maximum intensity north of 70°N (see Figure 4.2). Thus, the increase in temperature between 12° and 20° north of the level of the storm centre is likely where the composite is over and passed the North Pole, where the environmental temperature gradients would be lower than in mid-latitude regions.

4.4.3 Development of Winter Storms

The development in the 700 hPa temperature field of both the intense winter Arctic and North Atlantic storm composites is similar to that shown by the Norwegian Cyclone Model (characterised by occlusion) rather than the Shapiro-Keyser Model (characterised by frontal fracture and a secluded warm-core) (see Figure 4.7 and Figure 1.9 in Chapter 1). The 700 hPa temperature anomaly field is shown here as it is less affected by surface processes. Figure 4.7a shows that 48 hours before the time of maximum intensity, both composites start to grow over a region of high temperature gradients, which appears similar to what Bjerknes (1919, 1922) described as the Polar Front. At 48 hours before the time of maximum intensity, both composites show signs that cold air has began to advect to the southwest of the storm centre, and warm air has started to advect northeast of the storm centre (see Figure 4.7). At the time of maximum intensity, cold air has progressively advected further around the storm centre, indicating that occlusion is occurring (see Figure 4.7).

The 700 hPa temperature structure at the time of maximum intensity of each composites is similar to that described in stage III in the Norwegian Cyclone Model (Bjerknes, 1919, 1922), which shows the development of lower-tropospheric potential temperature (a similar field to 700 hPa temperature) centred on the storm centre (see Figure 1.9 in Chapter 1). Figure 4.7 ultimately shows that the development of winter intense Arctic and North Atlantic Ocean storms 48 hours before and after the time of maximum intensity is similar. Although temperature gradients within the North Atlantic Ocean storm composite are generally stronger than the Arctic storm

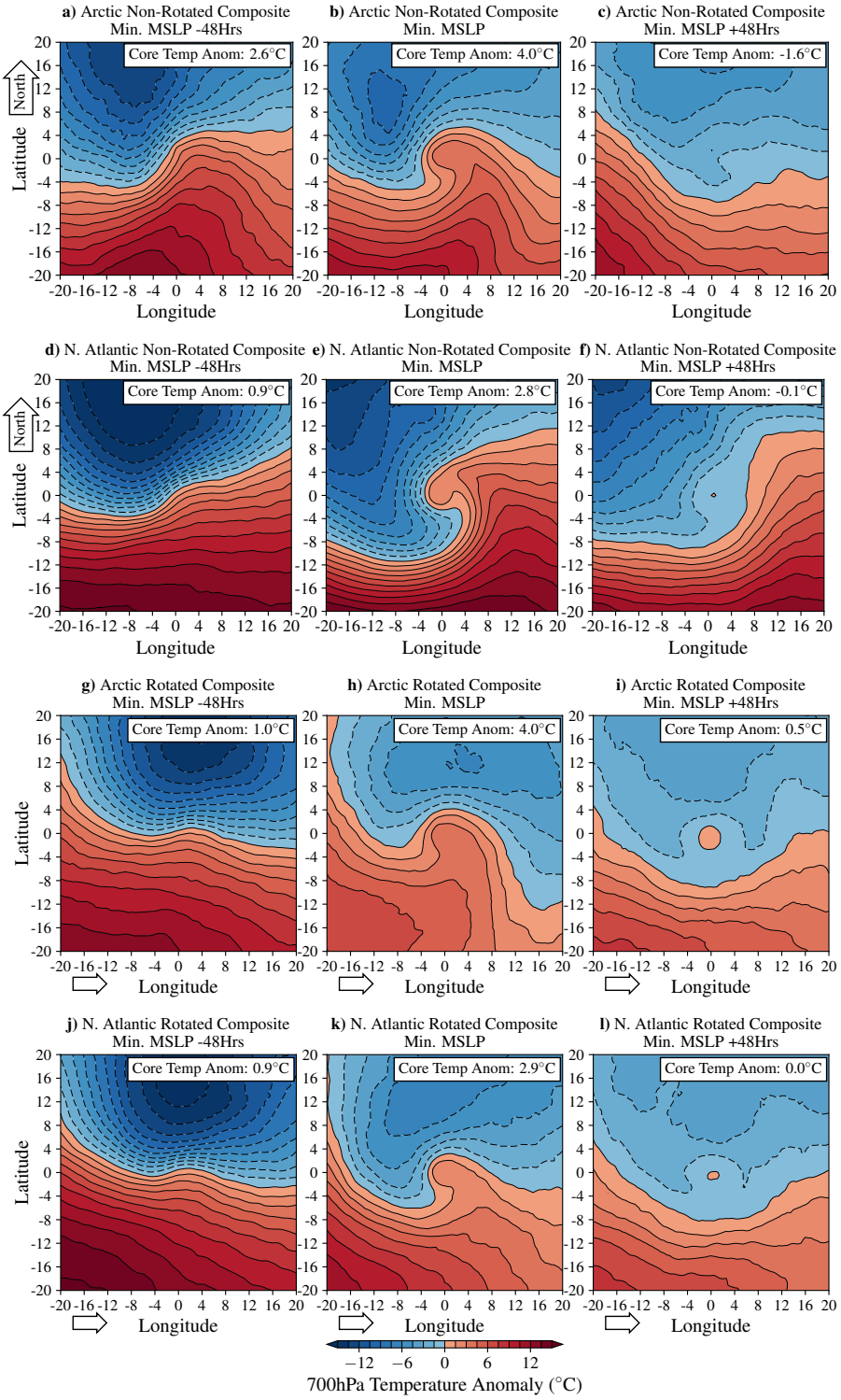

Figure 4.7: a) - f) Non-rotated and **g) - l)** rotated horizontal composite 700 hPa (lower tropospheric) temperature anomaly structure of the 100 most intense winter (DJF) **a) - c)** and **g) - i)** Arctic storms, and, **d) - f)** and **j) - l)** North Atlantic Ocean storms from 1979-2019 based on ERA5, at various stages of the storm cycle. **a), d), g) and j)** 48 hours before the time of maximum intensity (i.e. minimum mean sea level pressure), **b), e), h) and k)** at the time of maximum intensity, and **c), f), i) and l)** 48 hours after the time of maximum intensity. The arrow indicates the orientation of the storms before averaging.

composite, both showing signs that they follow a life-cycle similar to that described by the Norwegian Cyclone Model, where they grow in a region of large temperature gradients (i.e. Polar Front) and undergo occlusion (Bjerknes, 1919, 1922).

Storm development shown in the 700 hPa temperature composites of both types of storms is similar when the storm composite is computed by rotating each storm to their direction of propagation before averaging (see Figure 4.7). This also shows that both composites develop from a region of high temperature gradient 48 hours before the time of maximum intensity. As the storm progresses toward the time of maximum intensity, cold air is shown to advect further southward and wrapping around the storm centre (see Figure 4.7). However, the temperature gradients shown in the non-rotated storm composites appear stronger than the rotated composites, which is likely a consequence of the storm compositing method.

The development in the 700 hPa temperature composite structure of spring and autumn Arctic and North Atlantic Ocean storms is shown in Figures E.6 and E.7 in Appendix E, which also show cold air wrapping around the storm centre at the time of maximum intensity. This development in Arctic and North Atlantic Ocean storms in winter, spring and autumn is similar to that described by the Norwegian Cyclone Model (Bjerknes, 1919, 1922).

4.5 Composite Structure of Summer (JJA) Arctic and North Atlantic Ocean Storms

4.5.1 Surface Features

Summer storms are generally less intense than winter storms (see Figure 4.4), thus the minimum MSLP of the composite at the time of maximum intensity of the 100 most intense summer Arctic storms and North Atlantic Ocean storms is higher than that of winter storms (see Figures 4.5 and 4.8). Summer storms are also generally smaller than winter storms - inferred by comparing the area contained within the 1000 hPa contour between Figures 4.5a, 4.5d and 4.8a and 4.8d.

Pressure gradients within summer Arctic and North Atlantic Ocean storms appear to be generally weaker than those in winter storms (see Figures 4.5 and 4.8). The maximum

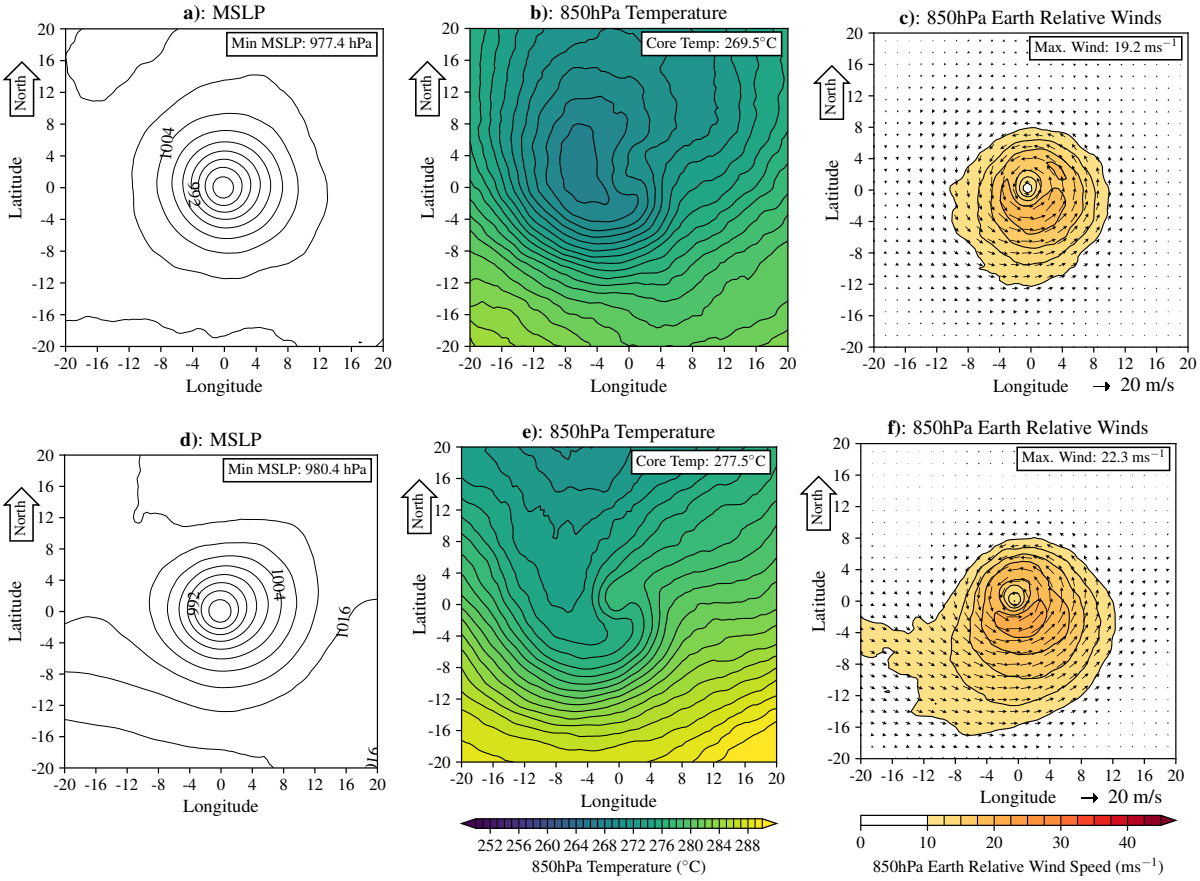

Figure 4.8: As Figure 4.5, but for the 100 most intense (based on minimum mean sea level pressure) summer (JJA) **a) - c)** Arctic storms and **d) - f)** North Atlantic Ocean storms.

earth-relative 850 hPa wind speeds of summer storms are also weaker than winter storms, with the composite of Arctic and North Atlantic storms showing a maximum earth-relative wind speed at 850 hPa of 19.2 and 22.3 ms^{-1} respectively. The maximum wind speeds are located similarly in summer and winter storms, occurring approximately 4° south of the storm centre.

At the time of maximum intensity, the composite 850 hPa temperature structure of Arctic summer storms shows some similarity with that of summer North Atlantic Ocean storms. Both composites show signs of occlusion, with cold air wrapping around the storm centre (see Figures 4.5b and 4.8e). However, the Arctic storm composite shows a large body of cold air 4-6 degrees west and north-west of the storm centre (see Figure 4.5b). When the composites are produced by rotating the storms to the direction of propagation before averaging, both composites have weaker temperature gradients (see Figure E.11 in Appendix E). But, also the Arctic summer storms are shown to have an axi-symmetric cold core structure at the time of

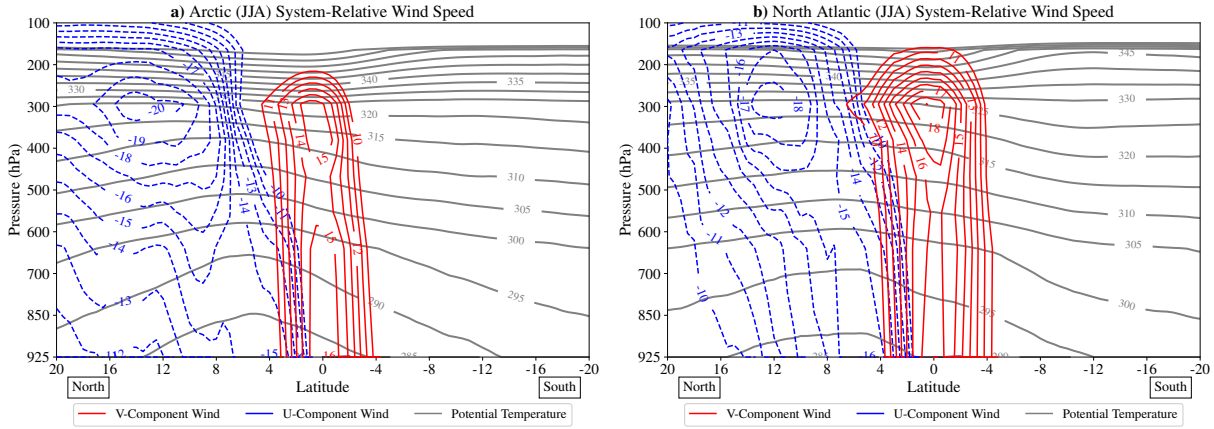

Figure 4.9: As Figure 4.6, but for the 100 most intense summer (JJA) **a)** Arctic storms and **b)** North Atlantic Ocean storms.

maximum intensity, and there are no signs of occlusion where cold air wrapping around the storm centre (see Figure E.11b in Appendix E).

4.5.2 Vertical Features

The vertical wind structure of the summer Arctic and North Atlantic Ocean storm composites shows that the structure of summer storms is slightly different to that of winter storms (see Figures 4.6 and 4.9). In the summer storm composites, zonal wind speeds 4° north of the level of the composite storm centre along this transect are less constrained to the surface. Instead, zonal wind speeds are more consistent throughout the troposphere north of the level of the composite storm centre. This suggests that the CCB, that occurs near the surface, is less well defined in summer Arctic and North Atlantic storms.

The slope of the isentropes of summer Arctic and North Atlantic storms is lower than winter Arctic and North Atlantic storms (see Figure 4.9). This is likely a consequence of lower environment temperatures in the mid-latitudes and Arctic in summer than in winter. The isentropes in the Arctic storm composite slope from warm (290 K) potential temperatures near the surface south of the level of the storm composite centre to colder potential temperatures (275 K) near the surface approximately 5° north of the level of the composite storm centre along this transect. There are high magnitude meridional (V-component) winds shown here in the composite, suggesting the presence of the WCB. However, from the point of this point, the

slope of the isentropes is reversed as they slope from cold to warm potential temperatures. At the time of maximum intensity, Arctic summer storms have developed a cold core (see Figure 4.8), thus a 'cold dome' is shown by the isentropes in Figure 4.9a.

4.5.3 Development of Summer Storms

The development in the composite 700 hPa temperature structure of summer Arctic and North Atlantic Ocean storms is shown in Figure 4.10. It shows that Arctic summer storms undergo a different development process to that of winter storms and that described by the Norwegian Cyclone Model and Shapiro-Keyser Model (Bjerknes, 1919, 1922; Shapiro and Keyser, 1990). Before the point of maximum intensity, summer Arctic and North Atlantic storms appear to follow a similar process of occlusion, where cold air begins to wrap around the composite storm centre (see Figure 4.10). However, after the time of maximum intensity, Arctic summer storms develop a more axi-symmetric cold core structure. This differs from the summer North Atlantic Ocean storm composite, and both the winter Arctic and North Atlantic Ocean storm composite, which typically continue to occlude.

From the point of maximum intensity, this cold core is shown to become colder (see Figure 4.10). The temperature anomaly at the storm centre at the time of maximum intensity is -3.8°C, whereas, the temperature anomaly at the storm centre 48 hours after the time of maximum intensity is -8.7°C (see Figure 4.10). This transition to an axi-symmetric cold core structure is also shown when the Arctic summer storm composite is made when rotating the storms to their direction of propagation before averaging (see Figure 4.10). Figure 4.11 shows that the Arctic storm composite retains this axi-symmetric cold core structure long after its time of maximum intensity. Further, this structure is also different to the development of storms as described by the Shapiro-Keyser conceptual model, which describes that storms may developed a warm-core after the process of frontal fracture (see Figure 1.9 in Chapter 1) (Shapiro and Keyser, 1990).

During this transition, the vertical temperature structure of the Arctic composite also changes. Figures 4.12 and 4.13 show the horizontal temperature anomaly, vertical velocity and wind speed between 925 and 100 hPa of the Arctic and North Atlantic Ocean storm composite, 48

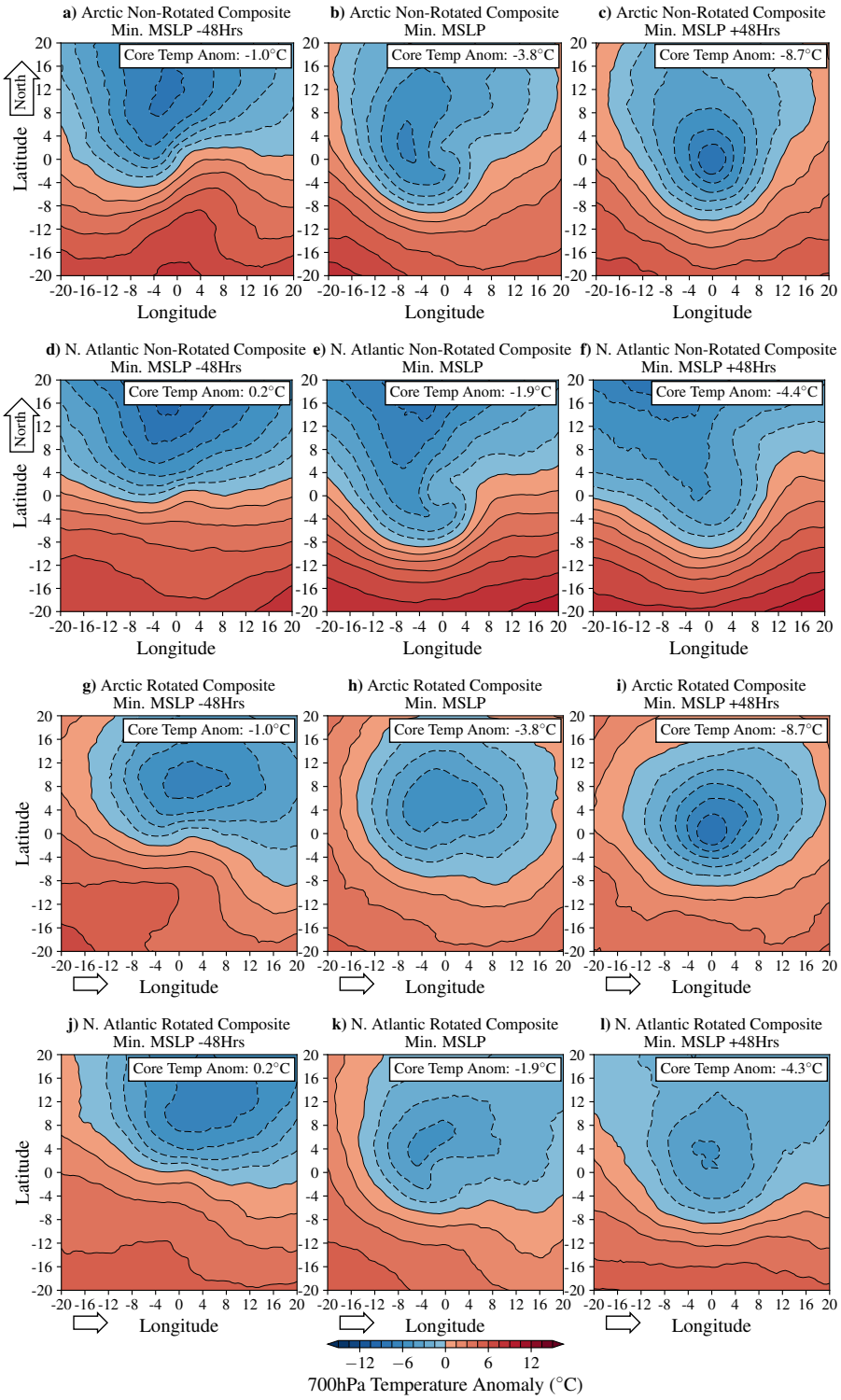

Figure 4.10: As for Figure 4.7, but for the 100 most intense summer (JJA) Arctic and North Atlantic Ocean storms from 1979-2019 based on ERA5.

hours before and after the time of maximum intensity. The Arctic and North Atlantic Ocean storm composites have a similar vertical structure 48 and 24 hours before the time of maximum intensity, a baroclinic structure with high temperature gradients near the centre of the storm (see Figures 4.12a, b and 4.13a, b). The Arctic storm composite shows a positive temperature

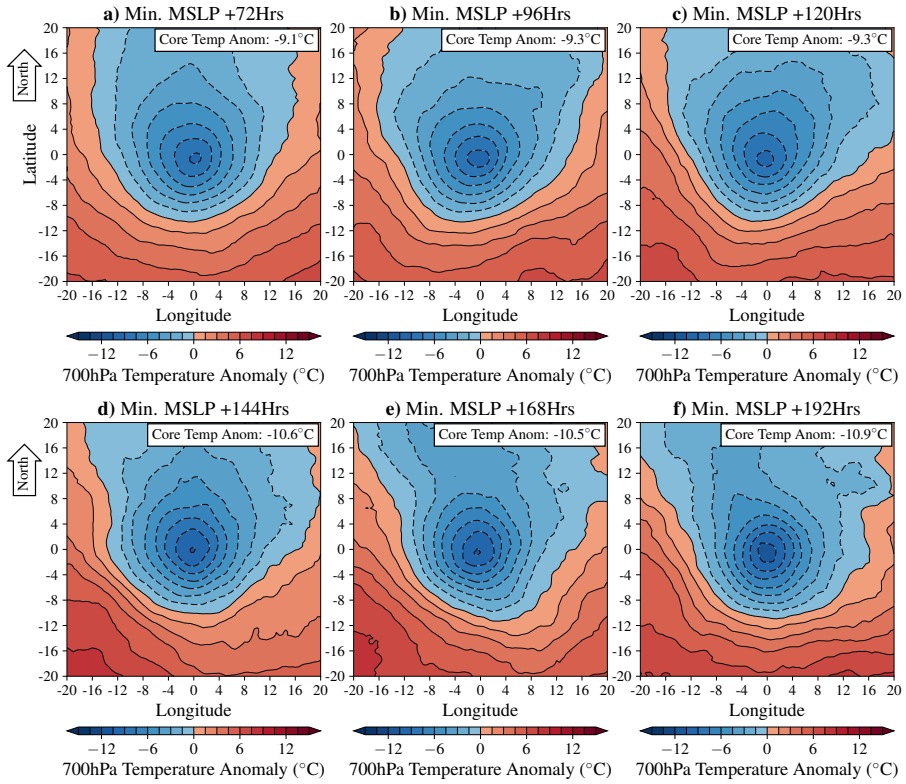

Figure 4.11: Horizontal composite structure of 700 hPa temperature anomaly of the 100 most intense summer (JJA) Arctic storms, between 1979 and 2019 based on the ERA5 reanalysis dataset, at various stages of the storm cycle. **a)** 72 hours, **b)** 96 hours, **c)** 120 hours, **d)** 144 hours, **e)** 168 hours and **f)** 192 hours after the time of maximum intensity. In producing these composites, storms have not been rotated before the composite is made, so that the top of each figure is north (see arrow).

anomaly in the stratosphere (between 100-300 hPa) west of the storm centre. There is ascending air near the centre of the storm throughout the troposphere, as shown by the negative vertical velocity 48 and 24 hours before the time of maximum intensity (see Figures 4.12f, 4.12g, 4.13f and 4.13g). As a result, MSLP at the surface decreases, and the storm would deepen.

After the time of maximum intensity, the vertical temperature structure of the summer Arctic and North Atlantic Ocean composites are different (see Figures 4.12 and 4.13). The Arctic storm composite shows a transition to an axi-symmetric cold core structure (see Figure 4.12d and 4.12e). This axi-symmetric structure is also shown in the vertical wind structure of the storm (see Figure 4.12o). Moreover, the height of the tropopause is lower in the Arctic composite than in the North Atlantic Ocean composite for a longer time after the time of maximum intensity (see Figures 4.12e and 4.13e). Wind speeds in the Arctic storm composite are more symmetric west and east of the composite centre than the North Atlantic Ocean composite 48 hours after the time of maximum intensity (see Figures 4.12o and 4.13o). After the time of maximum intensity, the vertical velocity is near-zero for both composites (see Figures 4.12j and 4.13j).

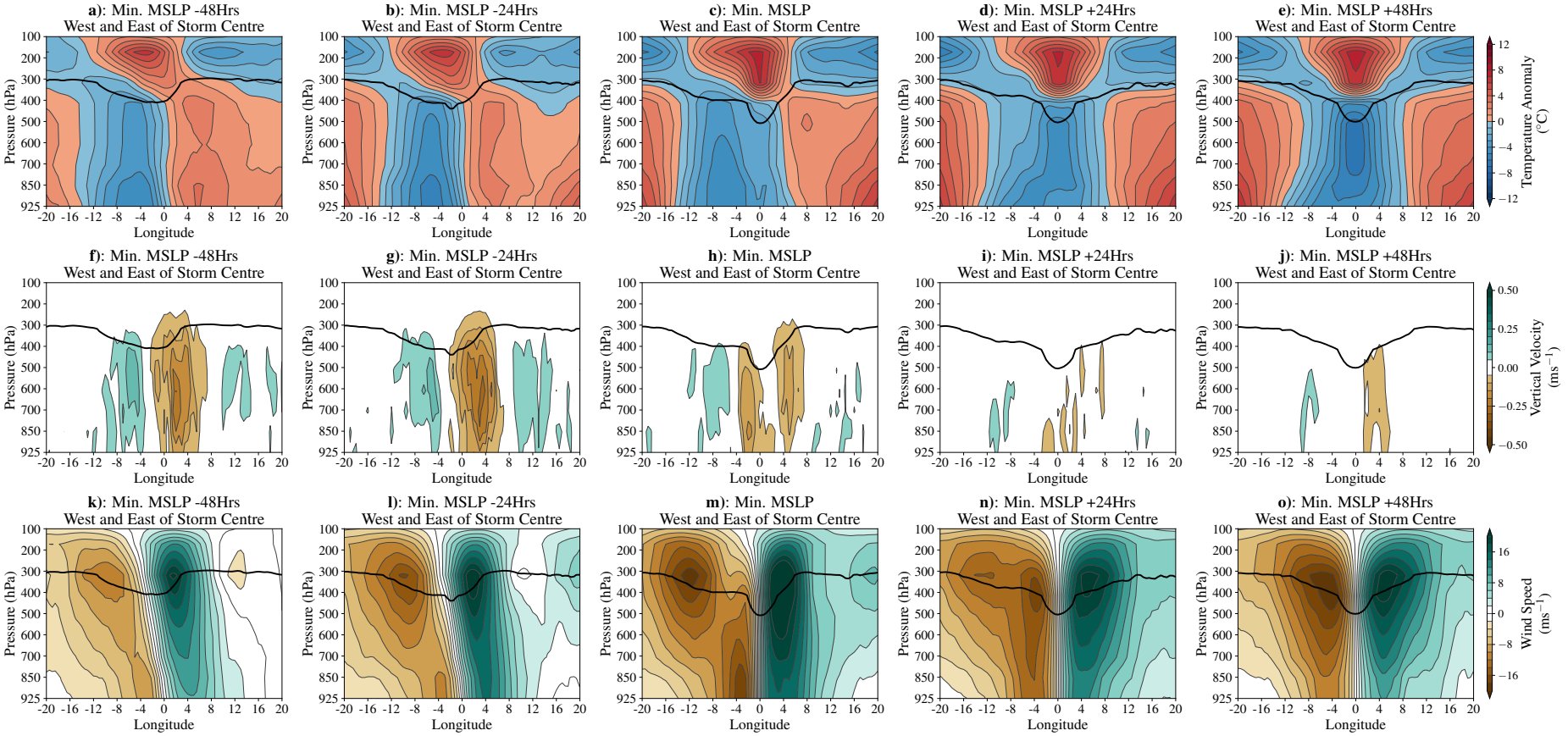

Figure 4.12: The vertical composite structure of the 100 most intense (based on minimum mean sea level pressure) summer (JJA) Arctic storms between 1979 and 2019 based on the ERA5 reanalysis dataset, through the transect west to east from the storm centre, at various stages of the storm cycle. **a) - e)** Temperature anomaly (anomaly calculated from mean at each level). **f) - j)** Vertical velocity (negative / positive values indicate areas of ascent / descent). **k) - o)** v-component earth relative wind speed. **a), f) and k)** 48 hours before the time of minimum mean sea level pressure (MSLP), **b), g) and l)** 24 hours before the time of minimum MSLP, **c), h) and m)** at time of minimum MSLP, **d), i) and n)** 24 hours after the time of minimum MSLP, and, **e), j) and o)** 48 hours after the time of minimum MSLP. The thick black contours indicates the level of the Tropopause (2PVU contour). In producing these composites, storms have not been rotated before the composite is made.

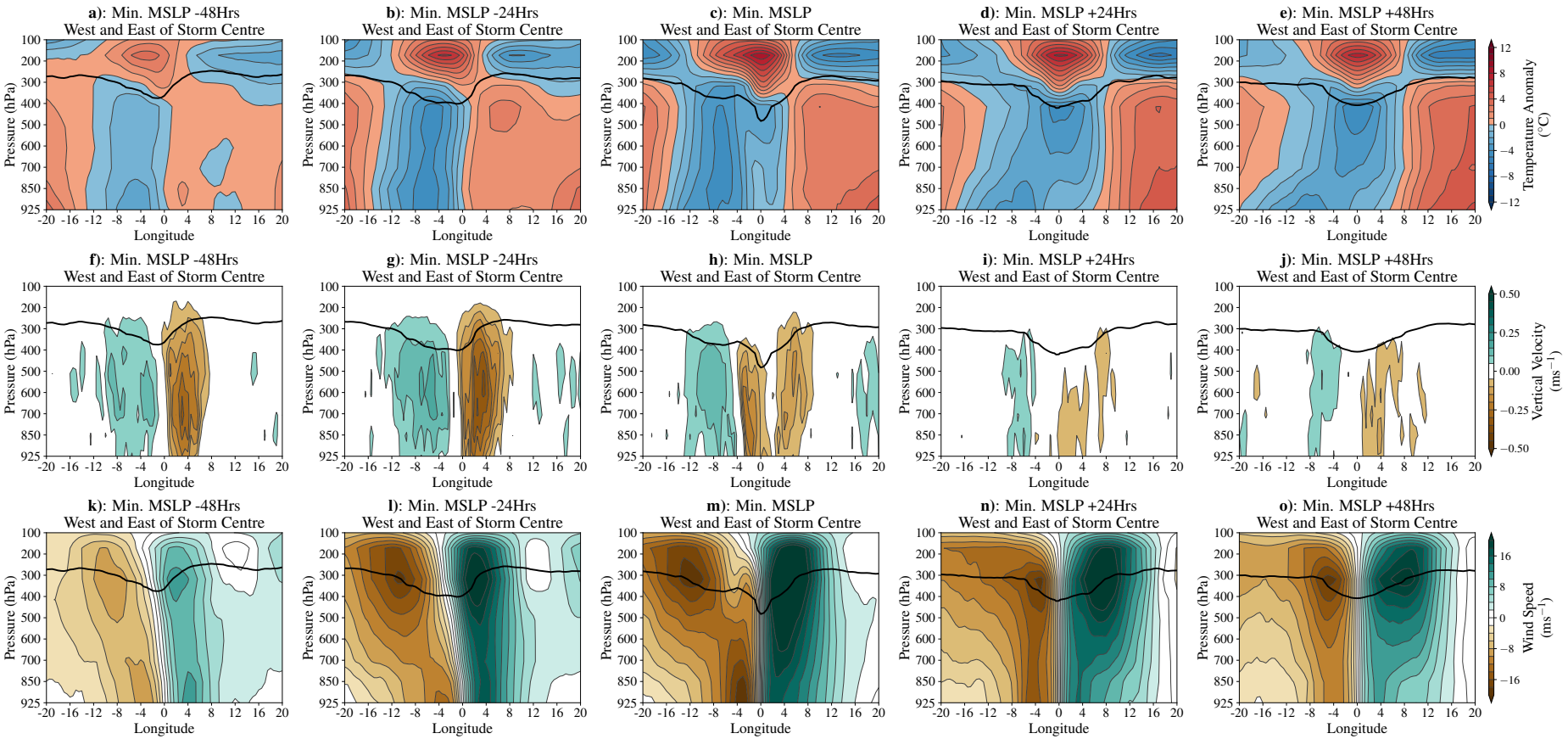

Figure 4.13: As Figure 4.12, but for the 100 most intense (based on minimum mean sea level pressure) summer (JJA) North Atlantic Ocean storms between 1979 and 2019 based on the ERA5 reanalysis dataset.

The change in vertical structure of Arctic summer storms is also shown when the composites are made by rotating the storms to the direction of propagation before averaging (see Figure E.12 in Appendix E). It shows that 48 hours after the time of maximum intensity, the Arctic storm composite has developed a cold core centre, with a low-lying tropopause (see Figure E.12a - e in Appendix E). This is different to the rotated summer North Atlantic storm composite (see Figure E.12f - j in Appendix E).

Overall, the composite structure of Arctic summer storms shows that intense Arctic summer storms typically undergo a transition around the time of maximum intensity. They initially develop in an area of high temperature gradients, similar to that described by the Norwegian Cyclone and Shapiro-Keyser Models (Bjerknes, 1919, 1922; Shapiro and Keyser, 1990). However, around the time of maximum intensity, the composite undergoes a structural transition, where the composite changes from a baroclinic structure (where cold air has started to wrap around the storm centre), to a more axi-symmetric cold core structure. This is unlike the summer North Atlantic Ocean composite, and the composite of intense winter Arctic and North Atlantic Ocean storms, and is different to existing conceptual models of storm development e.g. the Norwegian Cyclone Model and the Shapiro-Keyser Model (Bjerknes, 1919, 1922; Shapiro and Keyser, 1990).

4.5.4 Arctic summer storm composite compared to the Great Arctic Storm of 2012

It has been shown that the Great Arctic Storm of 2012 had a unique development, where the surface storm interacted with an upper-level Tropopause Polar Vortex (TPV) along its track (Simmonds and Rudeva, 2012; Aizawa and Tanaka, 2016). The Great Arctic Storm of 2012 had genesis over inland central Russia and was shown to intersect a TPV along its track over the Arctic Ocean (Simmonds and Rudeva, 2012). After this intersection, the upper-level TPV and surface storm travelled in sync toward the Canadian Archipelago for at least a further 4 days (Simmonds and Rudeva, 2012). The storm had a lifetime of 13 days (Simmonds and Rudeva, 2012), which makes it an exceptionally long-lived storm when compared to the mean lifetime of Arctic storms in winter, spring and autumn, which is about 6 days (see Figure 4.4).

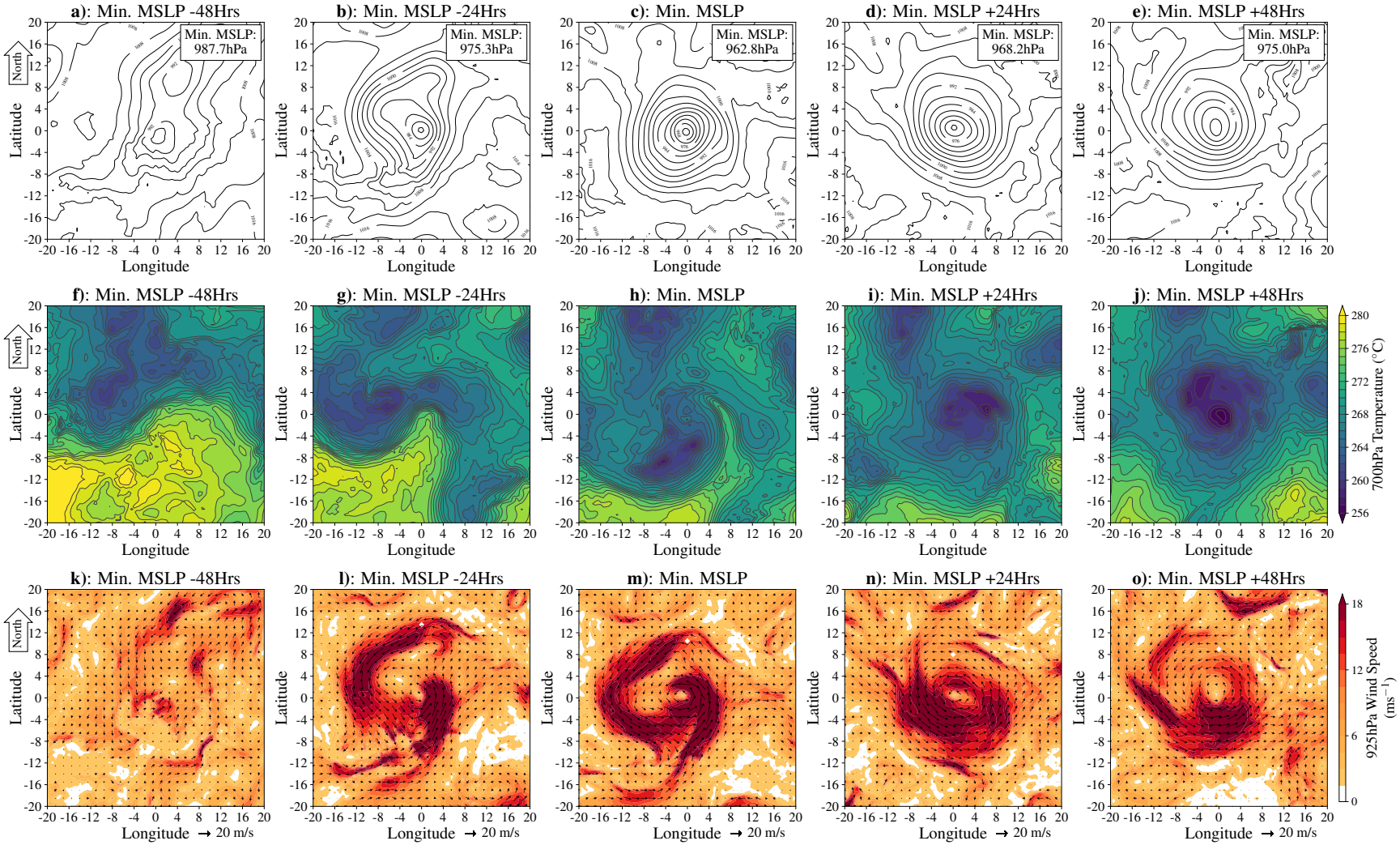

Figure 4.14: Horizontal composite structure of the Great Arctic Storm of 2012. **a) - e)** show the composite mean sea level pressure (MSLP) structure. **f) - j)** show the composite 700 hPa temperature structure. **k) and o)** show the composite 925 hPa wind speed (contours) and direction (vectors). **a), f) and k)** 72 hours, **b), g) and l)** 96 hours, **c), h) and m)** 120 hours, **d), i) and n)** 144 hours and **e), j) and o)** 168 hours after the time of maximum intensity (i.e. minimum MSLP). In producing these figures, the storm has not been rotated, so that the top of each figure is north (see arrow). Based on the ERA5 reanalysis dataset.

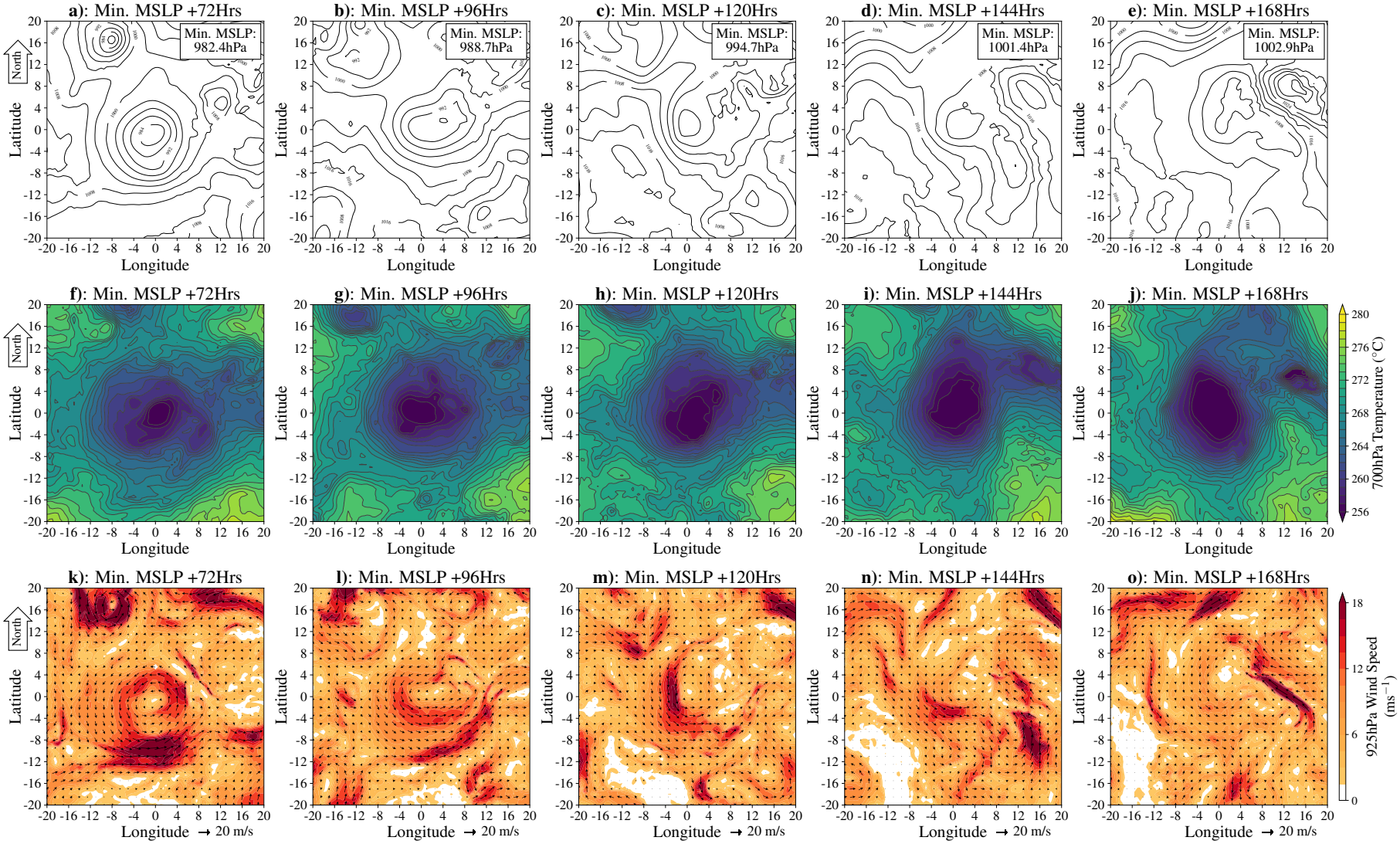

Figure 4.15: As Figure 4.14, but for **a), f) and k)** 72 hours, **b), g) and l)** 96 hours, **c), h) and m)** 120 hours, **d), i) and n)** 144 hours and **e), j) and o)** 168 hours after the time of maximum intensity of the storm (minimum MSLP). Based on the ERA5 reanalysis dataset.

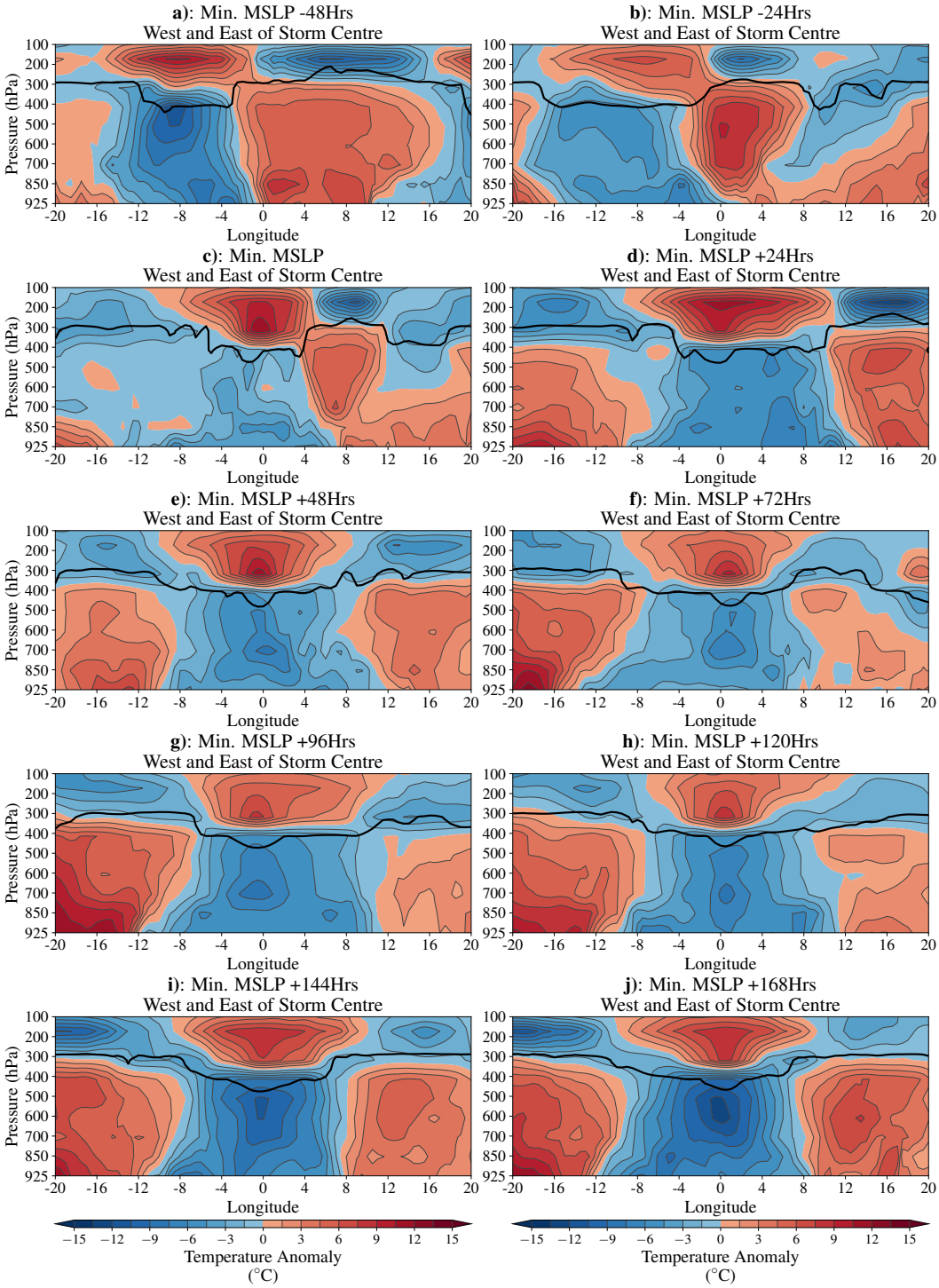

Figure 4.16: Vertical temperature structure of the Great Arctic Storm of 2012, west to east of the storm centre, at various stages of the its lifecycle. A horizontal temperature anomaly has been computed at each vertical level. The thick black contours indicates the level of the Tropopause (2PVU contour). **a)** 48 and **b)** 24 hours before the time of maximum intensity, **c)** at the time of maximum intensity, **d)** 24, **e)** 48, **f)** 72, **g)** 96, **h)** 120, **i)** 144 and **j)** 168 hours after the time of maximum intensity. Based on ERA5.

TPVs are coherent circulation features based on the tropopause that typically occur in polar regions, and typical have radii >1,500 km and lifetimes that may exceed 1 month (Cavallo and Hakim, 2010). TPVs can be identified as negative temperature anomalies at the tropopause (see

Figure 8 and 9 in Cavallo and Hakim, 2010). Tao et al. (2017) identified another case study where a TPV influenced an Arctic storm in September 2010 that had a similar structure to the Arctic summer storm composite, with a cold core throughout the troposphere.

Aizawa and Tanaka (2016) showed that the Great Arctic Storm of 2012 had an axi-symmetric cold core structure at the time of maximum intensity. This is also shown by the Arctic summer storm composite (see Figure 6 in Aizawa and Tanaka, 2016 and Figure 4.12). Figures 4.14, 4.15 and 4.16 expand on the results from Aizawa and Tanaka (2016), and show the horizontal and vertical structure of the Great Arctic Storm of 2012 up to 48 hours before and up to 168 hours after the time of maximum intensity, when the storm reached a minimum central pressure of 962.5 hPa at 12UTC on the 6th of August 2012.

The Great Storm of 2012 underwent a transition from a baroclinic structure before the time of maximum intensity, where cold air began to advect southwest and wrap around the storm centre, to an axi-symmetric cold core structure after the time of maximum intensity (see Figure 4.14f-j). This is similar to that shown in the composite structure of the 100 most intense Arctic storms (see Figure 4.12). Figure 4.14i and 4.14j show that 24 and 48 hours after the time of maximum intensity, the storm has developed a cold core centre. After this transition, high 925 hPa wind speeds of greater than 18 ms^{-1} occurred all around the storm centre (see Figure 4.14n). This differs to that of most mid-latitude storms, where the highest low-level winds occur south of the storm centre (Browning, 1997).

This transition is also shown in the change in the vertical structure of the Great Arctic Storm of 2012 (see Figure 4.16). After the time of maximum intensity, the Great Arctic Storm of 2012 developed a cold core centre throughout the troposphere. In addition, a large positive temperature anomaly is shown to occur in the stratosphere, which is approximately 8° west of the storm centre 48 hours before the time of maximum intensity of the storm. This may be the upper-level TPV, as they can be identified as a positive temperature anomaly in the stratosphere (Cavallo and Hakim, 2010). At the time of maximum intensity, this positive temperature anomaly becomes aligned with the centre of the storm (see Figure 4.16c). After this, the height of the tropopause above the centre of the storms decreases to approximately

500 hPa (denoted by the 2PVU contour) (see Figure 4.16i). The storm also develops a cold core centre throughout the troposphere (see Figure 4.16d-j), with a positive temperature anomaly in the stratosphere remaining above the storm centre.

The track of the Great Arctic Storm of 2012 48 hours before and after its time of maximum intensity is shown in Figure 4.17. Also shown, is the ERA5 potential temperature field on the 2PVU surface (at the level of the tropopause), at each time-step of the storm. Between 48 hours before the time of maximum intensity and the time of maximum intensity, the Great Arctic Storm of 2012 travels from the Eurasian continent to over the Arctic Ocean (see Figure 4.17). At 48 hours before the time of maximum intensity, the surface storm is under an area of high potential temperature on the 2 PVU surface of approximately 334 K. However, at the time of maximum intensity, the surface storm has travelled over the Arctic Ocean and is now under a region of extremely low potential temperature on the 2 PVU surface of approximately 308 K. This is likely a TPV. The surface storm and TPV then travel in sync across the Arctic Ocean after the time of maximum intensity (see Figure 4.17). This shows the merger of the Great Arctic Storm of 2012 with an upper-level TPV.

Simmonds and Rudeva (2012) showed that the Great Arctic Storm of 2012 gradually decayed from a minimum MSLP of 966 hPa to 1010 hPa over 8 days. From the time of maximum intensity, the storm retained this axi-symmetric cold core structure throughout the troposphere with a positive temperature anomaly in the stratosphere, until it eventually dissipated (see Figure 4.15j). Figure E.14 in Appendix E shows that after the time of maximum intensity, vertical velocity within the storm remained near zero. Thus, the storm gradually dissipated, not re-intensifying after the time of maximum intensity.

Tao et al. (2017) explained that as the storm and upper-level TPV align, the cyclonic circulation in the troposphere that is associated with this upper-level potential vorticity anomaly (Hoskins et al., 1985) can enhance the circulation of the storm. As air ascends within the storm, it will cool adiabatically, which in turn strengthens the cold core of the storm. This maintains the positive potential vorticity anomaly, as the cold atmosphere compacts and maintains the low-lying tropopause. This positive potential vorticity anomaly in turn maintains the storm. The

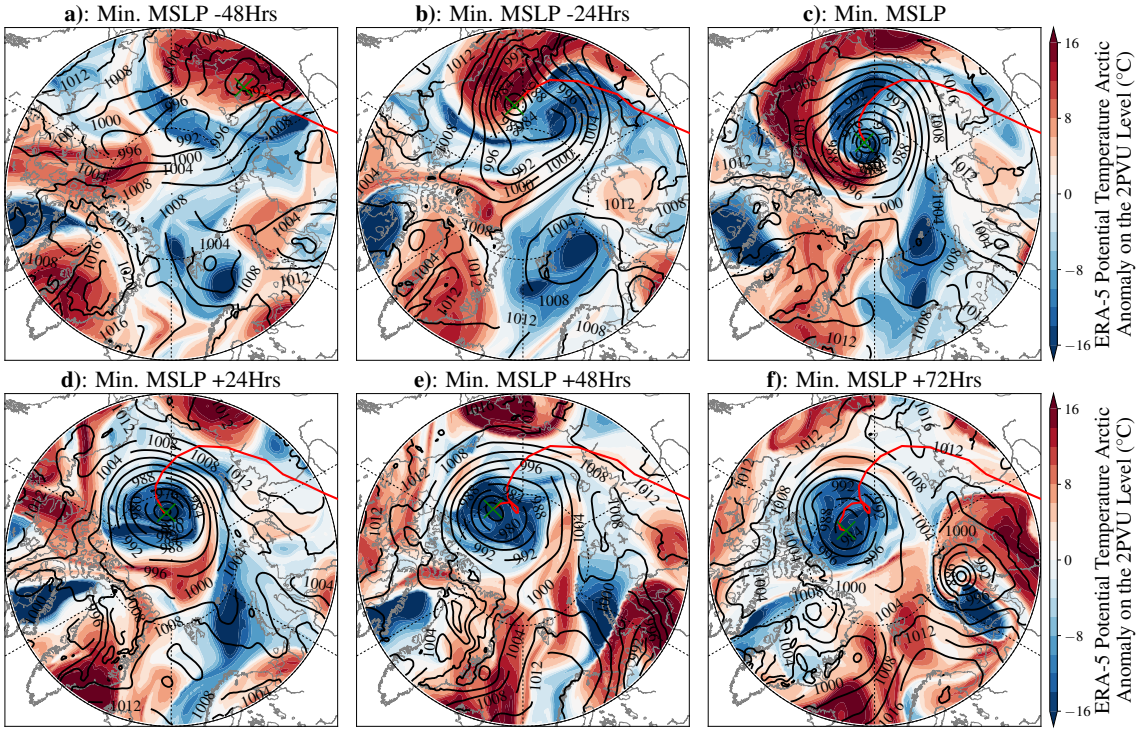

Figure 4.17: The track of the Great Arctic Storm of 2012 48 hours before to 72 hours after its time of maximum intensity. The red line indicates the storm track, with the storm centre indicated by the green cross. At each timestep of the storms, the mean sea level pressure field from ERA5 is shown by the thick black lines, and the coloured contours show the potential temperature field on the 2PVU surface north of 65°N from ERA5.

storm then dissipates as the lower-stratosphere positive potential vorticity anomaly weakens. This may have prolonged the life of the Great Arctic Storm of 2012, which took 8 days to dissipate (Simmonds and Rudeva, 2012). Moreover, Gray et al. (2021) also showed that the merger of Arctic summer storms and upper-level TPV may be a fairly common occurrence.

The Great Arctic Storm of 2012 and the storm described by Tao et al. (2017) have a similar structural transition to the Arctic summer storm composite. Perhaps in this sample of the 100 most intense Arctic summer storms there are other storms that interacted with a TPV, leading to this unique axi-symmetric cold core structure shown by the composite and these case studies.

4.6 Evaluation of the Aizawa and Tanaka (2012) Conceptual Model of Arctic summer storms

Aizawa and Tanaka (2016) proposed a conceptual model of Arctic summer storms based on just two Arctic storm case studies (see Figure 4.1). Here, the composite structure of the 100 most

intense Arctic summer storms has been determined, allowing for the evaluation of the Aizawa and Tanaka (2016) conceptual model compared to a greater sample of past Arctic storms. The conceptual model highlights six main features of Arctic summer storms, which include:

- Deep cyclonic circulation that stretches up to stratosphere (up to the 50 hPa level)
- Secondary circulation in the troposphere
- Downdraft in the lower stratosphere
- Warm core in the lower stratosphere and cold core in the troposphere
- Deep tropopause folding which descends down to 500 hPa from 300 hPa over the cyclone centre
- Horizontal scale of approximately 5,000km

In Figure 4.12, the composite vertical structure of the 100 most intense Arctic summer storms was shown, at times before the time of maximum intensity, and up to two days before and after this time. There are similarities to the Aizawa and Tanaka (2016) conceptual model. For example, it is shown that the composite vertical structure of Arctic summer storms extends to 100 hPa, where there is a warm anomaly in the stratosphere (see Figure 4.12c). In addition, the composite vertical structure of Arctic summer storms shows a warm anomaly in the lower stratosphere and a cold anomaly in the troposphere. There is also a deep tropopause fold that descends to 500 hPa shown in the Arctic summer storm composite (see Figure 4.12c).

Up to the time of maximum intensity, there also appears to be a secondary circulation. This leads to the convergence of air at the surface and the divergence of air at the tropopause, shown by high vertical velocity within the storm throughout the troposphere (see Figure 4.12f-h). Figure E.13 in Appendix E shows the composite vertical divergence structure of intense Arctic summer storms, and shows that up to the time of maximum intensity, there is convergence of air at near the surface (negative divergence values) and divergence at the tropopause (positive divergence values). The horizontal scale of Arctic storms is also quite large, with the cold core structure extending to 8-12° west and east of the storm centre. This indicates that the composite storm

has a horizontal scale approximately 2,500 km, which is smaller than the Aizawa and Tanaka (2016) conceptual model suggests.

Figure 4.12 shows that the summer Arctic storms undergo a transition to then have the structure described by the Aizawa and Tanaka (2016) conceptual model. The axi-symmetric cold core structure at the centre of the storm becomes colder and more pronounced after the time of maximum intensity (see Figure 4.12d and 4.12e). Arctic summer storms tend to retain this structure long after their point of maximum intensity. After this, there appears to be no secondary circulation within the composite (see Figure 4.12i and 4.12j). This secondary circulation would maintain the low pressure at the surface and prolong the storm. Thus, the explicit reason for why some Arctic storms have extremely long lifetimes is still uncertain.

4.7 Summary and Conclusions

It has been unclear whether the typical development and structure of Arctic storms is similar to that described by existing conceptual models of mid-latitude storm development (e.g. the Norwegian Cyclone Development Model from Bjerknes (1919, 1922) and the Shapiro-Keyser Model from Shapiro and Keyser (1990)) and of mid-latitude storm structure (e.g. Browning, 1997). Case studies of past Arctic storms have been identified, which do not follow these conceptual models (e.g. Tanaka et al., 2012; Aizawa and Tanaka, 2016; Tao et al., 2017).

Before this study, it was unclear whether the typical development and structure of Arctic storms is similar to that described by existing conceptual models of mid-latitude storm development and structure. Previous studies had identified particular cases that described how some Arctic storms have a different development and structure to that described in these conceptual models (e.g. Tanaka et al., 2012; Aizawa and Tanaka, 2016; Tao et al., 2017). This study has aimed to describe the typical development and structure of intense Arctic storms across the four seasons for the first time, using a larger sample of storms. The composite structure of the 100 most intense Arctic storms in each season has been obtained and compared to North Atlantic Ocean storms. Overall, it has been shown that Summer (JJA) Arctic storms

have a different development and structure to Arctic storms in the other seasons, and North Atlantic Ocean storms in all seasons.

- Intense summer (JJA) Arctic storms have significantly longer lifetimes than Arctic storms in other seasons, and North Atlantic Ocean storms in all seasons

Storms cause hazardous weather conditions, and it is found that Arctic summer storms are exceptionally long-lived and therefore could cause prolonged hazardous weather in the Arctic. The mean lifetime of the 100 most intense Arctic summer storms has been found to be about 3.5 days longer than Arctic storms in other seasons. Furthermore, the modal lifetime of these summer storms has been found to much greater than that of Arctic storms in other seasons. The modal lifetime of 100 most intense Arctic storms in winter, spring and autumn, and North Atlantic Ocean storms in all seasons has been found to be between 4-6 days, whereas the modal lifetime of the 100 most intense Arctic summer storms is greater than 10 days.

- The composite structure of intense summer (JJA) Arctic storms is different to that of intense Arctic storms in other seasons, and intense North Atlantic Ocean storms in all seasons

The development of the composite structure of the 100 most intense Arctic summer storms show differences to that of winter Arctic storms, along with summer and winter storms that occur over the North Atlantic Ocean. This is especially apparent at and after the time of maximum intensity. Arctic summer storms appear to develop in a region of high baroclinicity and initially start to occlude, similar to that described in the early phases of the Norwegian Cyclone Model (see stages I, II and III of the bottom panel in Figure 4.18, and Figure 4.7a, 4.7b, 4.7g and 4.7h). However, around the time of maximum intensity, the composite Arctic summer storm undergoes a transition from a baroclinic structure to an axi-symmetric cold core structure throughout the troposphere (see stage IV of the bottom panel in Figure 4.18, Figures 4.7c, 4.7i and 4.12). The composite storm then maintains this structure after its time of maximum intensity (see stage V of the bottom panel in Figure 4.18 and Figure 4.11). This is different to that of the winter Arctic

storm, and summer and winter North Atlantic Ocean storm composite that show a development more similar to the Norwegian Cyclone Model (see the top panel of Figure 4.18, Figures 4.7 and 4.10). The composite development of Arctic summer storms is also shown to differ to that of the Shapiro-Keyser Model (Shapiro and Keyser, 1990).

The composite structure of Arctic summer storms shows that they typically undergo a structural transition around the time of maximum intensity, from having a baroclinic structure to an axi-symmetric cold core structure throughout the troposphere. Hence, they may be associated with a cold front around the storm centre nearer the surface (see stage IV of the bottom panel in Figure 4.18). The composite shows that this cold core centre may become cooler after the time of maximum intensity as the storm dissipates, perhaps expanding this cold front from the centre of the storm (see stage V of the bottom panel in Figure 4.18). Summer Arctic storms also have longer lifetimes than Arctic storms in other seasons and North Atlantic Ocean storms in all seasons, hence the additional stage shown in Figure 4.18.

Similarities are found between the Arctic summer storm composite and the Great Arctic Storm of 2012. The Great Arctic Storm of 2012 was an intense storm that occurred over the high Arctic Ocean, with a minimum sea level pressure of 966 hPa (Simmonds and Rudeva, 2012). After analysing the Great Arctic Storm of 2012 in greater detail, it is shown that this storm underwent the structural transition shown in the Arctic summer storm composite, from having a baroclinic structure with signs that occlusion has begun to take place, to having axi-symmetric cold core structure in the troposphere with a warm temperature anomaly in the stratosphere. This storm has been shown to have interacted with a Tropopause Polar Vortex (TPV) around its time of maximum intensity (Simmonds and Rudeva, 2012) when the storm underwent a structural transition. It is possible that in this sample of the 100 most intense Arctic summer storms, there are other storms that interacted with a TPV, which may have led to this structural transition. If time allowed, this could have been investigated further by using a matching analysis could have been performed between TPVs and the sample of the 100 most intense Arctic summer storms, similar to Gray et al. (2021). Though, Gray et al. (2021) do show evidence that the merger of surface storm and upper-level TPV may be a common occurrence for Arctic summer storms, giving evidence for the hypothesis given in this study.

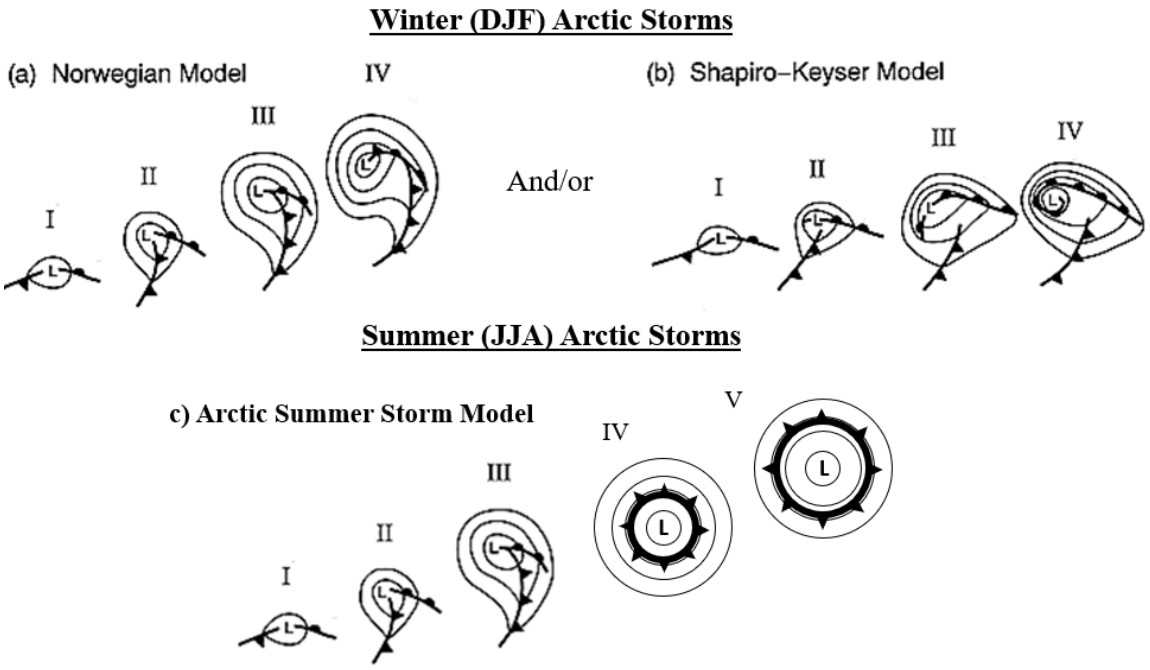

Figure 4.18: Conceptual models of typical winter (DJF) (top panel) and summer (JJA) (bottom panel) Arctic storm evolution showing lower-tropospheric (e.g., 850-hPa) geopotential height and fronts (black with circles indicating warm fronts, and, black with triangles indicating cold fronts). **(a) Norwegian cyclone model:** (I) incipient frontal cyclone, (II) and (III) narrowing warm sector, (IV) occlusion; **(b) Shapiro–Keyser cyclone model:** (I) incipient frontal cyclone, (II) frontal fracture, (III) frontal T-bone and bent-back front, (IV) frontal T-bone and warm seclusion; **(c) Arctic summer storm model:** (I) incipient frontal cyclone, (II) and (III) narrowing warm sector, (IV) structural transition, (V) prolonged lifetime. Adapted from Schultz et al. (1998).

- The composite structure of the intense summer (JJA) Arctic storms show similarities with the conceptual model proposed by Aizawa and Tanaka (2016).

Aizawa and Tanaka (2016) proposed a conceptual model of Arctic summer storms at the time of maximum intensity, based on the analysis of just two Arctic storm case studies. This model has been evaluated against the composite structure of the 100 most intense Arctic summer storms. This tests the generality of the model to a greater number of past Arctic storms Aizawa and Tanaka (2016). Overall, the model is similar to that shown in the composite structure of the 100 most intense Arctic storms, after the time of maximum intensity. The summer storm composite extends from the surface up into the stratosphere to at least 100 hPa, with a cold core throughout the troposphere and a warm core in the lower stratosphere. There is convergence of air at the surface and divergence of air near the tropopause, which indicates the presence of a secondary circulation. This leads to the ascent of air near the storms centre. The summer storm composite

also has a deep tropopause fold, descending to approximately 500 hPa. However, the composite doesn't show descent on the flanks of the storm, and the horizontal extent of the cold core in the troposphere is smaller than 5,000 km, as Aizawa and Tanaka (2016) suggested. After the time of maximum intensity, the Arctic summer storms retain this temperature structure until they dissipate.

The evolution in the structure of Arctic summer storms was not considered by Aizawa and Tanaka (2016). Results from this study highlight that Arctic summer storms typically undergo a structural transition from having a baroclinic structure to having a axi-symmetric cold core structure throughout the troposphere (similar to that described by the Aizawa and Tanaka (2016) conceptual model). Arctic summer storms typically maintain this structure until they dissipate. This is different to the structural transitions of mid-latitude storms that are described by the Norwegian Cyclone Model and Shapiro-Keyser Model (Bjerknes, 1919, 1922; Shapiro and Keyser, 1990).

Chapter 5

Response of Arctic Storms to Climate Change: Sensitivity to Model Horizontal Resolution

Anthropogenic climate change has changed the Arctic over the past few decades. Surface air temperatures have increased by as much as 3.26 °C above the 1951-1980 average (Lenssen et al., 2019; GISTEMP Team, 2021), and September Arctic sea ice extent has reduced from approximately 7.5 million km^2 in 1980 to just below 4 million km^2 in 2020 (see Figure 1 in Chapter 1). Climate change will continue to change the Arctic environment further over the 21^{st} century, with surface air temperatures expected to continue to increase, and sea ice extent projected to reduce further (Stroeve et al., 2007, 2012). This chapter aims to determine how Arctic storms may change in a future climate in response to climate change. It also aims to investigate whether the response of Arctic storms to climate change is sensitive to horizontal resolution, to further understand why future climate projections may differ between atmospheric models. This addresses the third research question of this thesis, which is:

RQ3: How might Arctic storms change in response to climate change? In particular, does the horizontal resolution of the climate model impact the response of Arctic storms to climate change?

5.1 Introduction

The Arctic is projected to warm the most through the 21st century of any region on Earth in response to anthropogenic climate change, due to the phenomenon of Arctic Amplification (Smith et al., 2019). Consequently, sea ice extent will continue to reduce over the 21st century (Stroeve et al., 2007, 2012; Collins et al., 2013; Stocker et al., 2014). This raises the question, will Arctic storminess (number, spatial distribution and intensity) change in a future climate, as the Arctic environment changes in response to climate change?

A main focus of previous research has been to determine the future response of Arctic storms in summertime, when sea ice is near its minimum extent and the exposure of human activity (e.g. shipping, oil exploration and tourism) to Arctic storms is highest (National Snow & Ice Data Centre, 2020b). Earlier studies showed that the number of Arctic storms that travel over the Arctic Ocean will increase in summer (e.g. Orsolini and Sorteberg, 2009; Akperov et al., 2015; Nishii et al., 2015), with Akperov et al. (2015) also highlighting that the intensity of summer Arctic storms over the Arctic Ocean may also increase. More recent studies show that the changes in Arctic storm track density may be different in regions across the Arctic, with the number of storms occurring over the Canadian Archipelago and around Greenland increasing, but the number of storms over Eurasia and the Arctic Ocean decreasing (Crawford and Serreze, 2017; Day et al., 2018).

The response of Arctic storms in other seasons has been less studied than in summer. Akperov et al. (2015) showed that the number of Arctic storms may decrease in the cold season (October-March). Day et al. (2018) showed that the track density of winter (DJF) storms over the Arctic Ocean will decrease in a future climate, particularly in the Greenland, Norwegian and Barents Seas. Human activity will likely occur in the Arctic year-round in the future, as sea ice extent reduces in all seasons (Stroeve et al., 2012). Thus, it is important to understand the response of Arctic storms to climate change in all seasons.

One of the main sources of uncertainty in future climate simulations arises from using multiple models to project the future atmosphere. Differences in how each model simulates the atmosphere, ocean, and land processes, can lead to differences in the future climate

simulations made by each model (Hawkins and Sutton, 2009). This creates uncertainty in which simulation to trust, and ultimately reduces the confidence in future climate simulations of the atmosphere.

Nishii et al. (2015) compared the response of Arctic storms in simulations from numerous models that are included in the CMIP-3 and CMIP-5 model ensemble, and highlighted that the differing horizontal resolution of models may be a primary factor contributing to differences between future climate simulations and uncertainty. It was noted that there is large inter-model spread in the response of Arctic storms to climate change, and that not all models project a consistent change in summer storm-track activity (Nishii et al., 2015). Baker et al. (2019) also highlighted that the response of storms that occur over the North Atlantic Ocean is sensitive to model horizontal resolution, with the response of storms to climate change being enhanced by higher horizontal resolution. Thus, there is a need to assess how horizontal resolution impacts future climate simulations of Arctic storms, to understand the uncertainty that can arise from differences in simulations from different models.

In this chapter, the future response of Arctic storms to anthropogenic climate change is determined from global climate simulations made using the atmosphere-only Hadley Centre Global Environmental Model (version 3) Global Atmosphere 3.0 model (hereafter HadGEM3-GA3.0) (Walters and Coauthors, 2011). These simulations were made as part of the United Kingdom on Partnership for Advanced Computing in Europe (PRACE): Weather-Resolving Simulations of Climate for Global Environmental Risk (UPSCALE) project (Mizielinski et al., 2014). Ensemble simulations of the present-day climate (1986-2010) and future climate (2086-2110) following the IPCC RCP8.5 pathway were made at three model horizontal resolutions: N96 (130km at 50° latitude), N216 (60km at 50° latitude) and N512 (25km at 50° latitude), with other aspects of the HadGEM3-GA3.0 configuration remaining constant between all simulations. A more detailed description of the HadGEM3-GA3.0 simulations is given in Section 2.2.2 in Chapter 2. These simulations provide the opportunity to assess how horizontal resolution impacts simulations of Arctic storms in the present-day and future climate, and to investigate whether simulations of Arctic storms are sensitive to horizontal resolution.

This will be achieved by the following objectives:

- Evaluate the representation of Arctic storms in the HadGEM3-GA3.0 present-day climate simulations against reanalysis datasets,
- Determine how Arctic storms may change in a future climate in response to climate change,
- Compare the response of Arctic storms to climate change in the HadGEM3-GA3.0 future climate simulations at horizontal resolutions of N96, N216 and N512.

In Section 5.2, the impact of horizontal resolution on present-day climate Arctic storm statistics (number, spatial distribution and intensity) determined from the HadGEM3-GA3.0 simulations are evaluated against reanalysis datasets. Secondly in Section 5.3, the response of Arctic storms to climate change in an RCP8.5 future climate is determined and compared between the N96, N216 and N512 HadGEM3-GA3.0 future climate simulations. A summary and conclusions are given in Section 5.4.

5.2 Evaluation of the HadGEM3-GA3.0 Present-Day Climate Simulations

Before analysing the future climate simulations from HadGEM3-GA3.0, it is necessary to evaluate the present-day climate simulations. These simulations are used as a reference to compare the future climate simulations against, to determine the future response of Arctic storms to climate change. It is therefore necessary to assess whether the HadGEM3-GA3.0 model reasonably simulates present-day Arctic storms. This analysis also provides the opportunity to determine how the representation of Arctic storms is sensitive to horizontal resolution when compared to reanalysis datasets. Arctic storms have been identified in the present-day climate simulations from each member of the HadGEM3-GA3.0 ensemble, using the same storm tracking methodology as in Chapter 3, using 850 hPa relative vorticity. Storm statistics from the HadGEM3-GA3.0 simulations are compared to the ERA5, ERA-Interim, JRA-55, MERRA-2 and NCEP-CFSR reanalysis datasets.

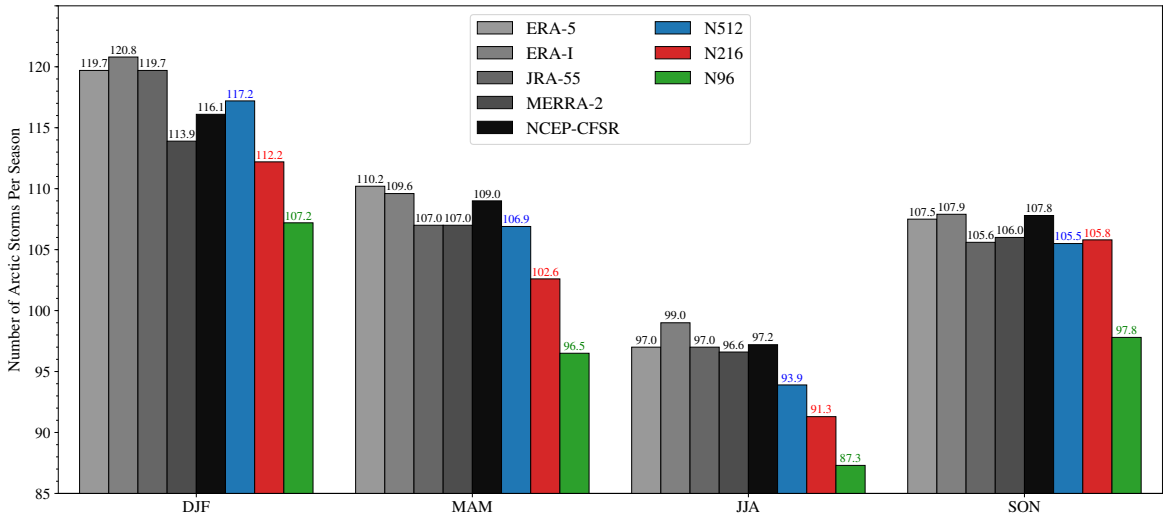

Figure 5.1: The ensemble mean number of Arctic storms per season from the N96, N216 and N512 HadGEM3-GA3.0 present-day climate simulations (1986-2010), and the ERA5, ERA-Interim (ERA-I), JRA-55, MERRA-2 and NCEP-CFSR reanalysis datasets.

5.2.1 Number of Arctic Storms

Across all horizontal resolutions, the seasonal cycle in Arctic storm number per season between 1986 and 2010 is captured well by HadGEM3-GA3.0 and compares well with all of the reanalysis datasets (see Figure 5.1). The reanalysis datasets and HadGEM3-GA3.0 show that Arctic storm number is highest in winter and lowest in summer. The ensemble mean average number of Arctic storms per season in the N96, N216 and N512 simulations is 107.1, 112.2 and 117.2 in winter, and, 96.5, 102.6 and 106.9 in summer respectively (see Figure 5.1).

As the horizontal resolution of HadGEM3-GA3.0 increases, the number of Arctic storms per season increases in all seasons and is more similar to that of the reanalysis datasets (see Figure 5.1). This is consistent with Jung et al. (2006), who also showed that the number of storms simulated by an atmospheric model increases with horizontal resolution. For example, in winter, the ensemble mean average number of Arctic storms in the N512 simulations is within the range of the reanalysis datasets, whereas, the mean number of Arctic storms in the N96 simulations is 6.9 storms per season lower than MERRA-2, which is the reanalysis dataset with the lowest number of storms per season (see Figure 5.1). Moreover, when using ERA5 as a reference, the number of storms per season from the N96 simulations are statistically significantly different to that of ERA5 in all seasons (see Table F.1 in Appendix F). The number of storms per season from the N216 simulations are also statistically significantly different to that of ERA5 in all

seasons except autumn (see Table F.1 in Appendix F). But, the number of storms per season from the N512 simulations are not statistically significantly different to ERA5 in any season (see Table F.1 in Appendix F).

Vessey et al. (2020) showed that approximately 50% of all Arctic storms have Arctic genesis (north of 65°N) and the rest mid-latitude genesis (south of 65°N). This is also shown in the all of the HadGEM3-GA3.0 simulations across all horizontal resolutions. The ratio of Arctic storms with Arctic and mid-latitude genesis from all the HadGEM3-GA3.0 simulations is between 55% and 45% across all seasons (see Table F.1 in Appendix F). In each season, this ratio is less than 3% different between the HadGEM3-GA3.0 simulations at each horizontal resolution. In addition, Vessey et al. (2020) showed that there are no trends in the number of Arctic storms from 1979 as shown by the modern global reanalysis datasets. This is also the case in all of the HadGEM3-GA3.0 simulations (see Figure F.1 in Appendix F).

5.2.2 Arctic Storm Spatial Distribution

Another aspect of present-day climate Arctic storms in the reanalysis datasets is that the storm tracks are seasonally dependent (Vessey et al., 2020). Generally, in winter, the track density of Arctic storms is highest over the Greenland, Norwegian and Barents Seas, whereas in summer, the track density of Arctic storms is highest over the Eurasian coastline and high Arctic Ocean (Vessey et al., 2020). This seasonality in Arctic storm track density is captured well in all of the HadGEM3-GA3.0 simulations at each horizontal resolution (see Figures 5.2 and 5.3). The ensemble mean Arctic storm track density in simulations at each horizontal resolution is highest over the Greenland, Norwegian and Barents Sea in winter (see Figure 5.2b - d), and over the Eurasian coastline in summer (see Figure 5.3b - d).

Generally, the differences between the HadGEM3-GA3.0 simulations and ERA5 decrease as the horizontal resolution increases from N96 to N512, in all seasons (see Figures 5.2, 5.3 and Figures F.4 and F.4 in Appendix F). For example, largest differences in Arctic storm track density between ERA5 and the N96 simulations in winter are more than 10 storms per season per unit area (5° spherical cap, approximately 10^6 km^2). Whereas between ERA5 and N512,

the largest differences are between 7-8 storms per season per unit area. But, there is a large difference in the genesis density of Arctic storms (> 2.5 storms per season per unit area) around Greenland in all seasons between the HadGEM3-GA3.0 simulations at all horizontal resolutions and ERA5 (see Figures F.6 and F.7 in Appendix F). The large differences in genesis density over Greenland in HadGEM3-GA3.0 compared to ERA5 is likely the cause of high differences in track density of Arctic storms around Greenland in winter and summer in all the N96, N216 and N512 simulations (see Figures 5.2b - d, and, 5.3b - d).

Arctic storm track density from the HadGEM3-GA3.0 simulations in winter and summer are compared to the other reanalysis datasets of ERA-Interim, JRA-55, MERRA-2 and NCEP-CFSR in Figures F.2 and F.3 (in Appendix F). Overall, the differences are shown to be similar to those shown in Figures 5.2 and 5.3, when ERA5 is used as the reference reanalysis dataset. The highest differences in Arctic storm track density in winter occur over the Greenland, Norwegian and Barents Seas, and in summer over the Eurasian continent and the Arctic Ocean. Additionally, there are high differences in Arctic storm track density around Greenland in both seasons when the HadGEM3-GA3.0 simulations are compared to all of the reanalysis datasets.

The largest differences between the N512, N216 and N96 HadGEM3-GA3.0 simulations generally occur where the track density of Arctic storms is largest in winter and summer (see Figures 5.2b - d, 5.2h - i, 5.3b - d and 5.3h - i). In winter, the largest differences are seen over Greenland, and the Greenland, Norwegian and Barents Seas (see Figure 5.2h and 5.2i). In summer, the largest differences occur over the Eurasian continent (see Figure 5.3h and 5.3i). These are all regions where climatological Arctic storm track density is high and typically greater than 15 storms per season per unit area (see Figures 5.2b - d, and 5.3b - d). Generally, Arctic storm track density is higher as horizontal resolution increases in all seasons. This is a consequence of more Arctic storms being simulated by HadGEM-GA3.0 at a higher horizontal resolution of N512 than N96 (see Figure 5.1).

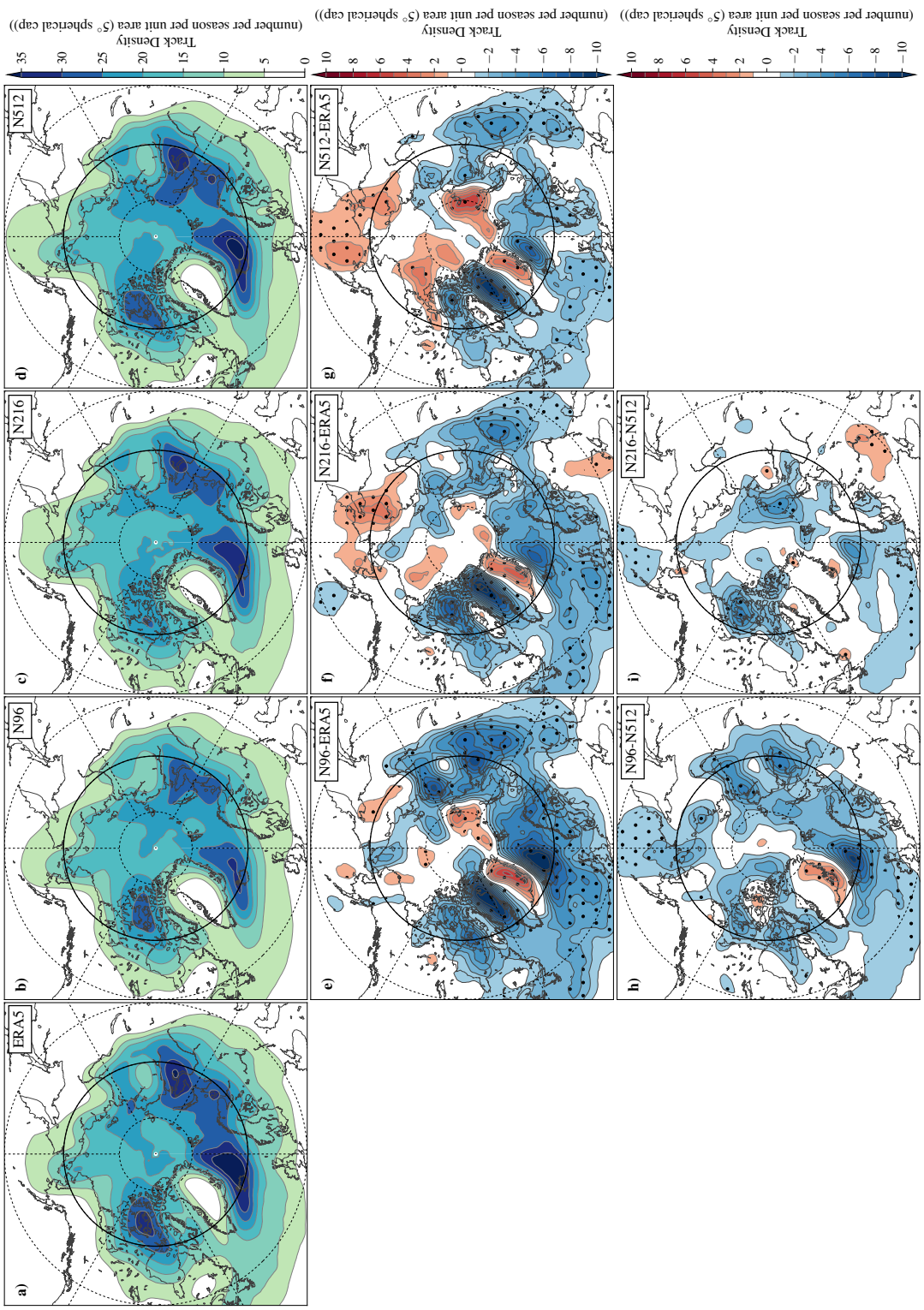

Figure 5.2: Winter (DJF) Arctic storm track density per season between 1986/87 and 2009/10 from the **a)** ERA5 reanalysis dataset, and the **b)** N96 ensemble (ens.) mean, **c)** N216 ens. mean and **d)** N512 ens. mean HadGEM3-GA3.0 present-day climate simulations. Differences in winter Arctic storm track density per season between **e)** N96 ens. mean minus ERA5, **f)** N216 ens. mean minus ERA5, **g)** N512 ens. mean minus ERA5, **h)** N96 minus N512 ens. mean and **i)** N216 minus N512 ens. mean. Longitudes are shown every 60°E, and latitudes are shown at 80°N, 65°N (bold) and 50°N. Stippling show areas where the differences are statistically significant to a 95% confidence level. Densities have units of number per season per unit area (5° spherical cap, $\approx 10^6$ km^2).

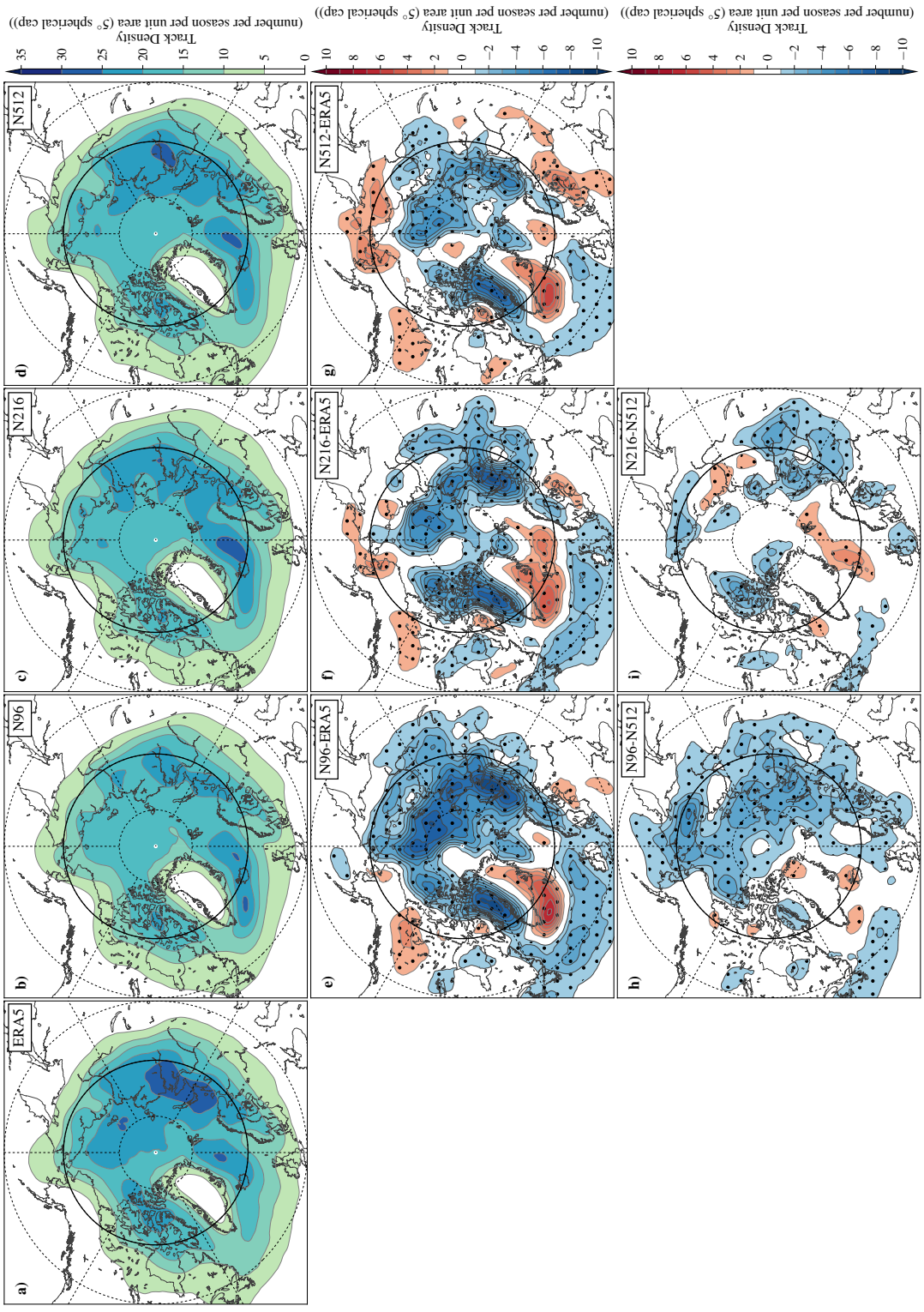

Figure 5.3: As **Figure 5.2**, but for present-day climate summer (JJA) Arctic storms between 1986-2010.

5.2.3 Arctic Storm Intensity

Vessey et al. (2020) showed that the representation of Arctic storm intensity can depend on the resolution of atmospheric reanalysis. The higher resolution global reanalysis datasets typically represent storms with higher intensities than the lower resolution global reanalyses (e.g. storms with lower minimum mean sea level pressure (MSLP) minima and higher 925 hPa wind speed maxima within the radius of Arctic storms). Models with low resolutions are less able to represent sharp gradients, which likely results in the higher resolution models representing storms to have higher intensities. Figure 5.4 shows that horizontal resolution of the HadGEM3-GA3.0 model also impacts Arctic storm intensity, with Arctic storms being more intense in the N512 present-day simulations than in the N96 present-day simulations. For example, in winter, the mean MSLP minima of Arctic storms is 988.5 and 991.8 hPa in the N512 and N96 present-day climate simulations respectively, with the mean 925 hPa wind speed maxima being 25.0 and 29.1 ms^{-1} for the N96 and N512 simulations respectively.

ERA5 shows Arctic storms are more intense in winter than in summer, which is also shown in all of the HadGEM3-GA3.0 simulations (see Figure 5.4). This is also common to the ERA-Interim, JRA-55, MERRA-2 and NCEP-CFSR reanalysis datasets also show this (Vessey et al., 2020). All of the HadGEM3-GA3.0 simulations show that winter Arctic storms can reach a minimum MSLP of approximately 940 hPa, whereas summer Arctic storms can only reach a minimum MSLP of approximately 960 hPa (see Figure 5.4).

ERA5 data are produced using a spectral model, and have a horizontal resolution of 31 km at both high and low latitudes (Hersbach et al., 2020). HadGEM3-GA3.0 uses a grid-point model that has a finer horizontal resolution in polar regions (high latitudes) than it has at the equator (low latitudes), approximately 25 km at the equator, and is a higher resolution than ERA5 (Walters and Coauthors, 2011). This may contribute to the N512 simulations representing Arctic storms as more intense than ERA5 particularly in the 925 hPa wind speed field, as shown by Figure 5.4.

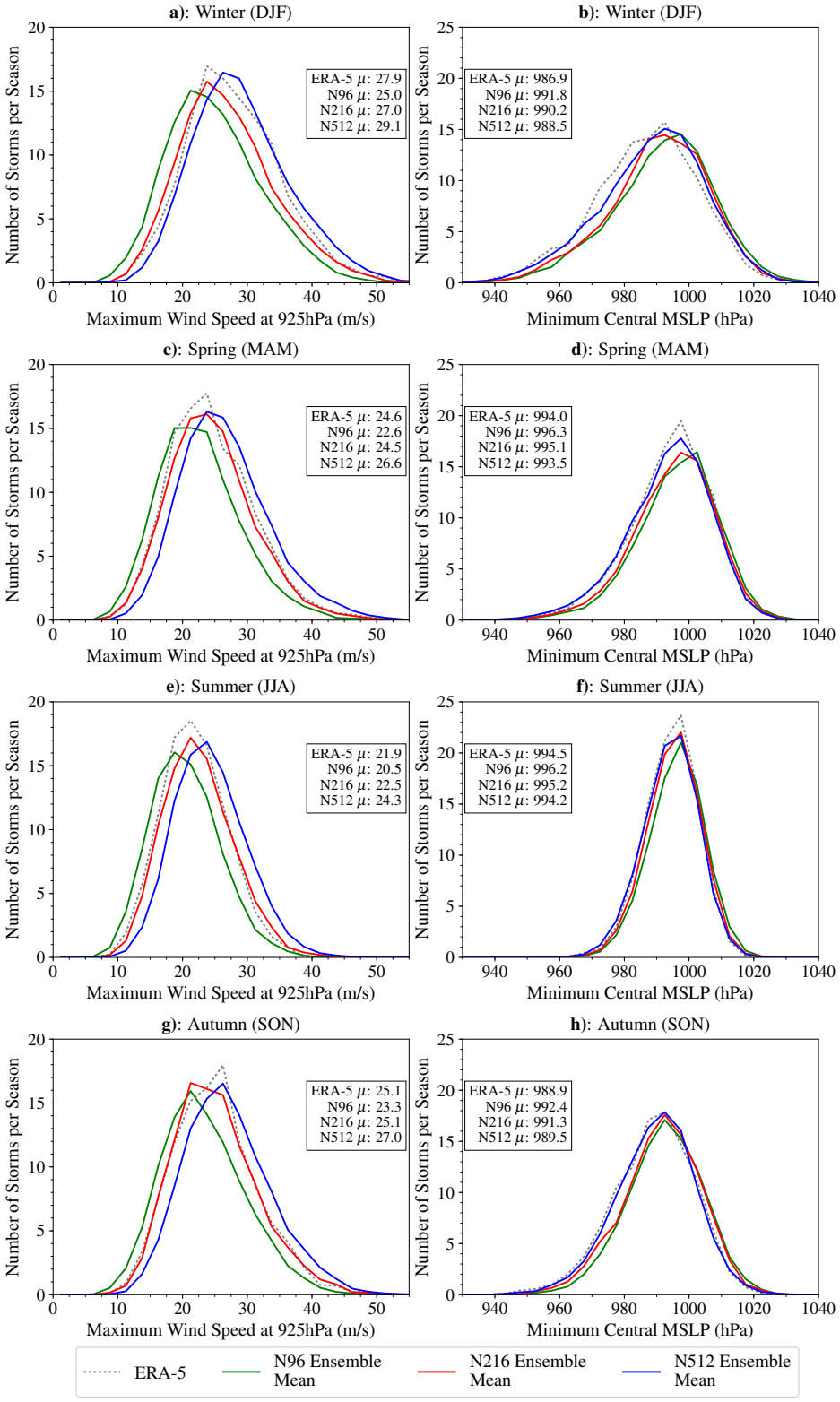

Figure 5.4: Winter (DJF) **a) & c)** and **b) & d)** summer (JJA) Arctic storm intensity between 1986 and 2010 from the ERA5 reanalysis dataset, and the N96 ensemble (ens.) mean, N216 ens. mean and N512 ens. mean HadGEM3-GA3.0 present-day climate simulations. **a) & b)** show the maximum intensity of 925hPa (near-surface) wind speeds (ms^{-1}) and **c) & d)** minimum mean sea level pressure (MSLP) (hPa) of Arctic storms when they are north of 65°N.

5.3 Response of Arctic Storms to Climate Change in HadGEM3-GA3.0

5.3.1 Changes in Arctic Storm Number

End of century (2086-2110) future climate simulations from HadGEM3-GA3.0, following the RCP8.5 future climate scenario, show that Arctic storm number per season will change. The largest change in the number of Arctic storms will occur in winter (see Figure 5.5a). All of the N96, N216 and N512 simulations show a reduction in the mean number of winter Arctic storms of 8.3, 8.2 and 6.9 storms per season respectively. As a percentage of the mean number of winter Arctic storms per season in the present-day climate simulations, the N96, N216 and N512 show that winter Arctic storm number will decrease by 15.1%, 13.4% and 13.8% respectively. All of the N96, N216 and N512 simulations show that this is primarily due to reductions in the number of storms with Arctic genesis, which outweigh the smaller changes in the number of Arctic storms with mid-latitude genesis (see Figure 5.5b and 5.5c).

In summer, the N512 and N216 future climate simulations show Arctic storm number to decrease by 3.0 and 1.3 storms per season respectively, but the N96 simulations show the number of summer Arctic storms to increase by 2.3 storms per season (see Figure 5.5a). These changes are fairly small when compared to the mean number of summer Arctic storms per season in the present-day climate simulations (+2.6%, -1.4% and -3.2% for the N96, N216 and N512 simulations respectively). However, the changes shown in the N216 and N96 future climate simulations compared to the present-day climate simulations are not statistically significant (see Figure 5.5a). In spring and autumn, all of the N96, N216 and N512 simulations show a statistically significant decrease in the number of Arctic storms with Arctic genesis, of 3.4 - 4.9 storms per season in spring and 2.6 - 4.0 storms per season in autumn (see Figure 5.5a). Generally, the changes in the number of Arctic storms with Arctic genesis are greater than changes in the number Arctic storms with mid-latitude genesis.

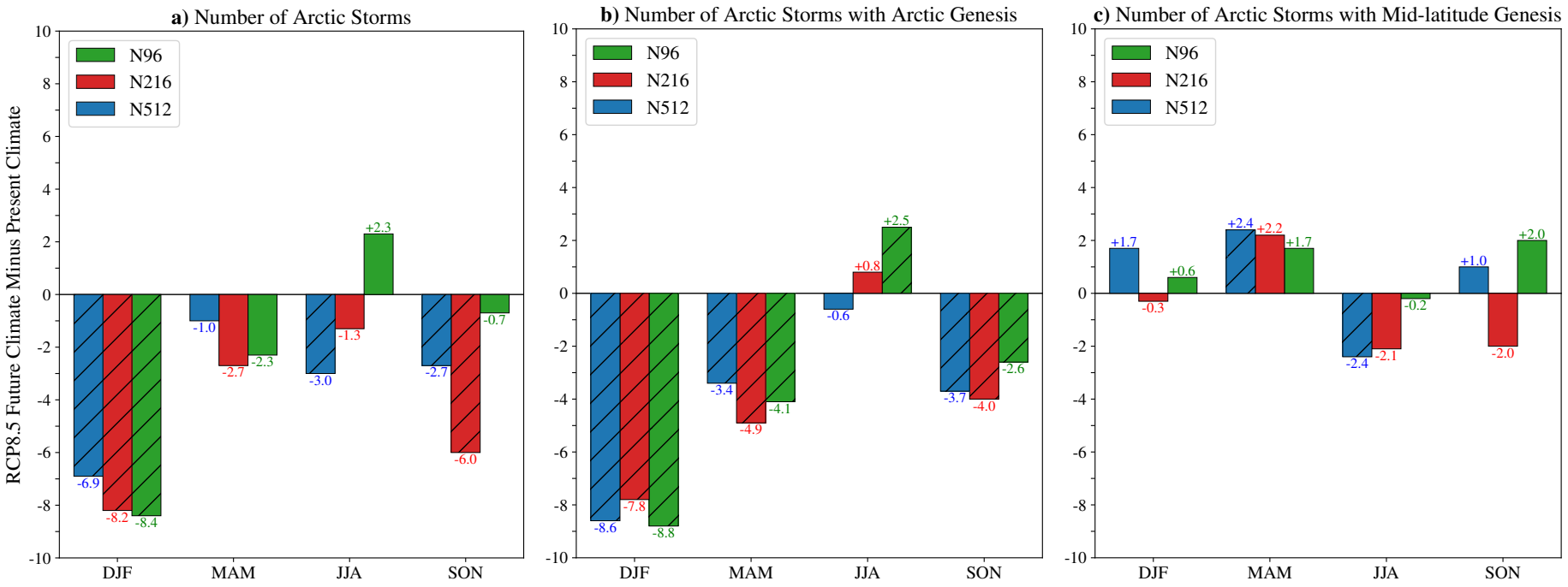

Figure 5.5: Difference in Arctic storm number per season between the HadGEM3-GA3.0 RCP8.5 future climate (2086-2110) simulations and the present-day climate (1986-2010) simulations, at horizontal resolutions of N96, N216 and N512. Difference in the **a)** number of Arctic storms, **b)** number of Arctic storms with Arctic genesis (north of 65°N), and **c)** number of Arctic storms with mid-latitude genesis (south of 65°N). Hatching shows if the change between the RCP8.5 future climate and present-day climate simulations are statistically significant to a 95% confidence interval, using the Students t-test on storm number per season.

5.3.2 Changes in Arctic Storm Spatial Distribution

Simulations from HadGEM3-GA3.0 show that the spatial distribution of Arctic storms will change in a RCP8.5 future climate (2086-2110). Figures 5.6 and 5.7 show the change in Arctic storm track density per season per unit area (5° spherical cap, approximately 10^6 km^2) in winter (DJF) and summer (JJA) for the N96, N216 and N512 future climate simulations. The corresponding plots for spring (MAM) and autumn (SON) are shown in Figures F.8 and F.9 in Appendix F.

In winter, Arctic storm track density is lower over the Arctic Ocean in all of the HadGEM3-GA3.0 RCP8.5 future climate simulations than in the present-day simulations (see Figure 5.6d - 5.6f). Arctic storm track density over the Arctic Ocean is lower by as much as 9 - 10 storms per season per unit area in the future climate simulations (see Figure 5.6d - 5.6f). The largest decreases in Arctic storm track density occur north of the Eurasian coastline. This response to climate change is consistent when comparing the present-day and future climate simulations from the HadGEM3-GA3.0 simulations at each horizontal resolution.

In summer, all of the HadGEM3-GA3.0 future climate simulations show an increase in Arctic storm track density around Greenland and a decrease in storm track density over the Eurasian continent (see Figure 5.7d - 5.7f). South of Greenland, the simulations at each horizontal resolution show the track density of Arctic storms to increase by greater than 10 storms per season per unit area. Over the Eurasian continent, the track density of Arctic storms is shown to decrease by as much as 6-7 storms per season per unit area (see Figure 5.7d - 5.7f). Like in winter, the changes in Arctic storm track density between the present-day and future climate simulations are consistent between all horizontal resolutions.

Figures F.8 and F.9 in Appendix F show the change in spring and autumn Arctic storm track density in the HadGEM3-GA3.0 RCP8.5 future climate simulations. In spring, the general response is similar to that shown in winter, with the future climate simulations showing a decrease in the track density of Arctic storms over the Arctic Ocean. But, unlike winter, there is an increase in the track density of Arctic storms south of Greenland (see Figure F.8 in

Appendix F). In autumn, the response of Arctic storms to climate change is similar to that shown in summer, with Arctic storm track density increasing south and east of Greenland and decreasing over the Eurasian continent (see Figure F.9 in Appendix F).

The general response to climate change is very similar between simulations at all of the horizontal resolutions, when comparing the present-day and future climate simulations (see Figures 5.6d - 5.6f and 5.7d - 5.7f). But, the number of Arctic storms simulated in the N512 future climate simulations is higher than in the N96 and N216 simulations (see Table F.2 in Appendix F). This leads to differences in Arctic storm track density when comparing the future climate simulations from each resolution, primarily in areas where Arctic storm track density is highest (see Figures 5.6g, 5.6h, 5.7g and 5.7h).

The spatial changes in Arctic storm track density shown in Figure 5.6 and 5.7 are similar to that shown in previous research. Day et al. (2018) analysed RCP8.5 future climate simulations using the CESM1 large model ensemble, and also showed that the track density of Arctic storms decreases in the Arctic Ocean in winter, and in summer, increases around Greenland and decreases over the Eurasian continent. Crawford and Serreze (2017) showed a similar response in a RCP8.5 future climate in summer, also using the CESM1 large model ensemble. But the magnitude of the changes around Greenland in summer from Crawford and Serreze (2017) are lower than is found in this study and to that shown by Day et al. (2018). Figure 5.7 shows the track density of Arctic storms to increase by 9-10 storms per season per unit area at each horizontal resolution in summer, but Crawford and Serreze (2017) show an increase of 2.4 - 4.8 storms per season.

Crawford and Serreze (2017) and Day et al. (2018) both analysed simulations from the CESM1 large ensemble using the same RCP8.5 climate change forcing. However, Crawford and Serreze (2017) used sea level pressure as the storm tracking variable, whereas, in this study and in Day et al. (2018), 850 hPa relative vorticity is used as the storm tracking variable. Vessey et al. (2020) showed that the number of Arctic storms identified by a storm tracking algorithm based on 850 hPa relative vorticity is greater than that based on mean sea level pressure. This may contribute towards the different magnitudes of changes described in this study and Day et al.

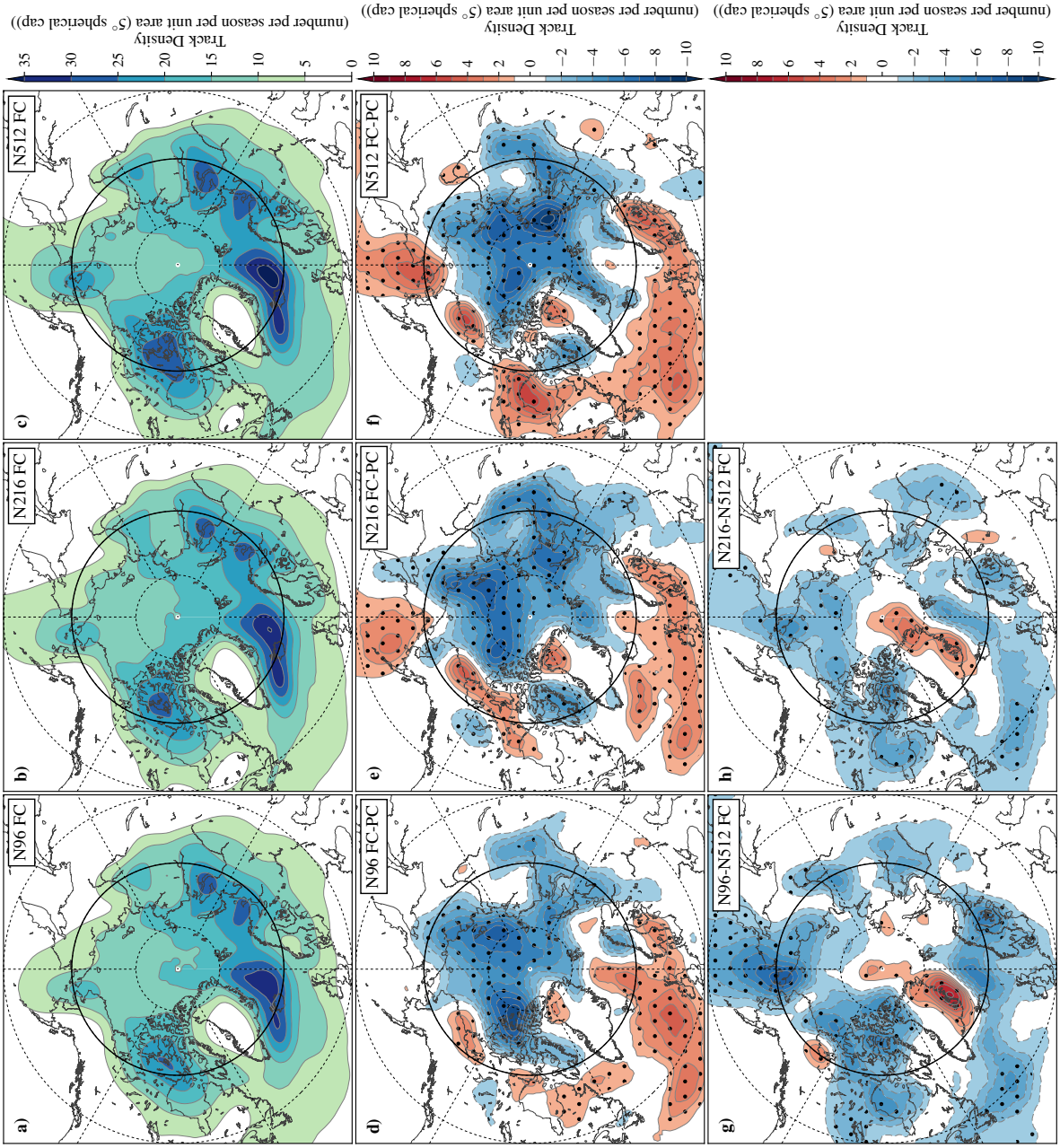

Figure 5.6: Winter (DJF) Arctic storm track density per season between 2086/87 and 2009/10 from the **a)** N96 ensemble (ens.) mean, **b)** N216 ens. mean and **c)** N512 ens. mean HadGEM3-GA3.0 RCP8.5 future climate simulations. **d)** N96 ens. mean future (2086/87-2109/10) minus present-day (1986/87-2009/2010) climate, **e)** N216 ens. mean future minus present climate, **f)** N512 ens. mean future minus present climate. **g)** N96 minus N512 ens. mean future climate and **h)** N216 minus N512 ens. mean future climate. Longitudes are shown every 60°E, and latitudes are shown at 80°N, 65°N (bold) and 50°N. Stippling show areas where the differences are statistically significant to a 95% confidence level. Densities have units of number per season per unit area (5° spherical cap, $\approx 10^6$ km^2).

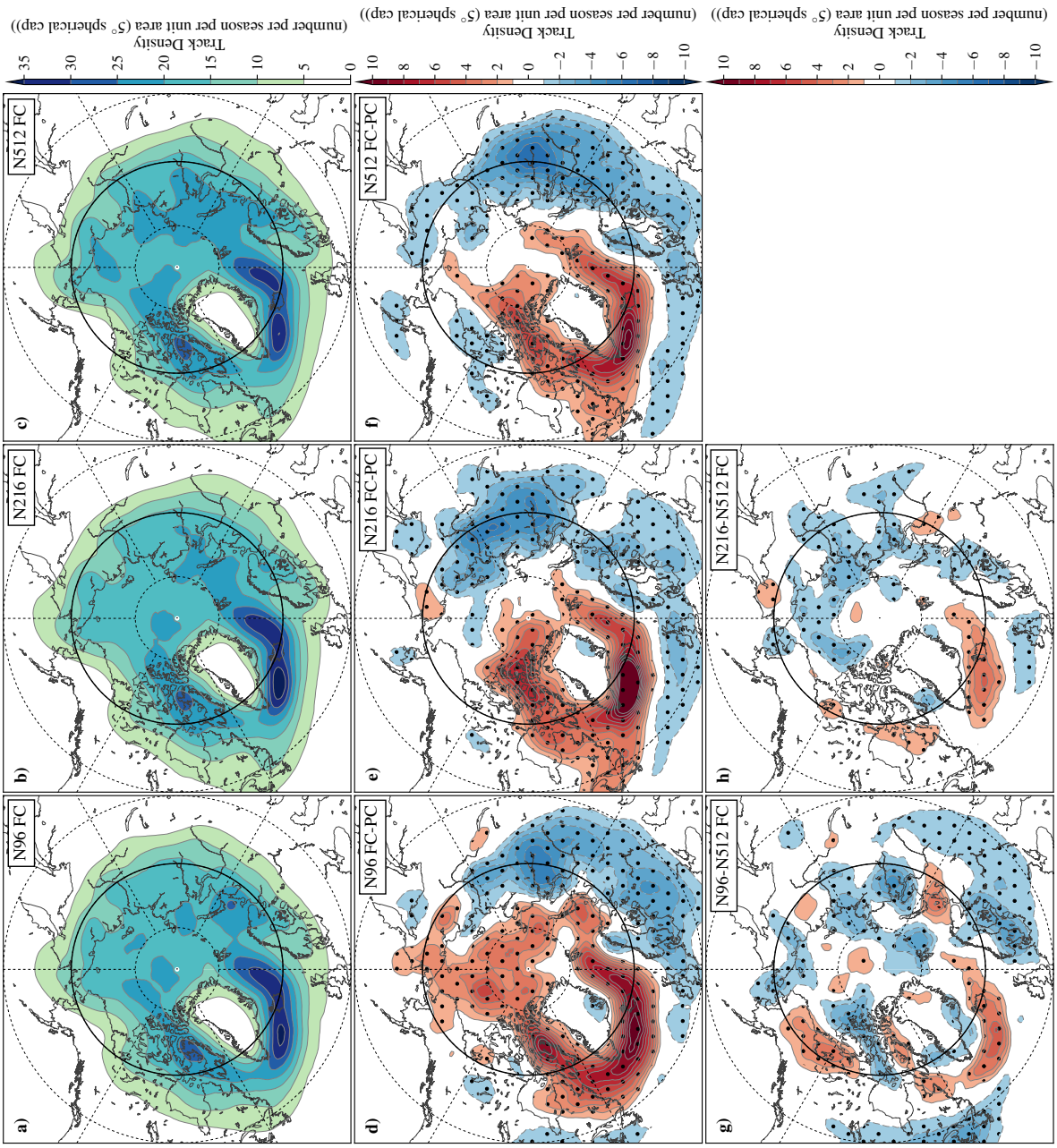

Figure 5.7: As **5.6**, but for RCP8.5 future climate summer (JJA) Arctic storms between 2086-2110.

(2018) compared to Crawford and Serreze (2017). Other contributing factors could include how storms are filtered once they have been identified and tracked, or how the statistics of track density are computed. The differences between this study, Crawford and Serreze (2017) and Day et al. (2018) show that the magnitude of the response of Arctic storms to climate change can be sensitive to the storm tracking method. But all methods appear to indicate a similar general spatial response of Arctic storms to climate change.

5.3.3 Relation of Changes to the Large-Scale Environment

As shown above, there is a response of Arctic storms to climate change. It is important to relate these changes to changes in the large-scale environment, as this helps to understand why these changes are occurring and gives confidence in the simulations from HadGEM3-GA3.0.

In winter, there is a significant decrease in the track density of Arctic storms over the Arctic Ocean, with a large reduction in the number of Arctic storms with Arctic genesis (see Figures 5.5 and 5.6). The development of storms is influenced by the baroclinicity of the atmosphere, with higher baroclinicity favouring storm development (Hoskins and Valdes, 1990). Baroclinicity is often quantified using the Eady Growth Rate (see Equation 1.1 in Chapter 1) (Hoskins and Valdes, 1990). Figure 5.8 shows the percentage changes in the Eady Growth Rate in winter between the present-day and RCP8.5 future climate HadGEM3-GA3.0 simulations at each horizontal resolution.

Overall, the response of the large-scale environment in the Arctic to climate change is very similar between the simulations at each horizontal resolution, and shows that the atmosphere will become less baroclinic over the Arctic in the future (see Figure 5.8). The highest decreases in baroclinicity will occur in the Greenland, Norwegian and Barents Seas, with a magnitude of up to 40% compared to the present-day climate (see Figure 5.8). This is consistent with Seiler and Zwiers (2016) and Semmler et al. (2016).

Figure 5.9a and 5.9b show the percentage changes in wind shear ($\frac{\partial U}{\partial Z}$), and the static stability (N) of the atmosphere (which is combined with the Coriolis force as $\frac{f}{N}$). These contribute to the Eady Growth Rate and baroclinicity (see Equation 1.1 in Chapter 1). In winter, the changes in wind shear and static stability of the atmosphere have a competing impact on baroclinicity. Generally in a future climate, wind shear decreases across the Arctic, particularly over the Barents Sea and Canadian Archipelago (see Figure 5.9a), but static stability of the atmosphere decreases across the high Arctic Ocean and Canadian Archipelago, causing $\frac{f}{N}$ to increase (see Figure 5.9b). The largest decrease in baroclinicity in the Arctic in winter occurs over the Greenland and Barents Seas, where decreases in wind shear are not as cancelled out by the decreases in static stability (increases in $\frac{f}{N}$).

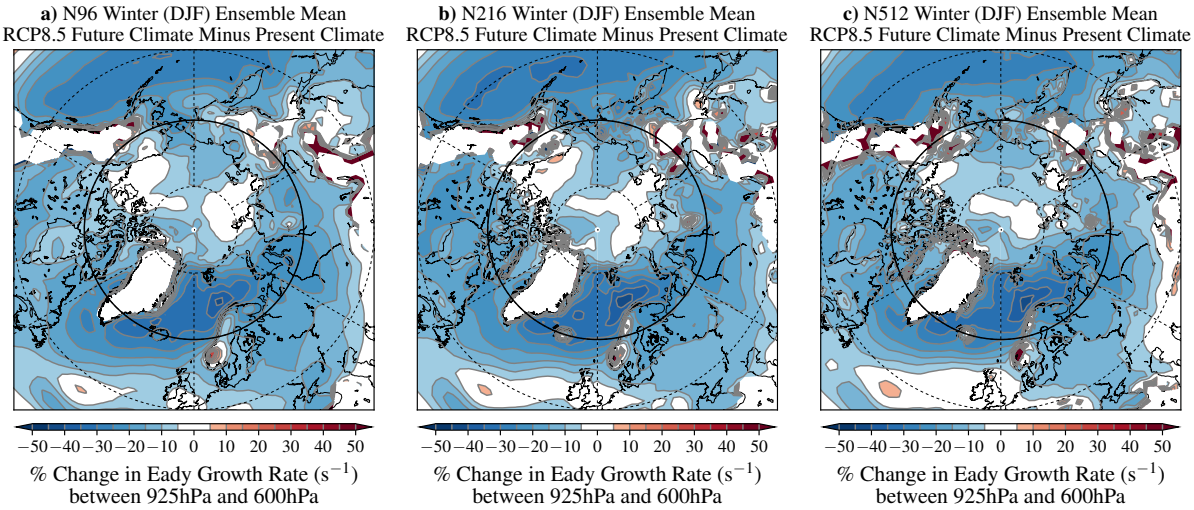

Figure 5.8: Difference in the winter (DJF) Eady Growth Rate between 925 hPa and 600 hPa, between the ensemble mean **a)** N96, **b)** N216 and **c)** N512 RCP8.5 future climate (2086/87-2109/10) and present-day (1986-2010) climate HadGEM3-GA3.0 simulations (future minus present climate).

This large-scale response of the atmosphere to climate change is similar in all HadGEM3-GA3.0 simulations at all horizontal resolutions (see Figure 5.8). All simulations at each horizontal resolution show that the largest decrease in the Eady Growth Rate occurs over the Greenland, Norwegian and Barents Seas. Additionally, they show a decrease in wind shear across the Arctic, with the largest reductions occurring over the Barents Sea and Canadian Archipelago (see Figure 5.9 and Figures F.12 and F.13 in Appendix F). The static stability of the atmosphere also decreases across the high Arctic Ocean and Canadian Archipelago, causing $\frac{f}{N}$ to increase (see Figure 5.9 and Figures F.12 and F.13 in Appendix F).

These changes in the baroclinicity, wind shear and static stability are caused by non-uniform warming of the Arctic in a future winter climate (see Figure 5.9c). This is likely a consequence of Arctic Amplification and reductions in Arctic sea ice extent. Warming from climate change will melt sea ice and change the surface type from ice to ocean (see Figure 2.2 in Chapter 2), which increases the amount of solar radiation absorbed by the surface and leads to further warming of the atmosphere (Arrhenius, 1896; Manabe and Stouffer, 1980; Serreze and Barry, 2011). The high Arctic Ocean and the Canadian Archipelago undergo greater warming than more southern regions of the Arctic such as the Greenland and Barents Seas (see Figure 5.9c). This acts to decrease meridional temperature gradients on the periphery of the regions that

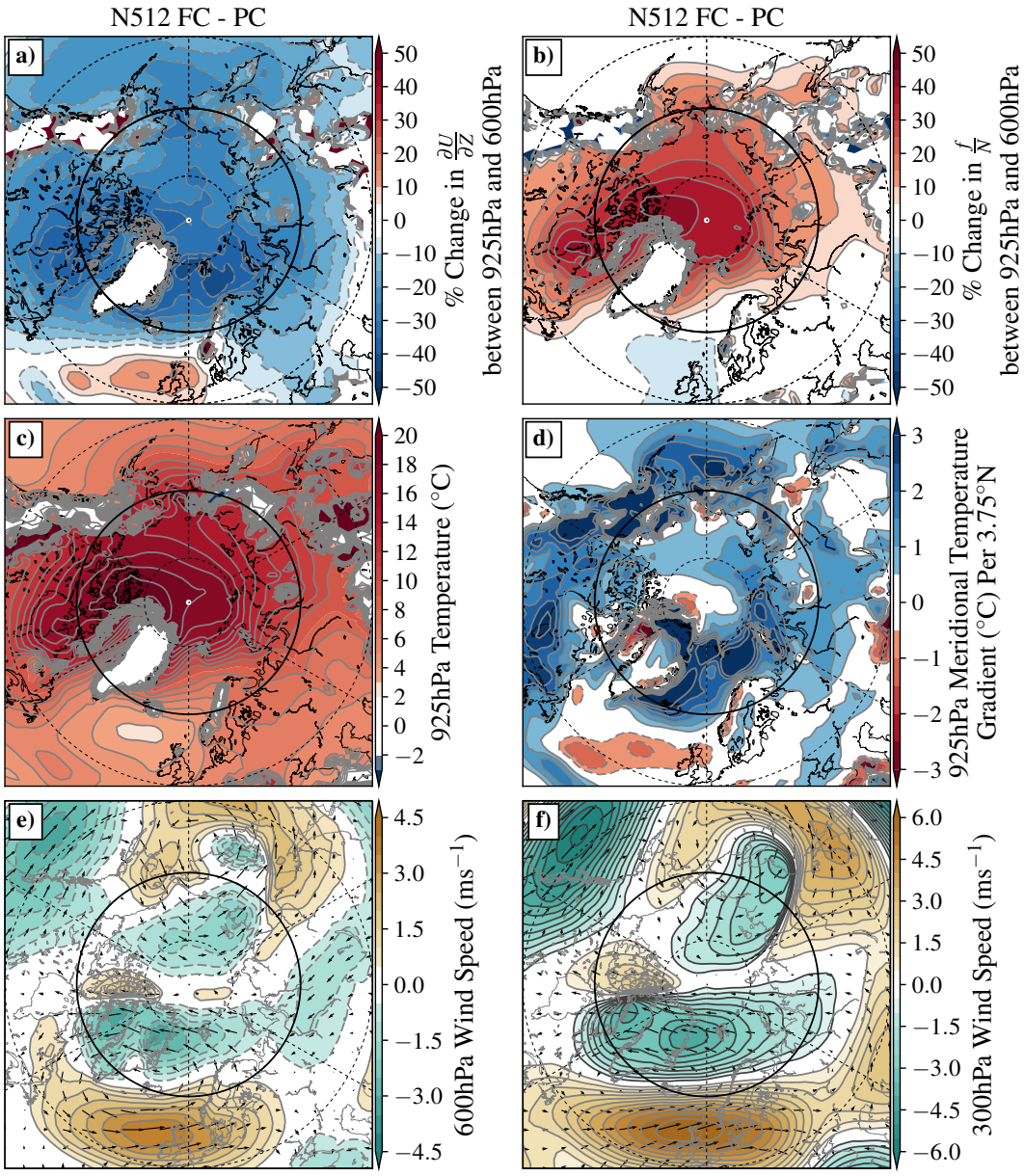

Figure 5.9: Differences in the winter (DJF) large scale environment between the RCP8.5 future climate (2086/87-2109/10) and present-day climate (1986/87-2009/10) N512 HadGEM3-GA3.0 simulations (future minus present climate). Percentage change in **a)** wind shear ($\frac{\partial U}{\partial Z}$) and **b)** Coriolis force divided by the Brunt Vaisala frequency ($\frac{f}{N}$), between 925 and 600 hPa. Change in **c)** 925 hPa temperature, **d)** meridional temperature gradient at 925 hPa temperature per 3.75°N, **e)** 600 hPa wind speed and direction, and, **f)** 300 hPa wind speed and direction.

undergo the greatest warming, which would lead to reductions in wind shear (following Thermal Wind Balance) that are shown in Figure 5.9a. The reduction in meridional temperature gradients in the Arctic is shown to be greatest over the Greenland and Barents Seas (see Figure 5.9d), which leads to reductions in 600 hPa and 300 hPa wind speed over the Greenland and Barents Seas (see Figure 5.9f).

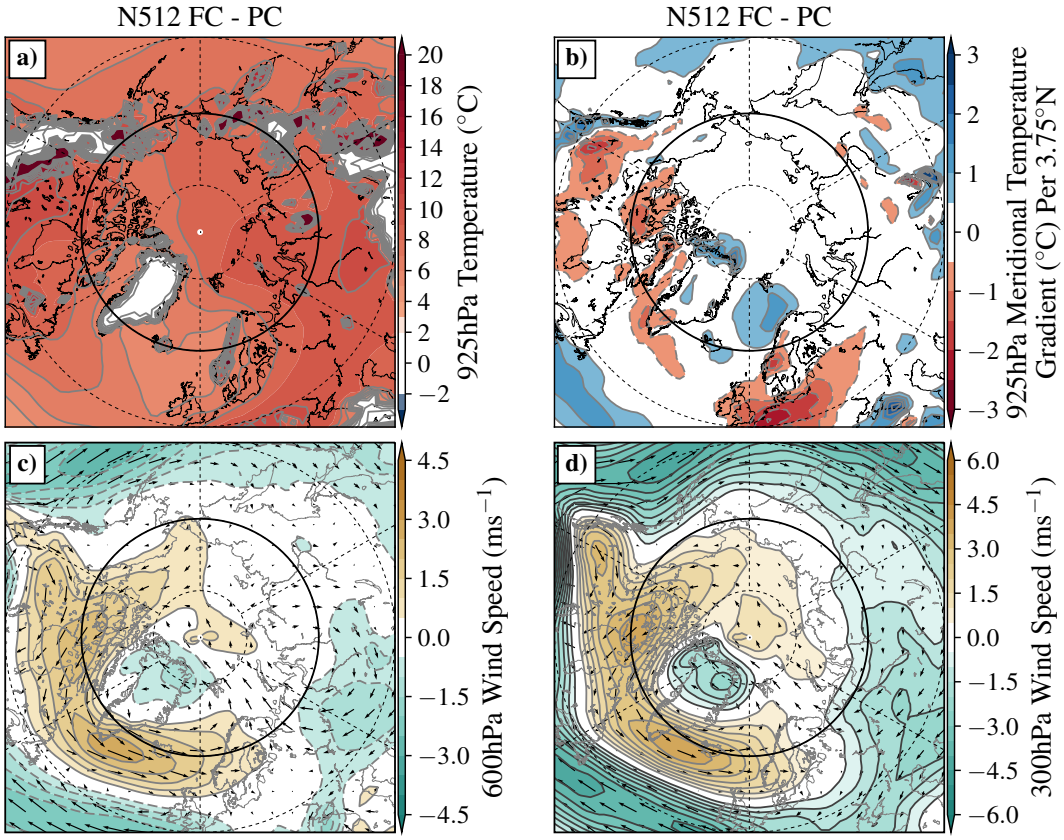

Figure 5.10: Differences in the summer (JJA) large scale environment between the RCP8.5 future climate (2086-2110) and present-day climate (1986/87-2009/10) N512 HadGEM3-GA3.0 simulations (future minus present climate). Change in **a)** 925 hPa temperature, **b)** meridional temperature gradient at 925 hPa temperature per 3.75°N, **c)** 600 hPa wind speed and direction, and, **d)** 300 hPa wind speed and direction.

In addition to decreasing wind shear over the Arctic, static stability of the atmosphere over the Arctic Ocean and the Canadian Archipelago also decreases in the HadGEM3-GA3.0 winter future climate simulations, causing an increase in $\frac{f}{N}$ (see Figure 5.9). This has a competing impact on baroclinicity to the changes in wind shear. Warming is greatest in lower levels (up to 850 hPa) of the atmosphere compared to higher levels (for example between 400-600 hPa) (see Figure F.14 in Appendix F). This would make the atmosphere more unstable, as air at the surface would be more buoyant than air aloft, thus decreasing static stability and increasing $\frac{f}{N}$. This is not the case over the Greenland, Norwegian and Barents Seas however, where static stability is similar between the HadGEM3-GA3.0 RCP8.5 future climate and present climate simulations (see Figure 5.9). Woollings et al. (2012) showed that the Atlantic Meridional Overturning Circulation is projected to weaken in response to climate change, leading to an increase to

static stability over the Greenland and Norwegian Seas. As a result, the largest changes in baroclinicity are found over the Greenland, Norwegian and Barents Seas in winter (see Figure 5.8), where changes in wind shear are highest (see Figure 5.8a) and not as negated by changes in static stability (see Figure 5.8b).

The reductions in baroclinicity in winter over the Greenland, Norwegian and Barents Seas correlate well with reductions in Arctic storm genesis density in a future climate across all horizontal resolutions (see Figure 5.12a-c). However, Figure 5.12 also shows that over the Chersky mountain range in northwest Siberia, there is a reduction in Arctic storm genesis in the future climate, which is not associated with changes in baroclinicity (see Figure 5.8). Instead, Figure 5.9f shows that in the future winter climate HadGEM3-GA3.0 simulations, wind speeds at the 300 hPa level over the Chersky mountain range decrease and increase south of the region at 50°N, perhaps leading to a reduction in genesis density in the region (see Figure 5.12a-c).

Changes in temperature between the present and RCP8.5 future climate are more uniform across the Arctic in summer than in winter, and changes in meridional temperature gradients are much smaller (see Figures 5.9c, 5.9d, 5.10a and 5.10b). There is a more noticeable change however in the 600 hPa and 300 hPa wind speed field (see Figure 5.10c and 5.10d). Over North America and the northern North Atlantic Ocean, wind speeds at 600 hPa and 300 hPa generally increase, but decrease over lower latitudes (south of 50°N).

The Jet Stream influences storm development, especially over the North Atlantic Ocean, where it can influence upper-level divergence and convergence, which can lead to the genesis of a storm at the surface (Dacre et al., 2012). Figure 5.11 shows a the northward shift in the Jet Stream over the northern North Atlantic Ocean is simulated by the HadGEM3-GA3.0 model at all horizontal resolutions. This northward shift in the Jet Stream in response to climate change is similar to results from Stocker et al. (2014); Barnes and Screen (2015). In all of these simulations, the greatest global atmospheric warming in summer occurs in the upper-levels of the tropical troposphere (see Figure 5.11a, 5.11c, 5.11e). As the atmosphere in this region warms in the upper topical troposphere, it will expand. This will consequently lead to the

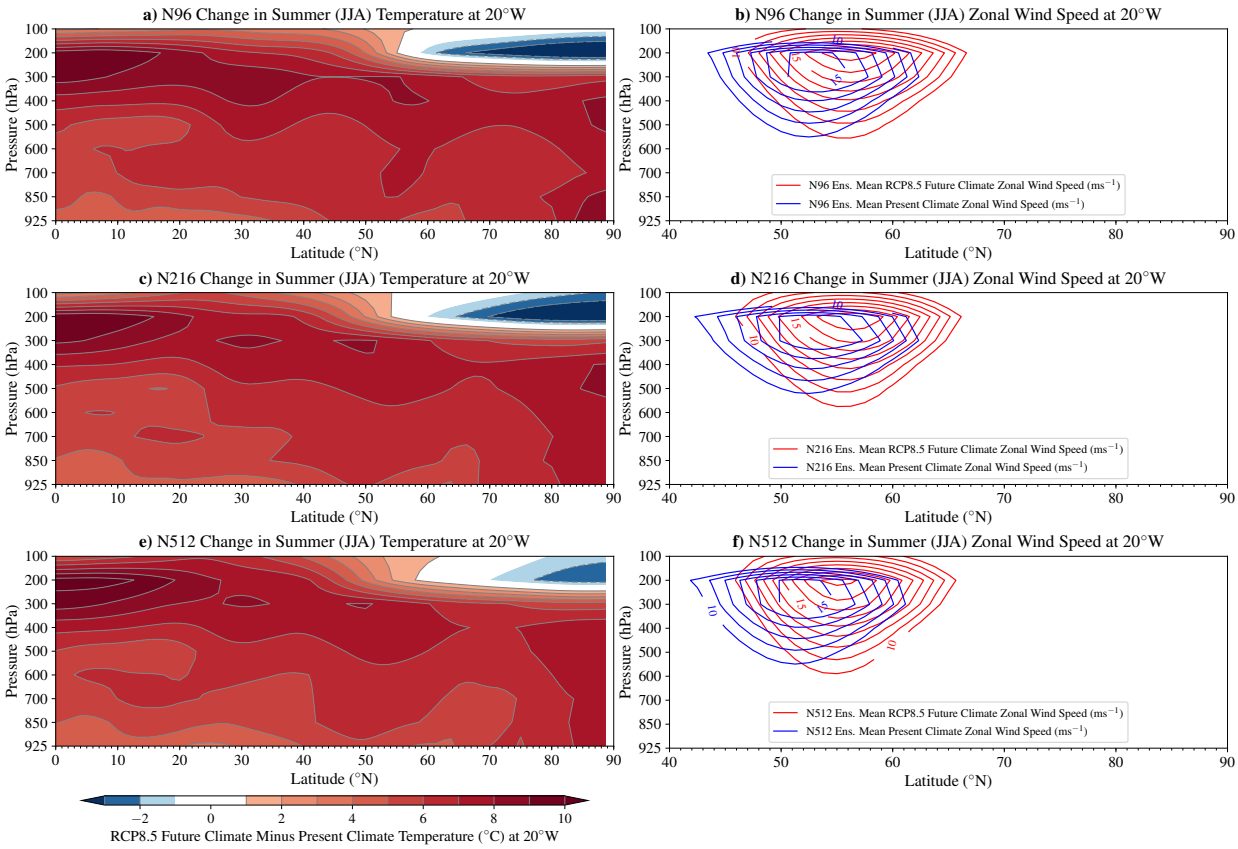

Figure 5.11: Differences in **a), c), d)** air temperature and **b), d), f)** zonal wind speed (u-component) at 20°W between the RCP8.5 future climate (2086-2110) and present-day climate (1986-2010) HadGEM3-GA3.0 simulations (future minus present climate) in summer (JJA) at a horizontal resolution of **a) & b)** N96, **c) & d)** N216 and **e) & f)** N512.

expansion of the Hadley cell to higher latitudes, which may shift the mid-latitude Jet Stream northward (Stocker et al., 2014; Barnes and Screen, 2015). All of the HadGEM3-GA3.0 simulations show that the Jet Stream will shift northward by approximately 4°N at 20°W (over the North Atlantic Ocean) (see Figure 5.11b, 5.11d, 5.11f).

It is plausible that the northward shift in the Jet Stream may lead to an increase in the genesis of storms over the northern North Atlantic Ocean and North America. Figure 5.12d-f show that this appears to be the case, as the genesis density of Arctic storms over the Canadian Archipelago, western North America and the southern lee-side of Greenland is higher in the future climate than in the present-day climate, across all HadGEM3-GA3.0 simulations. This is likely why there is an increase in the track density of Arctic storms around Greenland and over the Greenland and Barents Seas in summer (see Figure 5.7).

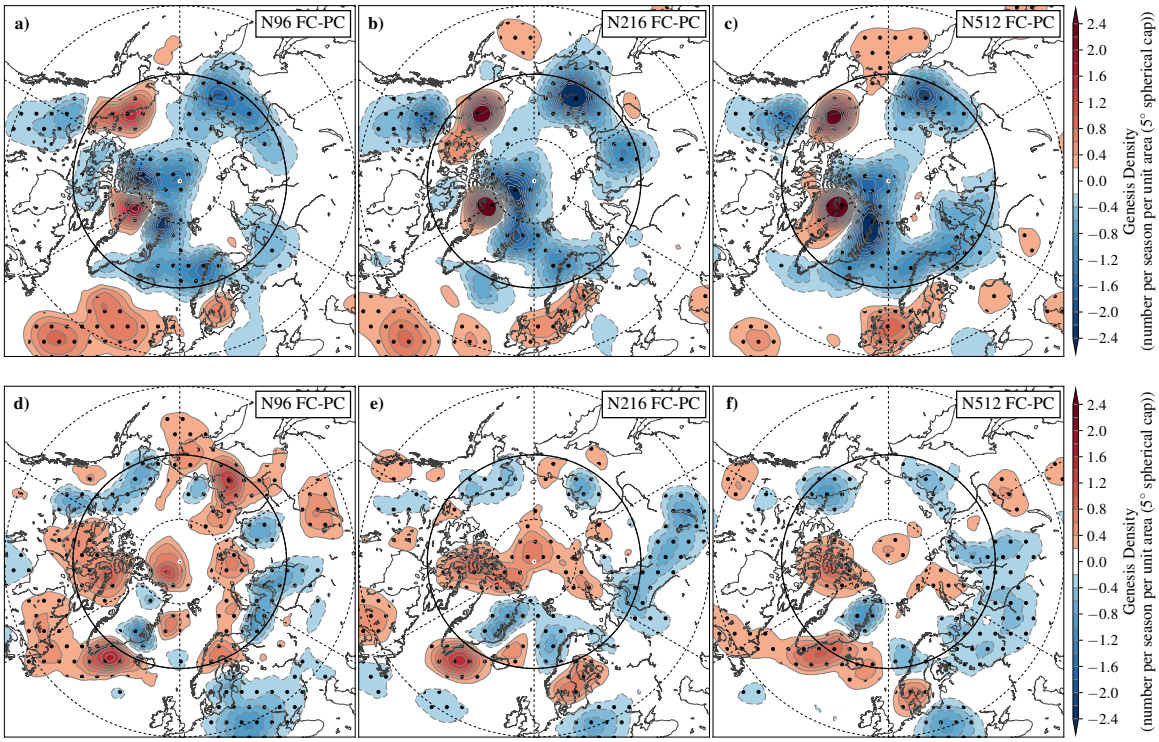

Figure 5.12: Changes in Arctic storm genesis density in **a) - c)** winter (DJF) and **d) - f)** summer (JJA) between the RCP8.5 future climate (2086-2110) and present-day climate (1986-2010) HadGEM3-GA3.0 simulations at a horizontal resolution of **a) and d)** N96, **b) and e)** N216 and **c) and f)** N512. Longitude and latitude bands, stippling and units are the same as Figure 5.2

Also in the RCP8.5 summer future climate, there is a reduction in Arctic storm track density over the Eurasian continent (see Figure 5.7). This response is also shown by Orsolini and Sorteberg (2009), Crawford and Serreze (2017) and Day et al. (2018). Crawford and Serreze (2017) showed that this is not primarily due to changes in the Arctic Frontal Zone, but due to changes in the Eurasian storm track. Crawford and Serreze (2017) showed that the Eurasian storm track becomes more zonal in a RCP8.5 future summer climate, decreasing the number of storms travelling into the Arctic (north of 65°N) from regions south of the Arctic such as Eurasia. Figure 5.10f shows that in the future summer climate HadGEM3-GA3.0 simulations there is also a reduction in the 300 hPa wind speeds over the Eurasian Continent, which may reduce storm genesis density over Eurasia and that number of Arctic storms from this region, as shown by Figure 5.12d-f.

In summary, it is shown in the RCP8.5 future climate (2086-2110) HadGEM3-GA3.0 simulations that climate change will lead to changes in the large-scale environment of the Arctic. This will consequently lead to changes in the spatial distribution of Arctic storms (see

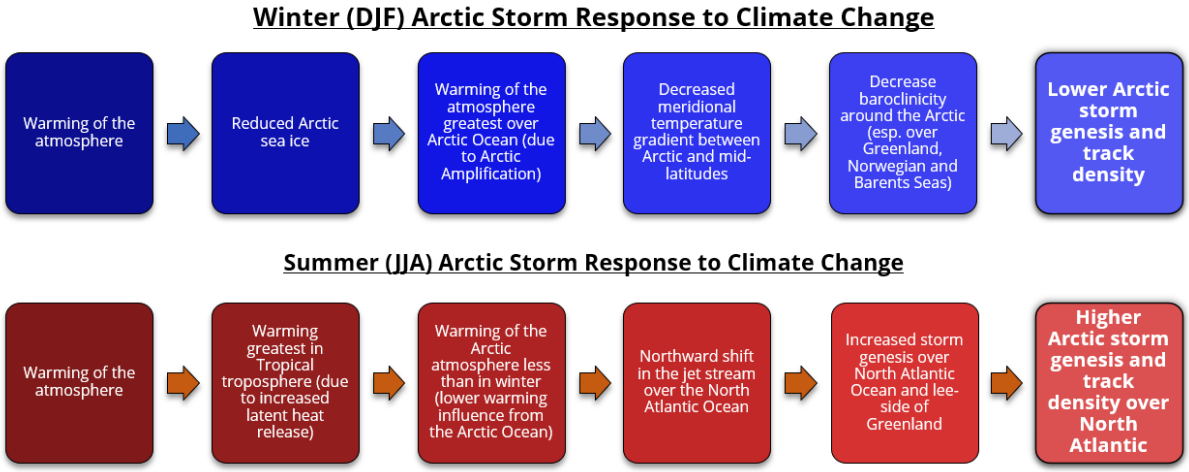

Figure 5.13: Flow chart that describes how the RCP8.5 future climate (2086-2110) HadGEM3-GA3.0 simulations show the large-scale environment of the Arctic to change in response to climate change (warming of hr atmosphere), and consequently may change Arctic storm track density in the future.

Figures 5.6 and 5.7). The impact of climate change on the large-scale environment of the Arctic that has been described in this Section are summarised in Figure 5.13. Ultimately, these simulations show that Arctic storm track density decreases over the Arctic Ocean in winter, and in summer, increase around Greenland but decreases over the Eurasian continent.

5.3.4 Arctic Storm Intensity

Despite large changes in the spatial distribution of Arctic storms in the RCP8.5 future climate HadGEM3-GA3.0 simulations, the maximum 925 hPa wind speeds of storms remains fairly similar between the present-day and RCP8.5 future climate HadGEM3-GA3.0 simulations. The mean maximum 925 hPa wind speed of all Arctic storms in all seasons is within 1.1 ms^{-1} between the present-day and future climate simulations in all seasons in the N512 simulations (see Figure 5.14). But, in winter, spring and autumn, the MSLP minima of Arctic storms is between 4.5 - 3.5 hPa lower in the RCP8.5 future climate simulations compared to the present-day climate simulations (see Figure 5.14). This is also shown in the N96 and N216 HadGEM3-GA3.0 simulations (see Figures F.10 and F.11 in Appendix F).

If two storms had the same size, then the storm with the lower MSLP minimum would typically have tighter pressure gradients and greater maximum wind speeds. Though, this is shown to

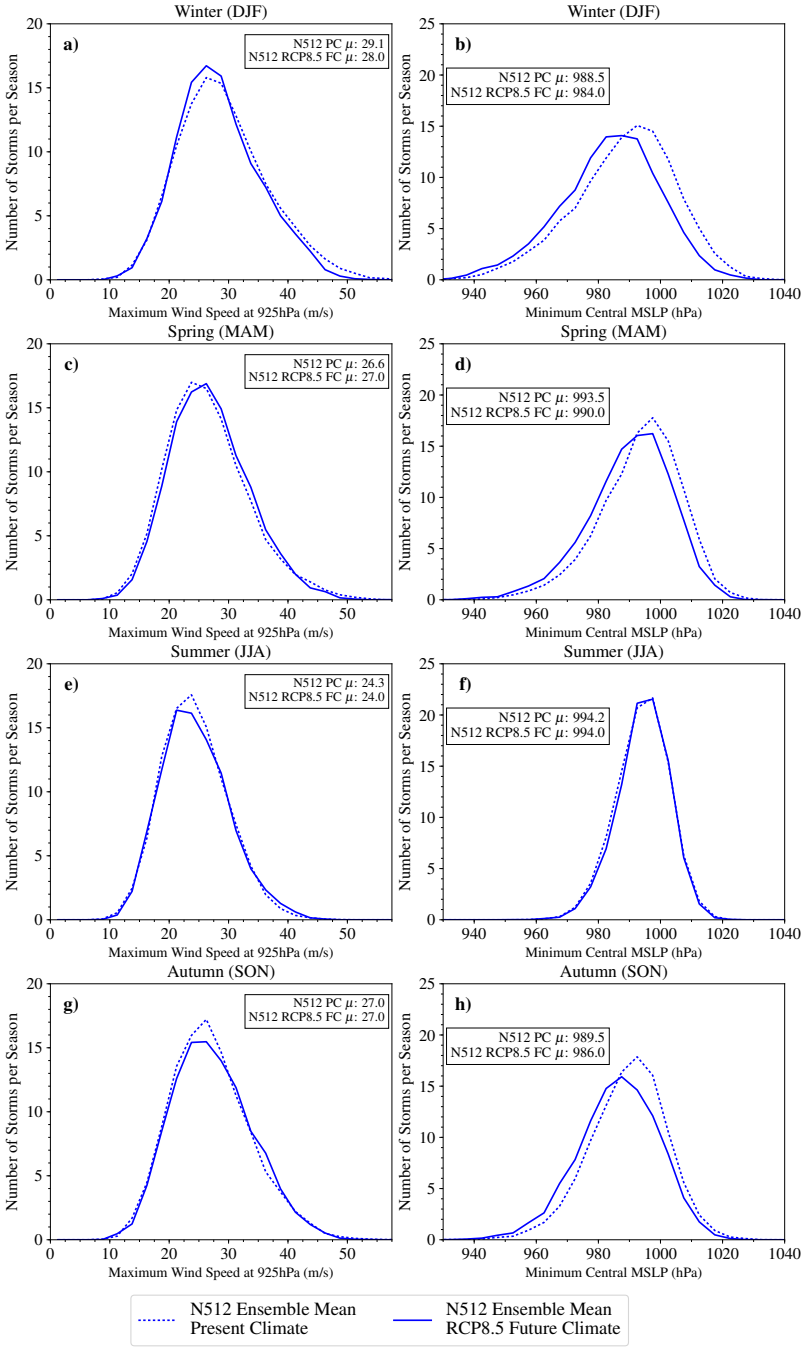

Figure 5.14: Arctic storm intensity in the present-day climate (1986-2010) and RCP8.5 future Climate (2086-2110) N512 HadGEM3-GA3.0 simulations, per season. **a), c), e) and g)** show the maximum 925hPa (near-surface) wind speeds (ms^{-1}) and **b), d), f) and h)** minimum mean sea level pressure (MSLP) (hPa) of Arctic storms when they are north of 65°N. **a) and b)** Winter (DJF), **c) and d)** spring (MAM), **e) and f)** summer (JJA) and **g) and h)** autumn (SON).

not be the case between the present and future HadGEM3-GA3.0 simulations (see Figure 5.14). Instead, the mean MSLP minimum of Arctic storms is lower in the future winter, spring and autumn climate, but that does not lead to an increase in the mean maximum 925 hPa wind speed of Arctic storms (see Figure 5.14). This suggests that Arctic storms in winter, spring and autumn may have a larger size in the future simulations than in the present simulations.

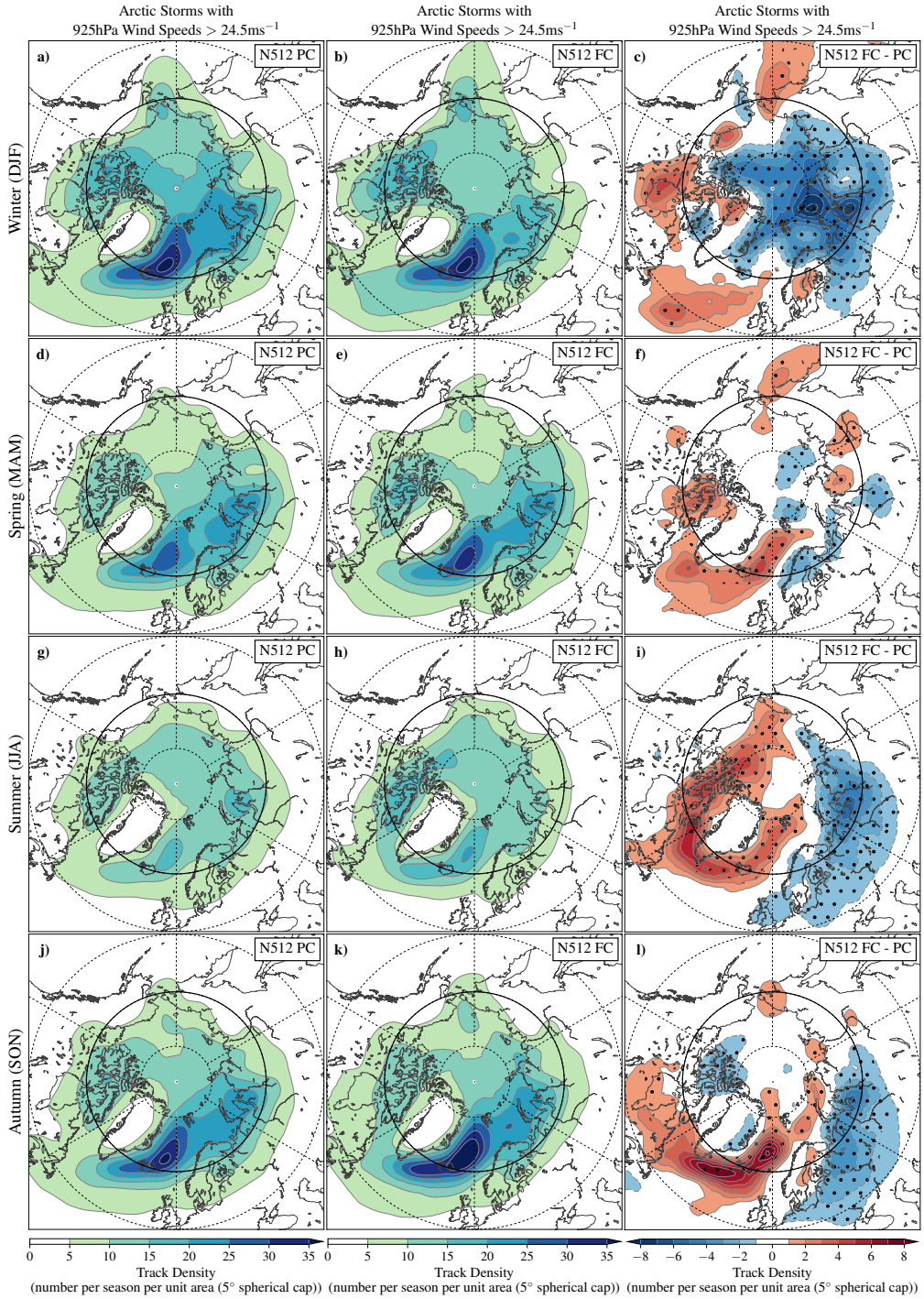

Figure 5.15: Arctic storm track density in the **a), d), g) and j)** present-day (1986-2010) and **b), e), h) and k)** RCP8.5 future climate (2086-2110) N512 HadGEM3-GA3.0 simulations per season, of storms with 925 hPa wind speeds >24.5 ms^{-1} (Beaufort 10 Scale). **a) - c)** Winter (DJF), **d) - f)** spring (MAM), **g) - i)** summer (JJA) and **j) - l)** autumn (SON). **c), f), i) and l)** show the difference between the future and present-day simulations (future minus present-day). Longitude and latitude bands, stippling and units are the same as Figure 5.2.

Figures 5.6 and 5.7 showed that the spatial distribution of Arctic storms will change significantly in the HadGEM3-GA3.0 RCP8.5 future climate simulations. The greatest risk to human activity will come from the more intense Arctic storms, as hazardous conditions caused

by these storms will be more severe. Figure 5.15 shows how the spatial distribution of intense Arctic storms (storms with 925 hPa wind speeds greater than 24.5 ms^{-1} - approximately equivalent to Beaufort Scale 10 (Simpson, 1906; Met Office, 2010)), will change in the RCP8.5 future climate HadGEM3-GA3.0 N512 simulations.

The changes in the spatial distribution of all Arctic storms translates into changes in the spatial distribution of intense Arctic storms (see Figure 5.15). In winter, the track density of intense Arctic storms is lower over the Arctic Ocean in the N512 future climate simulations (see Figure 5.15c). In particular, there is a lower density of storms over the Eurasian coastline, where the main shipping route of the Northern Sea Route presently is. In spring, summer and autumn, the track density of intense Arctic storms in the future climate simulations is higher around Greenland than in the present-day climate simulations (see Figures 5.15f, 5.15i and 5.15l). In summer, simulations also show an increase in the density of intense Arctic storms over the Canadian Archipelago, where the main shipping route of the North West Passage presently is (see Figure 5.15i). This shows that in a future climate, the areas of greatest risk to intense Arctic storms will likely change in response to climate change.

5.4 Summary and Conclusions

The response of Arctic storms to climate change has been assessed using RCP8.5 future climate simulations made using the atmosphere-only HadGEM3-GA3.0 model at different horizontal resolutions of N96, N216 and N512. These were created as part of the UPSCALE project (Mizielinski et al., 2014). These simulations provided the opportunity to assess how horizontal resolution impacts the response of Arctic storms to climate change.

- The number and spatial distribution of Arctic storms in the high resolution (N512) configuration of HadGEM3-GA3.0 agree better with observations (reanalysis datasets) than the low resolution (N96) configuration.

Overall, the HadGEM3-GA3.0 model captures the present-day climate characteristics of Arctic storms well, when compared to reanalysis datasets. But, storm statistics of storm number and track density from the present-day climate simulations from HadGEM3-GA3.0 are most similar

to these reanalysis datasets at a horizontal resolution of N512. The HadGEM3-GA3.0 model at a N512 horizontal resolution simulates more Arctic storms where the track density of Arctic storms is highest than at a horizontal resolution of N96. The resolution of the model was also shown to affect the intensity of Arctic storms. Arctic storms are shown to be more intense (lower mean MSLP minima and higher 925 hPa wind speed maxima) at the higher horizontal resolution in all seasons.

- In the HadGEM3-GA3.0 RCP8.5 future climate simulations (2086-2110), it was found that Arctic storm track density decreases over the Arctic Ocean in winter (DJF), and in summer (JJA), increases around Greenland but decreases over the Eurasian continent.

In the HadGEM3-GA3.0 RCP8.5 future climate (2086-2110) simulations, there are statistically significant changes in the spatial distribution of Arctic storms in both winter and summer. Results from this study also show that the spatial distribution of intense Arctic storms will also change in response to climate change. In winter, there is a reduction in the number of Arctic storms with Arctic genesis, and the track density of Arctic storms reduces over the Arctic Ocean by as much as 10 storms per season per unit area ($\approx 10^6$ km^2). This is approximately half of the present-day climate Arctic storm track density per season over the Arctic Ocean. In summer, the track density of Arctic storms increases in the Canadian Archipelago, the northern North Atlantic Ocean, and the Greenland, Norwegian and Barents Seas by more than 10 storms per season per unit area, approximately double the present-day Arctic storm track density in these regions. In summer there is also a reduction in Arctic storm track density over the Eurasian continent of up to 6 storms per season per unit area, approximately a third of the present-day Arctic storm track density in this region.

These changes are consistent with previous research (e.g. Orsolini and Sorteberg, 2009; Akperov et al., 2015; Nishii et al., 2015; Crawford and Serreze, 2017; Day et al., 2018). It is shown in this study that the changes in the spatial distribution of Arctic storms are associated with reductions in baroclinicity over the Arctic Ocean in winter, especially over the Greenland, Norwegian and Barents Seas. In summer, the change in spatial distribution of Arctic storms is associated with a northward shift in the Jet Stream over the North Atlantic Ocean. These

general responses to climate change are shown in all of the future climate simulations at all horizontal resolutions.

- The general response of Arctic storms to climate change is similar between the HadGEM3-GA3.0 simulations at horizontal resolutions of N96, N216 and N512.

Overall, the general response of Arctic storms to climate change is similar between the simulations from the HadGEM3-GA3.0 model at horizontal resolutions of N96, N216 and N512. When comparing the present-day and future climate simulations at the same horizontal resolution, the response and the magnitude of the response of Arctic storms to climate change is very similar between all simulations, adding confidence to the response presented above. But horizontal resolution can affect storm intensity, with higher horizontal resolutions representing storms with higher intensities. Moreover, more storms are generally simulated by HadGEM3-GA3.0 at a higher horizontal resolution in both the present-day climate and future climate simulations.

Chapter 6

The Risk of Arctic Storms to Shipping

This work was developed whilst on a secondment with the CASE sponsor of this PhD project, AXA XL, which took place between August and November 2019. The aim of this chapter was partly motivated by the interests of AXA XL, but it gives a key insight into the exposure of human activity to Arctic storms and helps to assess the risk to Arctic storms. This chapter aims to further understand the current level of human activity in the Arctic and the exposure to Arctic storms, focusing on shipping. This addresses the fourth and final research question of this thesis, which is:

RQ3: How can we best use information on Arctic storms and shipping to assess storm risk in the Arctic?

6.1 Introduction

Arctic sea ice has reduced substantially in the last few decades in response to anthropogenic climate change (see Figure 1 in Chapter 1). In September 1980, Arctic sea ice extent was 7.7 million km^2 over the Arctic Ocean, whereas in September 2012, sea ice extent reduced by over half and was 3.6 million km^2 (National Snow & Ice Data Centre, 2020b). This has increased the amount of open ocean in the Arctic, and has allowed for the movement of ships and access to the ocean floor. This has encouraged human activity (e.g. shipping, oil exploration and tourism) in the Arctic. Reduced sea ice cover over the Arctic Ocean offers shorter transits between major continents (see Table 1.1 in Chapter 1), access to previous inaccessible natural resources (Harsem et al., 2015), and new destinations for tourism (National Geographic, 2016).

But, the Arctic is a challenging environment for human activity. Cold temperatures can cause equipment failures (Larsen et al., 2016). Sea ice can damage ships, and also confine them to travel over shallow coastlines on the boundaries of the Arctic Ocean (see Figure 1.5). Additionally, there is a lack of critical infrastructure (e.g. ports, search and rescue services) to aid ships (The Polar Connection, 2019). Conditions can be made even more dangerous by the passage of a storm, which can cause rough sea conditions from high winds and high ocean waves (Thomson and Rogers, 2014; Liu et al., 2016; Waseda et al., 2018).

The risk that storms pose to human activity in the Arctic is dependent on the number and severity of storms, but also on the exposure of human activity to these hazards. One problem with quantifying this exposure is that data of historical ship transit tracks in the Arctic are privatised and not publicly available. Thus, there have been very few publicly available studies that describe shipping activity in the Arctic (e.g. Corbett et al., 2010; Eguiluz et al., 2016). These studies show that there is typically a high density of ships in the Barents Sea year-round, and that trans-arctic shipping along the Northern Sea Route (along the coastline of Eurasia and connects Europe and Asia) and the North-West Passage (through the Canadian Archipelago and connects North America and Asia) is currently limited to months where sea ice extent is near its minimum extent, typically in September. Due to the lack of freely available data, the exposure of ships to hazardous Arctic storms is unclear and has not yet been quantified.

This Chapter aims to describe Arctic shipping activity in recent years and to quantify the number of ship transits intersected by the past Arctic storms using publicly available shipping data. Such shipping data is available from the Norwegian Coastal Administration Sea Base (Kystverket Havbase), hereafter Havbase (Norwegian Coastal Administration, 2021), which can be used to simulate past ship transits in the Arctic. These simulated ship tracks are combined with historic storm tracks, to quantify the number of ships intersected by past intense Arctic storms. This will be achieved by the following objectives:

- Assess trends and the spatial distribution in the number of ships travelling through the Arctic from the Havbase database,
- Determine the number and spatial distribution of intense Arctic storms that cause rough sea conditions since 1979 identified in the ERA5 reanalysis dataset,
- Estimate the risk that storms pose to Arctic shipping through developing a method to simulate ship transits from the Havbase database, and use it to quantify the number of ship transits intercepted by past intense Arctic storms.

6.2 Arctic Shipping Activity from 2012

Ship transits are reported by Automated Identification Systems (AIS) that are installed on ships to transmit their location in real time, to improve their safety (International Maritime Organization, 2019). But historical ship tracks are not open source. Sources of historical ship tracks include Marine Traffic (2021) and Vessel Finder (2021) and are only obtained at a substantial price.

The Havbase database is a freely available tool and offers the opportunity to analyse Arctic shipping activity since 2012 (see Section 2.3 in Chapter 2). The database contains the number of ships that pass through gates that separate regions across the Arctic Ocean per month (see Figures 2.3, 2.4 and 2.5 in Chapter 2). The direction to which the ship passed through this gate and the type of ship are also given (see Figure 2.4 in Chapter 2). The number of ships

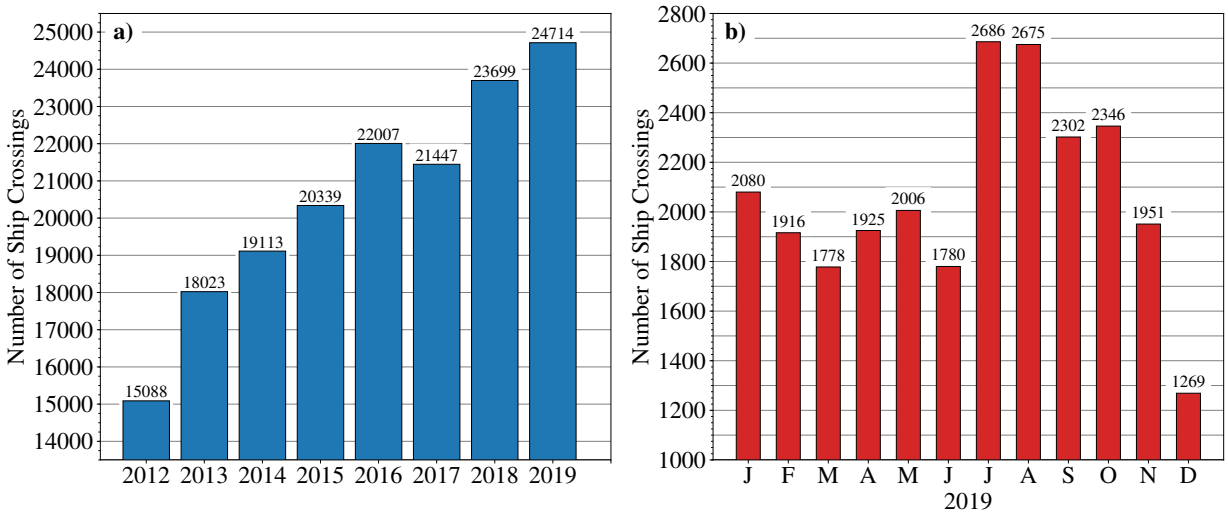

Figure 6.1: The number of gate crossings by ships across all Havbase gates in the Arctic **a)** per year between 2012 - 2019 and **b)** per month in 2019.

passing through these gates has been analysed to determine the number of gate crossings by ships around the Arctic between 2012 and 2019. Although the exact ship track is not given, the Havbase database can be used to gain insight into Arctic shipping since 2012.

6.2.1 Number of Gate Crossings by Ships

Since 2012, the number of gate crossings by ships in the Arctic has increased (see Figure 6.1a). The number of gate crossings by ships has increased from 15,088 in 2012 to 24,714 in 2019, an increase of 64%. There has been a fairly constant increase since 2013, with an initial sharp increase in the number of gate crossings by ships between 2012 and 2013 (see Figure 6.1a). This is likely because it became mandatory for all ships with a size greater than 18 metres to have AIS devices fitted in May 2013 (International Maritime Organization, 2019), thus increasing the number of ships reporting their position. Despite the record minimum sea ice extent occurring in 2012 (see Figure 1.6 in Chapter 1), the number of gate crossings by ships in the Arctic has generally increased per year since 2012, suggesting that more ships are using Arctic routes each year.

Arctic shipping activity is seasonally dependent, with the highest number of gate crossings by ships occurring in months near the minimum sea ice extent that typically occurs in September (see Figure 6.1b). In 2019, 2,686 gate crossings by ships occurred in July, whereas, only 1,269

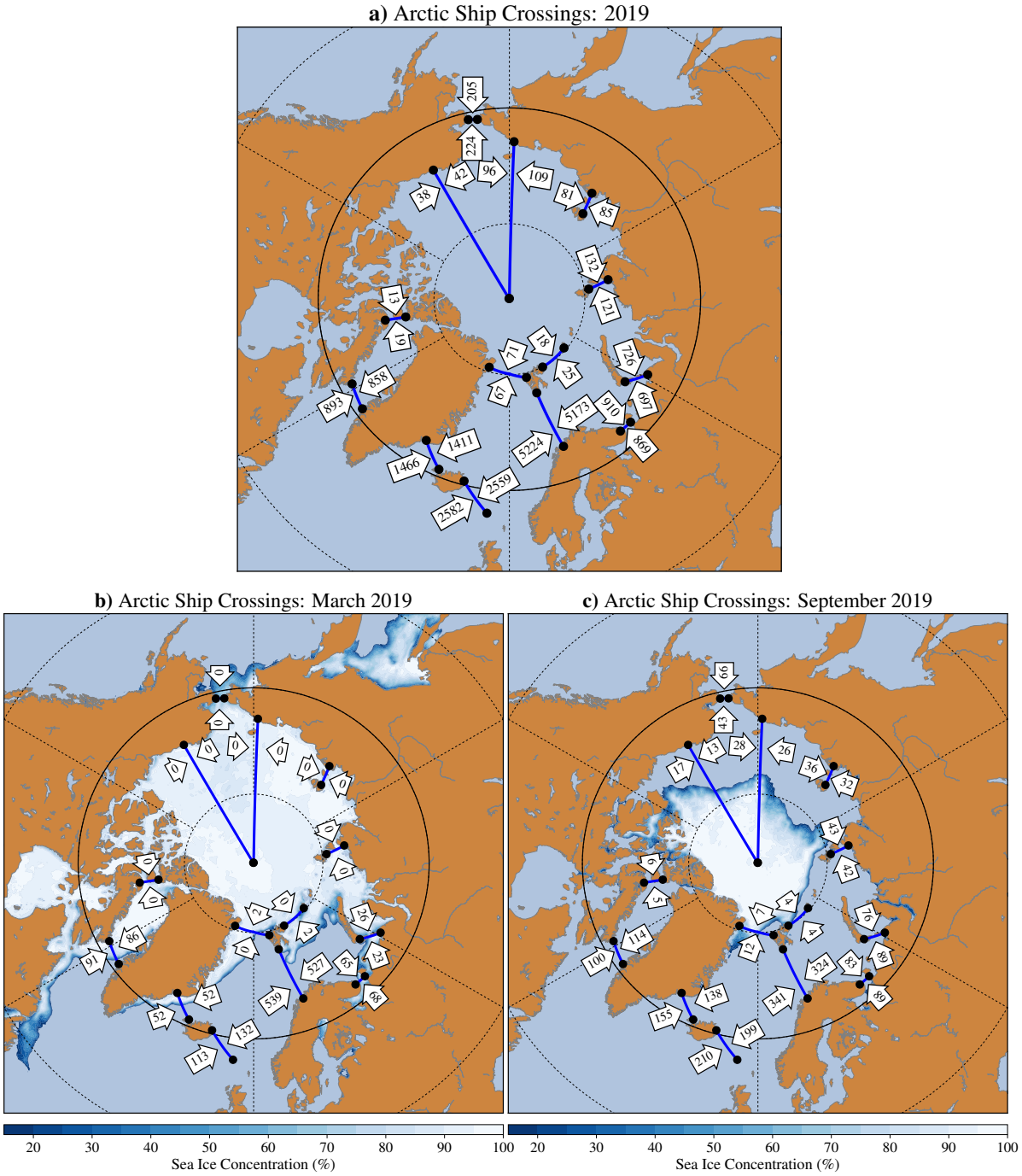

Figure 6.2: The number of gate crossings by ships through each gate from Havbase. The arrows indicate the direction to which a ship passed through the gate, with the blue and black dots indicating each Havbase gate. **a)** During 2019, **b)** during March 2019 and **b)** during September 2019. Sea ice extent is shown at a horizontal resolution of 12.5 km^2 from the National Snow and Ice Data Centre (National Snow & Ice Data Centre, 2021b).

gate crossings by ships occurred in December (see Figure 6.1b). Figure G.1 in Appendix G shows that the highest number of gate crossings by ships per month has typically occurred around the time of the minimum sea ice extent in September between other years from 2012 and 2018, with the lowest number of gate crossings by ships typically occurring around the time

of the maximum sea ice extent in March. Figure 6.1b shows that there is shipping in the Arctic year-round, and that ships are at risk to Arctic storms in all seasons.

The highest number of gate crossings by ships in 2019 occurred in the Greenland and Barents Seas, with a high number of gate crossings by ships also occurring around Iceland (see Figure 6.2a). In total, 5,224 and 5,173 gate crossings by ships were recorded over the gate in the Barents Sea, suggesting that many ships travel between Europe and the Barents Sea, and vice-versa (see Figure 6.2a). Other regions that had over 800 gate crossings by ships in 2019 include Baffin Bay (east of Greenland), around Iceland, the White Sea Inlet (south of the Barents Sea), and the Kara Sea (see Figure 6.2a). A similar spatial pattern in the number of gate crossings by ships is seen in all years between 2012 and 2019, with the highest number of gate crossings occurring over the Barents Sea, with high numbers of gate crossings also occurring in Baffin Bay, around Iceland, White Sea Inlet and the Kara Sea (see Figure G.2 in Appendix G).

The number of gate crossings by ships over the main trans-Arctic shipping routes of the Northern Sea Route (along the coastline of Eurasia) and the North-West Passage (through the Canadian Archipelago) is confined to when sea ice extent recedes from the major continents (see Figure 6.2b and 6.2c). In March 2019, the number of gate crossings by ships into and out of the Canadian Archipelago, as well as into and out of the Bering Strait, Siberian Sea and Laptev Sea was 0 (see Figure 6.2c). In 2019, gates along the Northern Sea Route had a higher number of gate crossings by ships than gates along the North-West Passage, with 123 and 121 gate crossings by ships occurring between the Laptev and Kara Seas, but 13 and 19 gate crossings by ships occurring between the Canadian Archipelago and Baffin Bay (see Figure 6.2a). Overall, the number of gate crossings by ships over these trans-Arctic routes is much less than that over the Barents Sea.

6.2.2 Ship Type

The number of gate crossings by ships is categorised by ship type in the Havbase database. The type of ship can affect the financial loss, if a disaster were to occur. For example, a large

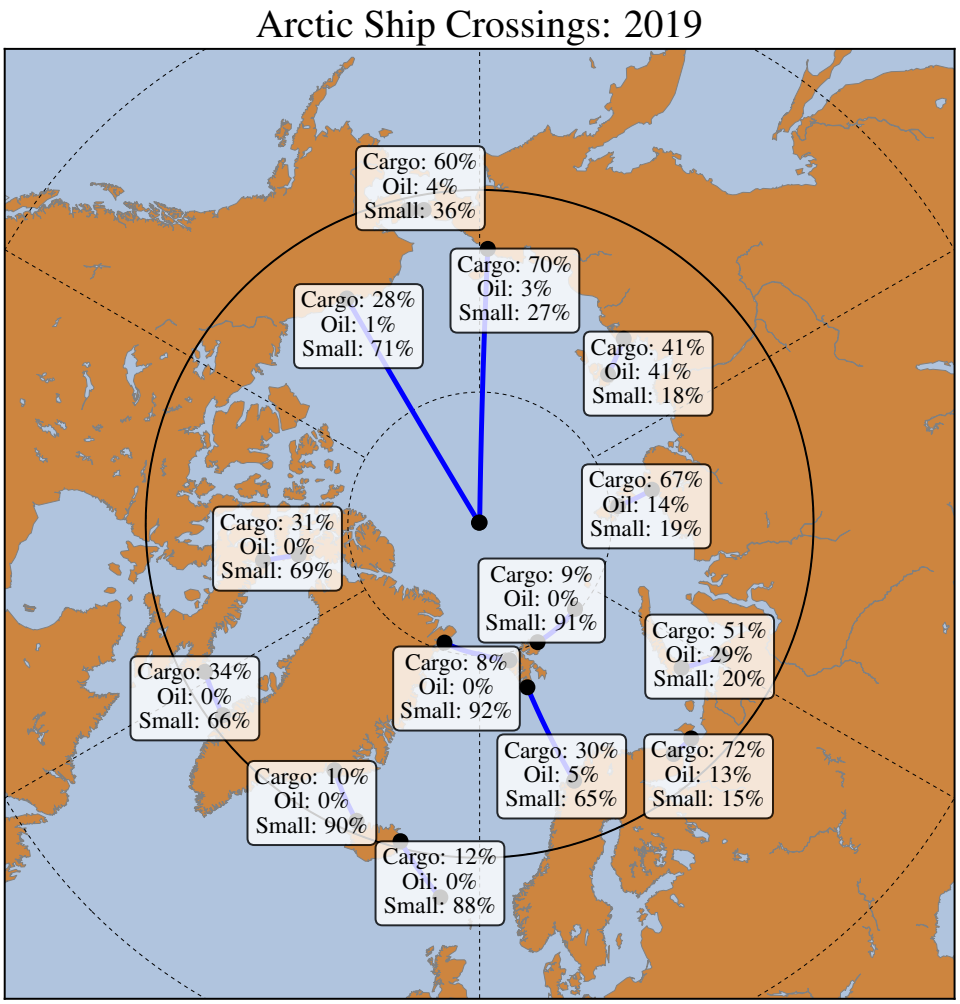

Figure 6.3: The percentage of gate crossings by ships categorised by ship type in 2019. A list of ships that are included in each of the "cargo", "oil" and "small" ship categories is given in Table G.1 in Appendix G.

container ship may perhaps have greater financial value than a smaller fishing ship, as a container ship is larger and if damaged, may incur additional costs such as the recovery of goods. Moreover, the type of goods carried by a ship also can impact financial loss. Damage to a crude oil tanker may lead to an oil spill; incurring costs for ship recovery and the clean-up of a potential oil spill. For example, the cost of the Exxon Valdez oil spill that occurred in 1989 is estimated to exceed $7 billion, largely due to the extent of the oil spill (Lyon and Weiss, 2010). A full list of the ship types from the Havbase database is given in Table G.1 in Appendix G, with the percentage of gate crossings by ships at each Havbase gate broken down into three collective ship types (small, cargo and oil) in Figure 6.3.

Overall, small ships account for the largest percentage of gate crossings by ships in the Arctic - 67.3% in 2019 (see Table G.1 in Appendix G). These small ships are typically confined to Baffin

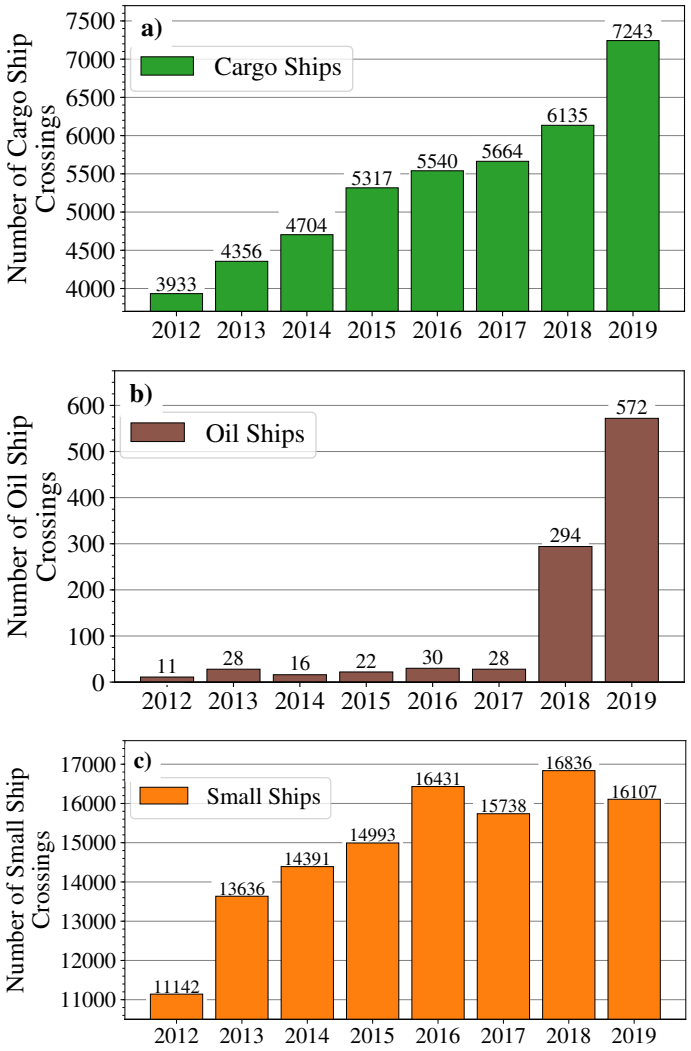

Figure 6.4: The number of gate crossings by **a)** cargo ships and **b)** oil ships and **c)** small ships through all of the Havbase gates between 2012 and 2019. A description of all of the ship types included in each category is given in Table G.1 in Appendix G.

Bay, around Iceland, in the Barents Sea and the Canadian Archipelago (see Figure 6.3). Around Iceland and Svalbard in 2019, small ships account for between 88-92% of all gate crossings by ships. Over Baffin Bay and into the Canadian Archipelago, small ships account for 66% and 69% of all gate crossings by ships. Along the Northern Sea Route (along the coastline of Eurasia), cargo ships are the predominant ship type, with 67% of all gate crossings by cargo ships through the Sannikov and Dmitry Laptev Straits, which join the Kara and Laptev Seas (see Figure 6.3). The number of gate crossings by ships that carry oil and oil products (oil ships) typically occur at gates along the Eurasian Coastline. These types of ship only accounted for 2.4% of all gate crossings by ships in 2019.

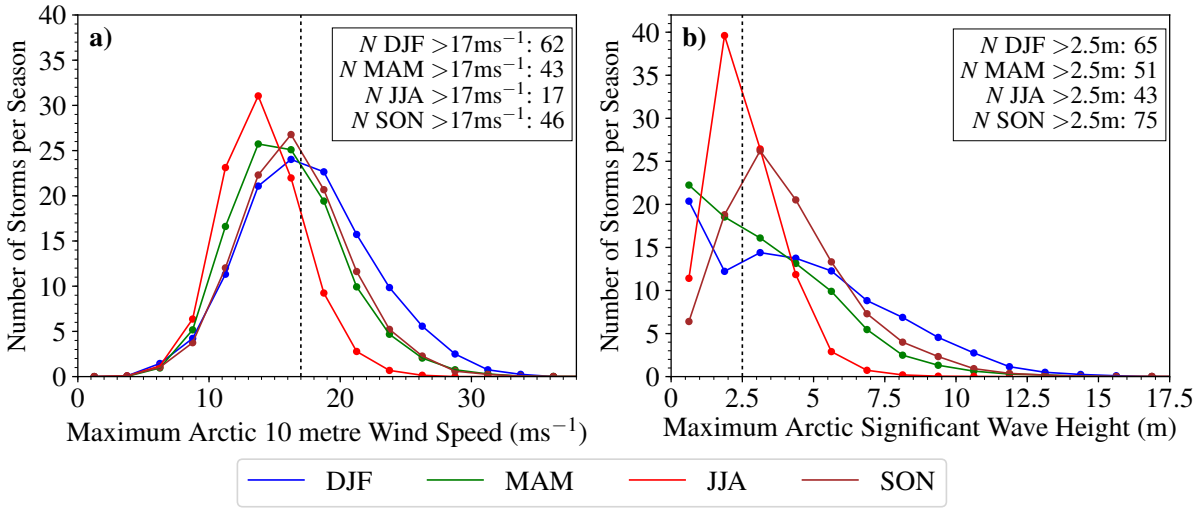

Figure 6.5: Maximum **a)** 10 metre wind speed and **b)** significant wave height distributions of Arctic storms when they are in the Arctic. Based on the ERA5 reanalysis dataset between 1980-2020 in spring (MAM), summer (JJA) and autumn (SON), and 1979/80-2019/20 in winter (DJF). Bin widths are 2.5 ms^{-1} for 10 metre wind speed and 1.25 metre (m) for significant wave height. The number (N) of storms with maximum 10 metre wind speeds greater than 17 ms^{-1} (dashed line) and significant wave heights greater than 2.5 m (dashed line) is shown for each season.

The total number of gate crossings in the Arctic by cargo and oil ships is increasing. The number of gate crossings by cargo ships has increased steadily from 3,933 in 2012 to 7,243 in 2019 (see Figure 6.4). There were only a small number of gate crossings by oil ships between 2012 and 2017 (< 30), but this sharply increased from 2017 to 2019, from 28 to 572 gate crossings (see Figure 6.4). Since 2016, the number of gate crossings in the Arctic by small ships plateaued at approximately 16,000 (see Figure 6.4). This suggests that in recent years, the increase in the number gate crossings by ships in the Arctic is primarily due to increases in the number of cargo and oil ships operating in the Arctic.

6.3 Frequency of Intense Arctic Storms per Season

The Beaufort Scale and Douglas Sea State Scale can be used to indicate the severity of hazardous conditions over the ocean, indicating when rough sea conditions may occur (Simpson, 1906; Schule, 1966; Met Office, 2010). The thresholds that result in rough sea conditions are marked at 17 ms^{-1} for surface wind speeds and 2.5 m for significant wave heights.

a) Winter (DJF)
Track Density of Storms with Winds $> 17 \mathrm{ms}^{-1}$

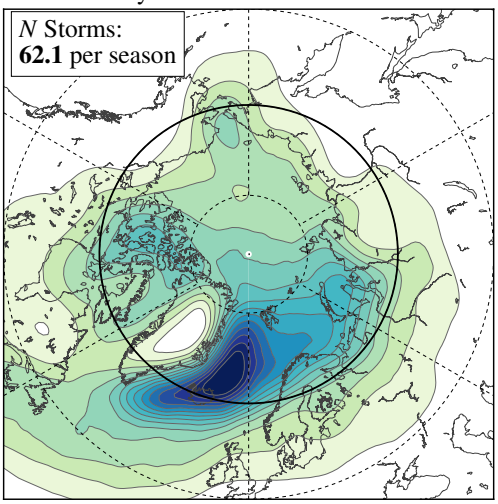

b) Winter (DJF)
Track Density of Storms with Waves > 2.5m

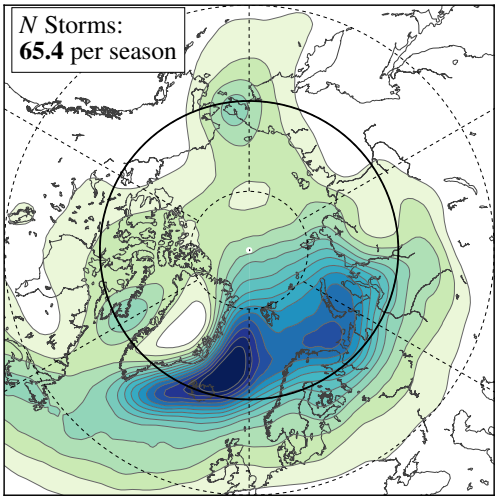

c) Spring (MAM)
Track Density of Storms with Winds $> 17 \mathrm{ms}^{-1}$

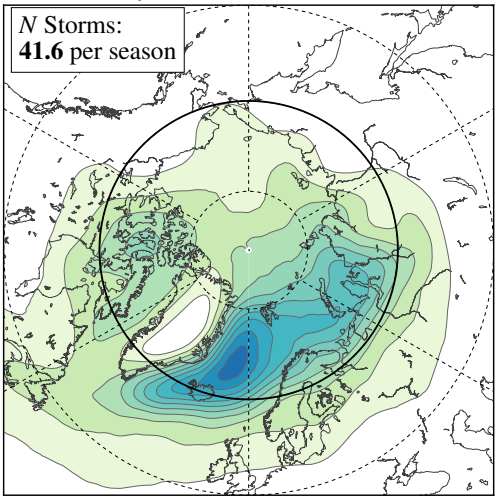

d) Spring (MAM)
Track Density of Storms with Waves > 2.5m

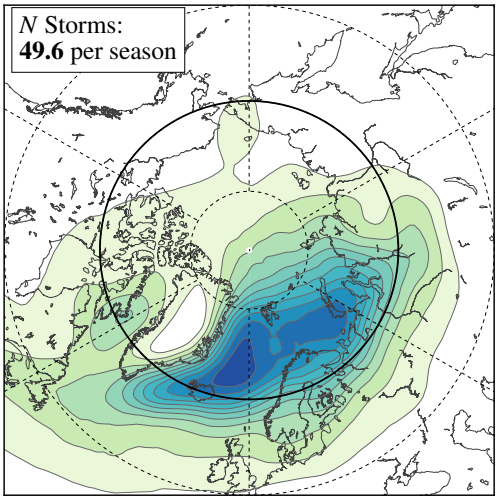

e) Summer (JJA)
Track Density of Storms with Winds $> 17 \mathrm{ms}^{-1}$

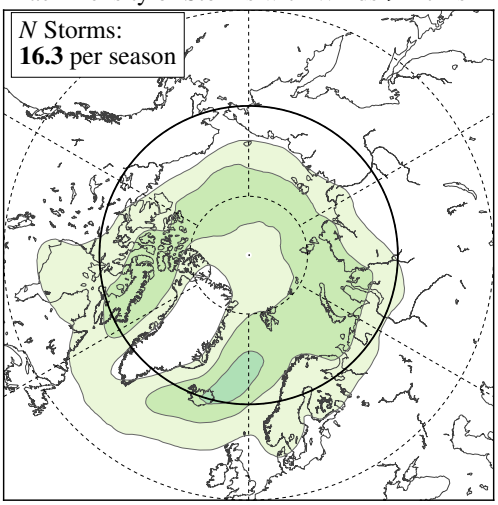

f) Summer (JJA)
Track Density of Storms with Waves > 2.5m

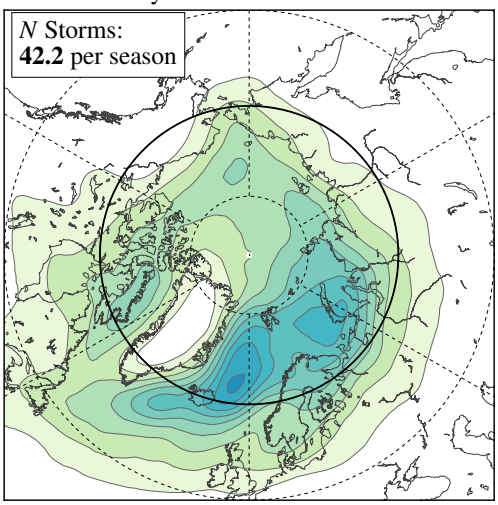

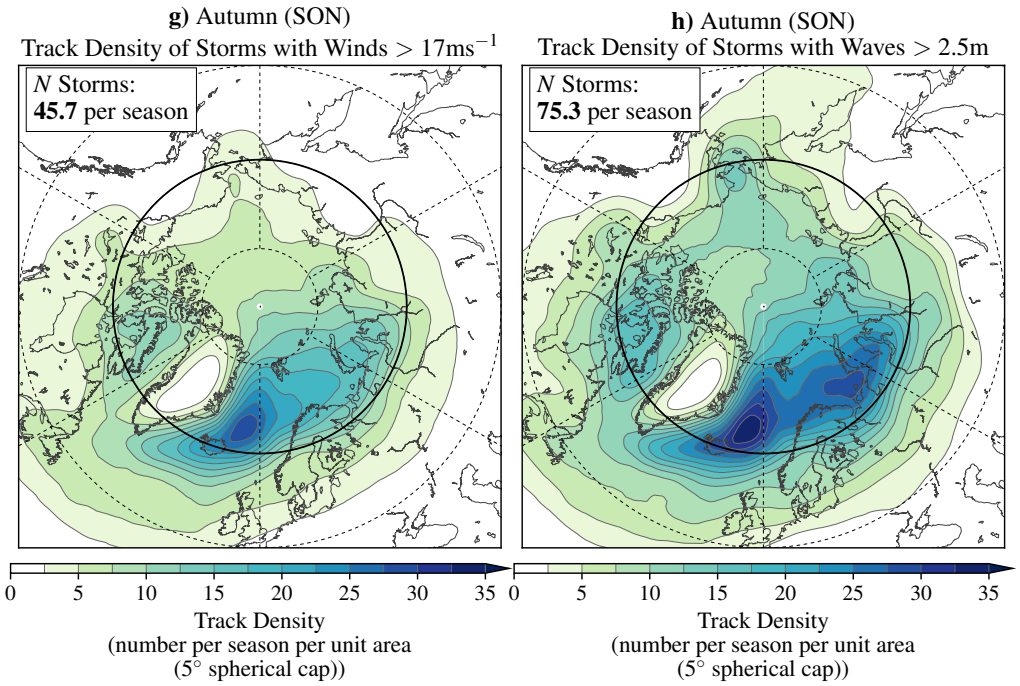

Figure 6.6: Track density of **a) and b)** winter (DJF), **c) and d)** spring (MAM), **e) and f)** summer (JJA) and **g) and h)** autumn (SON) Arctic storms, that have **a), c), e) and g)** maximum 10 m wind speeds in the Arctic greater than 17 ms^{-1}, and, **b), d), f) and h)** significant wave heights in the Arctic greater than 2.5 m. Based on the ERA5 reanalysis dataset between 1980-2020 in spring (MAM), summer (JJA) and autumn (SON), and 1979/80-2019/20 in winter (DJF). Track density indicates the number of storms that travel over a region and has units of number per season per unit area (5° spherical cap, $\approx 10^6$ km^2). Longitudes are shown every 60°E, and latitudes are shown at 80°N, 65°N (bold) and 50°N.

Historical Arctic storm tracks can be identified in the ERA5 reanalysis dataset using an automated storm tracking algorithm such as TRACK (Hodges, 1994, 1995, 1999) (see Section 2.4 in Chapter 2). Moreover, maximum 10 metre wind speeds and significant heights of combined wind waves and swell that occur within the radius of a storm can be determined from the ERA5 reanalysis dataset (see Section 2.4.1 in Chapter 2). This allows for the identification of intense Arctic storms that result in rough sea conditions, which are hazardous to shipping.

Within the radius of an Arctic storm, the ERA-5 reanalysis dataset suggests that 10 m wind speeds can reach 36 ms^{-1}, and significant wave heights can reach 13 m (see Figure 6.5). Generally, winter (DJF) Arctic storms may result in more severe 10 m wind speeds and significant wave heights than summer (JJA) Arctic storms (see Figure 6.5). Up to 65 Arctic storms per season have wind speeds and significant wave heights greater than these thresholds in winter. In summer, only 17 storms per season have 10 m wind speeds greater than 17 ms^{-1}.

Notably, in summer and autumn, the number of storms with significant wave heights above 2.5 m is greater than the number of storms with 10 m wind speeds greater than 17 ms^{-1}. In autumn, there are approximately 75 storms per season with significant wave heights greater than 2.5 m. The greater number of storms with hazardous significant wave heights than the number of Arctic storms with hazardous 10 m wind speeds may be due to there being a greater area of open ocean in summer and autumn, when sea ice extent is low. This may lead to greater fetch, potentially causing taller and more severe waves.

The highest track density of Arctic storms with intense 10 m wind speeds and significant wave heights occur over the Barents Sea and around Iceland (see Figure 6.6), where the density of ships in the Arctic is highest (see Figures 6.2). The spatial distribution of Arctic storms is typically seasonally dependent, with the highest track density per season in winter Arctic storms typically occurring over the Greenland, Norwegian and Barents Seas. Whereas in summer, the highest track density per season of Arctic storms typically occurs over the Eurasian Coastline and the Arctic Ocean (Vessey et al., 2020). Despite this, the spatial distribution of hazardous Arctic storms in all seasons is similar, occurring over the Greenland, Norwegian and Barents Seas (see Figure 6.6). Notably, the track density of Arctic storms with significant wave heights greater than 2.5 m is higher in summer and autumn than the track density of storms with 10 m wind speeds greater than 17 ms^{-1}. The Greenland, Norwegian and Barents Seas is also where the number of gate crossings by ships is highest (see Figure 6.2), showing that the highest density of ships is also where there is the highest track density of Arctic storms.

6.4 Shipping Risks from Arctic Storms

6.4.1 Arctic Storm and Ship Model Design

The number of gate crossings by ships from the Havbase database can be used to simulate ship transits between two gates. Ships are assumed to travel along a pre-determined ship route between two gates at a constant speed of 15 knots (see Figure 6.7). The total number of ships to travel along these pre-determined ship routes per month is given by the Havbase database.

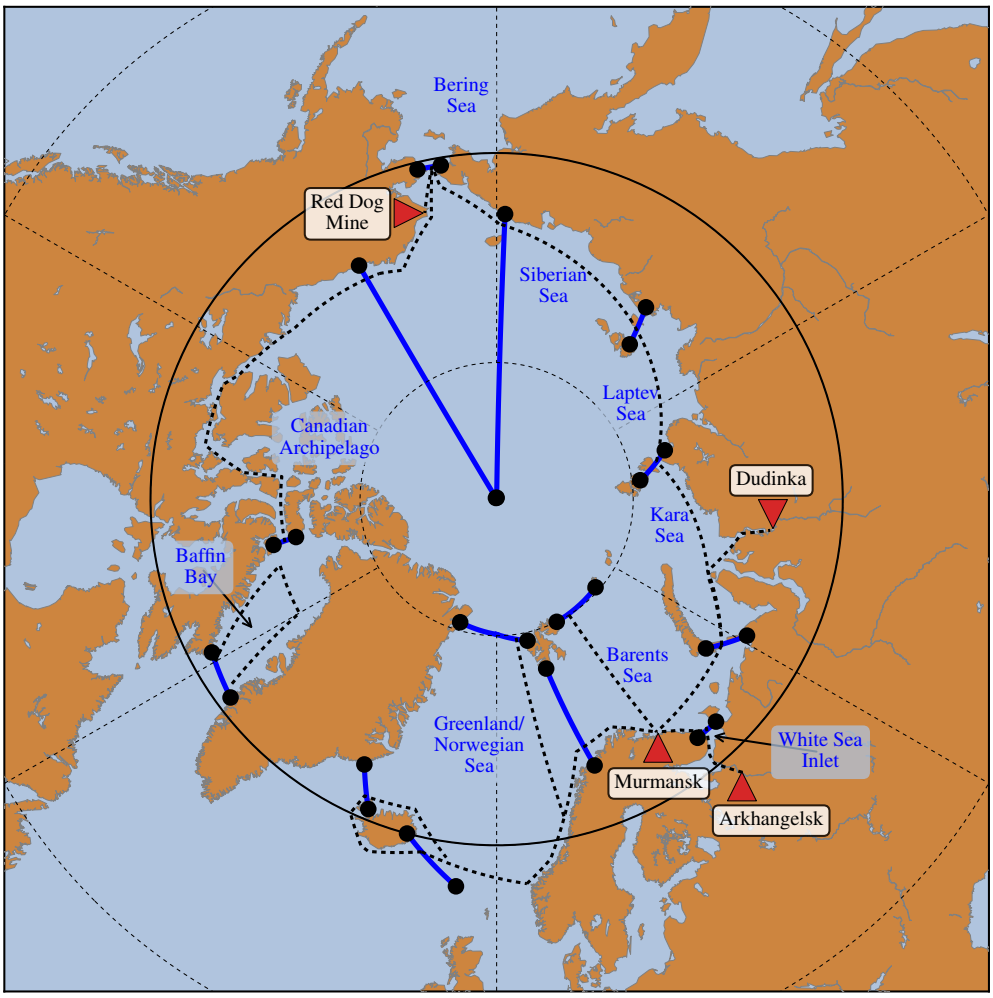

Figure 6.7: The pre-determined ship routes in the Arctic ship and storm model. The dotted black lines indicate the pre-determined ship route, blue lines indicate the Havbase gate that is used to give the number of ships travelling along each ship route per month. Also shown are the major Arctic shipping Ports of Murmansk, Arkhangelsk, Dubinka and Red Dog Mine (red triangles).

The pre-determined ship routes that the simulated ships travel upon are shown in Figure 6.7. If the number of ship crossings at a gate is not equalled by the number of ships crossings at the next gate, an additional shipping route is added to the major port within that area. The Havbase database contains the number of port calls for ports in the Arctic, which is used here to determined the busiest port in an area.

In 2019, the number of ships entering the Kara Sea from the Barents Sea was 697, but the number of ships leaving the Kara Sea into the Laptev Sea was only 121 (see Figure 6.2a). Therefore, ships likely travel to a destination within the Kara Sea. This is assumed to be the Port of Dubinka, which is the busiest port in the Kara Sea. The number of ships using this

ship route to the Port of Dubinka is determined by the difference between the number of ships entering and leaving the Kara Sea from the Barents and Laptev Seas (e.g. from Figure 6.2a: 697 - 121 = 576). The Port of Murmansk is the busiest Port in the Arctic. Therefore, ships travelling along the coastline of Scandinavia from Europe are assumed to travel beyond the Havbase gate over the Barents Sea, to the Port of Murmansk (see Figure 6.3). Ships travelling from Svalbard, the Kara Sea, and White Sea Inlet, are also assumed to travel to the Port of Murmansk.

The start time of each simulated ship transit from each gate is not given by the Havbase database and has been randomly generated for each ship in each month. This is iterated 1,000 times, so that the actual time that a ship made its transit from each gate is likely to be included. Each simulated ship travels along the ship route between gates at 6-hour intervals from its randomly determined start time, and it can be determined if each ship transit is intersected by an Arctic storm that causes rough sea conditions.

High-latitude storms typically have a diameter of approximately 1,000km, but the area of the most hazardous wind speeds at the surface is typically smaller (Catto et al., 2010; Martínez-Alvarado et al., 2014). In Chapter 4, it was shown that the most intense 850 hPa (near-surface) wind speeds in Arctic storms in all seasons occur over an area with radius of approximately 4° (1° $\approx$ 100 km) within the storm, typically south of the storm centre (see Figure 4.5). Similarly, Thomson and Rogers (2014) showed that ocean wave heights greater than 2.5 m caused by a storm can occur over an area with a radius of approximately 5°. Therefore, an intersection between a simulation ship transit and an Arctic storm occurs if the simulated ship is within 4° radius of the wind and wave footprint of the storm (the track of highest wind speeds and significant wave heights per time-step), and the 10 m wind speeds are greater than 17 ms^{-1} and significant wave heights are greater than 2.5 m. The sensitivity of the number of ships intersected by past storms to this distance threshold is tested, by setting the threshold to 2° and 6° from the point of highest 10 m wind speed and significant wave height (see Figures G.3 and G.4 in Appendix G).

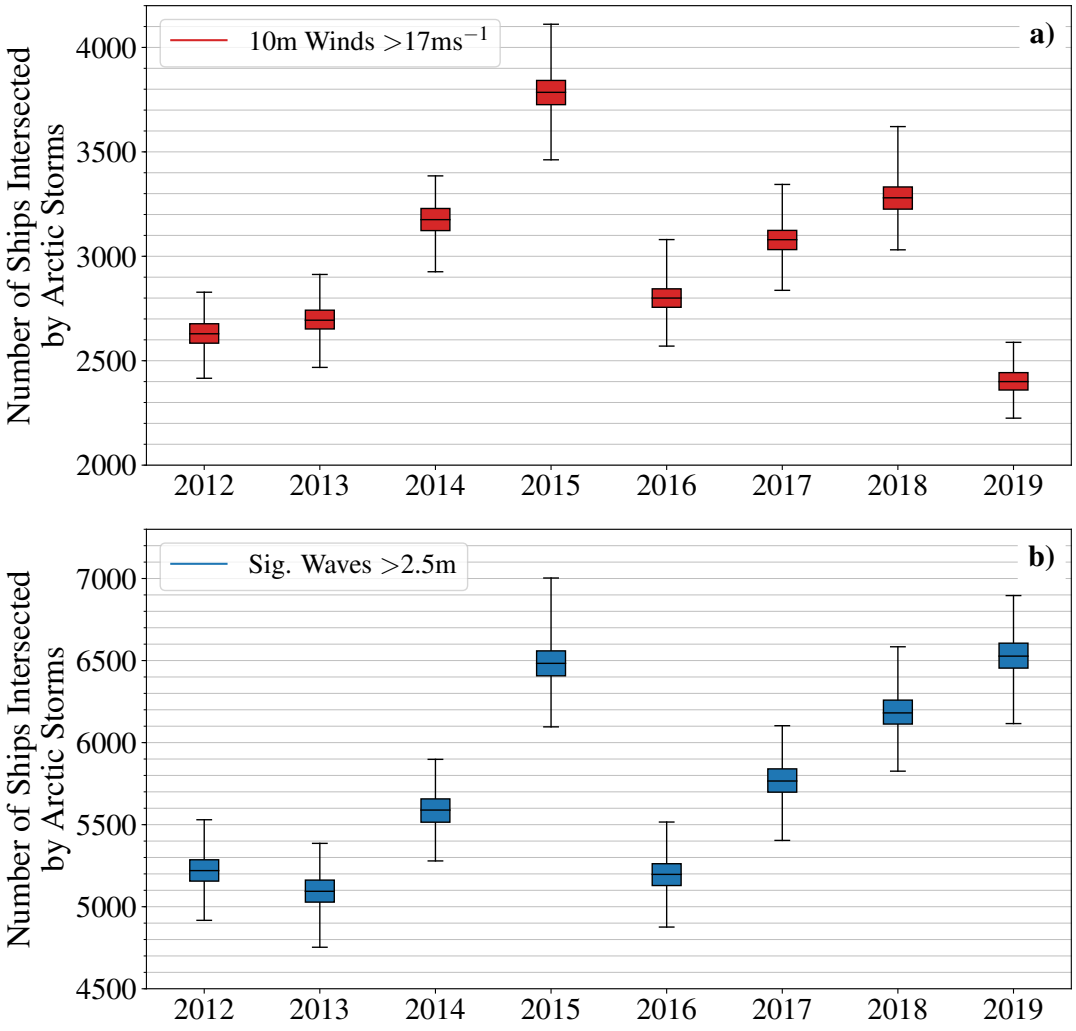

Figure 6.8: The number of simulated ships tracks that are intersected (within 4°) by Arctic storms with **a)** 10 m wind speeds > 17 ms^{-1} (Beaufort Scale 8) and **b)** significant wave heights > 2.5 m (Douglas Sea State Scale 5), from 2012 to 2019.

6.4.2 Number of Ships Intersected by Past Intense Arctic Storms

It is estimated that up to approximately 4,000 simulated ship transits are intersected by Arctic storms with 10 m wind speeds greater than 17 ms^{-1} per year, and approximately 6,500 ship transits are intersected by Arctic storms with significant wave heights greater than 2.5 m per year (see Figure 6.8). When considering highly intense Arctic storms that cause 10 m wind speeds greater than 24.5 ms^{-1} (> Beaufort Scale 10) and significant wave heights greater than 6 m (> Douglas Sea State Scale 7), up to 3,000 ships are intercepted by highly intense Arctic storms (see Figure G.5 in Appendix G).

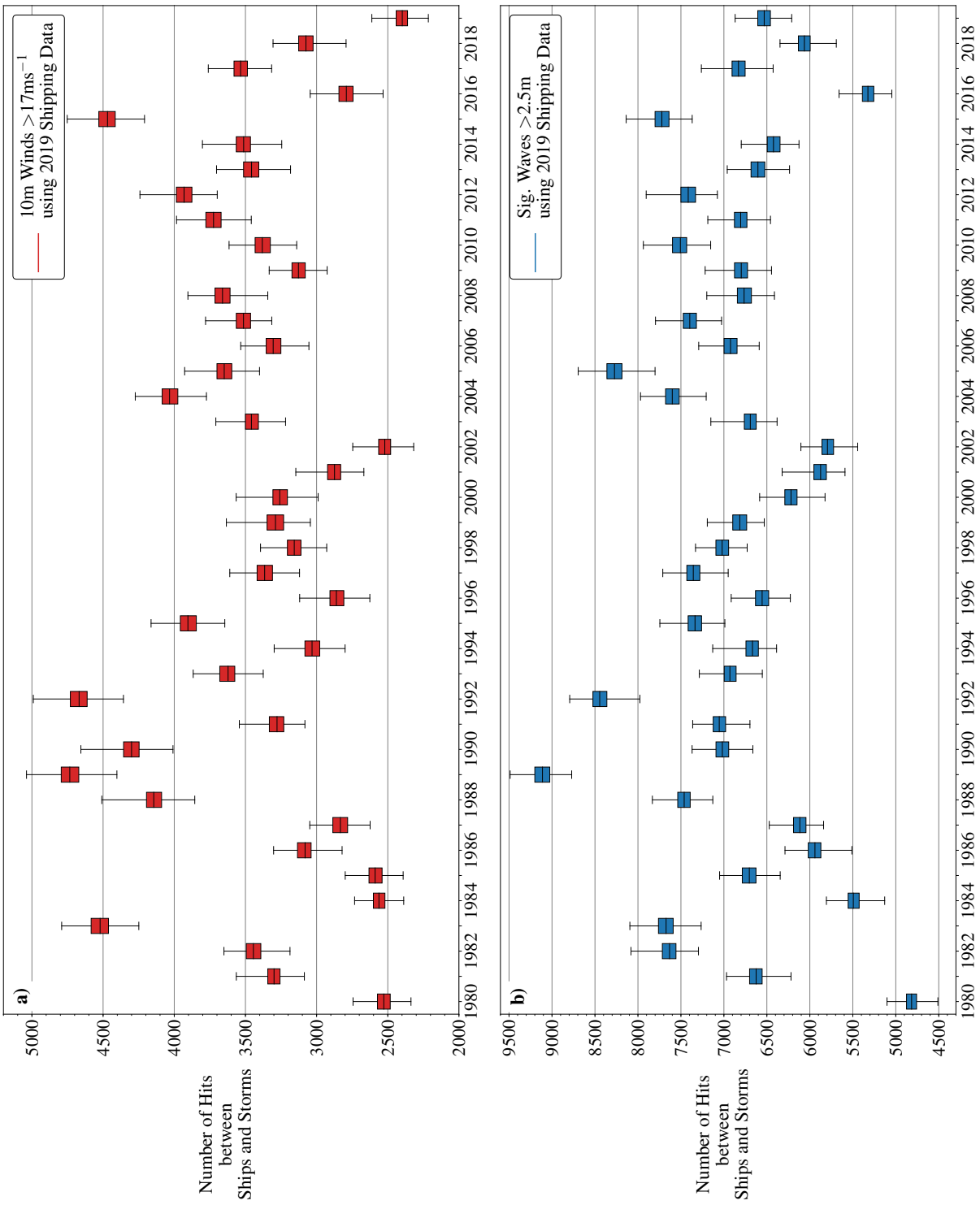

Figure 6.9: The number of simulated ships tracks that are intersected (within 4°) by Arctic storms with **a)** 10 m wind speeds > 17 ms^{-1} (Beaufort Scale 8) and **b)** significant wave heights > 2.5 m (Douglas Sea State Scale 5), using ship data from 2019 but storm track data from each year.

Despite the number of Arctic gate crossings by ships increasing from 15,088 in 2012 to 24,714 in 2019 (see Figure 6.1), the number of simulated ship transits intersected by intense Arctic storms has not increased year-on-year between 2012 and 2019. In 2015, there was greater track density of intense Arctic storms over the Greenland, Norwegian and Barents Seas than in 2019,

where the highest number of gate crossings by ships is (see Figure G.6 in Appendix G). This likely caused a higher number of ship and storm intersections in 2015. This result suggests that the regional inter-annual variability of Arctic storms plays an important role in determining risk the risk of Arctic storms to shipping.

The regional inter-annual variability of Arctic storminess is further investigated, by using the shipping data from 2019 and storm tracks per year between 1980 and 2019. It is shown that the number of ships intersected by storms would be higher if greater track density of Arctic storms that cause rough sea conditions were to occur. Up to 5,000 and 9,500 simulated ship transits could be intersected by Arctic storms with intense 10 m wind speeds and significant wave heights per year respectively (see Figure 6.9). In 1989, up to 5,000 and 9,500 simulated ship transits would have been intersected by Arctic storms with intense winds and waves respectively, higher than that shown in Figure 6.8. In 1989, there was very high track density of intense Arctic storms over the Greenland, Norwegian and Barents Sea, which coincides with where the highest density of ships is (see Figure 6.2 and Figure G.6 in Appendix G).

6.5 Summary and Conclusions

In this Chapter, Arctic shipping data has been analysed from the Norwegian Coastal Administration Sea Base (Havbase) (Norwegian Coastal Administration, 2021), which is a publicly available tool that provides the number ships crossing gates across regions over the Arctic. Havbase has been analysed to gain an insight into the risk that Arctic storms pose to shipping, which is seldom been reported upon previously. Moreover, this Chapter has developed a method to simulate ship tracks using data from Havbase, which have been combined with historical Arctic storm tracks, to quantify the number of ships intersected by past intense Arctic storms. The main findings from this work are summarised below.

- The amount of Arctic shipping activity has increased from 2012 to 2019, with the increase from 2016 being driven by an increase in the number of cargo and oil ships that have a high financial value.

From 2012 to 2019, the number of gate crossings by ships from the Havbase database has increased by approximately 64%, from 15,088 to 24,717. There has been a steady increase in the number of gate crossings by ships from 2012, suggesting that more ships are using the Arctic routes per year. Overall, the highest number of gate crossings by ships occur over the Greenland, Norwegian and Barents Seas, and when Arctic sea ice extent is near its minimum extent in September. Though, results show that there is shipping in the Arctic year-round. Havbase gives the number of gate crossings by ship type, and results show that from 2016 to 2019, the number of crossings by small ships has plateaued, while the number of gate crossings by cargo ships and oil ships has increased from 2016. These larger ships would have greater financial value and would incur a greater loss if a disaster were to occur. Ultimately, results show that the Arctic is being increasingly used for shipping.

- Intense Arctic storms that result in rough sea conditions typically occur over the Greenland, Norwegian and Barents Seas in all seasons, where the highest number of gate crossings by ships in the Arctic is.

In all seasons, the highest density of Arctic storms with intense 10 m wind speeds greater than 17 ms^{-1} and significant wave heights greater than 2.5 m has been found to occur over the Greenland, Norwegian, and Barents Seas, in all seasons. The Beaufort Scale and the Douglas Sea State Scale indicate that these conditions may result in rough sea conditions that are hazardous to shipping. The highest density of Arctic shipping is also found to be highest over the Greenland, Norwegian and Barents Seas. In winter, there are up to 65 Arctic storms per season that have surface wind speeds and significant wave heights greater than 17 ms^{-1} and 2.5 m, which can result in rough sea conditions. In summer, there are fewer Arctic storms per season that surpass these thresholds, with 16 and 42 storms with surface wind speeds and significant wave heights greater than 17 ms^{-1} and 2.5 m per season respectively. The number of storms with intense wave heights is highest in autumn when sea ice extent is lowest.

Wave heights depend on wind speed but also on fetch, which describes the area to which wind travels over the ocean surface. In the future, when sea ice extent has reduced further (Stroeve et al., 2012), Arctic storms may become more severe and may cause even taller wave heights

(Khon et al., 2014; Casas-Prat and Wang, 2020). Thus the number of storms that cause hazardous significant wave heights that cause rough sea conditions will likely increase.

- A simple risk model that combined simulated ship transits and historical storm tracks estimates that up to 9,500 simulated ships transits experience rough sea conditions cause by Arctic storms per year.

By combining simulated ship transits and past Arctic storm tracks between 2012 and 2019, it is shown that on average between 2012 and 2019 approximately 3,000 ship transits are within 4° of Arctic storms with wind speeds greater than 17 ms^{-1} per year. Additionally, it is estimated that up to 7,000 ship transits are within 4° of Arctic storms with significant wave heights greater than 2.5 m per year. Despite the number of simulated ship transits being highest in 2019, the number of ships intersected by intense Arctic storms is highest in 2015. This is due to a higher density of storms travelling over the Greenland, Norwegian and Barents Seas in 2015, where ship density is typically highest. After using ship data from 2019 and historical storm tracks from 1980, it is shown that up to 9,500 ship transits per year could be within 4° of Arctic storms that cause rough sea conditions. Results ultimately show that the regional inter-annual variability of storms plays an important role in determining the risk of Arctic storms to shipping.

There are still obstacles that may discourage the use of the Arctic for shipping. Arctic sea ice extent still restricts shipping, and it is shown by the Havbase database that there are typically no gate crossings by ships in areas covered in sea ice. In particular, the trans-Arctic shipping routes of the North-West Passage and Northern Sea Route are closed throughout most of the year, with no gate crossings being reported over these routes in March 2019, when sea ice extent was at its maximum extent. Moreover, the inter-annual variability in sea ice extent brings uncertainty, as it is unclear when (or if) a ship route may be navigable each year. In the future however, Arctic sea ice will continue to decline (Stroeve et al., 2012), meaning that ship lanes will be open for more days of the year (Melia et al., 2016), which will likely encourage more shipping in the Arctic. Another limitation is the lack of infrastructure in the Arctic that can

aid ships, making it less safe for shipping. But, in recent years, the Arctic is receiving major investment to improve shipping infrastructure and establish sufficient infrastructure to support the expansion of shipping in the Arctic (High North News, 2019; Arctic Today, 2019). There is also some inertia for shipping companies to change their operations from using more traditional mid-latitude shipping routes (e.g. the Suez Canal route between Europe and Asia), to new and unfamiliar Arctic shipping routes. With continuing reductions in sea ice extent and greater investment in the Arctic, it seems that these obstacles will be overcome in the coming decades, further encouraging shipping in the Arctic.

The number of ships intercepted by historical Arctic storms has been quantified using publicly available shipping data. This is of particular importance to AXA XL, who were previously unaware of the number of ships impacted by intense Arctic storms. If the limitations of Arctic shipping are overcome, the Arctic will likely be increasingly used for shipping, which will increase the exposure to Arctic storms further. Moreover, the occurrence and severity of rough sea conditions caused by the passage of a storm may increase as sea ice extent continues to decline. Thus, the potential for loss in the Arctic will likely increase in the future.

Chapter 7

Discussion and Conclusions

7.1 Thesis Overview

Arctic sea ice extent has reduced substantially in recent decades, and is expected to reduce further over the 21st century (Stroeve et al., 2007, 2012). This has encouraged more human activity in the Arctic, as the benefits of a more open Arctic Ocean are exploited. These include shorter transits between major ports in Europe, North America and Asia (Melia et al., 2016; Smith and Stephenson, 2013), access to previously inaccessible natural resources (Harsem et al., 2015), and new destinations for tourism (Maher, 2017).

However, the Arctic is a challenging environment for shipping, oil exploration and tourism. Air temperatures are cold and critical infrastructure is poorly established (e.g. search and rescue services and ports). Moreover, sea ice extent can confine ships to travel over shallow coastlines on the boundaries of the Arctic Ocean, where the depth is <100 metres. Conditions can be made even more perilous by the passage of a storm, which can lead to rough sea conditions (Thomson and Rogers, 2014). These storms can also break up sea ice (Parkinson and Comiso, 2013), which may drift toward shipping lanes. As the Arctic becomes increasingly used for shipping, oil exploration and tourism, the exposure to Arctic storms also increases. However, Arctic storms are not fully understood hazards. There are key research gaps in the understanding of Arctic storms that this thesis aimed to address. These were identified in Chapter 1 (see Section 1.7) and are summarised again below.

There is uncertainty in the present-day statistics of Arctic storms, and it is unclear whether the number of Arctic storms has changed due to recent reductions in Arctic sea ice extent. For example, Arctic storm number has been found to be higher in summer than in winter (Serreze, 1995; Serreze et al., 2001; Tilinina et al., 2014; Zahn et al., 2018), but Simmonds et al. (2008) found the number of Arctic storms in winter to be higher than in summer. Moreover, Sorteberg and Walsh (2008) and Sepp and Jaagus (2011) found that the number of Arctic storms has increased over recent decades, but the studies of Tilinina et al. (2014) and Zahn et al. (2018) found no trends in Arctic storm number across the same period. The reasons for these discrepancies between studies were unclear and may arise from each study using different cyclone detection methods, and/or different reanalysis datasets.

The typical structure and development of Arctic storms is also unclear. Case-studies have been identified of some Arctic summer storms that have a different development and structure to that of mid-latitude storms and existing conceptual models of storm development (e.g. Norwegian Cyclone Model and Shapiro-Keyser Model) (e.g. Tanaka et al., 2012; Aizawa and Tanaka, 2016; Tao et al., 2017). Moreover, additional case-studies have been identified that show that some Arctic summer storms are exceptionally long-lived (Simmonds and Rudeva, 2012; Yamagami et al., 2017). These studies are based on the analysis of a few case-studies, and it is unclear how typical they are to most Arctic storms in each season.

The Arctic will undergo substantial warming over the 21st century (Smith et al., 2019). Previous studies have shown that the spatial distribution of Arctic storms may change in the future in response to climate change (e.g. Orsolini and Sorteberg, 2009; Akperov et al., 2015; Crawford and Serreze, 2017; Nishii et al., 2015; Day et al., 2018). But differences between studies raise uncertainty in this response, which may in part be caused by comparing projections from different models (Hawkins and Sutton, 2009). Nishii et al. (2015) highlighted this by showing a large inter-model spread between projections made by numerous models from the CMIP-3 and CMIP-5 model ensembles. Models can differ in their horizontal resolution (Nishii et al., 2015), and it is unclear whether the response of Arctic storms to climate change is sensitive to horizontal resolution.

There is also little publicly available information on current Arctic shipping activity. The number of ships in the Arctic has likely increased in recent years, as sea ice extent has reduced. But it is currently unclear by how much, and where the highest density of ships is. Moreover, the exposure of ships to Arctic storms is yet to be determined, as the general number of ships impacted by past intense Arctic storms is unknown.

The overall aim of this thesis is to **improve the understanding of present and future risk associated with Arctic storms and the mechanisms that lead to their development**. To achieve this, four research questions (RQ) were devised to investigate these research gaps. These research questions were presented in Chapter 1 (see Section 1.8) and are addressed in the following sections.

7.2 Key Findings

7.2.1 RQ1: What are the present-day characteristics of Arctic storms, and, what is the uncertainty associated with the choice of reanalysis dataset and storm tracking identification variable?

Reanalysis datasets are often used to identify and analyse historic storms (e.g. Hodges et al., 2003). Reanalyses provide spatial and temporal homogeneous datasets of the past atmosphere states and are particularly useful in analysing the poorly observed Arctic (Jung et al., 2016). However, there are multiple reanalysis datasets available from multiple institutions. Tilinina et al. (2014) highlighted that the number of Arctic storms identified can differ between reanalysis datasets, with more storms being identified in the higher resolution datasets (Tilinina et al., 2014). This may impact subsequent storm statistics and introduce uncertainty associated with present-day Arctic storm characteristics.

Studies using older reanalysis datasets suggest that Arctic storm number has increased over the past few decades (e.g. Sorteberg and Walsh, 2008; Sepp and Jaagus, 2011). Other studies using more recent reanalysis datasets show no significant trend in Arctic storm number over the past few decades (e.g. Tilinina et al., 2014; Zahn et al., 2018). There is also a question as to the seasonality of Arctic storms, with most studies suggesting that the total number of Arctic storms is similar between winter and summer using a storm tracking algorithm using sea level pressure as the storm tracking variable (e.g. Serreze, 1995; Serreze et al., 2001; Tilinina et al., 2014; Zahn et al., 2018). In contrast, Simmonds et al. (2008) showed that storm number is higher in winter than in summer when using a storm tracking algorithm using the Laplacian of pressure (geostrophic vorticity) as the storm tracking variable.

Uncertainty in storm statistics can arise from the choice of storm tracking method. Neu et al. (2013) showed that the number of storms identified within a reanalysis dataset can depend on the choice of storm tracking algorithm, but focused on mid-latitude storms that occur over the North Atlantic Ocean. In particular, Neu et al. (2013) highlighted that the variable used for

storm identification can lead to a different number of storms being identified in the same dataset, and impact storm statistics. Storms are typically identified as mean sea level pressure (MSLP) minima or as lower tropospheric relative vorticity maxima (Neu et al., 2013). Other studies have also highlighted the impact of storm tracking identification variables on storm statistics (e.g. storm number and track density) (e.g. Sinclair, 1994; Hodges et al., 2003; Rudeva and Gulev, 2007). The impact of the choice of storm tracking identification variable, between MSLP and relative vorticity, on identifying Arctic storms in reanalysis datasets has yet to been determined.

Chapter 3 aimed to improve the understanding of present-day climate Arctic storm statistics by assessing multiple global reanalysis datasets and storm tracking methods. The datasets evaluated between 1980-2017 included ERA-Interim and ERA5 from ECMWF, JRA-55 from JMA, MERRA-2 from NASA, and NCEP-CFS from NCEP. The sensitivity of Arctic storm statistics was also determined by comparing statistics determined using a storm tracking algorithm based on relative vorticity or MSLP as the storm tracking identification variable.

Key Findings from Chapter 3:

No significant trend in Arctic storm number was found irrespective of the reanalysis dataset used, in any season. Arctic storms was further examined and divided into those with Arctic (north of 65°N) and mid-latitude genesis (south of 65°N), but still no significant trend in storm number was found between the reanalysis datasets, in any season. This is despite Arctic sea ice extent reducing by 60,000 km^2 per year from 1979 (see Figure 1.1).

Robust characteristics of Arctic storms were found that were consistent between all reanalysis datasets. In winter, Arctic storm track density was found to be highest over the Greenland, Norwegian and Barents Seas and the Canadian Archipelago. Whereas in summer, Arctic storm track density was found to be highest over and north of continental Eurasia. Approximately 50% of all Arctic storms have Arctic genesis and mid-latitude genesis. Arctic storms are more intense in winter than in summer, in terms of their minimum MSLP and maximum 925 hPa wind speed. The inter-annual variability in Arctic storm number is small, approximately 15% of the total storm number.

Less agreement between the reanalysis datasets was found in winter than in summer. Differences in the track and genesis density of Arctic storms was found to be larger in winter than in summer. The largest differences in Arctic storm track density in winter was found to be as much as 5–6 storms per season per unit area (5° spherical cap). In comparison, the largest differences in summer Arctic storm track density did not exceed 3–4 storms per season per unit area. Moreover, the mean correlation coefficient across all reanalysis datasets of Arctic storm number per season was found to lower in winter (0.73) than in summer (0.77). In particular, the mean correlation coefficient across all reanalysis datasets of the number of Arctic storms with Arctic genesis per season was found to be much lower in winter (0.55) than in summer (0.74). These results highlight the additional challenges (e.g. low density of conventional observations, modelling winter Arctic meteorology, and potentially greater differences the model background state and observations) in creating an atmospheric reanalysis dataset in winter.

Approximately 50% of all Arctic storms have genesis in the Arctic and the rest mid-latitude genesis in all seasons. Overall, greater differences between the reanalysis datasets were found when comparing storms with Arctic genesis than comparing Arctic storms with mid-latitude genesis. Thus, highlighting the additional challenges in producing atmospheric reanalyses in the Arctic compared to mid-latitude regions.

More Arctic storms are identified using a storm tracking algorithm based on 850 hPa relative vorticity than one based on mean sea level pressure. The differences between Arctic storm number found by using different tracking variables was found to be larger than was found between reanalysis datasets. Arctic storm number was found to differ between the reanalysis datasets by as much as 5% and 2% of the mean total number of Arctic storms per season in winter and summer, respectively. When using 850 hPa relative vorticity and MSLP as the storm tracking identification variable, Arctic storm number based on ERA-Interim was found to be 185% and 150% higher using 850 hPa relative vorticity rather than MSLP as the storm tracking identification variable in winter and summer, respectively. This led to greater differences in Arctic storm track density between the methods of storm tracking (where differences reached 22-24 storms per season per unit area) than between

reanalysis datasets (where differences reached 5-6 storms per season per unit area). The seasonality in storm number was also found to depend on storm tracking identification variable, with MSLP showing storm number to be similar in winter and summer, but 850 hPa relative vorticity showing storm number to be greater in winter than summer. Overall, this shows that the choice of storm tracking identification variable can add more uncertainty to present-day Arctic storm characteristics than the choice of reanalysis dataset.

7.2.2 RQ2: What is the typical development and structure of Arctic storms, and how does this differ to that of mid-latitude storms and existing conceptual models?

It is unclear whether the development and structure of Arctic storms is similar to that of mid-latitude storms and conceptual models of mid-latitude storm development e.g. the Norwegian Cyclone Model and Shapiro-Keyser Model (Bjerknes, 1919, 1922; Shapiro and Keyser, 1990). Previous studies have shown that some Arctic summer storms have a different structure and development to that described by these models (Tanaka et al., 2012; Tao et al., 2017; Aizawa and Tanaka, 2016). These studies show that some Arctic summer storms develop a more axi-symmetric and barotropic structure, which is different to the baroclinic structure of mid-latitude storms. Moreover, some Arctic storms have been found to have had exceptionally long lifetimes, potentially bringing prolonged hazardous conditions to the Arctic (Thomson and Rogers, 2014). One storm was found to have a lifetime greater than one month (Yamagami et al., 2017). These studies were based on the analysis of individual case-studies, and it is unclear how typical they are to all Arctic storms.

Chapter 4 aimed to better understand the typical structure and development of Arctic storms by analysing the composite structure of the 100 most intense Arctic storms per season (from 1979-2019) for the first time. Arctic storm composites were then contrasted with that of the 100 most intense mid-latitude storms that occurred over the North Atlantic Ocean.

Key Findings from Chapter 4:

Intense Arctic summer (JJA) storms are typically longer-lived than Arctic storms in other seasons, and mid-latitude storms in all seasons. The 100 most intense Arctic summer storms had a mean lifetime of 9.7 days, over 3 days greater than that of winter, spring and autumn Arctic storms, and 2.5 days greater than that of North Atlantic Ocean storms in all seasons. Of the 100 most intense Arctic summer storms, 42% of storms had a lifetime greater than 10 days, a much higher proportion than was found in the other seasons.

The composite structure of intense Arctic summer storms is different to that of intense Arctic storms in other seasons, and intense storms that occur over the North Atlantic Ocean in all seasons. The composite structure of Arctic summer storms show that these storms typically undergo different development to that of Arctic storms in other seasons and mid-latitude storms in all seasons. The development of mid-latitude storms (and Arctic storms in winter, spring and autumn) is characterised by occlusion, by which the cold front of a low-pressure system catches up with the warm front, so that the warm air is forced upwards (Bjerknes, 1919, 1922). In contrast, Arctic summer storms typically undergo a structural transition around the time of maximum intensity, from a baroclinic structure to an axi-symmetric cold-core structure throughout the troposphere. The Arctic summer storm composite showed that these storms retain this structure after the time of maximum intensity, which does not show signs of occlusion. This may contribute to extending their lifetime.

Aizawa and Tanaka (2016) showed that the Great Arctic Storm of 2012 had this axi-symmetric cold core structure. Building on this study, it was shown in Chapter 4 that the Great Arctic Storm of 2012 underwent a similar transition to that shown in the composite of intense Arctic summer storms. The Great Arctic Storm of 2012 had a baroclinic structure before the time of maximum intensity, but at and after the time of maximum intensity it had developed an axi-symmetric cold-core throughout the troposphere. It is shown that this storm kept this structure up to 7 days after its time of maximum intensity. This storm has been shown to have merged with an upper-level Tropopause Vortex (TPV) (Simmonds and Rudeva, 2012), which is shown to coincide with the time of the structural transition of the storm.

The similarity between the composite structure of intense Arctic summer storms and the Great Arctic Storm of 2012 suggests that the merger of Arctic summer storms with a TPV might be a common occurrence, which is supported by results from Gray et al. (2021). Moreover, results from this study suggest that this merger may cause the structural transition of Arctic summer storms. Though, the interactions between an Arctic storm and TPV are not well understood and require further work.

The composite structure of the intense Arctic summer storms show similarities with the conceptual model proposed by Aizawa and Tanaka (2016). Aizawa and Tanaka (2016) proposed a model of the structure of Arctic summer storms, based on the analysis of just two past storms. The composite of intense Arctic summer storms shows that after the time of maximum intensity, these storms are characterised by a deep cyclonic circulation that reaches up to the stratosphere, a cold core in the troposphere, a deep tropopause fold which descends to 500 hPa from 300 hPa. However, the composite structure of Arctic storms after the time of maximum intensity does show signs of a secondary circulation, which is highlighted by Aizawa and Tanaka (2016). The evolution in Arctic summer storm structure is not considered by Aizawa and Tanaka (2016). Results from this study show that intense Arctic summer storms undergo a structural transition, to then have a structure similar to that described by Aizawa and Tanaka (2016).

7.2.3 RQ3: How might Arctic storms change in response to climate change? In particular, does the horizontal resolution of the climate model impact the response of Arctic storms to climate change?

Previous research has shown that the spatial distribution of Arctic storms will change in a future climate in reponse to climate change (Orsolini and Sorteberg, 2009; Akperov et al., 2015; Nishii et al., 2015; Crawford and Serreze, 2017; Day and Hodges, 2018). These studies suggest that in winter there will be a decrease in Arctic storm track density over the Arctic Ocean, and in summer, an increase in Arctic storm track density around Greenland and a decrease over continental Eurasia. However, Nishii et al. (2015) highlighted that there is large inter-model

spread in the response of Arctic storms to climate change in the CMIP-3 and CMIP-5 model ensembles, and that not all models project a consistent change in summer storm-track activity.

These studies rely on projections from climate models, which differ in formulation, thus leading to uncertainty in the response of Arctic storms to climate change (Hawkins and Sutton, 2009). In Chapter 5, the response of Arctic storms to climate change was assessed in future climate (2086-2110) simulations from the Hadley Centre Global Environmental Model (version 3) Global Atmosphere 3.0 model (HadGEM3-GA3.0) following the RCP8.5 future climate scenario (Walters and Coauthors, 2011; Mizielinski et al., 2014). These simulations were made as part of the United Kingdom on Partnership for Advanced Computing in Europe (PRACE): Weather-Resolving Simulations of Climate for Global Environmental Risk (UPSCALE) project (Mizielinski et al., 2014). Simulations were made using HadGEM3-GA3.0 at three horizontal resolutions: N96 (130km at 50° latitude), N216 (60km at 50° latitude) and N512 (25km at 50° latitude). This allowed for the assessment of how the response of Arctic storms to climate change is sensitive to model horizontal resolution.

Key Findings in Chapter 5:

The number and spatial distribution of Arctic storms in high resolution (N512) configuration of HadGEM3-GA3.0 agree better with observations (reanalysis datasets) than low resolution (N96) configurations. More storms are simulated in the higher resolution HadGEM3-GA3.0 simulations than in the lower resolution simulations. For example, the number of winter Arctic storms per season from the N512 and N96 HadGEM3-GA3.0 present-day simulations is 117.2 and 107.2 respectively, with the average number of winter Arctic storms per season from the reanalysis datasets being 118.0. Horizontal resolution is also shown to impact the representation of Arctic storm intensity, as storms are represented by higher 925 hPa wind speed maxima and lower mean MSLP minima at a horizontal resolution of N512 than N96.

The spatial distribution of Arctic storms will change in the future in response to climate change. In winter, the track density of Arctic storms is found to decrease over the Arctic Ocean by as much as 10 storms per season per unit area ($\approx 10^6$ km^2), approximately half of the

present-day climate Arctic storm track density per season over the Arctic Ocean. In summer, Arctic storm track density is found to increase over the Canadian Archipelago, northern North Atlantic Ocean, and Greenland and Barents Seas by more than 10 storms per season per unit area, approximately double the present-day Arctic storm track density in these regions summer Arctic storm track density is also found to decrease over the Eurasian continent by as much as 6 storms per season per unit area.

This is similar to that found in previous studies (e.g. Orsolini and Sorteberg, 2009; Akperov et al., 2015; Crawford and Serreze, 2015; Day et al., 2018). It is shown that in winter, this change in the spatial distribution of Arctic storms is primarily driven by reduced baroclinicity in the Arctic, as warming is greatest over the Arctic Ocean than mid-latitude regions as a consequence of Arctic Amplification. In summer, the increase in track density of Arctic storms around Greenland is driven by a northward shift in the Jet Stream in this region.

Results from this study further show that the spatial distribution of intense Arctic storms will also change. When concentrating on intense Arctic storms, with 925 hPa wind speeds greater than 24.5 ms^{-1} - approximately equivalent to Beaufort Scale 10 (Simpson, 1906; Met Office, 2010), results show that the change in the spatial distribution of intense Arctic storms follows the spatial response of all Arctic storms. Thus, the areas of greatest risk to human activity, will likely change in a future climate in response to climate change.

The general response of Arctic storms to climate change is similar between the HadGEM3-GA3.0 simulations at horizontal resolutions of N96, N216 and N512. The response of Arctic storms to climate change, and the magnitude of this response, was found to be similar when comparing the present-day climate and RCP8.5 future climate HadGEM3-GA3.0 simulations at each horizontal resolution. This adds confidence in this response.

But it was found that more storms are typically generated by HadGEM3-GA3.0 at higher horizontal resolutions in all seasons, typically in regions where Arctic storm track density is highest. Despite the response of Arctic storms to climate change being similar between the projections at each horizontal resolutions, uncertainty can be introduced when comparing projections made by models with different horizontal resolutions.

7.2.4 RQ4: How can we best use information on Arctic storms and shipping activities to assess risk in the Arctic?

Arctic shipping information is hard to obtain. This is partly because ship track data is mainly held by commercial companies; it is privatised and is only available at a price. In Chapter 6, an insight into Arctic shipping activities was deduced using Arctic shipping information from the Norwegian Coastal Administration Sea Base (Havbase) Norwegian Coastal Administration (2021). This is a publicly available alternative, which provides the number and type of ships that cross gates that separate regions in the Arctic. Though Havbase does not give historical ship tracks, its information can be used to simulate past ship transits. Thus, number of ships intersected by historical storm tracks can be estimated.

Key Findings from Chapter 6:

The amount of Arctic shipping activity has increased from 2012 to 2019, with the increase from 2016 being driven by increases in the number of cargo and oil ships with high potential financial loss. The total number gate crossings by ships across the Arctic in Havbase has increased from 2012, with 15,088 gate crossings by ships recorded in 2012 and 24,714 in 2019. In 2019, the highest number of gate crossings by ships recorded over the Barents Sea, with just over 5,000 gate crossings being recorded by ships travelling into and out of the Barents Sea from the Norwegian Sea in 2019. The number of gate crossings by ships over the trans-arctic shipping routes of the North-West Passage and Northern Sea Route was much lower in 2019 than in the Barents Sea, being no greater than 150.

From 2016, the number of ship crossings recorded by small ships plateaued and remained approximately 16,000. In contrast, the number of ship crossings recorded by cargo ships and oil ships increased from 2016. These ships would incur greater financial loss if damaged.

Intense Arctic storms that can result in rough sea conditions typically occur over the Greenland, Norwegian and Barents Seas in all seasons, where the number of gate crossings by ships in the Arctic is highest. In winter, just over 60 storms per season occur that have 10 m wind speeds greater than 17 ms^{-1} and significant wave heights greater than 2.5

m, which would result in rough sea conditions. In summer, only 16 storms per season have 10 m wind speeds greater than 17 ms^{-1}, but 42 storms per season have significant wave heights greater than 2.5 m.

Wave heights depend on wind, but also fetch, which describes the area to which wind travels over the ocean surface. As sea ice extent continues to reduce, wave heights in the Arctic may increase as fetch increases. Thus in the future, the number of Arctic storms that cause high waves and rough sea conditions may increase, and these conditions may become more severe (Khon et al., 2014; Casas-Prat and Wang, 2020).

A simple risk model that combined ship transits and individual storm tracks estimates that up to 9,500 ships transits experience rough sea conditions cause by Arctic storms per year. The Havbase database gives the number of ships that cross gates that separate regions in the Arctic. A simple model has been devised in this thesis to use such data and simulate past ship transits in the Arctic. These simulated ship transits can be combined with past Arctic storm tracks, to estimate the number of ships impacted by intense Arctic storms. Using this model with shipping data from 2019 and historical Arctic storm tracks from 1979, it is estimated that up to 9,500 simulate ship transits are intersected by Arctic storms that cause rough sea conditions (either with 10 m wind speeds greater than 17 ms^{-1} or significant wave heights greater than 2.5 m).

Infrastructure to support shipping activity in the Arctic is currently poorly established and sea ice extent limits the amount of open ocean that is navigable for ships. Arctic sea ice extent is expected to reduce further over the 21st century (Stroeve et al., 2012), and the Arctic is receiving investment to developing infrastructure (Arctic Today, 2019; High North News, 2019). It is therefore likely that the amount of shipping in the Arctic will increase further over the next few decades, increasing the likelihood of a potential disaster and the need for Arctic insurance.

7.3 Limitations and Future Work

This thesis has investigated synoptic-scale Arctic storms and has found conclusions that improve the understanding these hazards and help to evaluate their risk. However, there are some limitations to this work.

Results from Chapters 3 - 6 are based on one storm tracking algorithm: TRACK (Hodges, 1994, 1995, 1999). Although the impact of using 850 hPa relative vorticity or mean sea level pressure as the storm tracking identification variable was investigated in Chapter 3, there are more ways that storm tracking algorithms can differ (Neu et al., 2013). For example, some schemes filter out storms over high orography, and use different filtering thresholds of the intensity, lifespan and track length of the storms (Rudeva et al., 2014; Pinto et al., 2005). To validate the results from this study, one could compare results from this study with results obtained using different storm tracking algorithms.

In Chapter 4, it was shown that intense Arctic summer storms typically have longer lifetimes than Arctic storms in other seasons and mid-latitude storms in all seasons. This would prolong hazardous conditions in the Arctic. Though, the reason for this was not explicitly found. There are multiple ways that Arctic summer storms can interact with the large-scale environment or other weather systems. These can include interacting with Tropopause Polar Vorticies (TPVs) (Simmonds and Rudeva, 2012; Tao et al., 2017), merging with other storms (Yamagami et al., 2017), and interacting with the Arctic Frontal Zone (Crawford and Serreze, 2016). It is currently unclear how many storms fit into each category or multiple categories, and whether one category tends to lead to longer-lived Arctic storms.

Moreover, the interactions themselves are not well understood. For example, it is unclear how storms interact with TPVs, with only a few case-studies being analysed in previous research. Results from Chapter 4 show that this interaction may be common of intense Arctic summer storms, and it may occur in more storms than has previously been identified. With the recent development of the ERA5 reanalysis dataset, which has a temporal resolution of 1 hour, there is an opportunity to gain a more in-depth insight into how a storm evolves when it interacts with

the large-scale environment, TPVs, and other weather systems. This would allow for a better understanding of how Arctic storms develop and may uncover the reason for their longevity. Results from this thesis provides evidence to suggest that the development of Arctic summer storms is different to that of conceptual models of mid-latitude storms. But more work is needed to fully understand the development of Arctic storms.

To better understand the interactions between storms and TPVs, a matching analysis between storms and TPVs could be performed, similar to that used in Chapter 3 (matching storms between reanalysis datasets) and Gray et al. (2021). This would help to identify more examples of Arctic storms that have interacted with a TPV during their life cycle. Secondly, to test the hypothesis deduced in this thesis that the merger of Arctic storms and TPVs may cause the structural transition of Arctic summer storms, the structure of these matched storms (from the matching analysis) could be examined. Thirdly, if TPVs were found to influence the structural transition of Arctic summer storms, then the energetics of the storm could be analysed, to quantify and determine how the atmosphere changes within a storm when they merge with a TPV. This would further understand how TPVs may influence Arctic storms.

The future response of Arctic storms and their sensitivity to model horizontal resolution was determined using the atmosphere-only HadGEM3-GA3.0 model, which is forced by changes in sea ice and sea surface temperature derived from projections made by the HadGEM2 Earth System climate model (Mizielinski et al., 2014). Other types of climate model exist, including coupled ocean-atmosphere climate models. In these models, the ocean and atmosphere can evolve and interact, whereas, in an atmosphere-only climate model, properties of the ocean surface, e.g. sea surface temperature and sea ice extent, are determined by an external dataset. For example, ocean conditions in the HadGEM3-GA3.0 simulations are determined by the OSTIA dataset and from projections made by the HadGEM2 model (Donlon et al., 2012; Mizielinski et al., 2014). An avenue of future work could be to assess the sensitivity of the response of Arctic storms to climate change to horizontal resolution using a coupled ocean-atmosphere climate model.

In 2015, 196 countries signed the Paris Agreement, which is a legally binding international treaty that aims to limit global warming to well below 2 °C and preferably to 1.5 °C, compared to pre-industrial levels (United Nations Climate Change, 2021). These recent political actions may have made the more extreme RCP8.5 future climate scenario less likely, which would likely result in the global surface air temperatures to warm by 2.6 - 4.8°C by the end of the 21st century (see Table SPM.2 in Stocker et al., 2014). Although insight can be gained by analysing future climate simulations under the RCP.5 future climate scenario, more work could be done analysing projections across more of the RCP future scenarios and climate models (e.g. CMIP6 - Carbon Brief, 2019). This would lead to a more complete understanding of the range of possible responses of Arctic storms to climate change.

In Chapter 5, it was found that horizontal resolution impacts the number of Arctic storms simulated by a model that can affect Arctic storm statistics in a future climate, with more storms being simulated in areas where Arctic storm track density. There was higher Arctic storm number per season in all seasons in the N512 HadGEM3-GA3.0 present-day and future climate simulations than the N96 HadGEM3-GA3.0 simulations. These higher resolution simulations in the present-day climate were more similar to reanalysis datasets. Future work could analyse future climate simulations from the HighResMIP project (Haarsma et al., 2016), to represent future climate Arctic storms more accurately in high-resolution models.

The main limitation of Chapter 6 was that ship transits had to be simulated using information from Havbase, as historical ship tracks were not available. Ships were assumed to travel across the pre-determined ship lanes at a constant speed of 15 knots. In reality, a ship would likely divert and avoid the storm, with the storm track being forecasted. The position of a ship is transmitted by on-board Automated Information Systems (AIS), and historical records are mainly held by commercial companies. If actual historical ship tracks could be acquired, a more accurate estimate of the number of ships impacted by past Arctic storms could be determined. This may provide a more accurate evaluation of Arctic storm risk. The methodology of simulating ship transits in the Arctic devised in this thesis, could also be combined with future climate Arctic storm tracks identified in climate model simulations. This would help to determine potential changes in the risk of Arctic storms to shipping.

The results from Chapter 6 are also limited to using the Beaufort Scale and Douglas Sea State Scale to infer when rough sea conditions occur (Simpson, 1906; Schule, 1966; Met Office, 2010). However, it is unclear at what wind speed and significant wave height thresholds are in fact hazardous to ships, which are typically built to withstand hazardous weather. Case-studies of shipping incidents that have been damaged due to Arctic storms could be identified, to build up a portfolio of incidents between Arctic storms and ships. These incidents could be checked against ERA5, for example, to determine the thresholds of hazardous weather that are dangerous to ships.

Arctic storms can also enhance the break-up of Arctic sea ice (Simmonds and Keay, 2009; Asplin et al., 2012; Parkinson and Comiso, 2013; Peng et al., 2021), which can cause the additional hazard to shipping of sea ice drifts. This hazard to shipping was not considered in this thesis, when determining how many ships are impacted by Arctic storms. Sea ice data is now available at horizontal resolutions of 1 km^2 (e.g. National Snow & Ice Data Centre, 2021a), allowing for smaller ice drifts to be identified. In this thesis, it was identified that the Barents Sea is the region with the highest density of ships in the Arctic. Further work could investigate how often ice drifts into such areas of high ship density (e.g. the Barents Sea), to determine how often the hazard of sea ice drifts impacts ships in the Arctic.

Overall, this thesis has furthered the understanding of synoptic-scale Arctic storms and provides a better assessment of the risk that they pose to human activities such as shipping, oil exploration and tourism, in the Arctic. Climate change will lead to further reductions in sea ice extent over the 21^{st} century (Stroeve et al., 2012), and further investment is being made to develop infrastructure in the Arctic (Arctic Today, 2019; High North News, 2019). It is therefore likely that the Arctic will be increasingly used for shipping, oil exploration and tourism over the coming decades, and the exposure to Arctic storms will increase further. This makes the findings from this thesis increasingly relevant. Arctic research is also gaining interest, with several observational campaigns ongoing. These include the Year of Polar Prediction (Jung et al., 2016;

Bauer et al., 2016b), the deployment of the Polarstern Research Vessel to the Arctic Ocean as part of the Multidisciplinary drifting Observatory for the Study of Arctic Climate (MOSAiC) project (MOSAiC, 2020), and the planned observing flight through an Arctic summer storm led by the University of Reading (University of Reading, 2021). It is hoped that this thesis provides insight for such and future projects.

Chapter 8

References

Aizawa, T., and H. Tanaka, 2016: Axisymmetric structure of the long lasting summer Arctic cyclones. *Polar Sci.*, **10 (3)**, 192–198.

Aizawa, T., H. Tanaka, and M. Satoh, 2014: Rapid development of Arctic cyclone in June 2008 simulated by the cloud resolving global model NICAM. *Meteorol. Atmos. Phys.*, **126 (3)**, 105–117.

Akperov, M., I. Mokhov, A. Rinke, K. Dethloff, and H. Matthes, 2015: Cyclones and their possible changes in the Arctic by the end of the twenty first century from regional climate model simulations. *Theor. Appl. Climatol.*, **122 (1)**, 85–96.

Alfred Wegener Institute, 2019: Sea ice thickness (CryoSat-2). Accessed 12 Jan 2019, https://data.seaiceportal.de/gallery/index_new.php?lang=en_US.

Arctic Council, 2018: First Arctic shipping status report from PAME Working Group highlights increase in Arctic shipping traffic. Accessed 12 Nov 2020, https://www.pame.is/projects/arctic-marine-shipping/arctic-shipping-status-reports.

Arctic Monitoring & Assessment Programme: Working Group of the Arctic Council, 2020: Arctic topography and bathymetry. Accessed 09 Dec 2020, https://www.amap.no/documents/doc/Arctic-topography-and-bathymetry/570.

Arctic Monitoring and Assessment Programme, 2012: Arctic Climate Issues 2011: Changes in Arctic snow, water, ice and permafrost. SWIPA 2011 Overview Report. Accessed 11 Dec 2020, https://www.amap.no/documents/download/2267/inline.

Arctic Today, 2019: Rosatom looks to invest $7 billion to create an Arctic shipping service. Accessed 12 Nov 2020, https://www.arctictoday.com/rosatom-looks-to-make-7-billion-investment-in-arctic-shipping-service/.

Arrhenius, S., 1896: XXXI. On the influence of carbonic acid in the air upon the temperature of the ground. *The London, Edinburgh, and Dublin Philosophical Magazine and Journal of Science*, **41 (251)**, 237–276.

Arzel, O., T. Fichefet, and H. Goosse, 2006: Sea ice evolution over the 20th and 21st century centuries as simulated by current AOGCMs. *Ocean Modelling*, **12 (3-4)**, 401–415.

Asplin, M. G., R. Galley, D. G. Barber, and S. Prinsenberg, 2012: Fracture of summer perennial sea ice by ocean swell as a result of Arctic storms. *J. Geophys. Res.: Oceans*, **117 (C6)**.

Baker, A. J., and Coauthors, 2019: Enhanced climate change response of wintertime North Atlantic circulation, cyclonic activity, and precipitation in a 25-km-resolution global atmospheric model. *J. Clim.*, **32 (22)**, 7763–7781.

Barnes, E. A., and J. A. Screen, 2015: The impact of Arctic warming on the midlatitude jet-stream: Can it? Has it? Will it? *WIREs Clim. Change.*, **6 (3)**, 277–286.

Bauer, M., and A. D. Del Genio, 2006: Composite analysis of winter cyclones in a gcm: Influence on climatological humidity. *Journal of climate*, **19 (9)**, 1652–1672.

Bauer, P., L. Magnusson, J.-N. Thépaut, and T. M. Hamill, 2016a: Aspects of ECMWF model performance in polar areas. *Q. J. R. Meteorol. Soc.*, **142 (695)**, 583–596.

Bauer, P., and Coauthors, 2016b: WWRP Polar Prediction Project Implementation Plan for the Year of Polar Prediction (YOPP). World Meteorological Organization.

BBC, 2016: Arctic Ocean shipping routes "to open for months". Accessed 01 Feb 2021, https://www.bbc.co.uk/news/science-environment-37286 750.

BBC, 2018: Is the Arctic set to become a main shipping route? Accessed 12 Nov 2020, https://www.bbc.co.uk/news/business–45527 531.

BBC, 2021: Egypt's Suez Canal blocked by huge container ship. Accessed 24 Jun 2021, https://www.bbc.co.uk/news/world-middle-east-56505 413.

Bengtsson, L., K. I. Hodges, M. Esch, N. Keenlyside, L. Kornblueh, J.-J. Luo, and T. Yamagata, 2007: How may tropical cyclones change in a warmer climate? *Tellus*, **59 (4)**, 539–561.

Bengtsson, L., K. I. Hodges, and N. Keenlyside, 2009: Will extratropical storms intensify in a warmer climate? *J. Clim.*, **22 (9)**, 2276–2301.

Bird, K. J., and Coauthors, 2008: Circum-Arctic resource appraisal: Estimates of undiscovered oil and gas north of the Arctic Circle. Tech. rep., US Geological Survey.

Bjerknes, J., 1919: On the structure of moving cyclones. *Mon. Weather Rev.*, **47 (2)**, 95–99.

Bjerknes, J., 1922: Life cycle of cyclones and the polar front theory of atmospheric circulation. *Geophys. Publik.*, **3 (1)**, 1–18.

Blackmon, M. L., 1976: A climatological spectral study of the 500 mb geopotential height of the Northern Hemisphere. *J. Atmos. Sci.*, **33 (8)**, 1607–1623.

Blender, R., and M. Schubert, 2000: Cyclone tracking in different spatial and temporal resolutions. *Mon. Weather Rev.*, **128 (2)**, 377–384.

Boeke, R. C., and P. C. Taylor, 2018: Seasonal energy exchange in sea ice retreat regions contributes to differences in projected Arctic warming. *Nat. Commun.*, **9 (1)**, 1–14.

Bromwich, D., and Coauthors, 2018: The Arctic system reanalysis, version 2. *Bulletin of the American Meteorological Society*, **99 (4)**, 805–828.

Browning, K., 1997: The dry intrusion perspective of extra-tropical cyclone development. *Meteor. Appl.*, **4 (4)**, 317–324.

Browning, K., 2004: The sting at the end of the tail: Damaging winds associated with extra-tropical cyclones. *Q. J. R. Meteorol. Soc.*, **130 (597)**, 375–399.

Carbon Brief, 2019: CMIP6: the next generation of climate models explained. Accessed 27 Jun 2021, https://www.carbonbrief.org/cmip6-the-next-generation-of-climate-models-explained.

Carlson, T. N., 1961: Lee-side frontogenesis in the Rocky Mountains. *Mon. Weather Rev.*, **89 (5)**, 163–172.

Carlson, T. N., 1980: Airflow through mid-latitude cyclones and the comma cloud pattern. *Mon. Weather Rev.*, **108 (10)**, 1498–1509.

Casas-Prat, M., and X. L. Wang, 2020: Projections of extreme ocean waves in the Arctic and potential implications for coastal inundation and erosion. *J. Geophys. Res.: Oceans*, **125 (8)**, e2019JC015 745.

Catto, J. L., L. C. Shaffrey, and K. I. Hodges, 2010: Can climate models capture the structure of extra-tropical cyclones? *J. Clim.*, **23 (7)**, 1621–1635.

Cavallo, S. M., and G. J. Hakim, 2010: Composite structure of tropopause polar cyclones. *Mon. Weather Rev.*, **138 (10)**, 3840–3857.

Charney, J. G., 1947: The dynamics of long waves in a baroclinic westerly current. *J. Meteorol.*, **4**, 136–162.

Climate Data, 2020: Albedo measurements. Accessed 03 Jun 2021, http://www.climatedata.info/forcing/albedo/.

Collins, M., and Coauthors, 2013: Long-term climate change: projections, commitments and irreversibility. *Climate Change 2013-The Physical Science Basis: Contribution of Working Group I to the Fifth Assessment Report of the Intergovernmental Panel on Climate Change*, Cambridge University Press, 1029–1136.

Collins, W., and Coauthors, 2011: Development and evaluation of an Earth-System model–HadGEM2. *Geosci. Model Dev. Discuss*, **4 (2)**, 997–1062.

Corbett, J. J., D. A. Lack, J. J. Winebrake, S. Harder, J. A. Silberman, and M. Gold, 2010: Arctic shipping emissions inventories and future scenarios. *Atmos. Chem. Phys.*, **10 (19)**, 9689–9704.

Crawford, A., and M. Serreze, 2015: A new look at the summer Arctic Frontal Zone. *J. Clim.*, **28 (2)**, 737–754.

Crawford, A. D., and M. C. Serreze, 2016: Does the summer Arctic frontal zone influence Arctic Ocean cyclone activity? *J. Clim.*, **29 (13)**, 4977–4993.

Crawford, A. D., and M. C. Serreze, 2017: Projected changes in the Arctic Frontal Zone and summer Arctic cyclone activity in the CESM large ensemble. *J. Clim.*, **30 (24)**, 9847–9869.

Dacre, H., 2020: A review of extra-tropical cyclones: observations and conceptual models over the past 100 years. *Weather*, **75 (1)**, 4–7.

Dacre, H., M. Hawcroft, M. Stringer, and K. Hodges, 2012: An extra-tropical cyclone atlas: A tool for illustrating cyclone structure and evolution characteristics. *Bull. Am. Meteorol. Soc.*, **93 (10)**, 1497–1502.

Day, J. J., and K. I. Hodges, 2018: Growing land-sea temperature contrast and the intensification of Arctic cyclones. *Geophys. Res. Lett.*, **45 (8)**, 3673–3681.

Day, J. J., M. M. Holland, and K. I. Hodges, 2018: Seasonal differences in the response of Arctic cyclones to climate change in CESM1. *Clim. Dyn.*, **50 (9-10)**, 3885–3903.

Dee, D. P., and Coauthors, 2011: The ERA-Interim reanalysis: Configuration and performance of the data assimilation system. *Q. J. R. Meteorol. Soc.*, **137 (656)**, 553–597.

Donlon, C. J., M. Martin, J. Stark, J. Roberts-Jones, E. Fiedler, and W. Wimmer, 2012: The operational sea surface temperature and sea ice analysis (OSTIA) system. *Remote Sens. Environ.*, **116**, 140–158.

Dzerdzeevskii, B. L., 1945: Tsirkuliatsionnye skhemy v troposfere Tsentral' noi Arktiki.

Izdatel' svo Akad. *Nauk.*, 28. (English translation in Scientific Rep. 3 under Contract AF 19(122)–3228 to Dept. of Meteorology, University of California, Los Angeles).

Eady, E. T., 1949: Long waves and cyclone waves. *Tellus*, **1 (3)**, 33–52.

Eguiluz, V. M., J. Fernández-Gracia, X. Irigoien, and C. M. Duarte, 2016: A quantitative assessment of Arctic shipping in 2010-2014. *Sci. Rep.*, **6**, 30 682.

European Space Agency, 2008: Arctic sea ice annual freeze-up underway. Accessed 16 Nov 2020, https://www.esa.int/Applications/Observing_the_Earth/Space_for_our_climate/Arctic_sea_ice_annual_freeze_nobr_-up_nobr_underway.

European Space Agency, 2011: Arctic shipping routes open. Accessed 16 Nov 2020, https://www.esa.int/Applications/Observing_the_Earth/Space_for_our_climate/Arctic_shipping_routes_open.

Financial Times, 2013: Chinese cargo ship sets sail for Arctic short-cut. Accessed 12 Nov 2020, https://www.ft.com/content/05daa11e-0274-11e3-880d-00 144feab7de.

Flake, L. E., 2013: Navigating an ice-free Arctic: Russia's policy on the Northern Sea Route in an era of climate change. *The RUSI Journal*, **158 (3)**, 44–52.

Gates, W. L., and Coauthors, 1999: An overview of the results of the Atmospheric Model Intercomparison Project (AMIP I). *Bull. Am. Meteorol. Soc.*, **80 (1)**, 29–56.

Gazprom Neft, 2020: Gazprom Neft at a glance. Accessed 24 Nov 2020, https://www.gazprom-neft.com/company/about/at-a-glance/.

Gelaro, R., and Coauthors, 2017: The Modern-Era Retrospective Analysis for Research and Applications, version 2 (MERRA-2). *J. Clim.*, **30 (14)**, 5419–5454.

GISTEMP Team, 2021: GISS Surface Temperature Analysis (GISTEMP), version 4. Accessed 17 Jun 2021, https://data.giss.nasa.gov/gistemp/.

Google, 2021: Google Earth Pro. Accessed 18 May 2021, https://www.google.com/intl/en_uk/earth/desktop/.

Gray, S. L., K. I. Hodges, J. L. Vautrey, and J. Methven, 2021: The role of tropopause polar vortices in the intensification of summer Arctic cyclones. *Weather and Climate Dynamics Discussions*, 1–31.

Gray, S. L., O. Martínez-Alvarado, D. Ackerley, and D. Suri, 2020: Development of a prototype real-time sting-jet precursor tool for forecasters. *Weather*.

Haarsma, R. J., and Coauthors, 2016: High resolution model intercomparison project (highresmip v1. 0) for cmip6. *Geoscientific Model Development*, **9 (11)**, 4185–4208.

Hansen, C. Ø., P. Grønsedt, C. L. Graversen, and C. Hendriksen, 2016: *Arctic Shipping: Commercial Opportunities and Challenges*. CBS Maritime.

Harsem, Ø., K. Heen, J. Rodrigues, and T. Vassdal, 2015: Oil exploration and sea ice projections in the Arctic. *The Polar Record*, **51 (1)**, 91.

Hawcroft, M., L. Shaffrey, K. Hodges, and H. Dacre, 2012: How much Northern Hemisphere precipitation is associated with extra-tropical cyclones? *Geophys. Res. Lett.*, **39 (24)**.

Hawkins, E., and R. Sutton, 2009: The potential to narrow uncertainty in regional climate predictions. *Bull. Am. Meteorol. Soc.*, **90 (8)**, 1095–1108.

Hersbach, H., 2019: ECMWF's ERA5 reanalysis extends back to 1979. *ECMWF Newsletter*, **158 (1)**.

Hersbach, H., and Coauthors, 2020: The ERA5 global reanalysis. *Q. J. R. Meteorol. Soc.*,

146 (730), 1999–2049.

High North News, 2019: Rosatom To Invest $7bn in Arctic Shipping to Compete with Suez Canal. Accessed 28 May 2021, https://www.highnorthnews.com/en/rosatom-invest-7bn-arctic-shipping-compete-suez-canal.

Hodges, K., 1994: A general method for tracking analysis and its application to meteorological data. *Mon. Weather Rev.*, **122 (11)**, 2573–2586.

Hodges, K., 1995: Feature tracking on the unit sphere. *Mon. Weather Rev.*, **123 (12)**, 3458–3465.

Hodges, K., 1996: Spherical non-parametric estimators applied to the UGAMP model integration for AMIP. *Mon. Weather Rev.*, **124 (12)**, 2914–2932.

Hodges, K., 1999: Adaptive constraints for feature tracking. *Mon. Weather Rev.*, **127 (6)**, 1362–1373.

Hodges, K., 2008: Confidence intervals and significance tests for spherical data derived from feature tracking. *Mon. Weather Rev.*, **136 (5)**, 1758–1777.

Hodges, K. I., B. J. Hoskins, J. Boyle, and C. Thorncroft, 2003: A comparison of recent reanalysis datasets using objective feature tracking: Storm tracks and tropical easterly waves. *Mon. Weather Rev.*, **131 (9)**, 2012–2037.

Hodges, K. I., R. W. Lee, and L. Bengtsson, 2011: A comparison of extra-tropical cyclones in recent reanalyses ERA-Interim, NASA MERRA, NCEP CFSR, and JRA-25. *J. Clim.*, **24 (18)**, 4888–4906.

Holton, J. R., 2004: An introduction to dynamic meteorology, Forth Edition. *Elsevier Academic Press.*

Hoskins, B. J., and K. I. Hodges, 2002: New perspectives on the Northern Hemisphere winter storm tracks. *J. Atmos. Sci.*, **59 (6)**, 1041–1061.

Hoskins, B. J., M. E. McIntyre, and A. W. Robertson, 1985: On the use and significance of isentropic potential vorticity maps. *Q. J. R. Meteorol. Soc.*, **111 (470)**, 877–946.

Hoskins, B. J., and P. J. Valdes, 1990: On the existence of storm-tracks. *J. Atmos. Sci.*, **47 (15)**, 1854–1864.

Houghton, J., 2001: Climate Change 2001: The Scientific Basis.

International Maritime Organization, 2016: *Polar Code: International Code for Ships Operating in Polar Waters*. International Maritime Organization.

International Maritime Organization, 2019: AIS transponders. Accessed 06 Jan 2021, https://www.imo.org/en/OurWork/Safety/Pages/AIS.aspx.

Jung, T., S. Gulev, I. Rudeva, and V. Soloviov, 2006: Sensitivity of extratropical cyclone characteristics to horizontal resolution in the ECMWF model. *Q. J. R. Meteorol. Soc.*, **132 (619)**, 1839–1857.

Jung, T., and Coauthors, 2012: High-resolution global climate simulations with the ECMWF model in Project Athena: Experimental design, model climate, and seasonal forecast skill. *J. Clim.*, **25 (9)**, 3155–3172.

Jung, T., and Coauthors, 2016: Advancing polar prediction capabilities on daily to seasonal time scales. *Bull. Am. Meteorol. Soc.*, **97 (9)**, 1631–1647.

Khon, V., I. Mokhov, F. Pogarskiy, A. Babanin, K. Dethloff, A. Rinke, and H. Matthes, 2014: Wave heights in the 21st century Arctic Ocean simulated with a regional climate model.

Geophys. Res. Lett., **41 (8)**, 2956–2961.

Kobayashi, S., and Coauthors, 2015: The JRA-55 reanalysis: General specifications and basic characteristics. *J. Meteorol. Soc. Jpn.*, **93 (1)**, 5–48.

Larsen, L.-H., B. Kvamstad-Lervold, K. Sagerup, V. Gribkovskaia, A. Bambulyak, R. Rautio, and T. E. Berg, 2016: Technological and environmental challenges of Arctic shipping A case study of a fictional voyage in the Arctic. *Polar Res.*, **35 (1)**, 27 977.

Lasserre, F., 2019: Arctic shipping: A contrasted expansion of a largely destinational market. *The Global Arctic Handbook*, Springer, 83–100.

Lawrence, H., J. Farnan, I. Sandu, N. Bormann, P. Bauer, and L. Magnusson, 2019: *An assessment of the use of observations in the Arctic at ECMWF*. European Centre for Medium Range Weather Forecasts.

Leckebusch, G. C., U. Ulbrich, L. Fröhlich, and J. G. Pinto, 2007: Property loss potentials for European midlatitude storms in a changing climate. *Geophys. Res. Lett.*, **34 (5)**.

Lenssen, N. J., G. A. Schmidt, J. E. Hansen, M. J. Menne, A. Persin, R. Ruedy, and D. Zyss, 2019: Improvements in the GISTEMP uncertainty model. *J. Geophys. Res.: Atmos.*, **124 (12)**, 6307–6326.

Lindsay, R., and J. Zhang, 2005: The thinning of Arctic sea ice, 1988–2003: Have we passed a tipping point? *J. Clim.*, **18 (22)**, 4879–4894.

Liu, Q., A. V. Babanin, S. Zieger, I. R. Young, and C. Guan, 2016: Wind and wave climate in the Arctic Ocean as observed by altimeters. *J. Clim.*, **29 (22)**, 7957–7975.

Lloyds of London, 2013: The challenges and implications of removing shipwrecks in the 21st century. Accessed 04 Jun 2021, https://www.lloyds.com/~/media/lloyds/reports/emerging%20risk%20reports/wreck%20report%20final%20version%20aw.pdf.

Lyon, S., and D. Weiss, 2010: Oil spills by the numbers. Accessed 19 May 2021, https://www.americanprogress.org/issues/green/news/2010/04/30/7620/oil-spills-by-the-numbers.

Maher, P. T., 2017: Tourism futures in the Arctic. *The Interconnected Arctic — UArctic Congress 2016*, Springer, Cham, 213–220.

Manabe, S., and R. J. Stouffer, 1980: Sensitivity of a global climate model to an increase of CO^2 concentration in the atmosphere. *J. Geophys. Res.: Oceans*, **85 (C10)**, 5529–5554.

Marine Traffic, 2021: MarineTraffic: Global Ship Tracking Intelligence | AIS Marine Traffic. Accessed 01 Jul 2021, https://www.marinetraffic.com/cz/ais/home/centerx:-32.3/centery:63.0/zoom:3.

Martínez-Alvarado, O., L. H. Baker, S. L. Gray, J. Methven, and R. S. Plant, 2014: Distinguishing the cold conveyor belt and sting jet airstreams in an intense extra-tropical cyclone. *Mon. Weather Rev.*, **142 (8)**, 2571–2595.

Maykut, G. A., 1985: An introduction to ice in the polar oceans. Tech. rep., Technical Report APL-UW 8510, Department of Atmospheric Sciences, University of Washington.

Melia, N., K. Haines, and E. Hawkins, 2016: Sea ice decline and 21st century trans-Arctic shipping routes. *Geophys. Res. Lett.s*, **43 (18)**, 9720–9728.

Met Office, 2010: Fact sheet 6 The Beaufort Scale. Accessed 20 May 2021, https://www.metoffice.gov.uk/research/library-and-archive/publications/factsheets.

Mizielinski, M., and Coauthors, 2014: High resolution global climate modelling; the UPSCALE project, a large simulation campaign. *Geosci. Model Dev.*, **7 (4)**, 1629–1640.

MOSAiC, 2020: The Expedition. Accessed 17 Nov 2020, https://mosaic-expedition.org/expedition/.

Munich RE, 2021: Winter storms: A risk to entire continents. Accessed 28 May 2021, https://www.munichre.com/en/risks/natural-disasters-losses-are-trending-upwards/winter-storms.html.

National Geographic, 2016: A luxury cruise Liner is about to sail the Arctic's northwest passage. Accessed 13 Nov 2020, https://www.nationalgeographic.com/news/2016/08/crystal-serenity-luxury-cruise-arctic-northwest-passage.

National Snow & Ice Data Centre, 2019a: EASE-Grid sea ice age, version 4. Accessed 12 Jan 2019, https://nsidc.org/data/nsidc-0611/versions/4.

National Snow & Ice Data Centre, 2019b: Sea Ice Index. Accessed 13 March 2019, https://nsidc.org/data/seaice_index.

National Snow & Ice Data Centre, 2020a: Sea ice data and analysis tools. Accessed 09 Nov 2020, https://nsidc.org/arcticseaicenews/sea-ice-tools/.

National Snow & Ice Data Centre, 2020b: Sea Ice Index Animation Tool. Accessed 11 Nov 2020, https://nsidc.org/data/seaice_index/archives/image_select.

National Snow & Ice Data Centre, 2020c: Thermodynamics: Albedo. Accessed 17 Nov 2020, https://nsidc.org/cryosphere/seaice/processes/albedo.html.

National Snow & Ice Data Centre, 2021a: IMS Daily Northern Hemisphere Snow and Ice Analysis at 1 km, 4 km, and 24 km Resolutions, Version 1. Accessed 13 Jul 2021, https://nsidc.org/data/G02 156/versions/1.

National Snow & Ice Data Centre, 2021b: Sea Ice Concentration Maps Daily and Monthly Sea Ice Concentration Maps (Near Real Time), Version 1. Accessed 05 May 2021, https://nsidc.org/data/NSIDC-0673/versions/1.

Neu, U., and Coauthors, 2013: IMILAST: A community effort to inter-compare extra-tropical cyclone detection and tracking algorithms. *Bull. Am. Meteorol. Soc.*, **94 (4)**, 529–547.

Nishii, K., H. Nakamura, and Y. J. Orsolini, 2015: Arctic summer storm track in CMIP3/5 climate models. *Clim. Dyn.*, **44 (5-6)**, 1311–1327.

Norwegian Coastal Administration, 2021: Sea base Web Interface. Accessed 06 Jan 2021, havbase.no/havbase_arktis.

Orsolini, Y. J., and A. Sorteberg, 2009: Projected changes in Eurasian and Arctic summer cyclones under global warming in the Bergen climate model. *Atmos. Ocean. Sci. Lett.*, **2 (1)**, 62–67.

Pachauri, R. K., and Coauthors, 2014: *Climate change 2014: synthesis report. Contribution of Working Groups I, II and III to the fifth assessment report of the Intergovernmental Panel on Climate Change*. IPCC.

Parkinson, C. L., and J. C. Comiso, 2013: On the 2012 record low Arctic sea ice cover: Combined impact of preconditioning and an august storm. *Geophys. Res. Lett.*, **40 (7)**, 1356–1361.

Peng, L., X. Zhang, J.-H. Kim, K.-H. Cho, B.-M. Kim, Z. Wang, and H. Tang, 2021: Role

of intense Arctic storm in accelerating summer sea ice melt: an in situ observational study. *Geophys. Res. Lett.*, **48 (8)**, e2021GL092 714.

Persson, P. O. G., C. W. Fairall, E. L. Andreas, P. S. Guest, and D. K. Perovich, 2002: Measurements near the Atmospheric Surface Flux Group tower at SHEBA: Near-surface conditions and surface energy budget. *J. Geophys. Res.: Oceans*, **107 (C10)**, SHE–21.

Petrick, S., K. Riemann-Campe, S. Hoog, C. Growitsch, H. Schwind, R. Gerdes, and K. Rehdanz, 2017: Climate change, future Arctic sea ice, and the competitiveness of European Arctic offshore oil and gas production on world markets. *Ambio*, **46 (3)**, 410–422.

Pinto, J. G., M. K. Karremann, K. Born, P. M. Della-Marta, and M. Klawa, 2012: Loss potentials associated with European windstorms under future climate conditions. *Climate Research*, **54 (1)**, 1–20.

Pinto, J. G., T. Spangehl, U. Ulbrich, and P. Speth, 2005: Sensitivities of a cyclone detection and tracking algorithm: individual tracks and climatology. *Meteor. Z.*, **14 (6)**, 823–838.

Pinto, J. G., S. Ulbrich, T. Economou, D. B. Stephenson, M. K. Karremann, and L. C. Shaffrey, 2016: Robustness of serial clustering of extratropical cyclones to the choice of tracking method. *Tellus*, **68 (1)**, 32 204.

Pithan, F., and Coauthors, 2016: Select strengths and biases of models in representing the Arctic winter boundary layer over sea ice: the Larcform 1 single column model inter-comparison. *J. Adv. Model. Earth Syst.*, **8 (3)**, 1345–1357.

Raible, C., P. Della-Marta, C. Schwierz, H. Wernli, and R. Blender, 2008: Northern Hemisphere extratropical cyclones: A comparison of detection and tracking methods and different reanalyses. *Mon. Weather Rev.*, **136 (3)**, 880–897.

Reed, R. J., and B. A. Kunkel, 1960: The Arctic circulation in summer. *J. Meteorol.*, **17 (5)**, 489–506.

Rigor, I. G., R. L. Colony, and S. Martin, 2000: Variations in surface air temperature observations in the Arctic, 1979–97. *J. Clim.*, **13 (5)**, 896–914.

Rudeva, I., and S. K. Gulev, 2007: Climatology of cyclone size characteristics and their changes during the cyclone life cycle. *Mon. Weather Rev.*, **135 (7)**, 2568–2587.

Rudeva, I., S. K. Gulev, I. Simmonds, and N. Tilinina, 2014: The sensitivity of characteristics of cyclone activity to identification procedures in tracking algorithms. *Tellus*, **66 (1)**, 24 961.

Saha, S., and Coauthors, 2010: The NCEP climate forecast system reanalysis. *Bull. Am. Meteorol. Soc.*, **91 (8)**, 1015–1058.

Saha, S., and Coauthors, 2014: The NCEP climate forecast system version 2. *J. Clim.*, **27 (6)**, 2185–2208.

Sandu, I., A. Beljaars, P. Bechtold, T. Mauritsen, and G. Balsamo, 2013: Why is it so difficult to represent stably stratified conditions in numerical weather prediction (NWP) models? *J. Adv. Model. Earth Syst.*, **5 (2)**, 117–133.

Schule, J., 1966: Sea state. Reinhold Publishing, 786–792 pp.

Schultz, D. M., 2001: Reexamining the cold conveyor belt. *Monthly Weather Review*, **129 (9)**, 2205–2225.

Schultz, D. M., and K. A. Browning, 2017: What is a sting jet? *Weather*, **72 (3)**, 63–66.

Schultz, D. M., D. Keyser, and L. F. Bosart, 1998: The effect of large-scale flow on low-level frontal structure and evolution in mid-latitude cyclones. *Mon. Weather Rev.*, **126 (7)**,

1767–1791.

Screen, J. A., and I. Simmonds, 2010a: Increasing fall-winter energy loss from the Arctic Ocean and its role in Arctic temperature amplification. *Geophys. Res. Lett.*, **37 (16)**.

Screen, J. A., and I. Simmonds, 2010b: The central role of diminishing sea ice in recent Arctic temperature amplification. *Nature*, **464 (7293)**, 1334–1337.

Seiler, C., and F. W. Zwiers, 2016: How will climate change affect explosive cyclones in the extratropics of the Northern Hemisphere? *Clim. Dyn.*, **46 (11)**, 3633–3644.

Semmler, T., L. Stulic, T. Jung, N. Tilinina, C. Campos, S. Gulev, and D. Koracin, 2016: Seasonal atmospheric responses to reduced Arctic sea ice in an ensemble of coupled model simulations. *J. Clim.*, **29 (16)**, 5893–5913.

Sepp, M., and J. Jaagus, 2011: Changes in the activity and tracks of Arctic cyclones. *Clim. Change.*, **105 (3-4)**, 577–595.

Serreze, M., J. Box, R. Barry, and J. Walsh, 1993: Characteristics of Arctic synoptic activity, 1952–1989. *Meteorol. Atmos. Phys.*, **51 (3)**, 147–164.

Serreze, M. C., 1995: Climatological aspects of cyclone development and decay in the Arctic. *Atmos.-Ocean*, **33 (1)**, 1–23.

Serreze, M. C., and A. P. Barrett, 2008: The summer cyclone maximum over the central Arctic Ocean. *J. Clim.*, **21 (5)**, 1048–1065.

Serreze, M. C., and R. G. Barry, 2011: Processes and impacts of Arctic amplification: A research synthesis. *Glob. Planet. Change*, **77 (1-2)**, 85–96.

Serreze, M. C., A. H. Lynch, and M. P. Clark, 2001: The Arctic frontal zone as seen in the NCEP-NCAR reanalysis. *J. Clim.*, **14 (7)**, 1550–1567.

Shapiro, M. A., and D. Keyser, 1990: Fronts, jet streams and the tropopause. *Extratropical Cyclones: The Eric Palmen Memorial Volume*, Springer, 167–191.

Simmonds, I., C. Burke, and K. Keay, 2008: Arctic climate change as manifest in cyclone behavior. *J. Clim.*, **21 (22)**, 5777–5796.

Simmonds, I., and K. Keay, 2009: Extraordinary September Arctic sea ice reductions and their relationships with storm behavior over 1979–2008. *Geophys. Res. Lett.*, **36 (19)**.

Simmonds, I., and I. Rudeva, 2012: The great Arctic cyclone of August 2012. *Geophys. Res. Lett.*, **39 (23)**.

Simpson, C., 1906: The beaufort scale of wind-force report of the director of the meteorological office. Official.

Sinclair, M. R., 1994: An objective cyclone climatology for the Southern Hemisphere. *Mon. Weather Rev.*, **122 (10)**, 2239–2256.

Smith, D. M., and Coauthors, 2019: The Polar Amplification Model Intercomparison Project (PAMIP) contribution to CMIP6: Investigating the causes and consequences of polar amplification. *Geosci. Model Dev.*, **12 (3)**, 1139–1164.

Smith, L. C., and S. R. Stephenson, 2013: New trans-arctic shipping routes navigable by midcentury. *Proceedings of the National Academy of Sciences*, **110 (13)**, E1191–E1195.

Sorteberg, A., and J. E. Walsh, 2008: Seasonal cyclone variability at 70∘N and its impact on moisture transport into the Arctic. *Tellus*, **60 (3)**, 570–586.

Stocker, T. F., and Coauthors, 2014: *Climate change 2013: the physical science basis: Working Group I contribution to the Fifth assessment report of the Intergovernmental Panel on Climate*

Change. Cambridge university press.

Stroeve, J., M. M. Holland, W. Meier, T. Scambos, and M. Serreze, 2007: Arctic sea ice decline: Faster than forecast. *Geophys. Res. Lett.*, **34 (9)**.

Stroeve, J., T. Markus, L. Boisvert, J. Miller, and A. Barrett, 2014: Changes in Arctic melt season and implications for sea ice loss. *Geophys. Res. Lett.*, **41 (4)**, 1216–1225.

Stroeve, J. C., V. Kattsov, A. Barrett, M. Serreze, T. Pavlova, M. Holland, and W. N. Meier, 2012: Trends in Arctic sea ice extent from CMIP5, CMIP3 and observations. *Geophys. Res. Lett.*, **39 (16)**.

Tanaka, H. L., A. Yamagami, and S. Takahashi, 2012: The structure and behavior of the Arctic cyclone in summer analyzed by the JRA-25/JCDAS data. *Polar Sci.*, **6 (1)**, 55–69.

Tao, W., J. Zhang, and X. Zhang, 2017: The role of stratosphere vortex downward intrusion in a long-lasting late-summer Arctic storm. *Q. J. R. Meteorol. Soc.*, **143 (705)**, 1953–1966.

Têtu, P.-L., J. Dawson, and F. Lasserre, 2019: The evolution and relative competitiveness of global Arctic cruise tourism destinations. *Arctic Shipping: Climate Change, Commercial Traffic and Port Development*, 94.

The Arctic Institute, 2013: Arctic Oil and Gas: The Role of Regions. Accessed 01 Feb 2021, https://www.thearcticinstitute.org/arctic-oil-and-gas-role-regions/.

The Polar Connection, 2019: The trillion-dollar reason for an Arctic infrastructure standard. Accessed 28 Jun 2021, https://polarconnection.org/arctic-infrastructure-standard/.

Thomson, J., and W. E. Rogers, 2014: Swell and sea in the emerging Arctic Ocean. *Geophys. Res. Lett.*, **41 (9)**, 3136–3140.

Tilinina, N., S. K. Gulev, and D. H. Bromwich, 2014: New view of Arctic cyclone activity from the Arctic System Reanalysis. *Geophys. Res. Lett.*, **41 (5)**, 1766–1772.

Tilinina, N., S. K. Gulev, I. Rudeva, and P. Koltermann, 2013: Comparing cyclone life cycle characteristics and their inter-annual variability in different reanalyses. *J. Clim.*, **26 (17)**, 6419–6438.

Tous, M., G. Zappa, R. Romero, L. Shaffrey, and P. L. Vidale, 2016: Projected changes in medicanes in the HadGEM3 N512 high-resolution global climate model. *Clim. Dyn.*, **47 (5-6)**, 1913–1924.

United Nations Climate Change, 2021: The Paris Agreement. Accessed 01 June 2021, https://unfccc.int/process-and-meetings/the-paris-agreement/the-paris-agreement.

University of Reading, 2021: Arctic Summertime Cyclones: Dynamics and Sea-Ice Interaction. Accessed 01 June 2021, https://research.reading.ac.uk/arctic-summertime-cyclones/.

UPSCALE, 2021: UPSCALE Project Overview. Accessed 05 Jan 2021, http://proj.badc.rl.ac.uk/upscale.

US Dept. of Defense, 2020: U.S.-British Arctic Exercise Shows U.S. Concern for Region. Accessed 12 Nov 2020, https://www.defense.gov/Explore/News/Article/Article/2180 254/us-british-arctic-exercise-shows-us-concern-for-region/.

Van Vuuren, D. P., and Coauthors, 2011: The representative concentration pathways: An overview. *Clim. Change.*, **109 (1)**, 5–31.

Vavrus, S. J., 2013: Extreme Arctic cyclones in CMIP5 historical simulations. *Geophys. Res. Lett.*, **40 (23)**, 6208–6212.

Vessel Finder, 2021: Free AIS Ship Tracking of Marine Traffic - Vesselfinder. Accessed 01 Jul 2021, https://www.vesselfinder.com/.

Vessey, A. F., K. I. Hodges, L. C. Shaffrey, and J. J. Day, 2020: An inter-comparison of Arctic synoptic scale storms between four global reanalysis datasets. *Clim. Dyn.*, **54 (5)**, 2777–2795.

Walters, D., and Coauthors, 2011: The Met Office Unified Model global atmosphere 3.0/3.1 and JULES global land 3.0/3.1 configurations. *Geosci. Model Dev*, **4**, 919–941.

Wang, C.-C., and J. C. Rogers, 2001: A composite study of explosive cyclogenesis in different sectors of the north atlantic. part i: Cyclone structure and evolution. *Monthly Weather Review*, **129 (6)**, 1481–1499.

Wang, M., and J. Overland, 2012a: Summer Arctic sea ice will be gone sooner or later-an update from CMIP5 models. *Geophys. Res. Lett.*, **39**, L18 501.

Wang, M., and J. E. Overland, 2009: A sea ice free summer Arctic within 30 years? *Geophys. Res. Lett.*, **36 (7)**.

Wang, M., and J. E. Overland, 2012b: A sea ice free summer arctic within 30 years: An update from cmip5 models. *Geophysical Research Letters*, **39 (18)**.

Waseda, T., A. Webb, K. Sato, J. Inoue, A. Kohout, B. Penrose, and S. Penrose, 2018: Correlated increase of high ocean waves and winds in the ice-free waters of the Arctic Ocean. *Sci. Rep.*, **8 (1)**, 1–9.

Woollings, T., B. Harvey, M. Zahn, and L. Shaffrey, 2012: On the role of the ocean in projected atmospheric stability changes in the atlantic polar low region. *Geophys. Res. Lett.*, **39 (24)**.

Yamagami, A., M. Matsueda, and H. L. Tanaka, 2017: Extreme Arctic cyclone in August 2016. *Atmos. Sci. Lett.*, **18 (7)**, 307–314.

Zach Labe, 2021: Arctic Temperatures. Accessed 03 Jun 2021, https://sites.uci.edu/zlabe/arctic-temperatures/.

Zahn, M., M. Akperov, A. Rinke, F. Feser, and I. I. Mokhov, 2018: Trends of cyclone characteristics in the Arctic and their patterns from different reanalysis data. *J. Geophys. Res.: Atmos.*, **123 (5)**, 2737–2751.

Zappa, G., L. Shaffrey, and K. Hodges, 2014: Can polar lows be objectively identified and tracked in the ECMWF operational analysis and the ERA-Interim reanalysis? *Mon. Weather Rev.*, **142 (8)**, 2596–2608.

Zappa, G., L. C. Shaffrey, K. I. Hodges, P. G. Sansom, and D. B. Stephenson, 2013: A multimodel assessment of future projections of North Atlantic and European extratropical cyclones in the CMIP5 climate models. *J. Clim.*, **26 (16)**, 5846–5862.

Zhang, X., and J. E. Walsh, 2006: Toward a seasonally ice-covered Arctic Ocean: Scenarios from the IPCC AR4 model simulations. *Journal of Climate*, **19 (9)**, 1730–1747.

Zhang, X., J. E. Walsh, J. Zhang, U. S. Bhatt, and M. Ikeda, 2004: Climatology and interannual variability of Arctic cyclone activity: 1948-2002. *J. Clim.*, **17 (12)**, 2300–2317.

Appendix A

Chapter 2 Supplementary Material

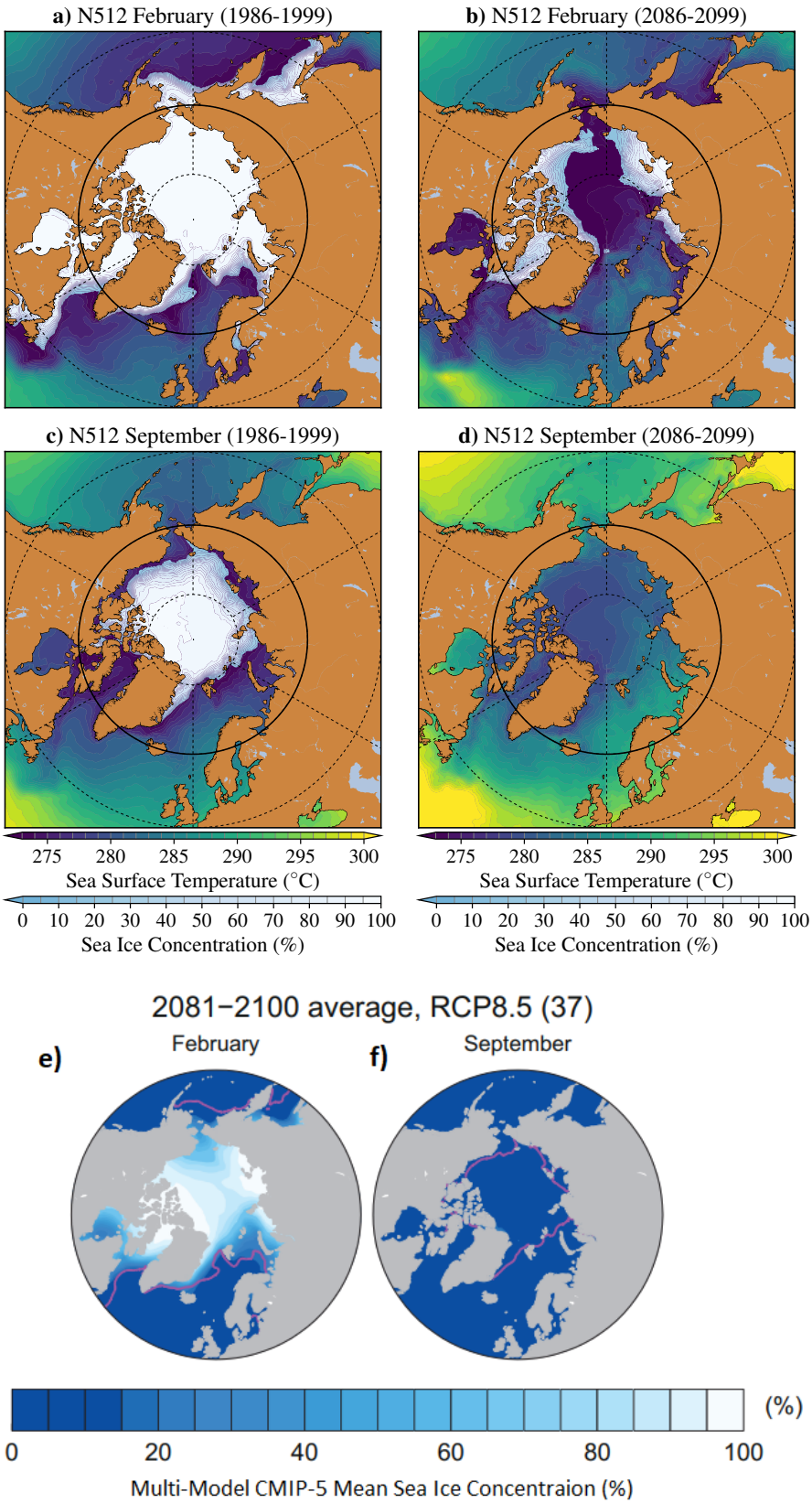

Figure A.1: Change in **a) and b)** February and **c) and d)** September sea surface temperature (SST) and sea ice extent in the **N512** HadGEM3-GA3.0 **a) and c)** present climate (1986-2010) and **b) and d)** RCP8.5 future climate simulations (2086-2110). **e) and f)** show the multi-model mean CMIP-5 change in February and September Arctic sea ice extent in a RCP8.5 future climate (2081-2100) from Collins et al. (2013).

Appendix B

Chapter 3 Supplementary Material

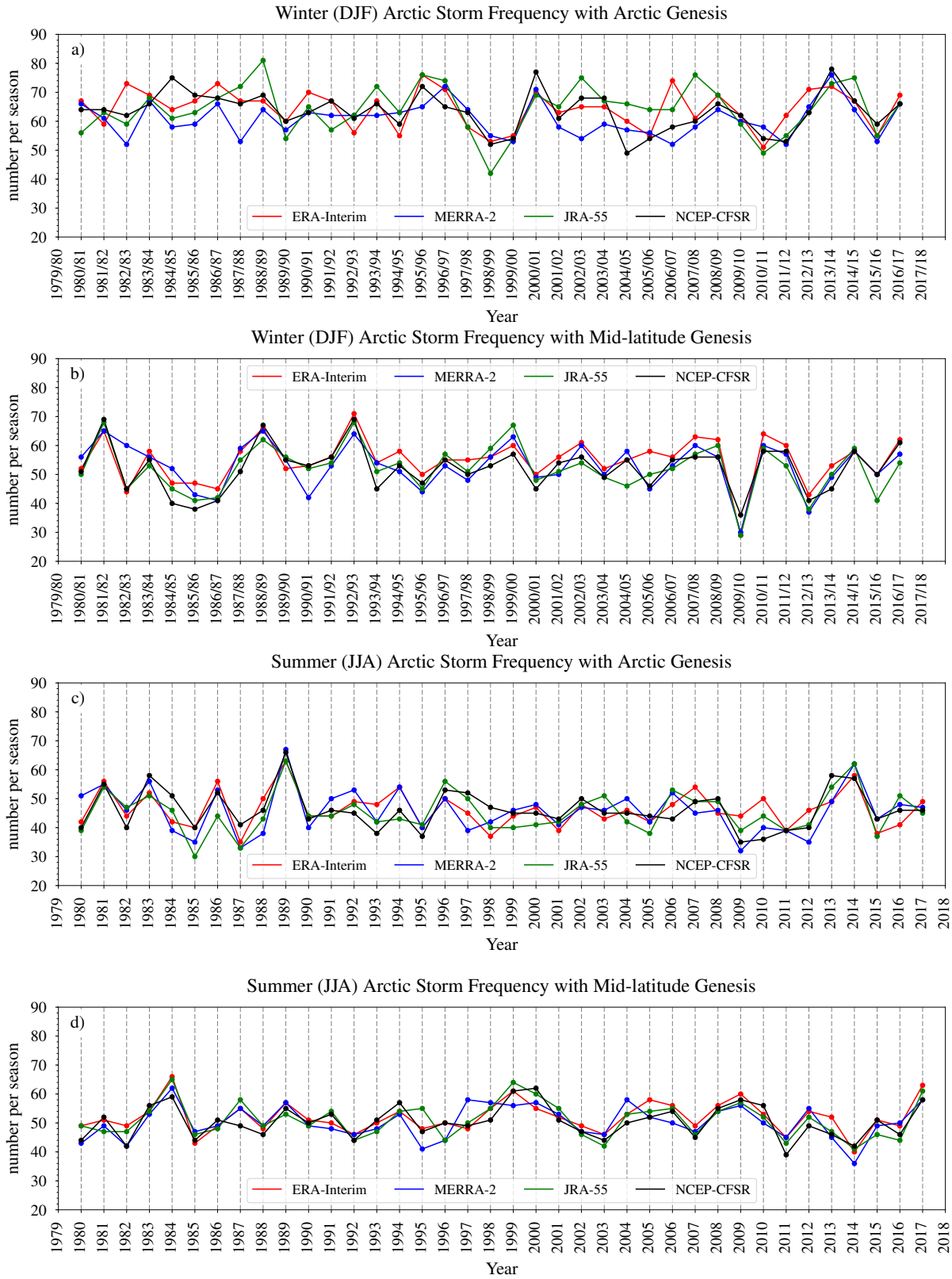

Figure B.1: A time series of the frequency of all Arctic storms that travel north of 65°N that have Arctic genesis (north of 65°N) or mid-latitude genesis (south 65°N) from the ERA-Interim, JRA-55, MERRA-2 and NCEP-CFSR reanalysis dataset between 1980/81-2016/17 in winter (DJF) and 1980-2017 in summer (JJA). **a)** winter (DJF) Arctic storm frequency of storms with Arctic genesis, **b)** winter (DJF) Arctic storm frequency of storms with mid-latitude genesis, **c)** summer (JJA) Arctic storm frequency of storms with Arctic genesis, **d)** summer (JJA) Arctic storm frequency of storms with mid-latitude genesis.

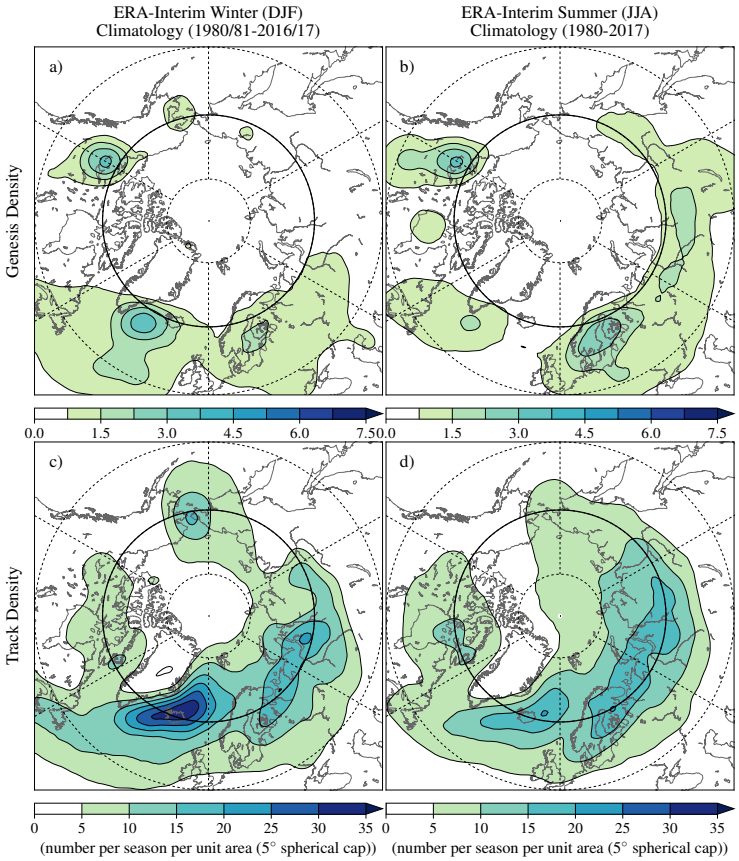

Figure B.2: Climatological winter (DJF) (1980/81-2016/17) and summer (1980-2017) (JJA) storm genesis (**a) and b)**) and track (**c) and d)**) density of Arctic storms with **mid-latitude genesis** (south of 65°N), using ERA-Interim. Densities have units of number per season per unit area (5° spherical cap, $\approx 10^6$ km^2). Longitudes are shown every 60°E, and latitudes are shown at 80°N, 65°N (bold) and 50°N.

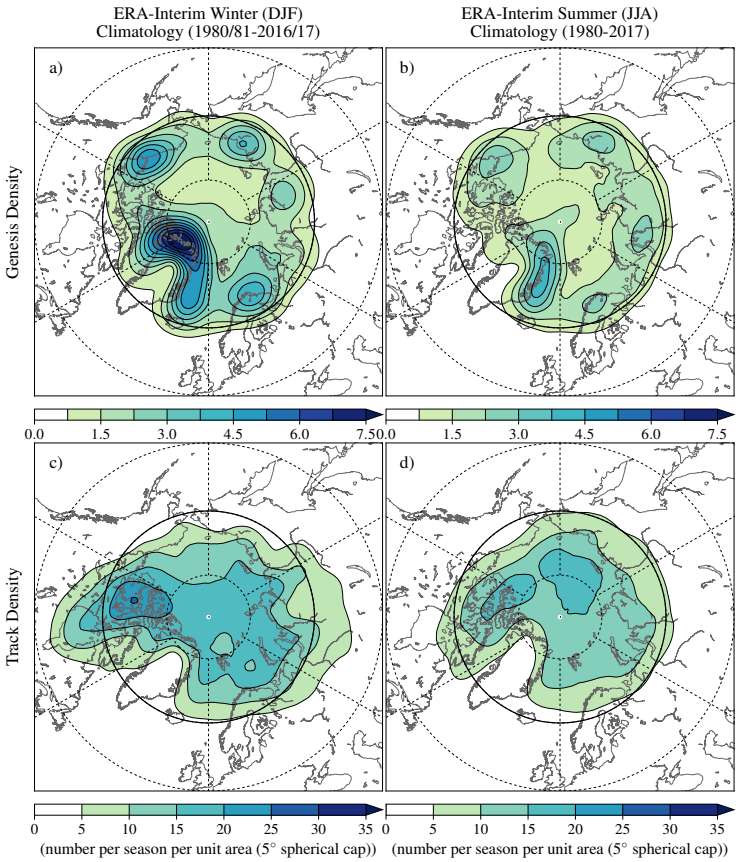

Figure B.3: As Figure B.2, but for Arctic storms with **Arctic genesis** (north of 65°N).

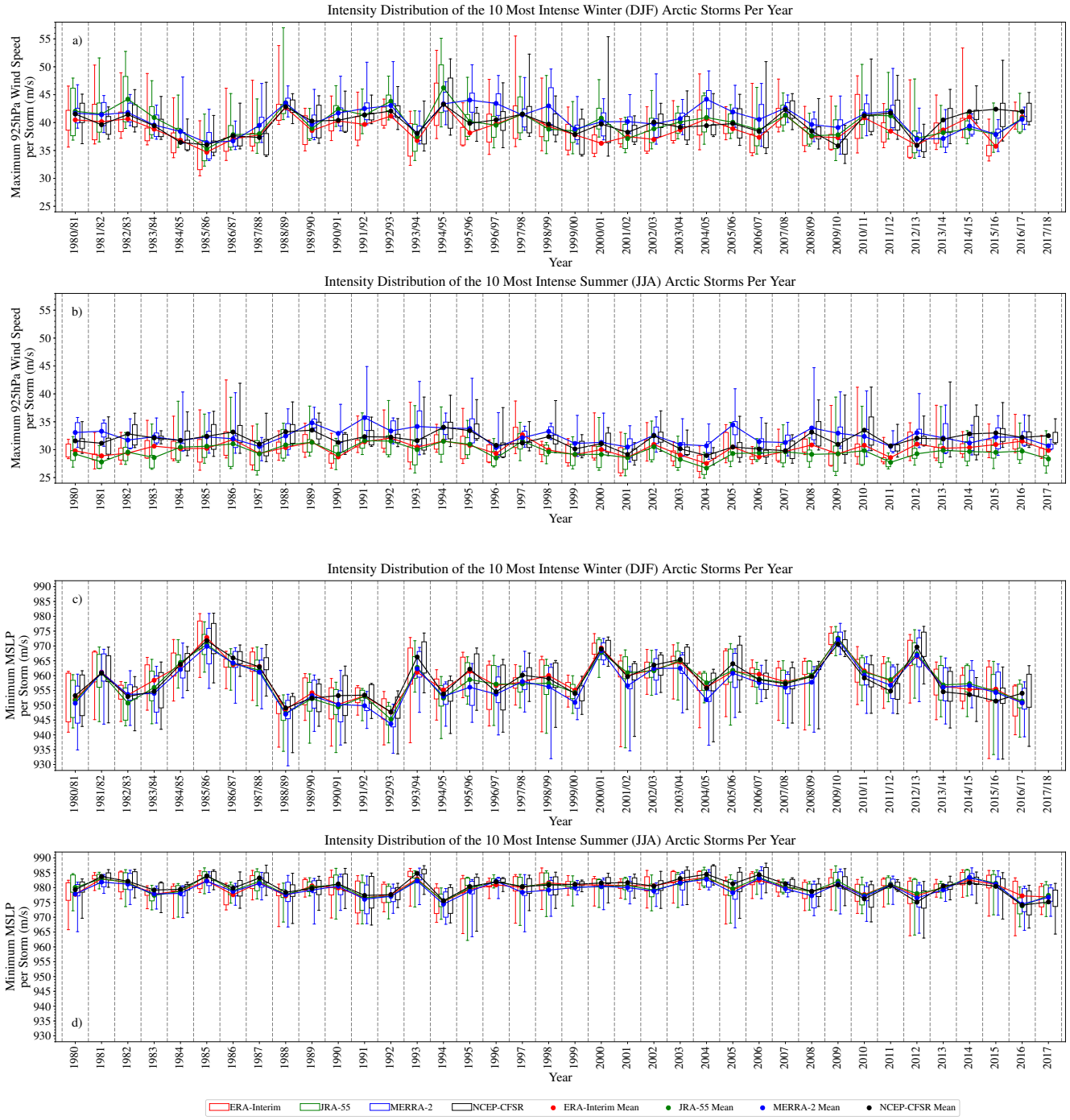

Figure B.4: Distribution of the **a)** and **b)** maximum 925 hPa wind speed, and **c)** and **d)** minimum central mean sea level pressure (MSLP) of the 10 most intense Arctic storms per season between **a)** and **c)** 1980/81-2016/17 in winter (DJF), and **b)** and **d)** 1980-2017 summer (JJA), from ERA-Interim, JRA-55, MERRA-2 and NCEP-CFSR. Intensity is taken when the storm is north of 65°N.

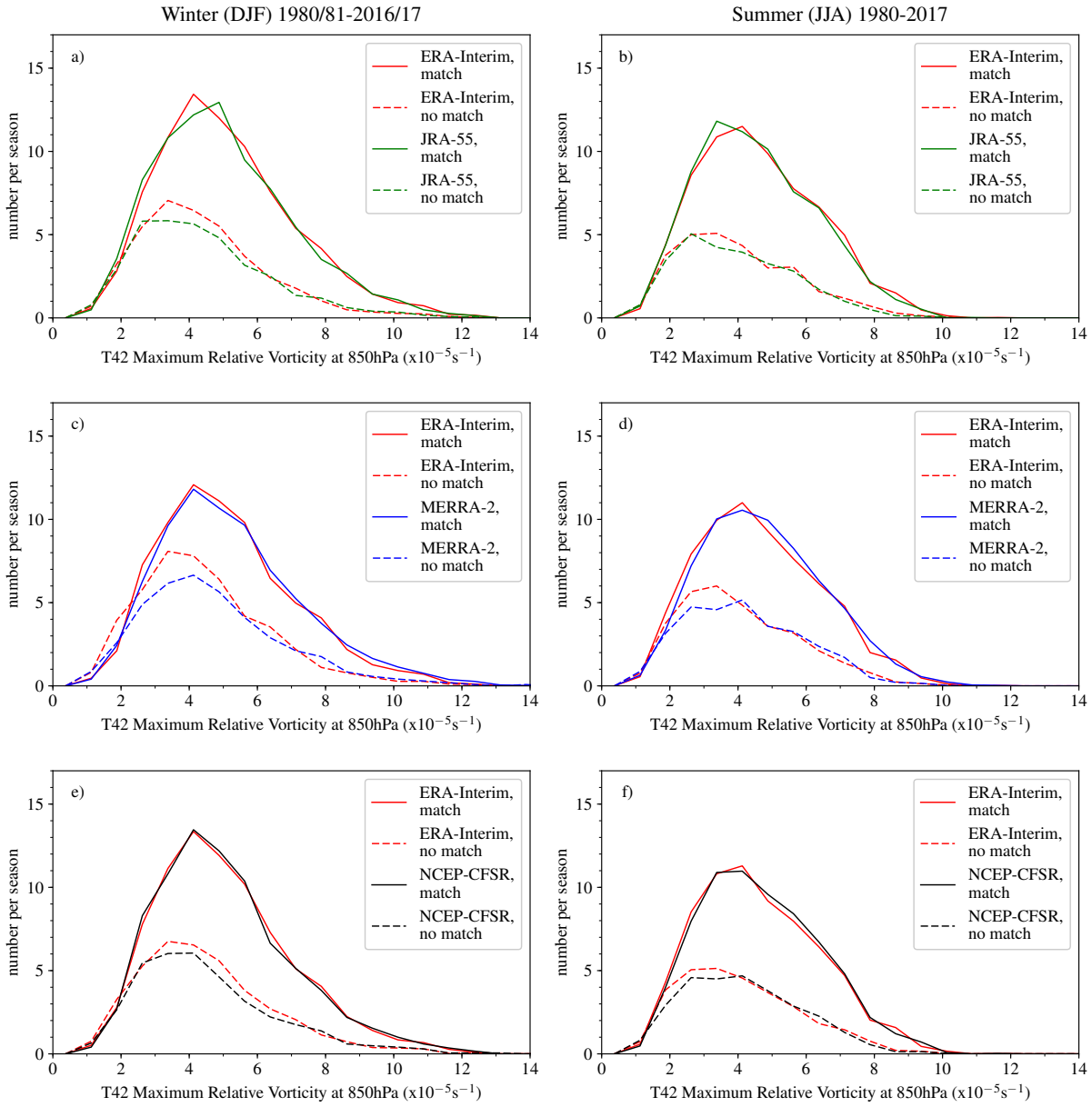

Figure B.5: Maximum 850hPa vorticity distributions of winter (DJF) and summer (JJA) Arctic storms that match between **a) and b)** ERA-Interim and JRA-55, **c) and d)** ERA-Interim and MERRA-2, and **e) and f)** ERA-Interim NCEP-CFSR, using ERA-Interim as a frame of reference, between the period of **a), c) and e)** 1980/81-2016/17 in winter and **b), d) and f)** 1980-2017 in summer. Storms tracks match if the track from the reanalysis datasets are within a distance of 2° (geodesic) and 75% of the track occurs at the same time. Bin widths are 0.75x10^{-5}s^{-1}. Intensity is taken when the storm is north of 65°N.

Table B.1: Percentage of Arctic storms storms that travel and have genesis north of 65°N) and mid-latitude Storms (storms that travel and have genesis between 35°N and 65°N) that match between the ERA-Interim, JRA-55, MERRA-2 and NCEP-CFSR reanalysis datasets in winter (DJF) between 1980/81-2016/17 and in summer (JJA) between 1980-2017. Matching criteria are that the storm tracks must have a mean separation distance less than 2° (geodesic), and overlap in time by at least 75% of the points in their life cycle.

	Winter (DJF)		Summer (JJA)	
	Arctic Storms	Mid-Latitude Storms	Arctic Storms	Mid-Latitude Storms
ERA-Interim, JRA-55	67.5%	69.6%	70.5%	72.3%
ERA-Interim, MERRA-2	61.6%	69.1%	67.0%	66.4%
ERA-Interim, NCEP-CFSR	66.7%	70.8%	69.2%	67.9%
JRA-55, MERRA-2	60.1%	67.4%	65.7%	65.1%
JRA-55, NCEP-CFSR	65.5%	69.4%	67.9%	66.8%
MERRA-2, NCEP-CFSR	64.3%	68.7%	68.9%	67.6%
Average	**64.3%**	**69.2%**	**68.2%**	**67.7%**

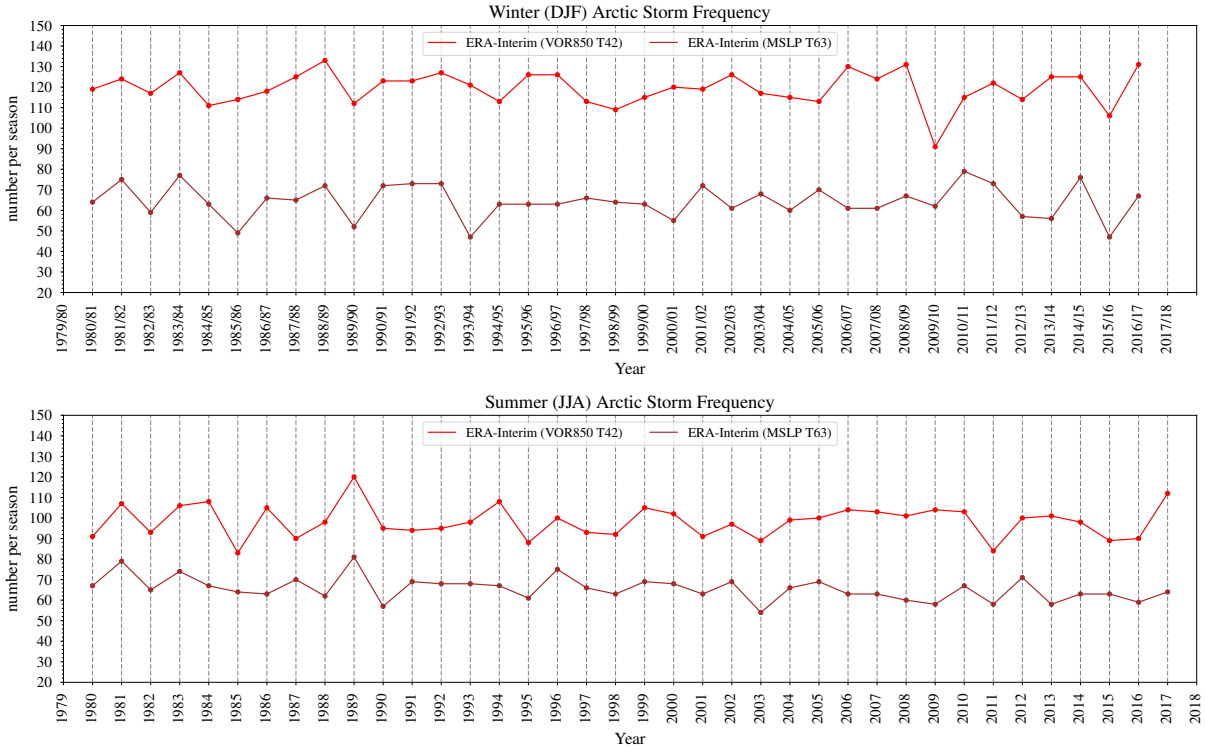

Figure B.6: Number of Arctic storms per season from the ERA-Interim reanalysis dataset when using a storm tracking algorithm using the tracking variable T42 850 hPa relative vorticity (VOR850 T42) and the tracking variable T63 mean sea level pressure (MSLP) (MSLPT63) between (top panel) 1980/81-2016/17 in winter (DJF), and, (bottom panel) 1980-2017 in summer (JJA).

Appendix C

Present-Day Climate Arctic Storm Statistics in the ERA5 Reanalysis Dataset

C.1 Arctic Storm Frequency

Table C.1: Frequency of Arctic storms and the percentage with Arctic (north of 65°N) or mid-latitude genesis (south of 65°N) genesis between ERA5, ERA-Interim, JRA-55, MERRA-2 and NCEP-CFSR, in winter (DJF) (1980/81-2016/17) and summer (JJA) (1980-2017).

	Winter (DJF) (1980/81-2016/17) (per season)			Summer (JJA) (1980-2017) (per season)		
	Total number of Arctic Storms	% of Total with Arctic Genesis	% of Total with Mid-latitude Genesis	Total number of Arctic Storms	% of Total with Arctic Genesis	% of Total with Mid-latitude Genesis
ERA5	118.9	54.7%	45.3%	96.7	48.4%	51.6%
ERA-Interim	119.4	54.0%	46.0%	98.3	47.1%	52.9%
JRA-55	116.3	55.3%	44.7%	96.4	47.0%	53.0%
MERRA-2	113.7	53.4%	46.6%	96.2	47.6%	52.4%
NCEP-CFSR	115.6	54.9%	45.1%	96.6	47.8%	52.2%
Average	**116.3**	**54.4%**	**45.6%**	**96.9**	**47.4%**	**52.6%**

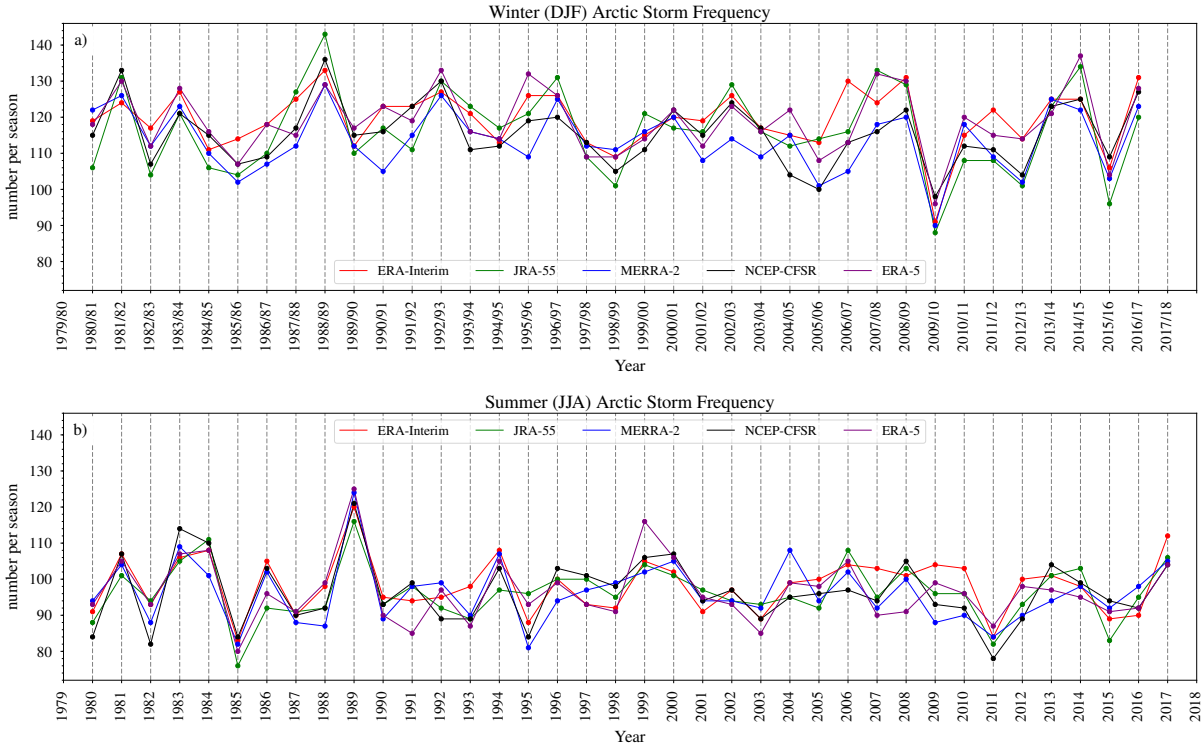

Figure C.1: Number of Arctic storms per season from the ERA-Interim, ERA5, JRA-55, MERRA-2 and NCEP-CFSR reanalysis datasets between **a)** 1980/81-2016/17 in **a)** winter (DJF), and, **b)** 1980-2017 in summer (JJA).

C.2 Arctic Storm Spatial Characteristics

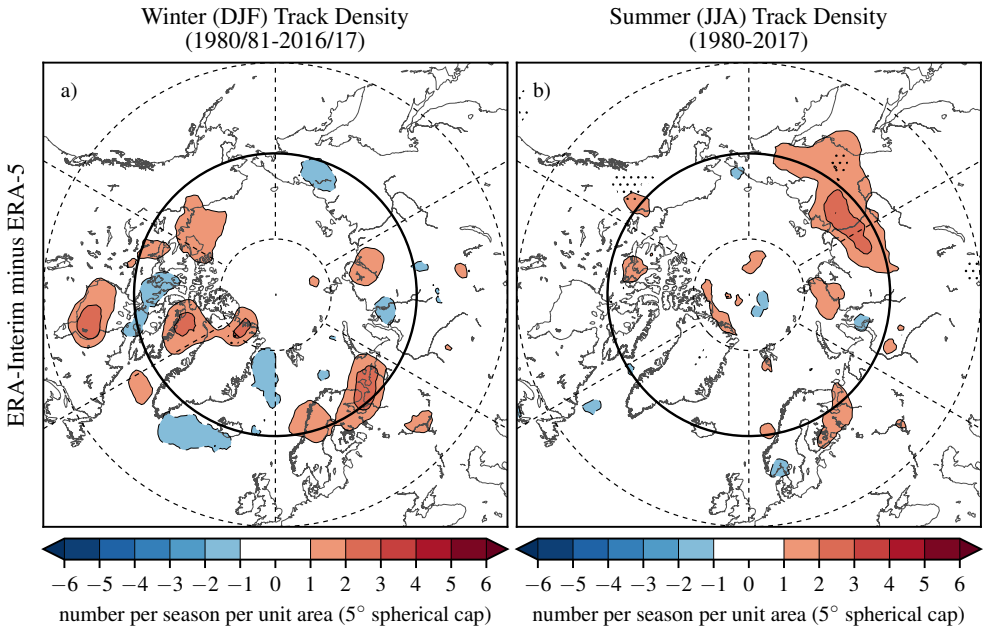

Figure C.2: Differences in the climatological storm track density of Arctic storms between ERA-Interim and ERA5 between **a)** 1980/81-2016/17 in winter (DJF) and **b)** 1980-2017 in summer (JJA). Densities have units of number per season per unit area (5° spherical cap, $\approx 10^6$ km^2). Longitudes are shown every 60°E, and latitudes are shown at 80°N, 65°N (bold) and 50°N. Stippling show areas where the differences are statistically significant to a 95% confidence level. See Figure 3.2 in Chapter 3 for Arctic storm track density from ERA-Interim.

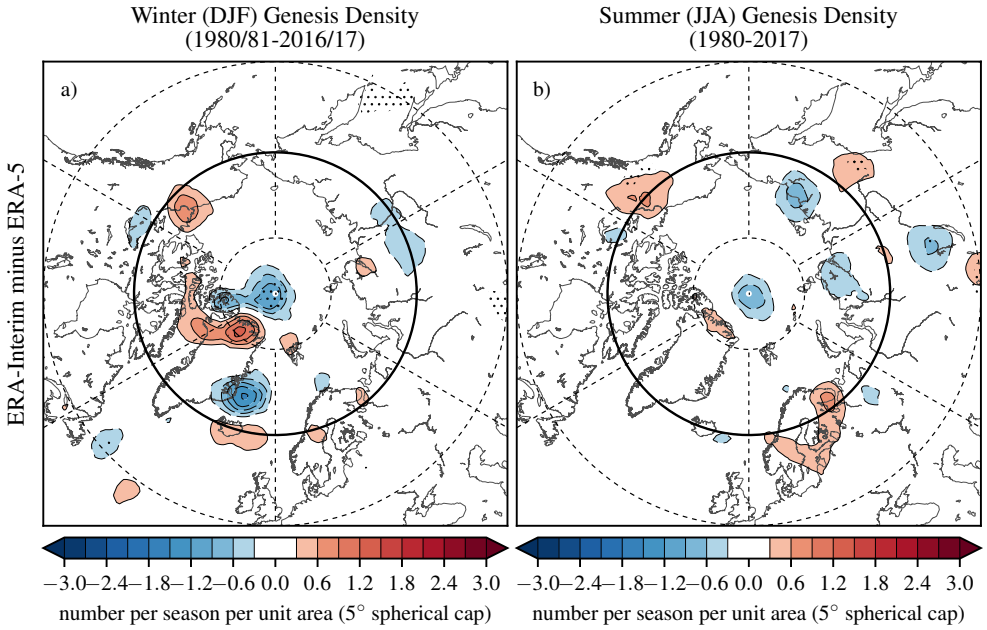

Figure C.3: As Figure C.2, but for Arctic storm genesis density.

Table C.2: Pearson's correlation coefficients of the inter-annual variability in the frequency per season of all Arctic storms, Arctic storms with Arctic genesis (north of 65°N) and Arctic storms with mid-latitude genesis (south of 65°N), between the ERA-Interim, JRA-55, MERRA-2 and NCEP-CFSR reanalysis datasets between 1980/81-2016/17 in winter (DJF) and 1980-2017 in summer (JJA).

	Winter (DJF)			Summer (JJA)		
	All Arctic Storms	Arctic Genesis	Mid-latitude Genesis	All Arctic Storms	Arctic Genesis	Mid-latitude Genesis
ERA5, ERA-Interim	0.79	0.64	0.91	0.82	0.81	0.84
ERA5, JRA-55	0.80	0.57	0.86	0.76	0.67	0.84
ERA5, MERRA-2	0.77	0.56	0.80	0.74	0.78	0.69
ERA5, NCEP-CFSR	0.78	0.58	0.88	0.73	0.72	0.70
ERA-Interim, JRA-55	0.81	0.58	0.89	0.77	0.70	0.86
ERA-Interim, MERRA-2	0.68	0.43	0.80	0.73	0.72	0.79
ERA-Interim, NCEP-CFSR	0.76	0.65	0.88	0.79	0.64	0.82
JRA-55, MERRA-2	0.73	0.42	0.82	0.72	0.73	0.75
JRA-55, NCEP-CFSR	0.78	0.57	0.86	0.80	0.76	0.81
MERRA-2, NCEP-CFSR	0.79	0.62	0.79	0.83	0.71	0.73
Average	**0.77**	**0.56**	**0.85**	**0.77**	**0.77**	**0.78**

C.3 Storm Intensity

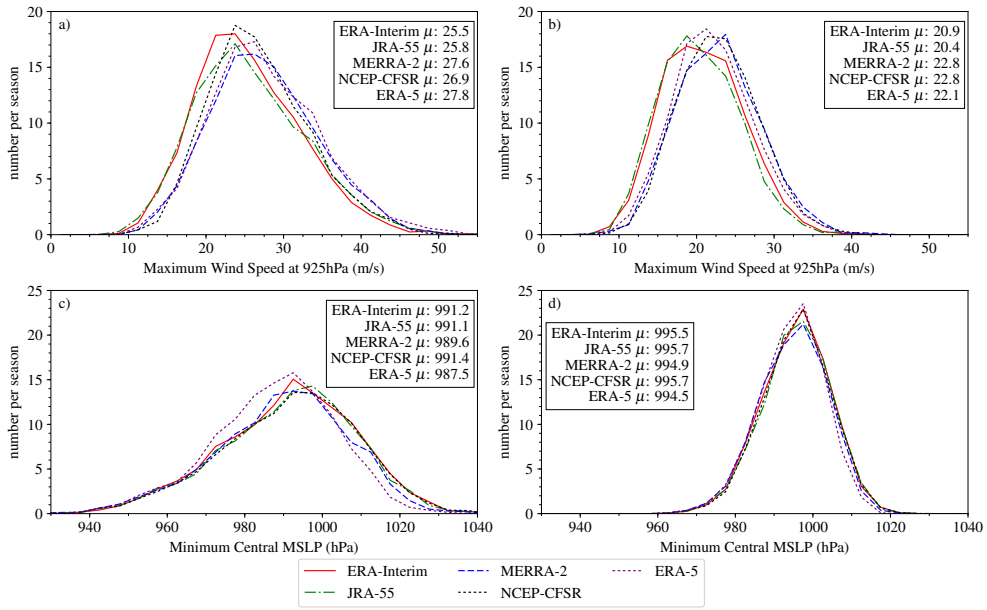

Figure C.4: Frequency distributions of the maximum **a) and b)** 925 hPa wind speed, and **c) and d)** minimum central mean sea level pressure (MSLP) of all winter (DJF) Arctic storms (1980/81-2016/17) (left panel) and summer (JJA) Arctic storms (1980-2017) (right panel) from ERA-Interim, JRA-55, MERRA-2, NCEP-CFSR and ERA5. Bin widths are 2.5m/s for 925 hPa wind speed and 5 hPa for MSLP and the mean (μ) is given for each dataset. Intensity is taken when the storm is north of 65°N.

Appendix D

Spring and Autumn Present-Day Climate Arctic Storm Statistics

D.1 Arctic Storm Frequency

Table D.1: Frequency of Arctic storms and the percentage with Arctic (north of 65°N) or mid-latitude genesis (south of 65°N) genesis between ERA5, ERA-Interim, JRA-55, MERRA-2 and NCEP-CFSR, in spring (MAM) and autumn (SON) between 1980-2017.

	Spring (MAM) (1980-2017) (per season)			Autumn (SON) (1980-2017) (per season)		
	Total number of Arctic Storms	% of Total with Arctic Genesis	% of Total with Mid-latitude Genesis	Total number of Arctic Storms	% of Total with Arctic Genesis	% of Total with Mid-latitude Genesis
ERA5	110.2	53.9%	46.1%	106.4	48.6%	51.4%
ERA-Interim	110.3	52.8%	47.2%	107.0	48.5%	51.5%
JRA-55	107.7	53.1%	46.9%	104.2	49.3%	50.7%
MERRA-2	107.6	53.1%	46.9%	105.3	48.4%	51.6%
NCEP-CFSR	108.3	52.6%	47.4%	105.1	49.5%	50.5%
Average	**116.3**	**54.4%**	**45.6%**	**96.9**	**47.4%**	**52.6%**

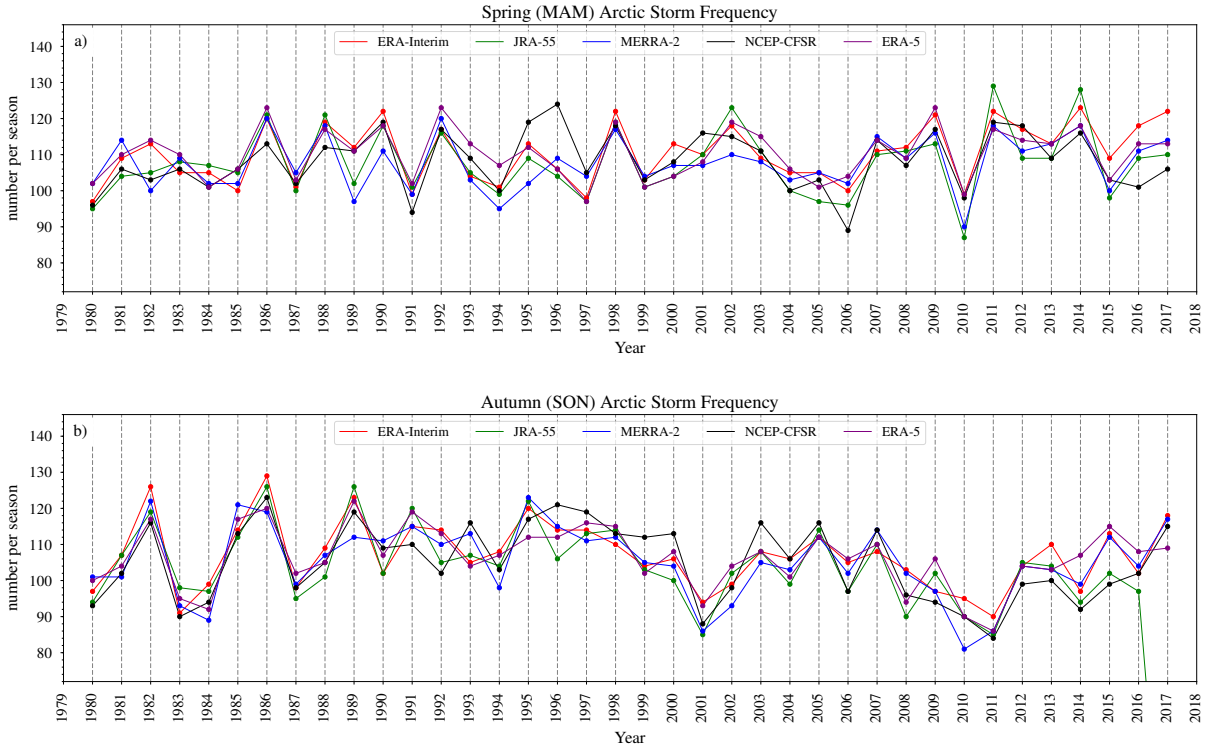

Figure D.1: Number of Arctic storms per season from the ERA-Interim, JRA-55, MERRA-2, NCEP-CFSR and ERA5 reanalysis datasets in **a)** spring (MAM), and, **b)** autumn (SON) between 1980-201.

Table D.2: Pearson correlation coefficients of the inter-annual variability in the frequency per season of all Arctic storms that travel north of 65°N, Arctic storms with Arctic genesis (north of 65°N) and Arctic storms with mid-latitude genesis (south of 65°N), between the ERA-Interim, JRA-55, MERRA-2, NCEP-CFSR and ERA5 reanalysis datasets between 1980-2017 in spring (MAM) and autumn (MAM).

	Spring (MAM)			Autumn (SON)		
	All Arctic Storms	Arctic Genesis	Mid-latitude Genesis	All Arctic Storms	Arctic Genesis	Mid-latitude Genesis
ERA5, ERA-Interim	0.85	0.72	0.85	0.84	0.74	0.85
ERA5, JRA-55	0.83	0.84	0.82	0.86	0.50	0.83
ERA5, MERRA-2	0.75	0.73	0.69	0.85	0.67	0.79
ERA5, NCEP-CFSR	0.68	0.58	0.85	0.77	0.66	0.85
ERA-Interim, JRA-55	0.84	0.66	0.77	0.88	0.71	0.80
ERA-Interim, MERRA-2	0.76	0.55	0.72	0.86	0.69	0.88
ERA-Interim, NCEP-CFSR	0.69	0.57	0.84	0.82	0.71	0.84
JRA-55, MERRA-2	0.81	0.66	0.68	0.81	0.65	0.82
JRA-55, NCEP-CFSR	0.71	0.63	0.78	0.84	0.69	0.86
MERRA-2, NCEP-CFSR	0.62	0.49	0.69	0.85	0.68	0.85
Average	**0.75**	**0.64**	**0.77**	**0.84**	**0.67**	**0.84**

D.2 Arctic Storm Frequency Across All Seasons from All Five Reanalysis Datasets

Table D.3: Number of Arctic storms per season between ERA5, ERA-Interim, JRA-55, MERRA-2, NCEP-CFSR and ERA5, for the period of 1980/81-2016/17 in winter (DJF) and 1980-2017 in spring (MAM), summer (JJA) and autumn (SON). Based on T42 VOR850 tracking method.

	Winter (DJF)	Spring (MAM)	Summer (JJA)	Autumn (SON)
ERA5	118.9	110.2	96.7	106.4
ERA-Interim	119.4	110.3	98.3	107.0
JRA-55	116.3	107.7	96.4	104.2
MERRA-2	113.7	107.6	96.2	105.3
NCEP-CFSR	115.6	108.3	96.6	105.1
Average	**116.8**	**108.8**	**96.8**	**105.6**

D.3 Arctic Storm Spatial Characteristics

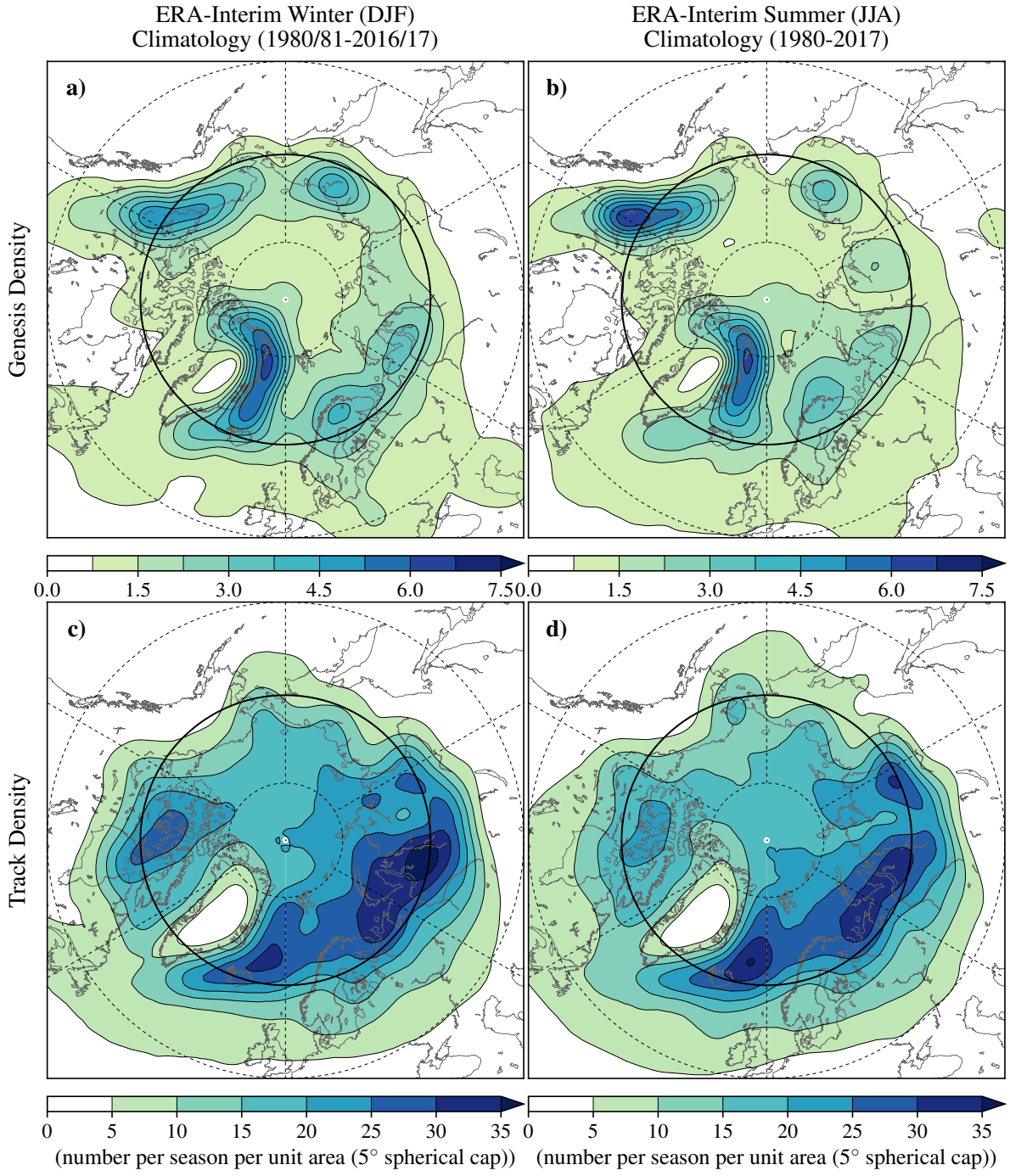

Figure D.2: Climatological **a) and b)** storm genesis and **c) and d)** track density of all Arctic storms that travel north of 65°N between 1980-2017 in spring (MAM) (left panel) and in autumn (SON) (right panel), based on the ERA-Interim reanalysis dataset. Densities have units of number per season per unit area (5° spherical cap, $\approx 10^6$ km^2). Longitudes are shown every 60°E, and latitudes are shown at 80°N, 65°N (bold) and 50°N.

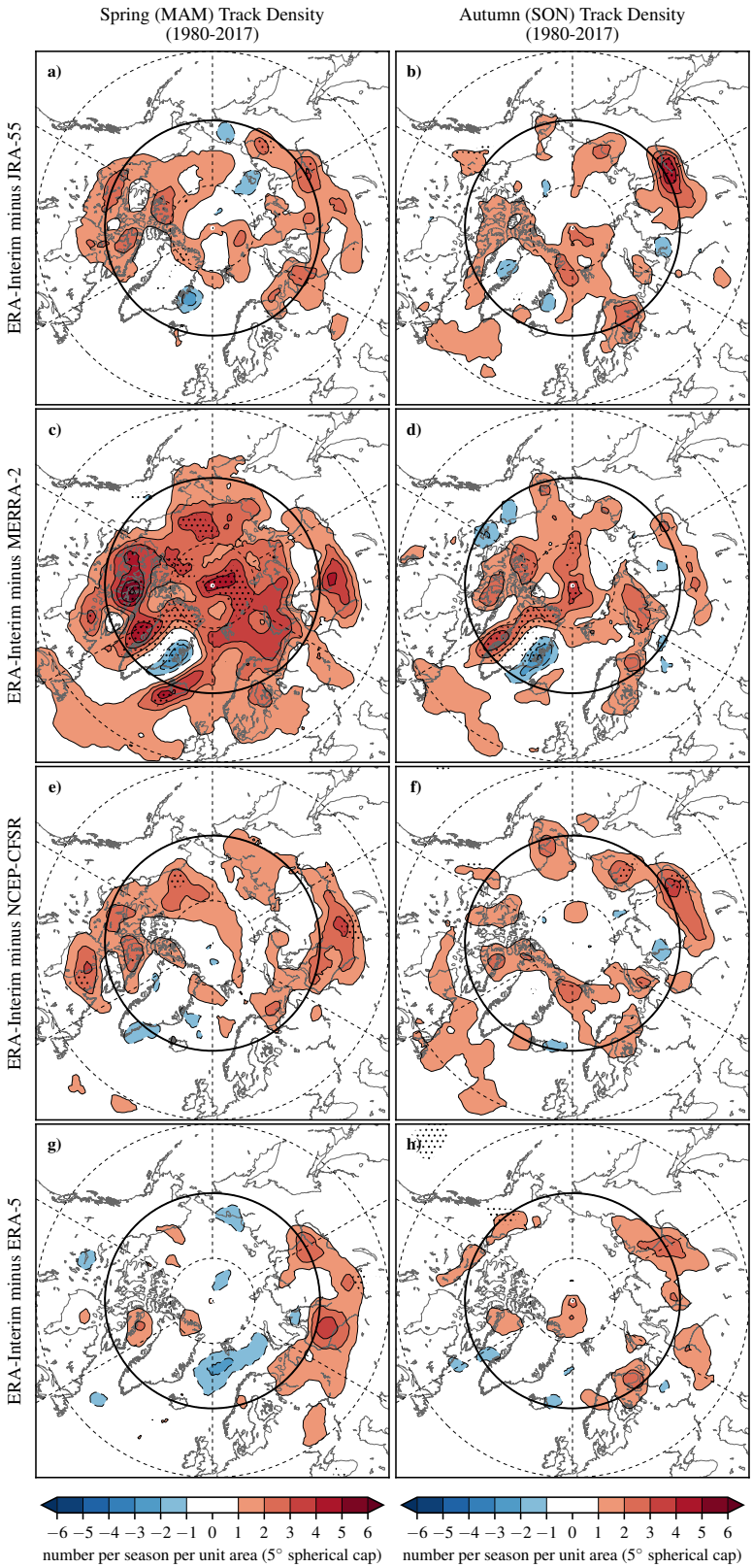

Figure D.3: Differences in the climatological storm track density of all Arctic storms that travel north of 65°N between **a) and b)** ERA-Interim and JRA-55, **c) and d)** ERA-Interim and MERRA-2, **e) and f)** ERA-Interim and NCEP-CFSR, and **g) and h)** ERA-Interim and ERA5 between in spring (MAM) (left panel) and autumn (SON) (right panel) between 1980-2017. Densities have units of number per season per unit area (5° spherical cap, $\approx 10^6$ km^2). Longitudes are shown every 60°E, and latitudes are shown at 80°N, 65°N (bold) and 50°N. Stippling show areas where the differences are statistically significant to a 95% confidence level.

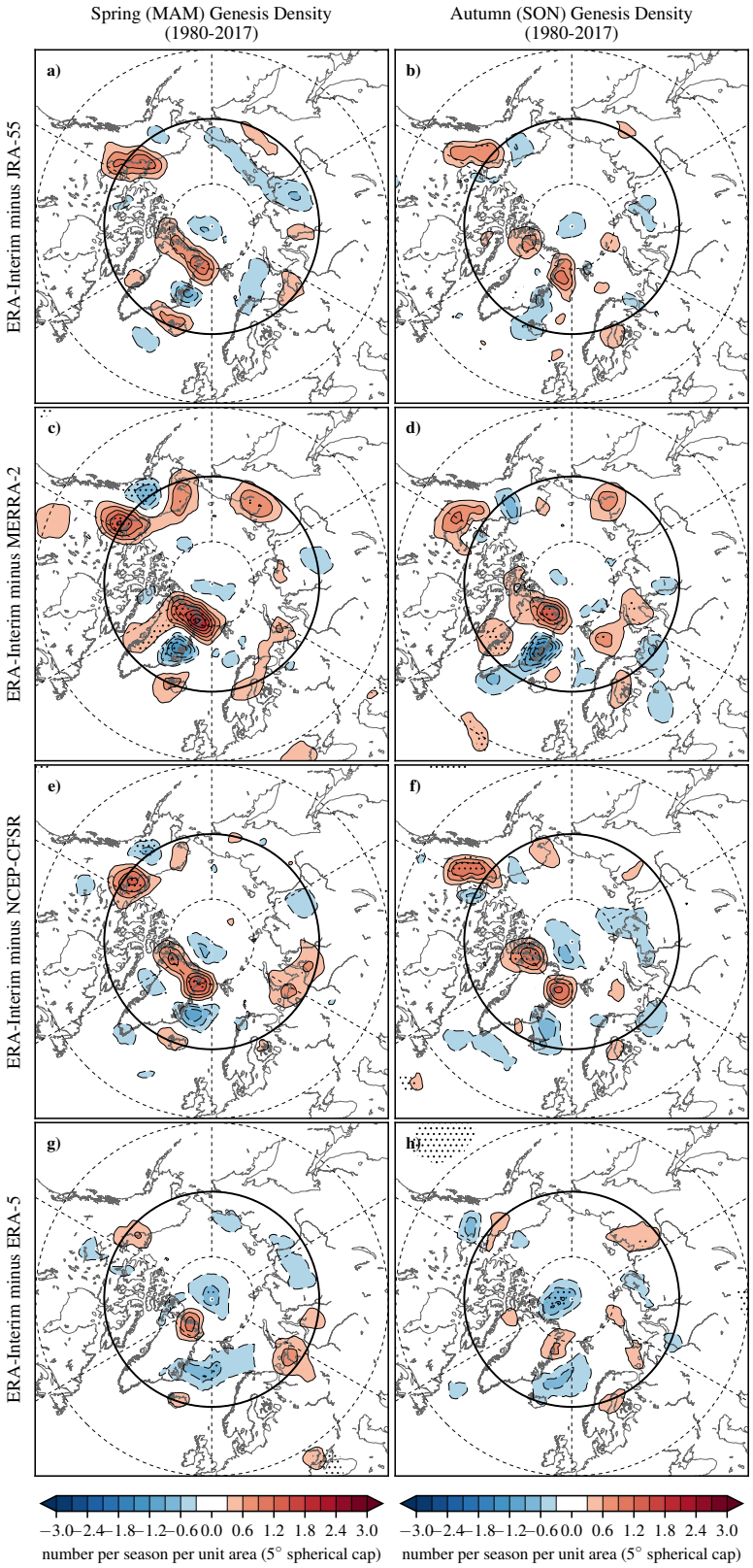

Figure D.4: As Figure D.3, but for Arctic storm genesis density.

D.4 Storm Intensity

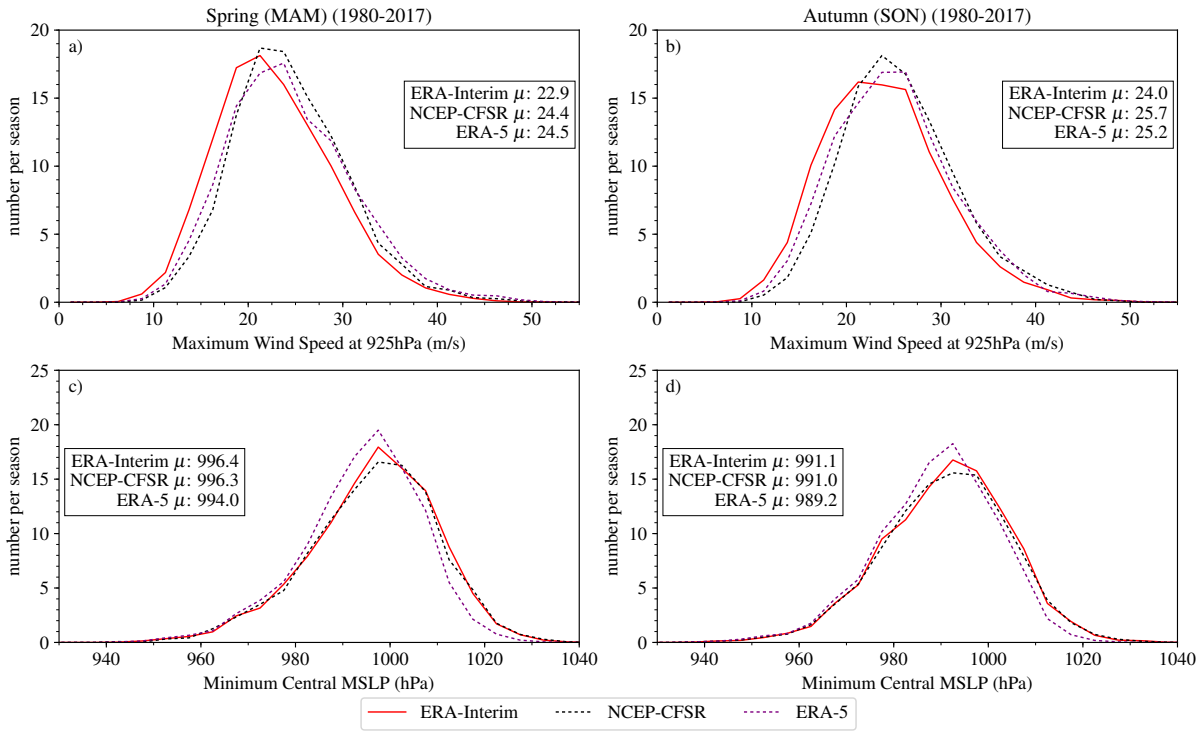

Figure D.5: Frequency distributions of the maximum intensity of **a) and b)** 925 hPa wind speed, and **c) and d)** minimum central mean sea level pressure (MSLP) of all spring (MAM) (left panel) and autumn (SON) Arctic storms between 1980-2017 (right panel) from ERA-Interim, ERA5 and NCEP-CFSR reanalysis datasets. Bin widths are 2.5m/s for 925 hPa wind speed and 5 hPa for MSLP and the mean (μ) of the distribution is given for each dataset. Intensity is taken when the storm is north of 65°N.

D.5 Comparison of the Seasonality in Arctic Storm Frequency between Storm Tracking Identification Variables

Table D.4: Frequency of all Arctic storms that travel north of 65°N in ERA-Interim using a T42 VOR850 tracking method and T63 MSLP tracking method. Between 1980/81-2016/17 in winter (DJF) and 1980-2017 for spring (JJA), summer (JJA) and autumn (SON).

	Winter (DJF)	Spring (MAM)	Summer (JJA)	Autumn (SON)
ERA-Interim T42 VOR850	119.4	110.3	98.3	107.0
ERA-Interim T63 MSLP	64.4	67.8	65.6	68.7

Appendix E

Chapter 4 Supplementary Material

E.1 Spring (MAM) and Autumn (SON) Composites

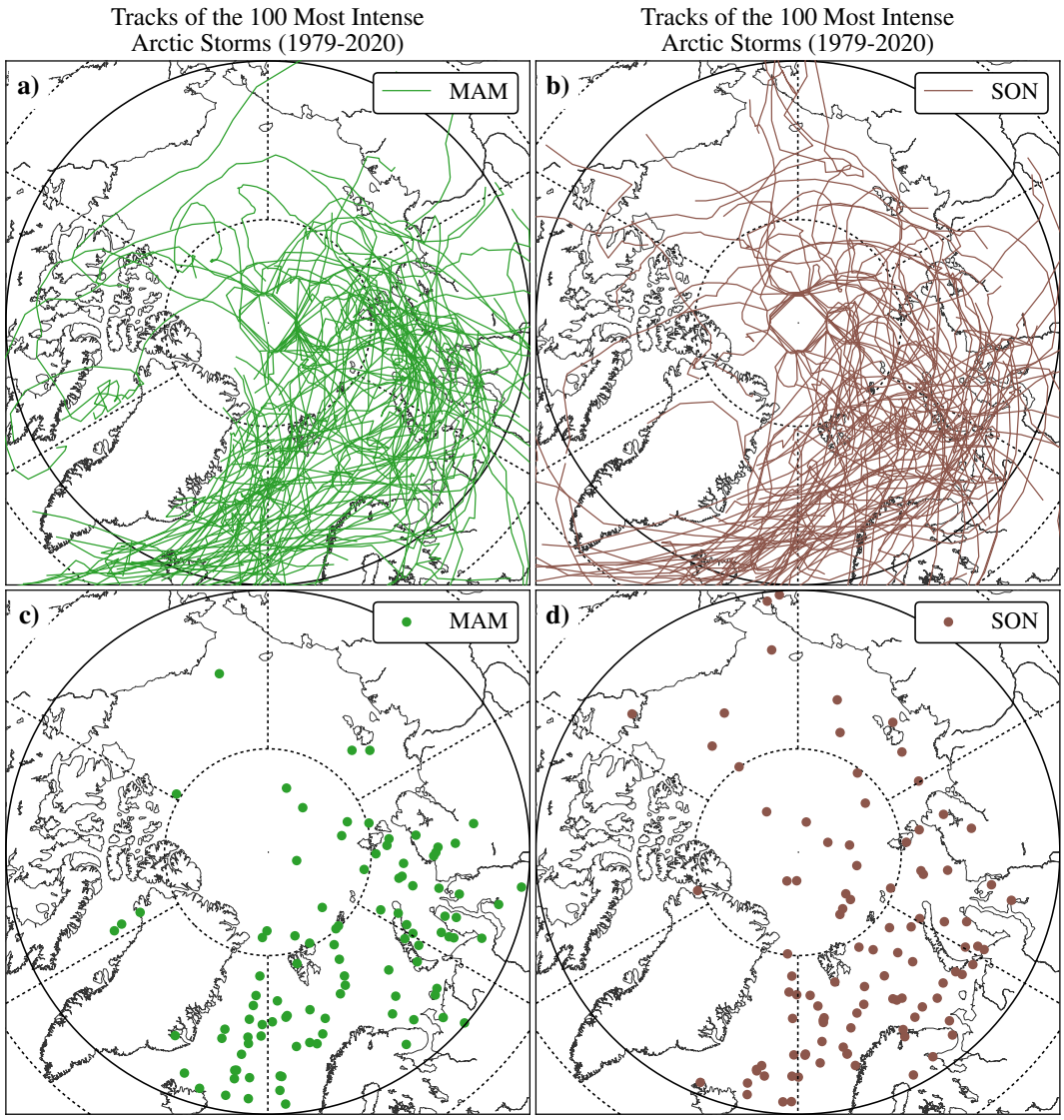

Figure E.1: Individual tracks of the 100 most intense **a)** spring (MAM) and **b)** autumn (SON) Arctic storms, and the locations of the minimum mean sea level pressure of each **c)** winter and **d)** summer storms between 1979 and 2019 based on the ERA5 reanalysis dataset.

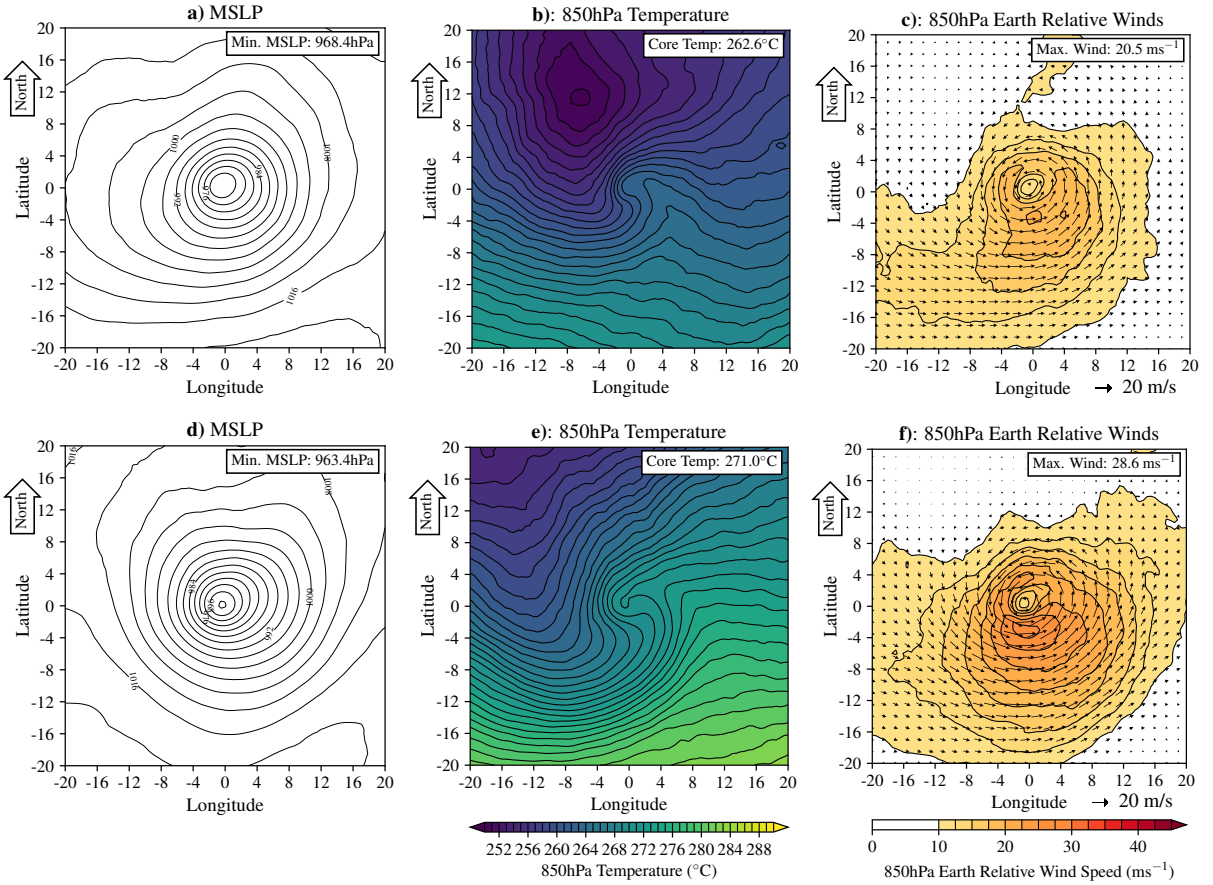

Figure E.2: Horizontal composite structure at the time of maximum intensity (i.e. the time of minimum mean sea level pressure - MSLP) of the 100 most intense spring (MAM) **a) - c)** Arctic storms and **d) - f)** North Atlantic Ocean storms. **a) and d)** show the composite mean sea level pressure (MSLP) structure. **b) and e)** show the composite 850 hPa temperature structure. **c) and f)** show the composite 850 hPa wind speed (contours) and direction (vectors). In producing these composites, storms have not been rotated before averaging, so that the top of each figure is north (see arrow).

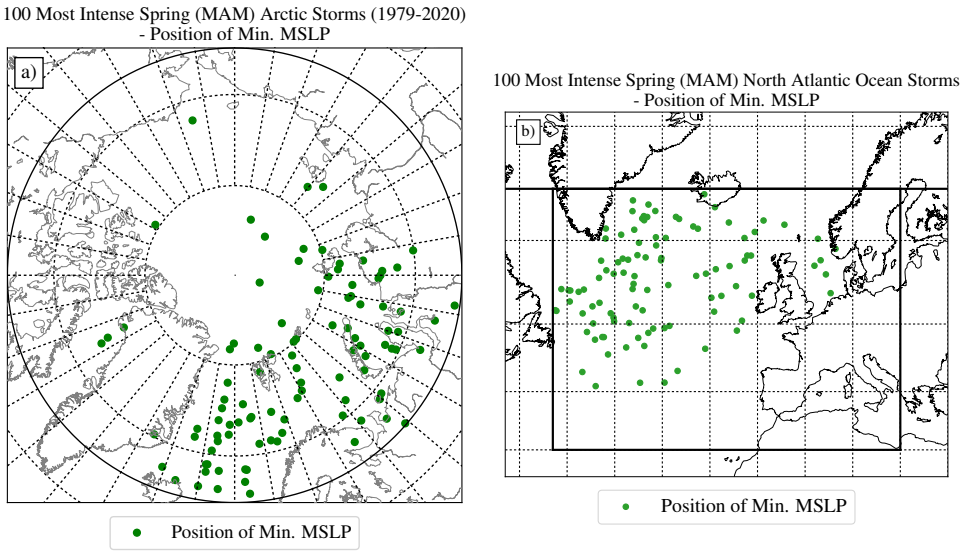

Figure E.3: Locations of the minimum mean sea level pressure (MSLP) of each of the 100 most intense spring (MAM) **a)** Arctic and **b)** North Atlantic Ocean storms between 1979-2020based on ERA5.

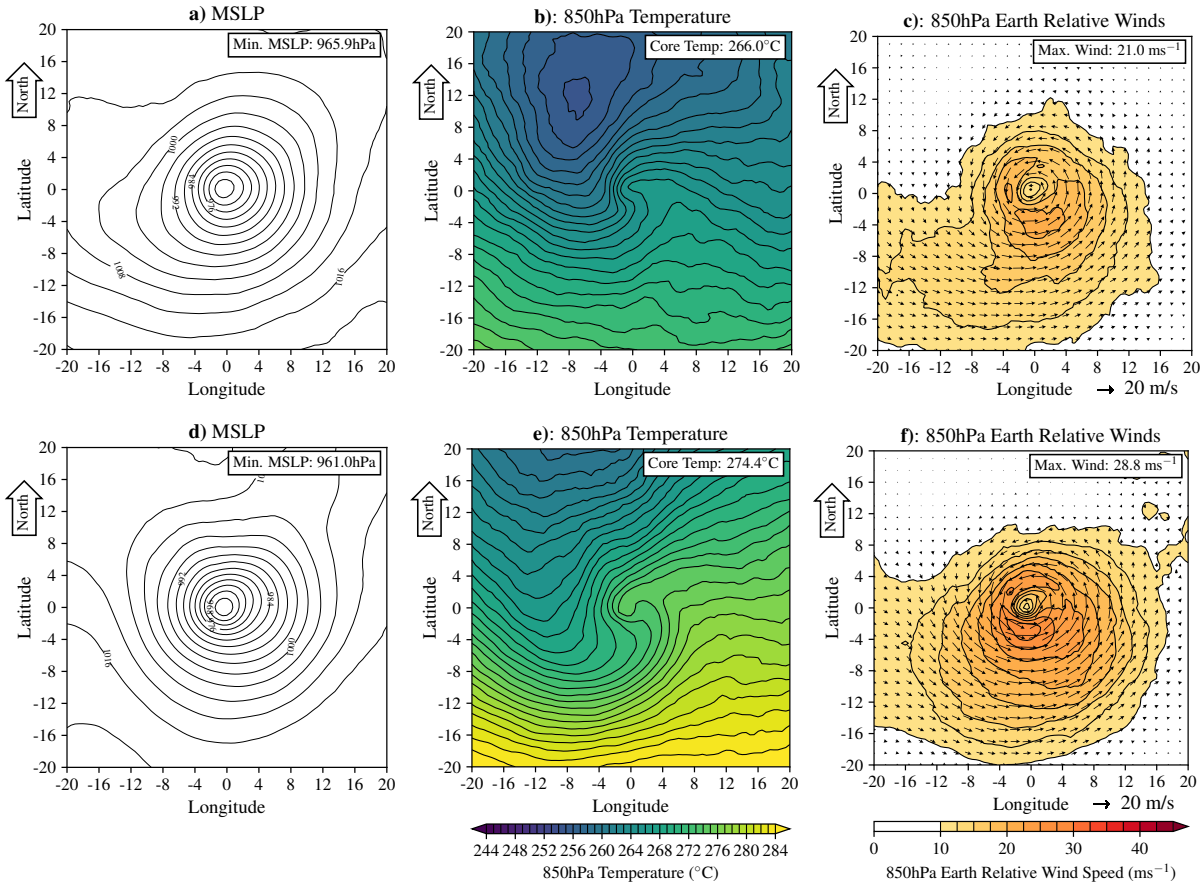

Figure E.4: As for Figure E.2, but for the 100 most intense autumn (SON) Arctic and North Atlantic Ocean storms from 1979-2019 based on ERA5.

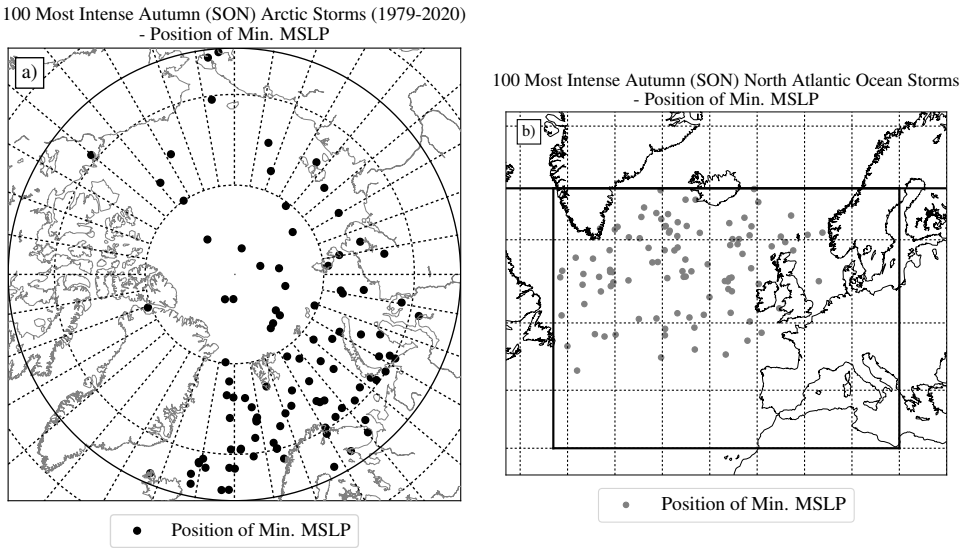

Figure E.5: Locations of the minimum mean sea level pressure (MSLP) of each of the 100 most intense autumn (SON) **a)** Arctic and **b)** North Atlantic Ocean storms between 1979-2020 based on ERA5.

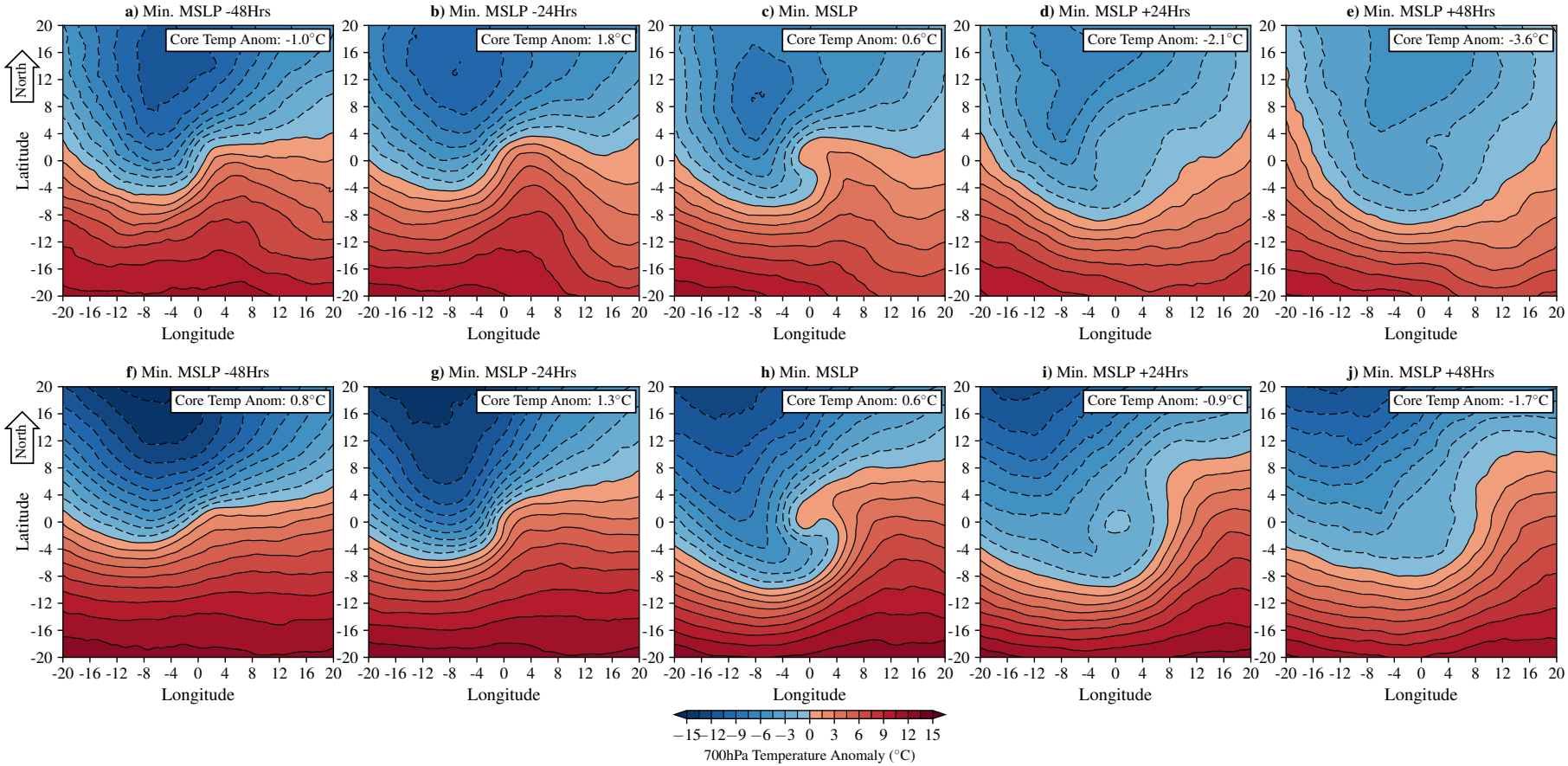

Figure E.6: Horizontal composite 700 hPa (lower tropospheric) temperature anomaly structure of the 100 most spring (MAM) **a) - e)** Arctic storms, and, **f) - j)** North Atlantic Ocean storms, at different stages of the storm cycle. **a) and f)** 48 hours before the time of maximum intensity (i.e. minimum mean sea level pressure), **b) and g)** 24 hours before the time of maximum intensity, **c) and h)** at the time of maximum intensity, **d) and i)** 24 after the time of maximum intensity, and, **e) and j)** 48 hours after the time of maximum intensity. In producing these composites, storms have not been rotated before the composite is made, so that the top of each figure is north (see arrow).

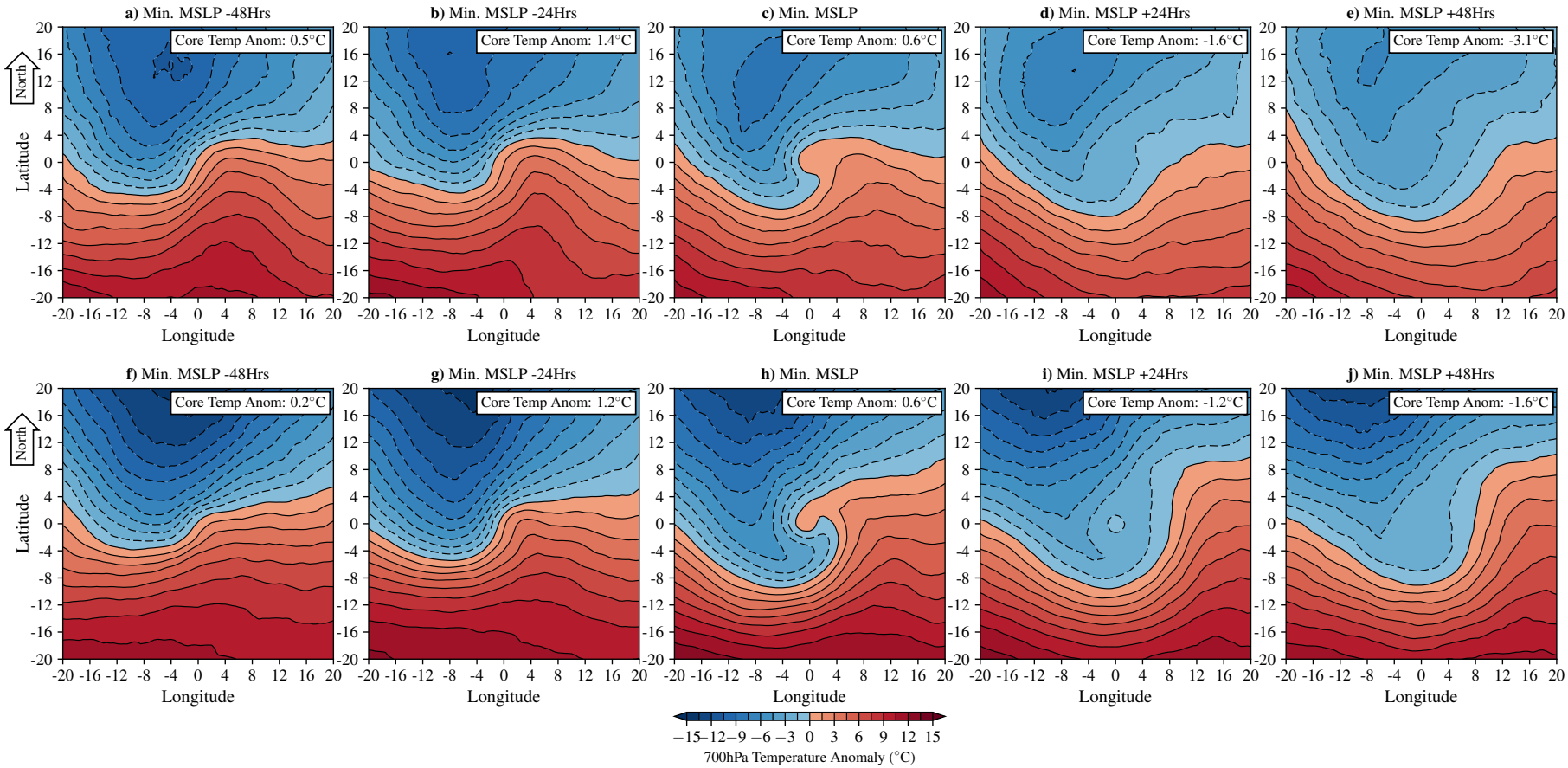

Figure E.7: Horizontal composite 700 hPa (lower tropospheric) temperature anomaly structure of the 100 most autumn (SON) **a) - e)** Arctic storms, and, **f) - j)** North Atlantic Ocean storms, at different stages of the storm cycle. **a) and f)** 48 hours before the time of maximum intensity (i.e. minimum mean sea level pressure), **b) and g)** 24 hours before the time of maximum intensity, **c) and h)** at the time of maximum intensity, **d) and i)** 24 after the time of maximum intensity, and, **e) and j)** 48 hours after the time of maximum intensity. In producing these composites, storms have not been rotated before the composite is made, so that the top of each figure is north (see arrow).

E.2 Winter (DJF) Rotated Composites

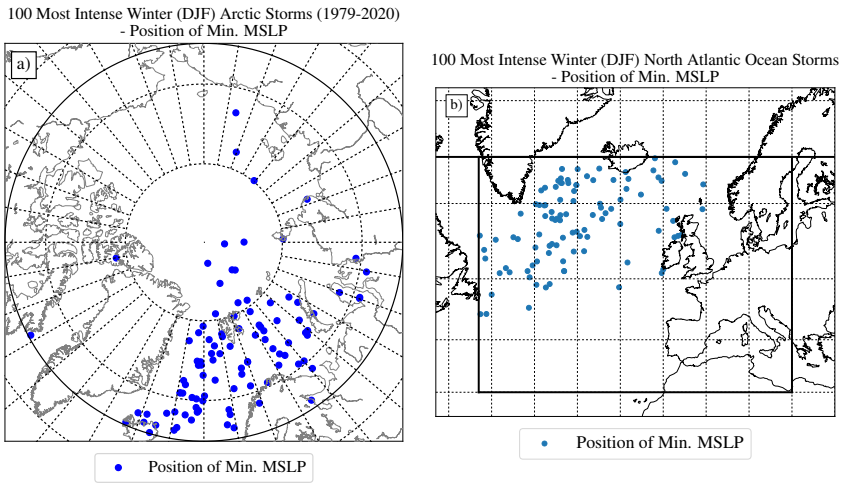

Figure E.8: Locations of the minimum mean sea level pressure (MSLP) of each of the 100 most intense winter (DJF) **a)** Arctic and **b)** North Atlantic Ocean storms between 1979-2020 based on ERA5.

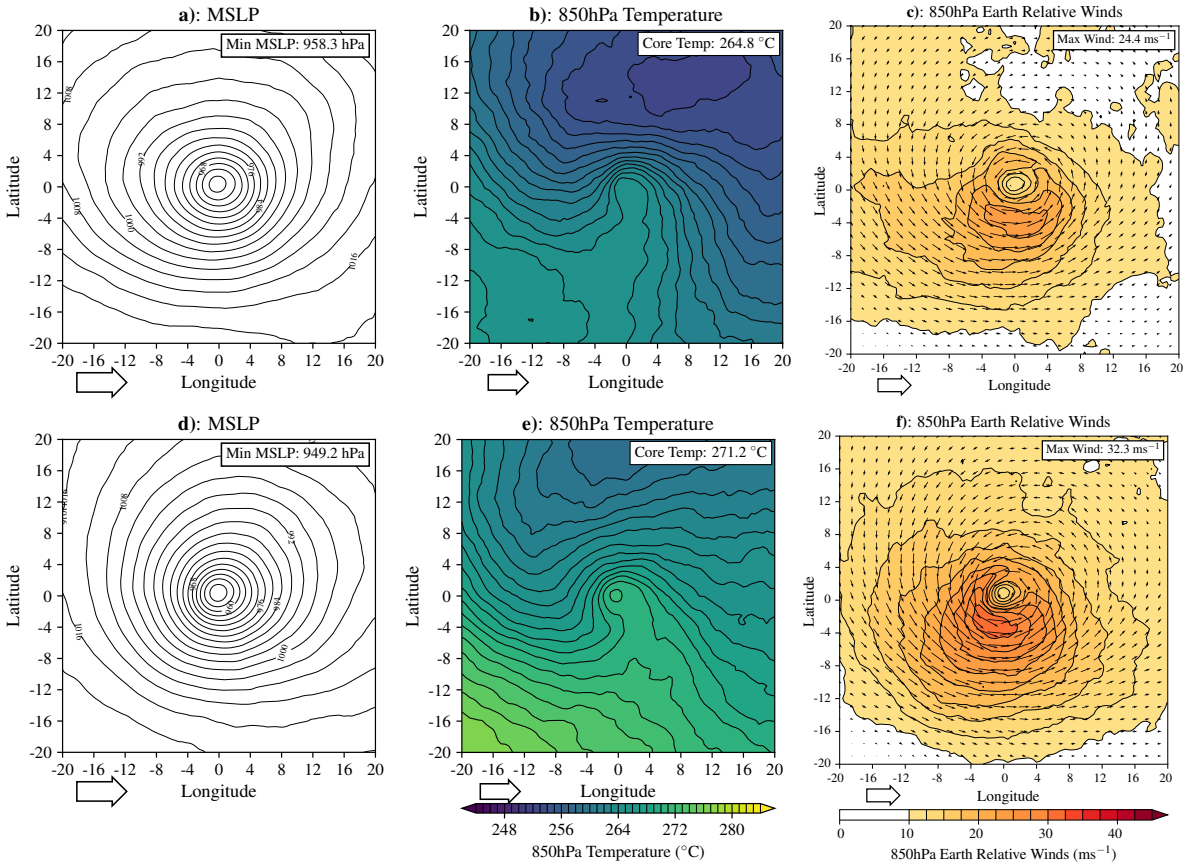

Figure E.9: Horizontal composite structure at the time of maximum intensity (i.e. time of minimum mean sea level pressure - MSLP) of the 100 most intense winter (DJF) **a) - c)** Arctic storms and **d) - f)** North Atlantic Ocean storms. **a) and d)** mean sea level pressure (MSLP) structure, **b) and e)** 850 hPa temperature structure, and **c) and f)** 850 hPa wind speed (contours) and direction (vectors) structure. Storms have been rotated to the direction of propagation before the composite is made (see arrow).

E.3 Summer (JJA) Rotated Composites

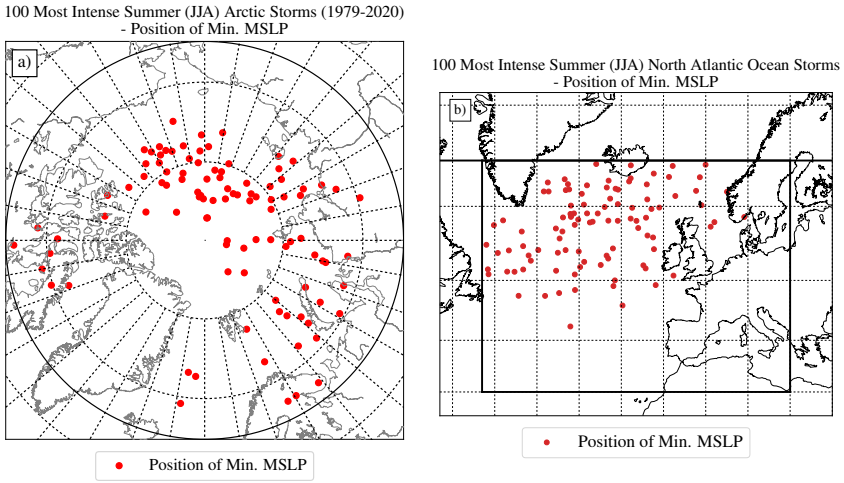

Figure E.10: Locations of the minimum mean sea level pressure (MSLP) of the 100 most intense summer (JJA) **a)** Arctic and **b)** North Atlantic Ocean storms between 1979-2020 from the ERA-5 reanalysis dataset.

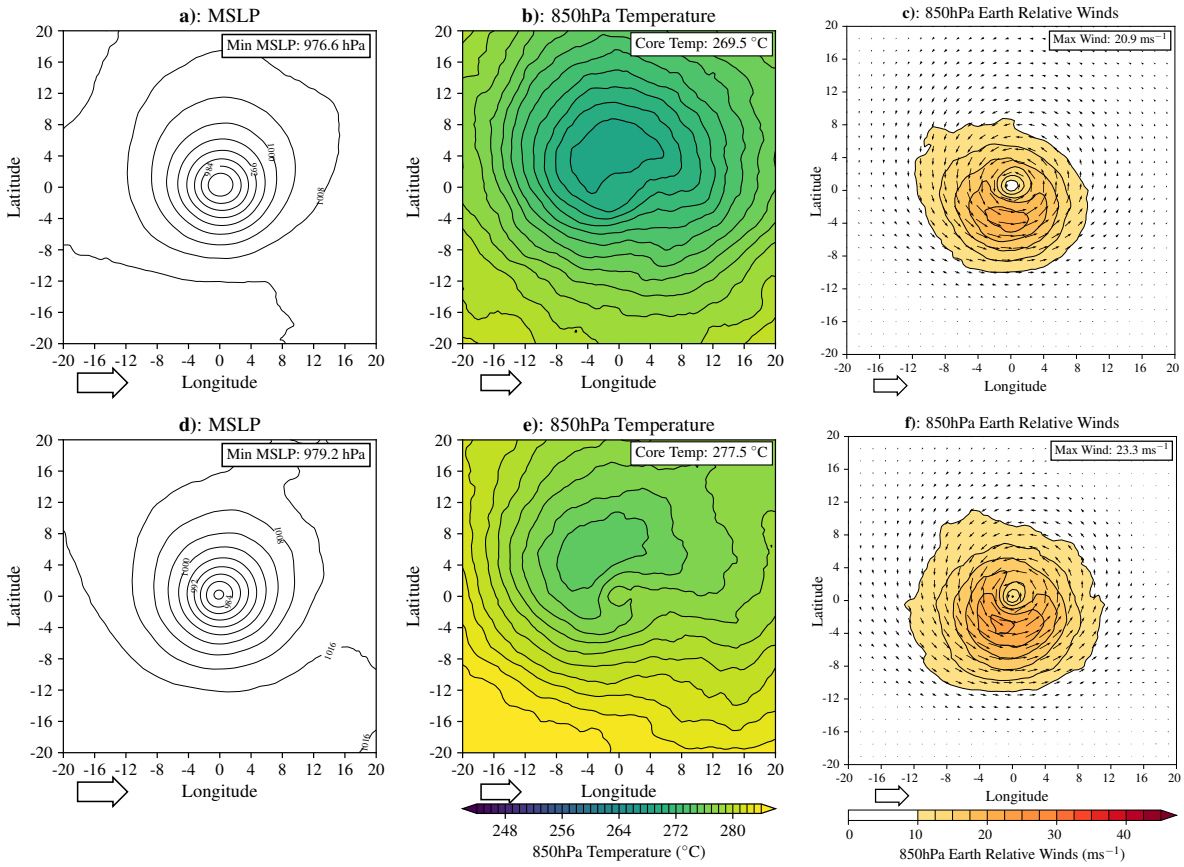

Figure E.11: As Figure E.9, but for the 100 most intense summer (JJA) Arctic and North Atlantic Ocean storms from 1979-2019 based on ERA5.

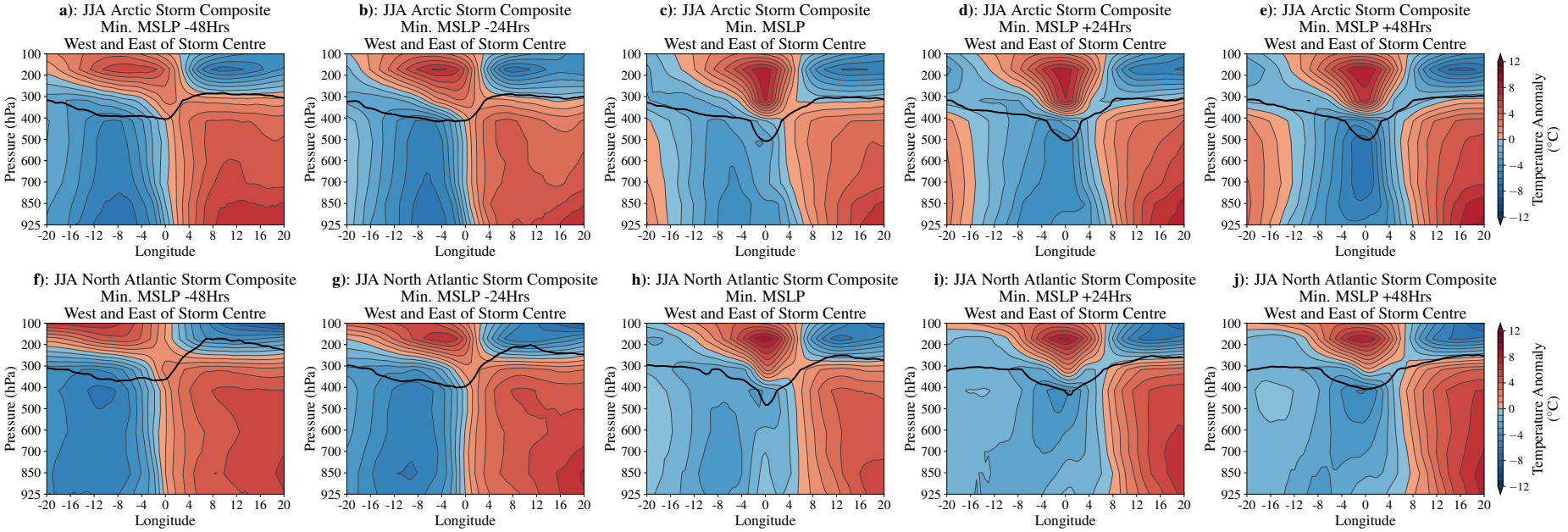

Figure E.12: The change in the vertical temperature composite structure of the 100 most intense summer (JJA) **a) - e)** Arctic storms and **f) - j)** North Atlantic Ocean storms, west to east from the storm centre, at different stages of the storm cycle. **a) and f)** 48 hours before the time of maximum intensity, **b) and g)** 24 hours before the time of maximum intensity, **c) and h)** at the time of maximum intensity, **d) and i)** 24 hours after the time of maximum intensity, and, **e) and j)** 48 hours after the time of maximum intensity. The thick black contours indicates the level of the Tropopause (2PVU). In producing these composites, storms have been rotated to the direction of propagation before the composite is made, so that the top of each figure is north.

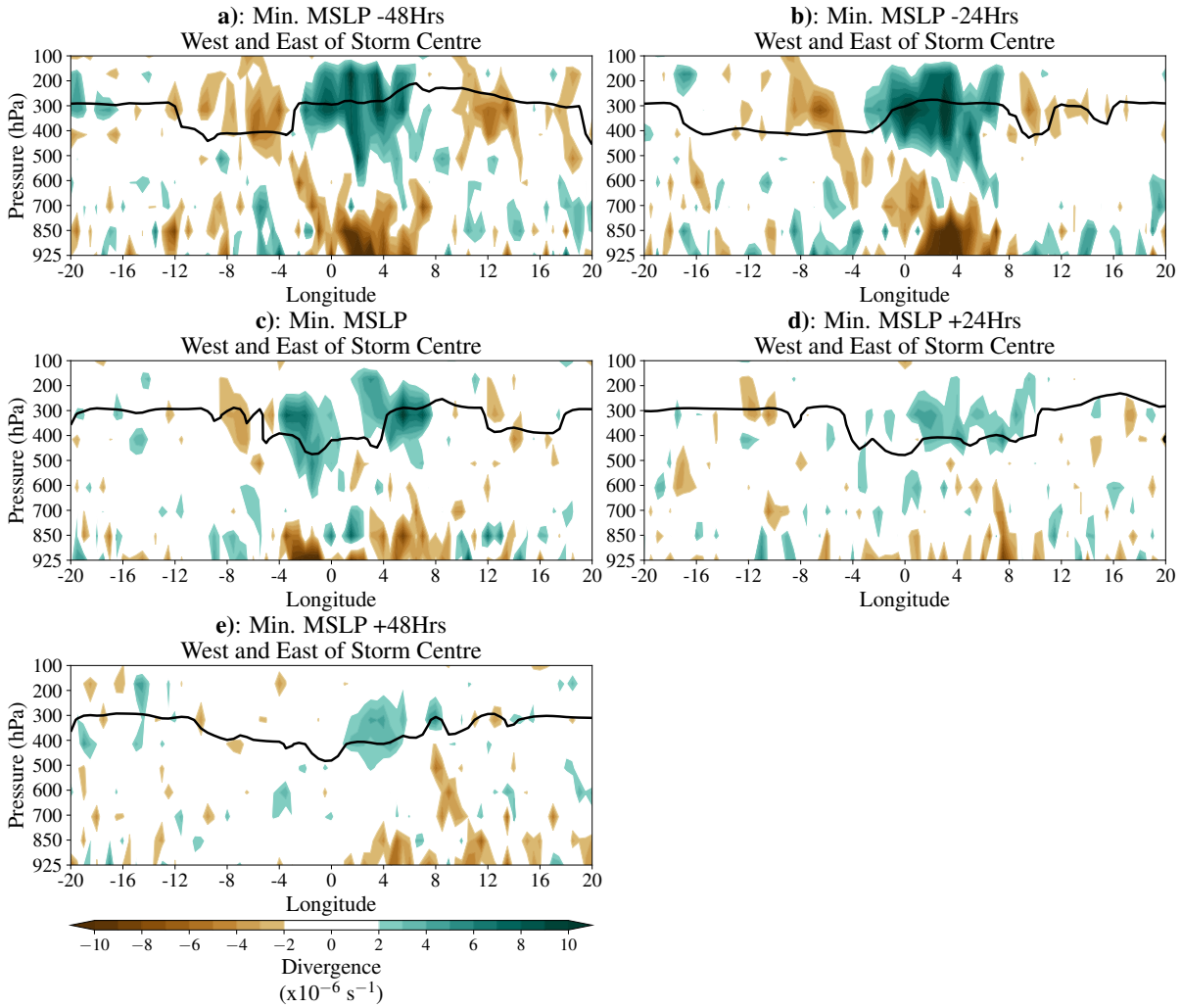

Figure E.13: The composite divergence structure of the 100 most intense summer (JJA) Arctic storms, west to east from the storm centre, at different stages of the storm cycle. The thick black contours indicates the level of the Tropopause (2PVU contour). **a)** 48 hours and **b)** 24 hours before the time of maximum intensity, **c)** at the time of maximum intensity, and **d)** 24 hours and **e)** 48 hours after the time of maximum intensity.

E.4 Great Arctic Storm of 2012 Structure

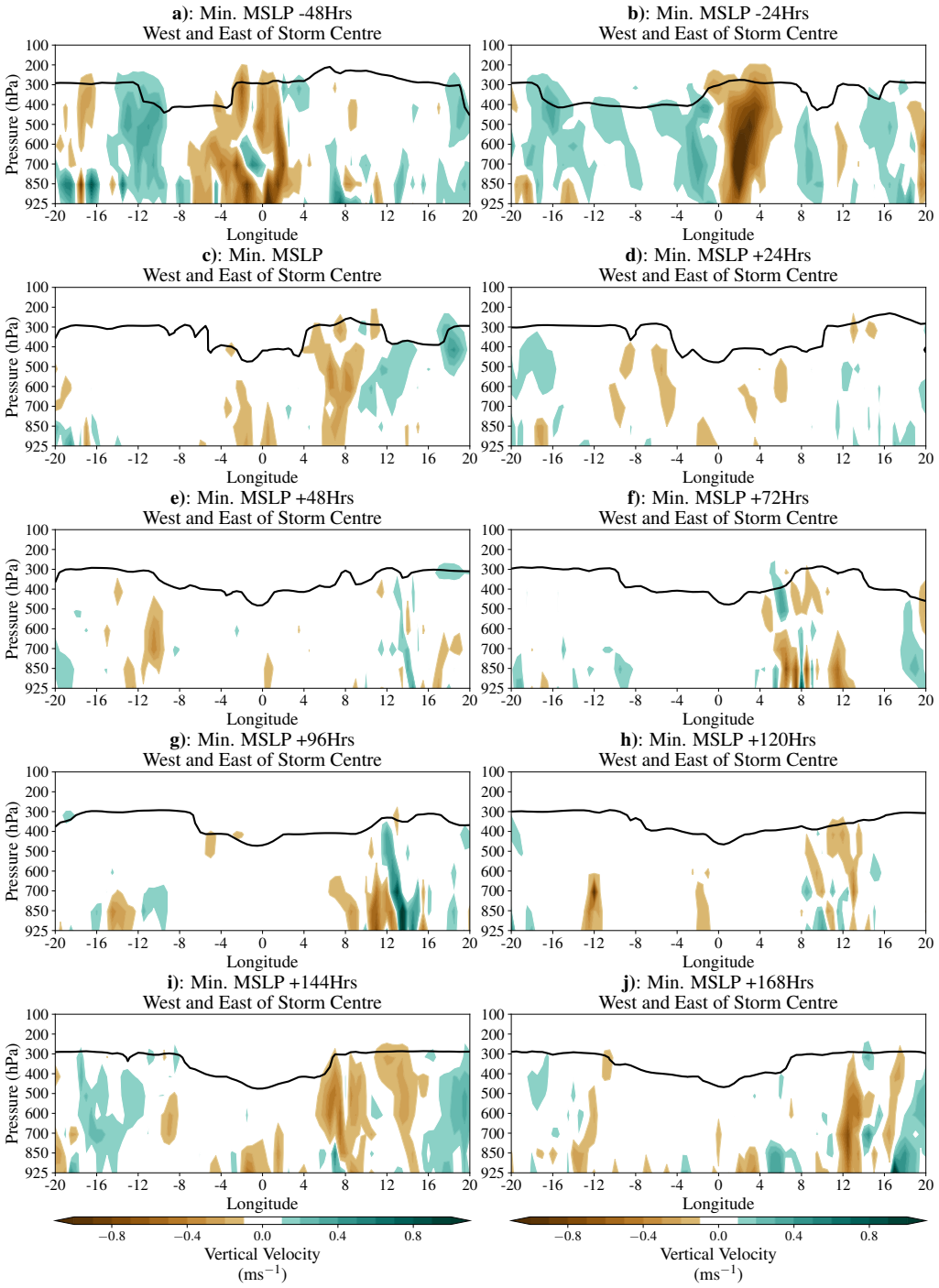

Figure E.14: The change in the vertical velocity (w-component of wind) structure of the Great Arctic Storm of 2012, west to east from the storm centre, at different stages of the storm cycle. The thick black contours indicates the level of the Tropopause (2PVU contour). **a)** 48 hours and **b)** 24 hours before the time that the storm reached its maximum intensity (minimum mean sea level pressure - MSLP), **c)** the time that the storm reached its maximum intensity, and **d)** 24 hours, **e)** 48 hours, **f)** 72 hours, **g)** 96 hours, **h)** 120 hours, **i)** 144 hours and **j)** 168 hours after the time that the storm reached its maximum intensity.

Appendix F

Chapter 5 Supplementary Material

F.1 HadGEM3-GA3.0 Present-Day Climate Simulations

Table F.1: Present-day climate (1986-2010) number of Arctic storms per season that travel north of 65°N and the percentage of Arctic storms with Arctic genesis (north of 65°N) or mid-latitude genesis (south of 65°N) in all seasons between ERA-5 and present-day simulations from HadGEM3-GA3.0 at horizontal resolutions of N512 (N512 ens. mean), N216 (N216 ens. mean) and N96 (N96 ens. mean). Between the period of 1986/87-2009/10 in winter, and 1986-2010 in spring, summer and autumn. Storm numbers in **bold** are statistically significant differences to ERA-5 to a 95% confidence interval.

Number of **All Arctic Storms** Per Season				
	Winter (DJF)	Spring (MAM)	Summer (JJA)	Autumn (SON)
ERA-5	118.7	110.2	97.0	107.5
N512 Ens. Mean	117.2	106.9	94.9	105.5
N216 Ens. Mean	**112.2**	**102.6**	**91.3**	105.8
N96 Ens. Mean	**107.1**	**96.5**	**87.3**	**97.8**

% of Arctic Storms with **Arctic Genesis** and **Mid-Latitude Genesis** Per Season								
	Winter (DJF)		Spring (MAM)		Summer (JJA)		Autumn (SON)	
	Arctic Genesis	Mid-Lat Genesis	Arctic Genesis	Mid-Lat Genesis	Arctic Genesis	Mid-Lat Genesis	Arctic Genesis	Mid-Lat Genesis
ERA-5	54.4%	45.6%	54.0%	46.0%	47.9%	52.1%	48.5%	51.5%
N512 Ens. Mean	53.0%	47.0%	51.2%	49.8%	45.5%	54.5%	48.6%	51.4%
N216 Ens. Mean	51.2%	48.8%	54.0%	46.0%	45.6%	54.4%	47.9%	52.1%
N96 Ens. Mean	54.3%	45.7%	54.2%	47.3%	47.3%	52.7%	50.3%	49.7%

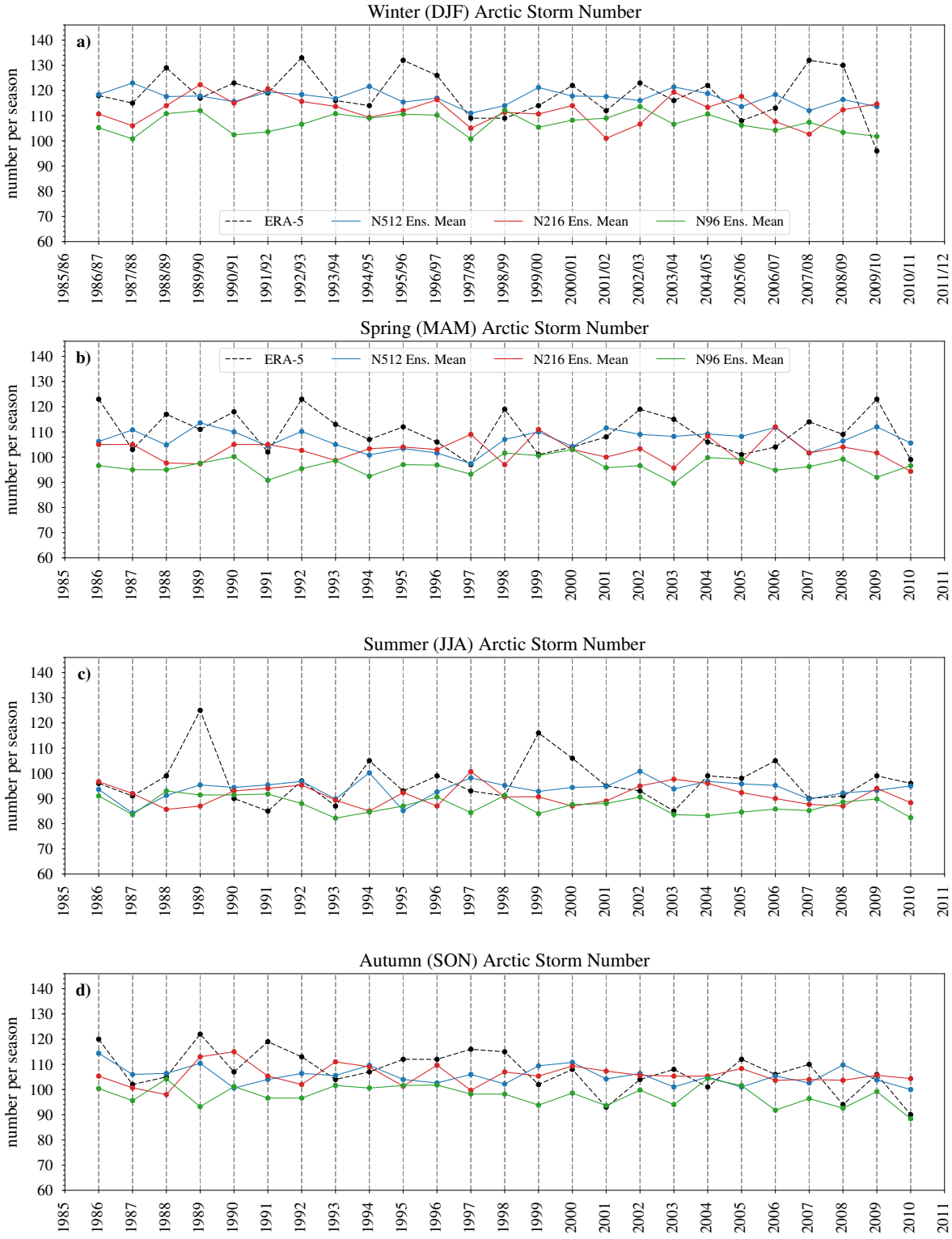

Figure F.1: Arctic storm number per year in the N96, N216 and N516 HadGEM3-GA3.0 present-day climate simulations and the ERA-5 reanalysis dataset.

Table F.2: Number of Arctic storms per season in the HadGEM3-GA3.0 RCP8.5 future climate (2086-2110) simulations, at a horizontal resolutions of N512 (N512 ens. mean), N216 (N216 ens. mean) and N96 (N96 ens. mean).

Change in Frequency of **All Arctic Storms** Per Season				
	Winter (DJF)	Spring (MAM)	Summer (JJA)	Autumn (SON)
N512 Ens. Mean	110.3	105.9	90.9	102.8
N216 Ens. Mean	104.0	99.9	90.0	99.8
N96 Ens. Mean	98.8	94.2	89.6	97.1

Change in Frequency of Arctic Storms with **Arctic Genesis** and **Mid-Latitude Genesis** Per Season								
	Winter (DJF)		Spring (MAM)		Summer (JJA)		Autumn (SON)	
	Arctic Genesis	Mid-Lat Genesis	Arctic Genesis	Mid-Lat Genesis	Arctic Genesis	Mid-Lat Genesis	Arctic Genesis	Mid-Lat Genesis
N512 Ens. Mean	53.7	56.7	51.4	54.5	42.1	48.8	47.5	55.3
N216 Ens. Mean	50.6	53.4	50.5	49.4	42.4	47.6	46.7	53.1
N96 Ens. Mean	49.4	49.7	48.2	45.9	43.8	45.8	46.5	50.6

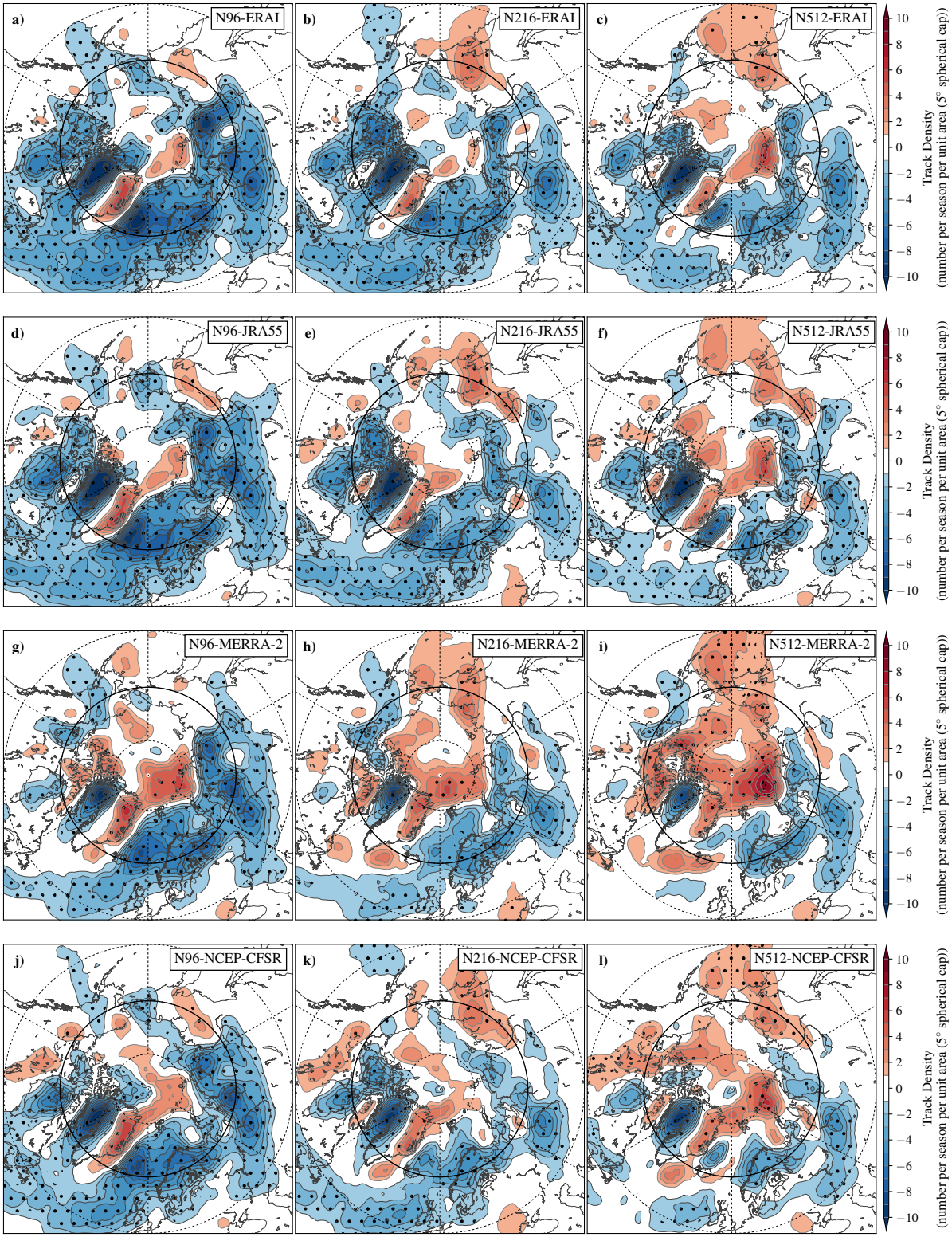

Figure F.2: Difference between the HadGEM3-GA3.0 present-day climate (1986-2010) winter (DJF) Arctic storm track density per season and reanalysis datasets. **a) - c)** Comparison to ERA-Interim, **d) - f)** comparison to JRA-55, **g) - i)** comparison to MERRA-2 and **j) - l)** comparison to NCEP-CFSR. **a), d), g) and j)** N96 simulations, **b), e), h) and k)** N216 simulations and **c), f), i) and l)** N512 simulations. Longitudes are shown every 60°E, and latitudes are shown at 80°N, 65°N (bold) and 50°N. Stippling show areas where the differences are statistically significant to a 95% confidence level. Densities have units of number per season per unit area (5° spherical cap, $\approx 10^6$ km^2).

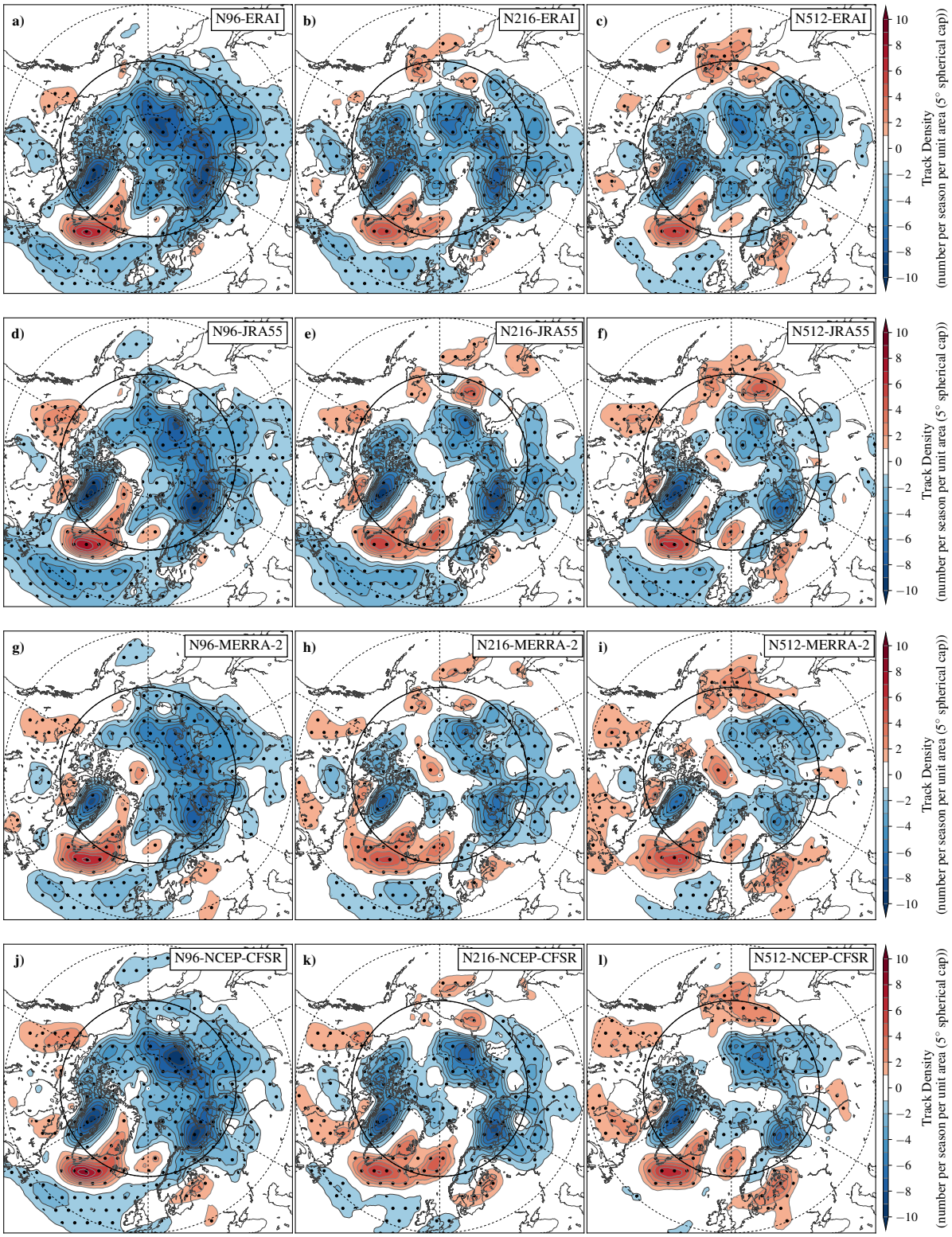

Figure F.3: Description same as Figure **F.2**, but for present-day climate (1986-2010) summer (JJA) Arctic storms.

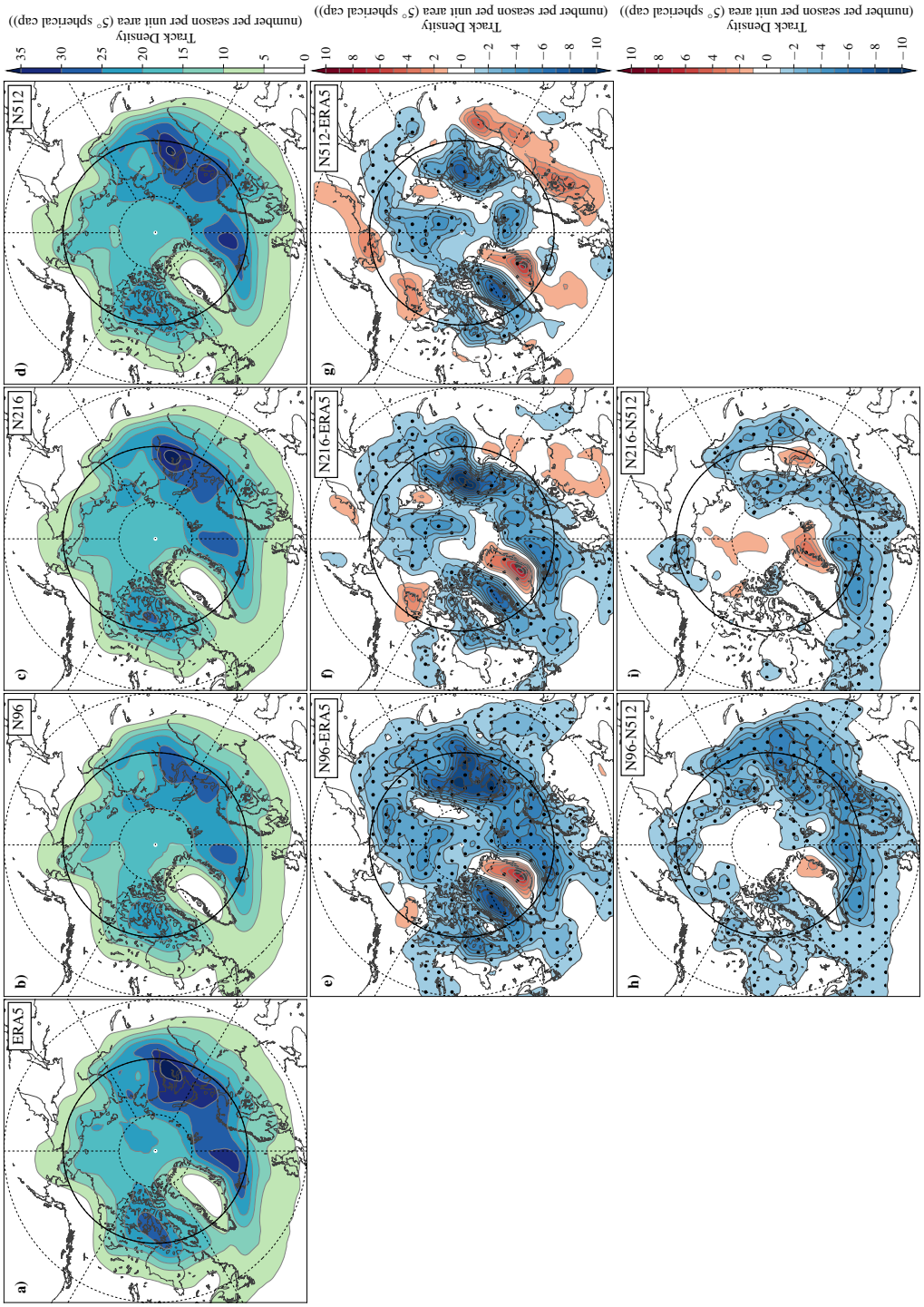

Figure F.4: Present-day climate (1986-2010) spring (MAM) Arctic storm track density per season from the **a)** ERA-5 reanalysis dataset, **b)** N96 ensemble (ens.) mean, **c)** N216 ens. mean and **d)** N512 ens. mean. Differences in Arctic storm track density per season between **e)** N96 ens. mean minus ERA-5, **f)** N216 ens. mean minus ERA-5, **g)** N512 ens. mean minus ERA-5, **h)** N96 minus N512 ens. mean and **i)** N216 minus N512 ens. mean. Longitudes are shown every 60°E, and latitudes are shown at 80°N, 65°N (bold) and 50°N. Stippling show areas where the differences are statistically significant to a 95% confidence level. Densities have units of number per season per unit area (5° spherical cap, $\approx 10^6$ km^2).

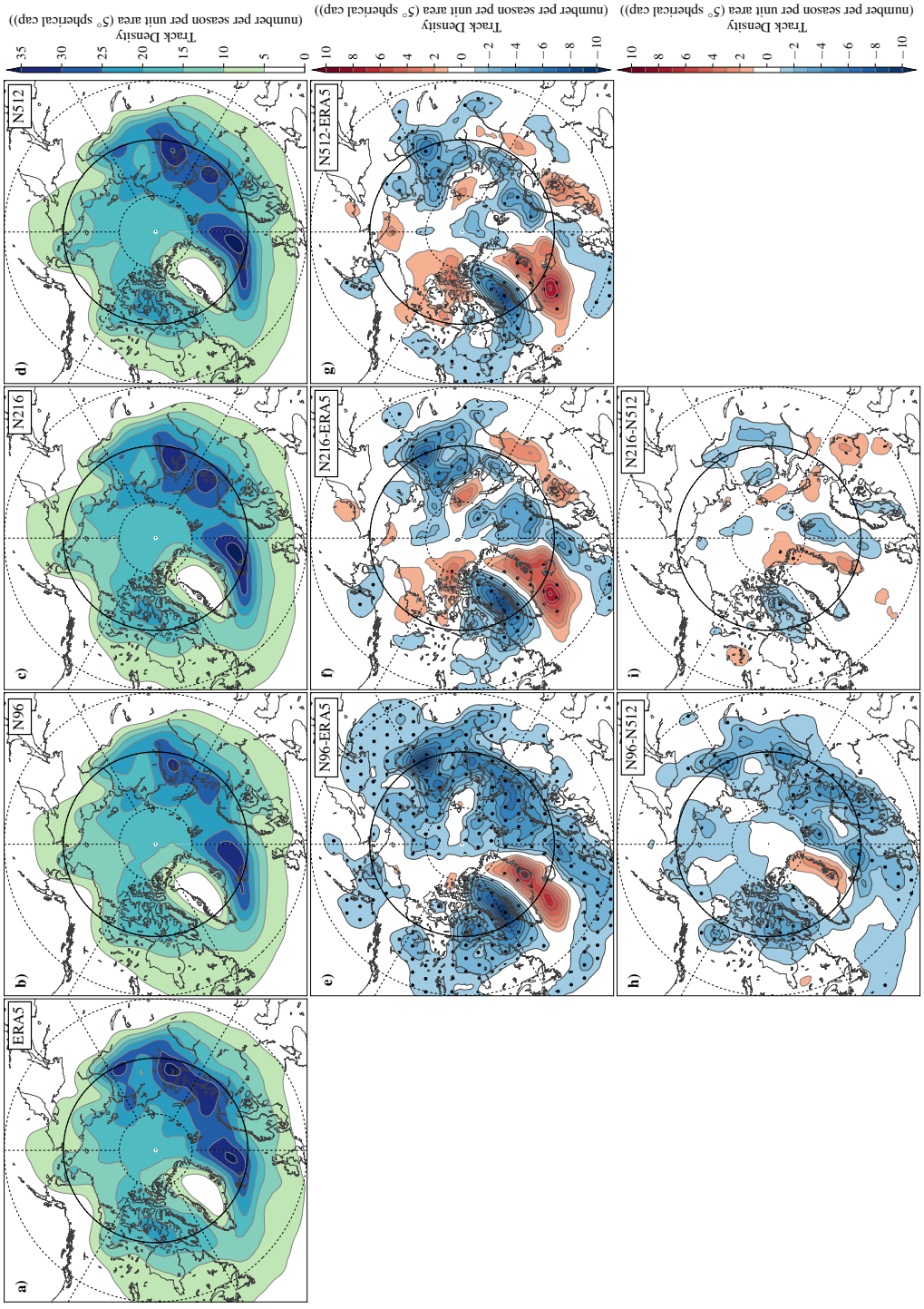

Figure F.5: Description same as Figure **F.4**, but for present-day climate autumn (SON) Arctic storms between 1986-2010.

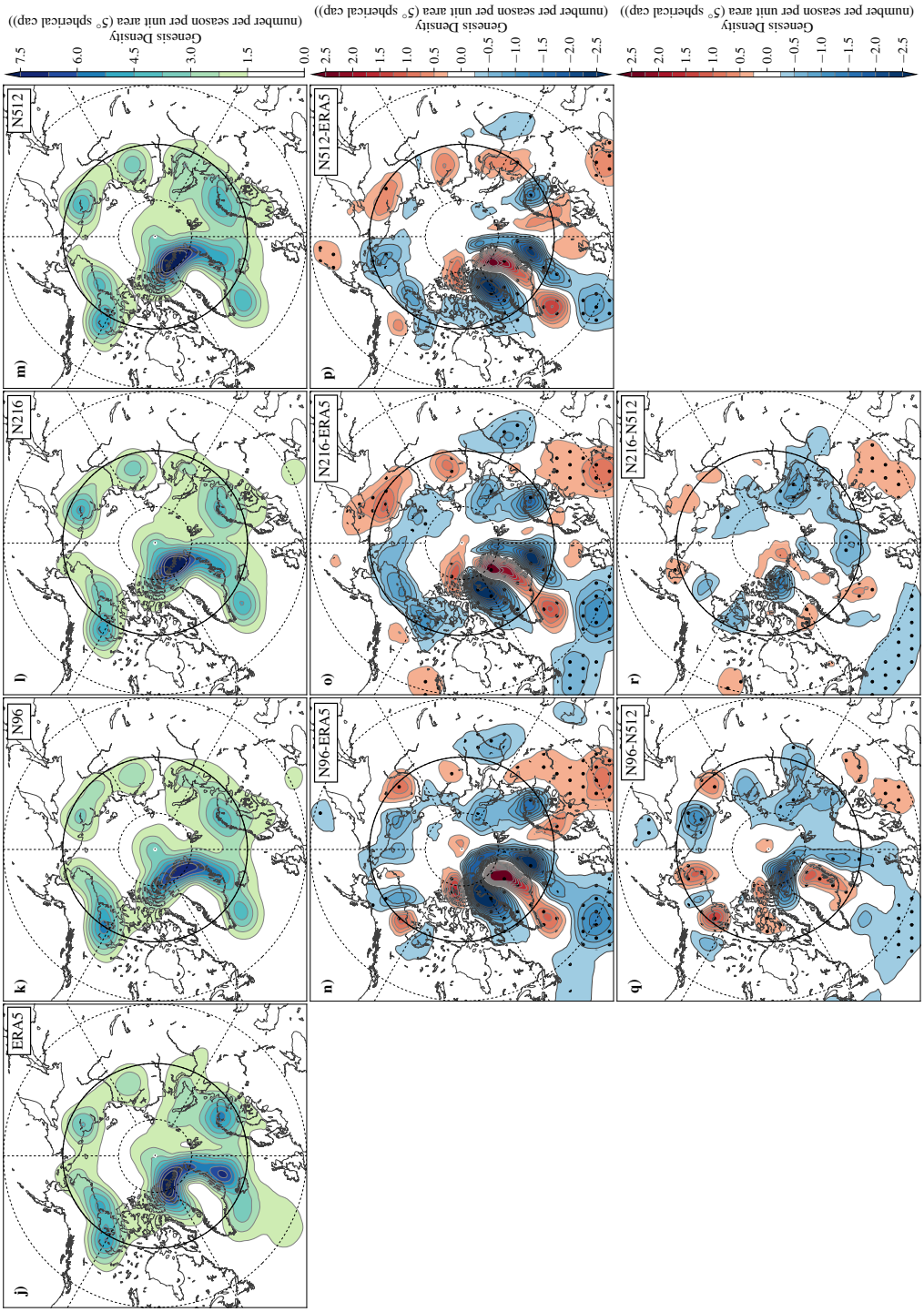

Figure F.6: Present-day climate (1986-2010) winter (DJF) Arctic storm genesis density per season from the **a)** ERA-5 reanalysis dataset, **b)** N96 ensemble (ens.) mean, **c)** N216 ens. mean and **d)** N512 ens. mean. Differences in Arctic storm track density per season between **e)** N96 ens. mean minus ERA-5, **f)** N216 ens. mean minus ERA-5, **g)** N512 ens. mean minus ERA-5, **h)** N96 minus N512 ens. mean and **i)** N216 minus N512 ens. mean. Longitudes are shown every 60°E, and latitudes are shown at 80°N, 65°N (bold) and 50°N. Stippling show areas where the differences are statistically significant to a 95% confidence level. Densities have units of number per season per unit area (5° spherical cap, $\approx 10^6$ km^2).

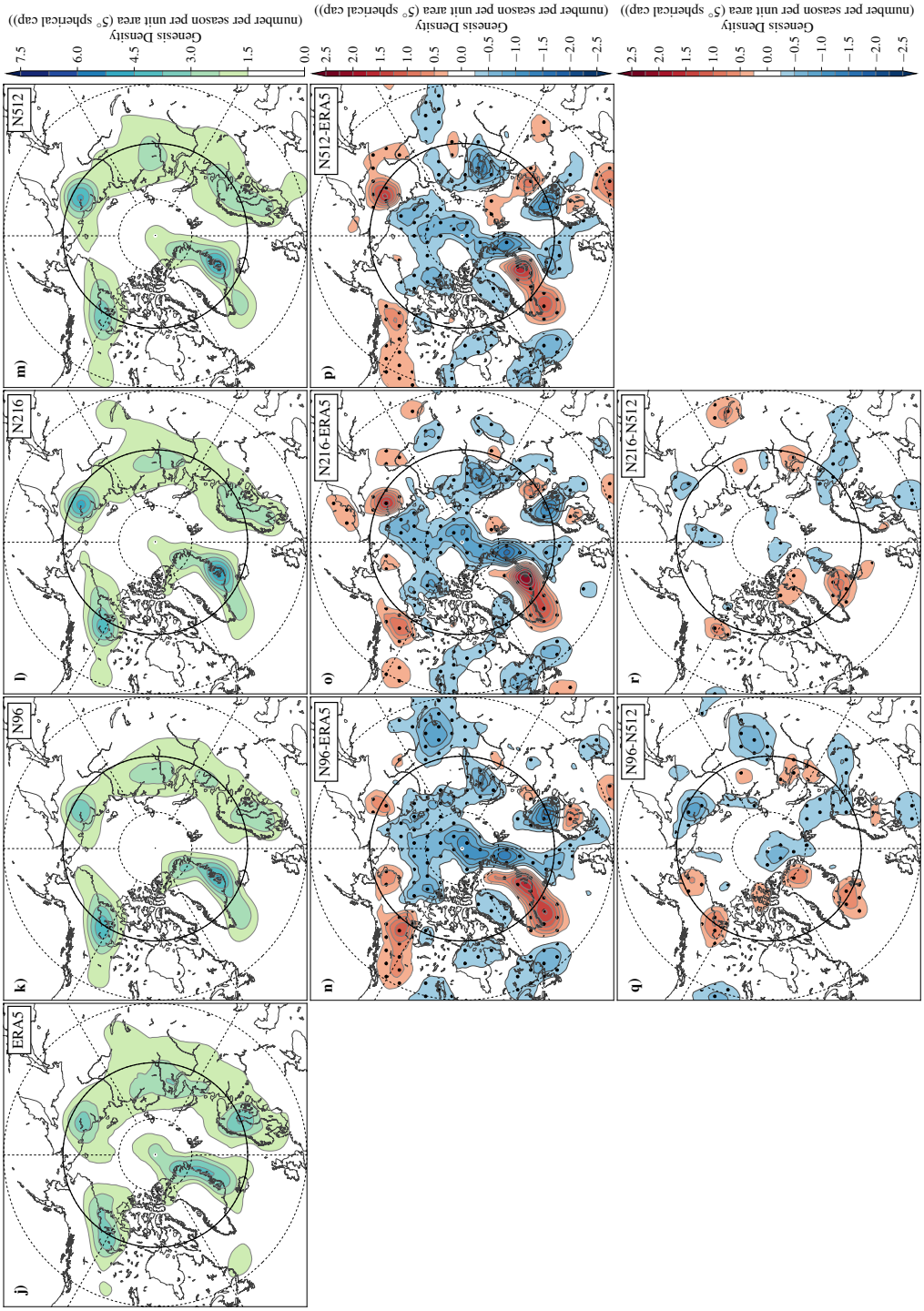

Figure F.7: Description same as **F.6**, but for present-day climate summer (JJA) Arctic storms between 1986-2010.

F.2 HadGEM3-GA3.0 RCP8.5 Future Climate Simulations

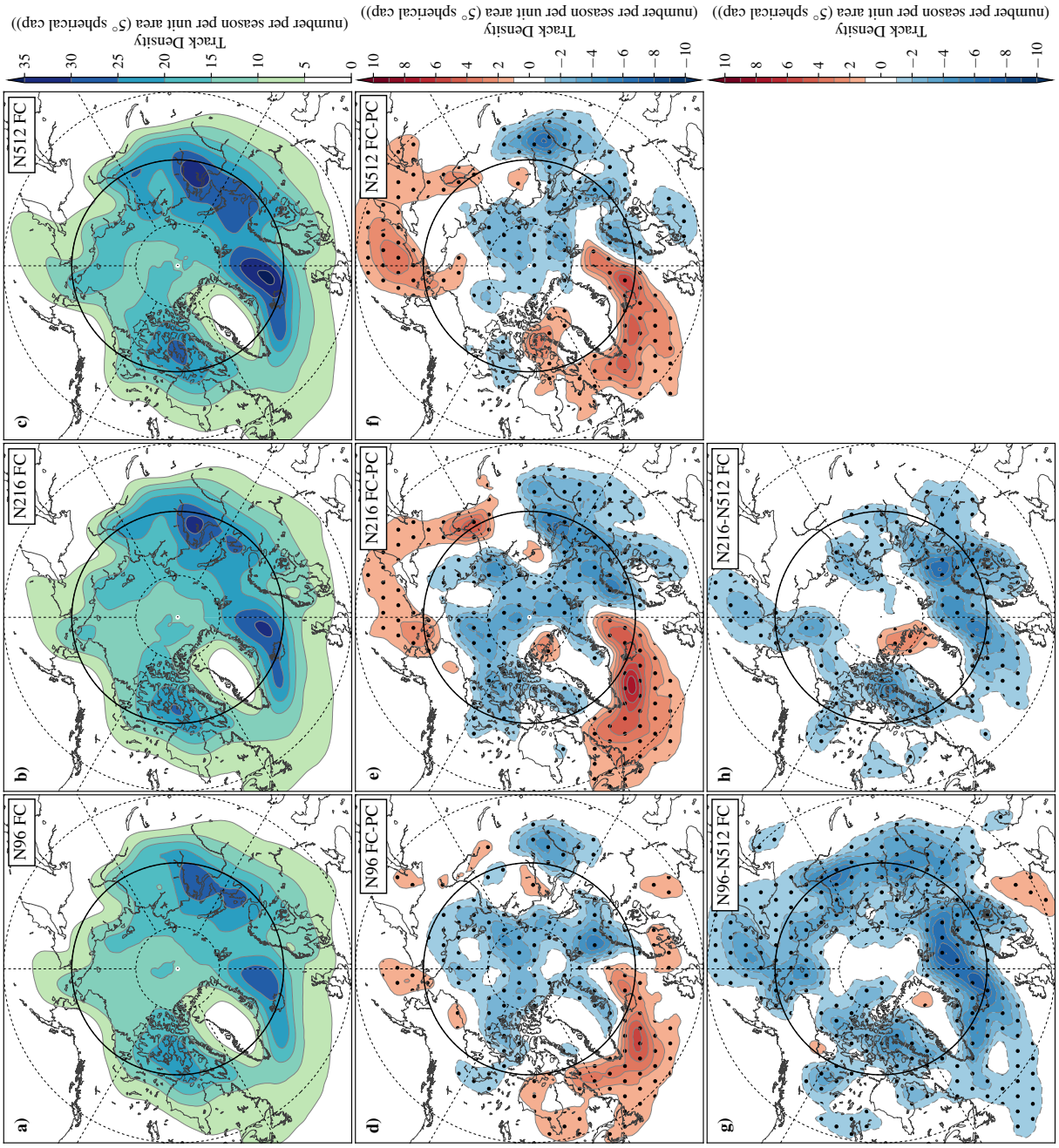

Figure F.8: RCP8.5 future climate (2086-2110) spring (MAM) Arctic storm track density per season from the **a)** N96 ensemble (ens.) mean, **b)** N216 ens. mean and **c)** N512 ens. mean. Differences in Arctic storm track density per season between the future and present-day climate in the **d)** N96 **e)** N216 and **f)** N512 simulations. Differences in Arctic storm track density in the future climate between **g)** N96 minus N512 ens. mean and **h)** N216 minus N512 ens. mean. Longitudes are shown every 60°E, and latitudes are shown at 80°N, 65°N (bold) and 50°N. Stippling show areas where the differences are statistically significant to a 95% confidence level. Densities have units of number per season per unit area (5° spherical cap, $\approx 10^6$ km^2).

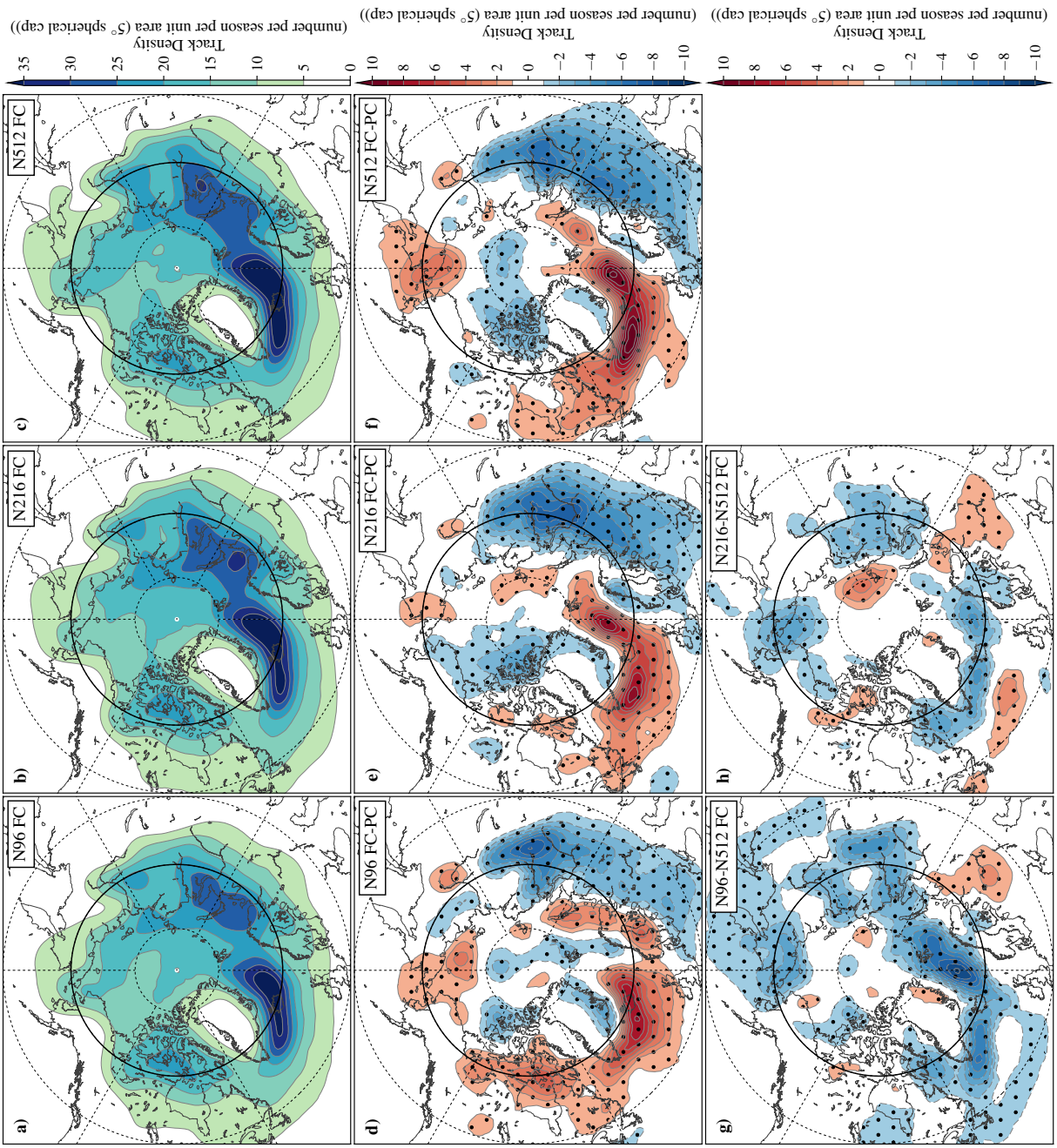

Figure F.9: Description same as Figure **F.8**, but for RCP8.5 future climate autumn (SON) Arctic storms between 2086-2110.

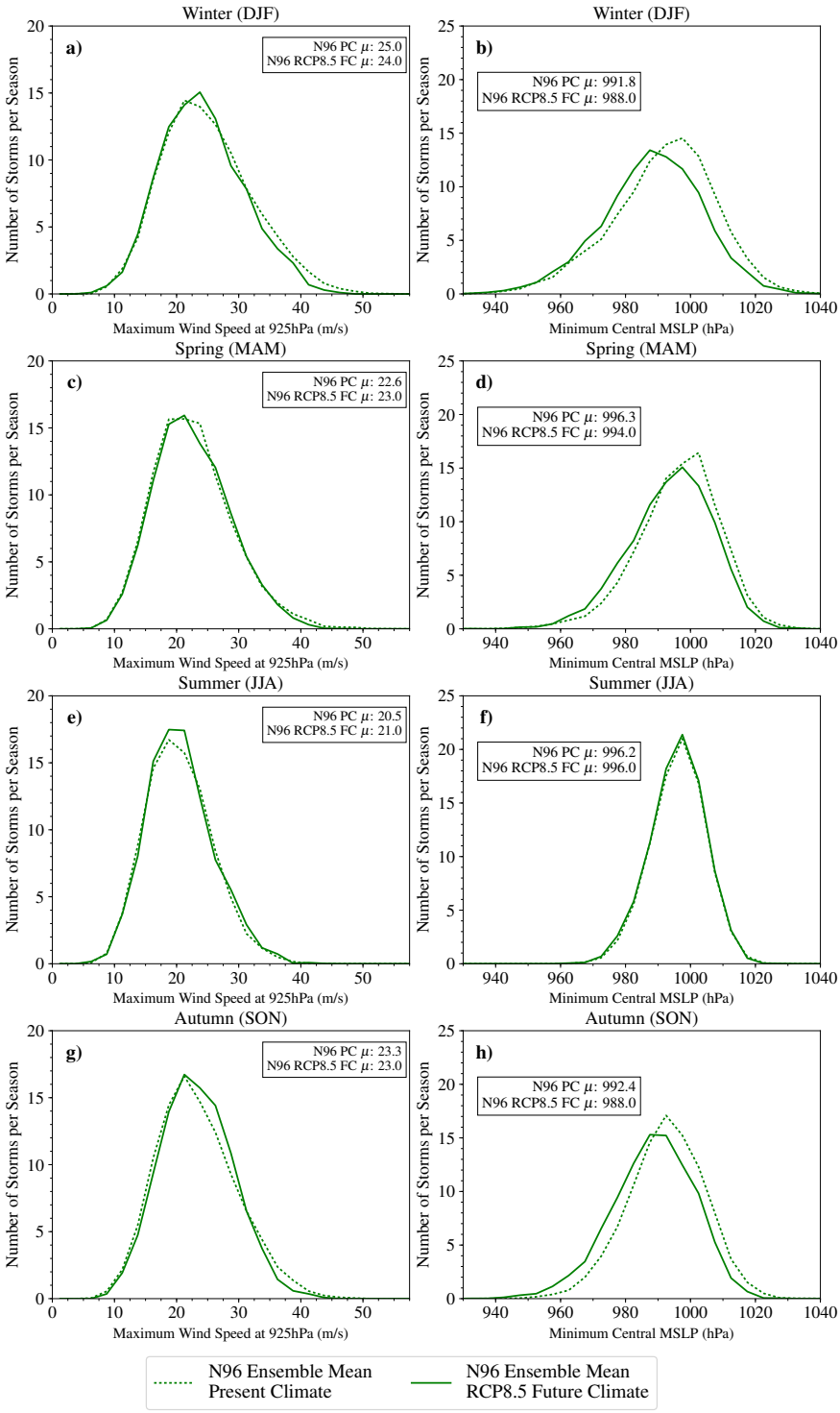

Figure F.10: Present-day climate (1986-2010) and RCP8.5 Future Climate (2086-2110) Arctic storm intensity from the N96 HadGEM3-GA3.0 simulations across all seasons. **a), c), e) and g)** show the maximum 925hPa (near-surface) wind speeds (ms^{-1}) and **b), d), f) and h)** minimum mean sea level pressure (MSLP) (hPa) of Arctic storms when they are north of 65°N. **a) and b)** Winter (DJF), **c) and d)** Spring (MAM), **e) and f)** Summer (JJA) and **g) and h)** Autumn (SON).

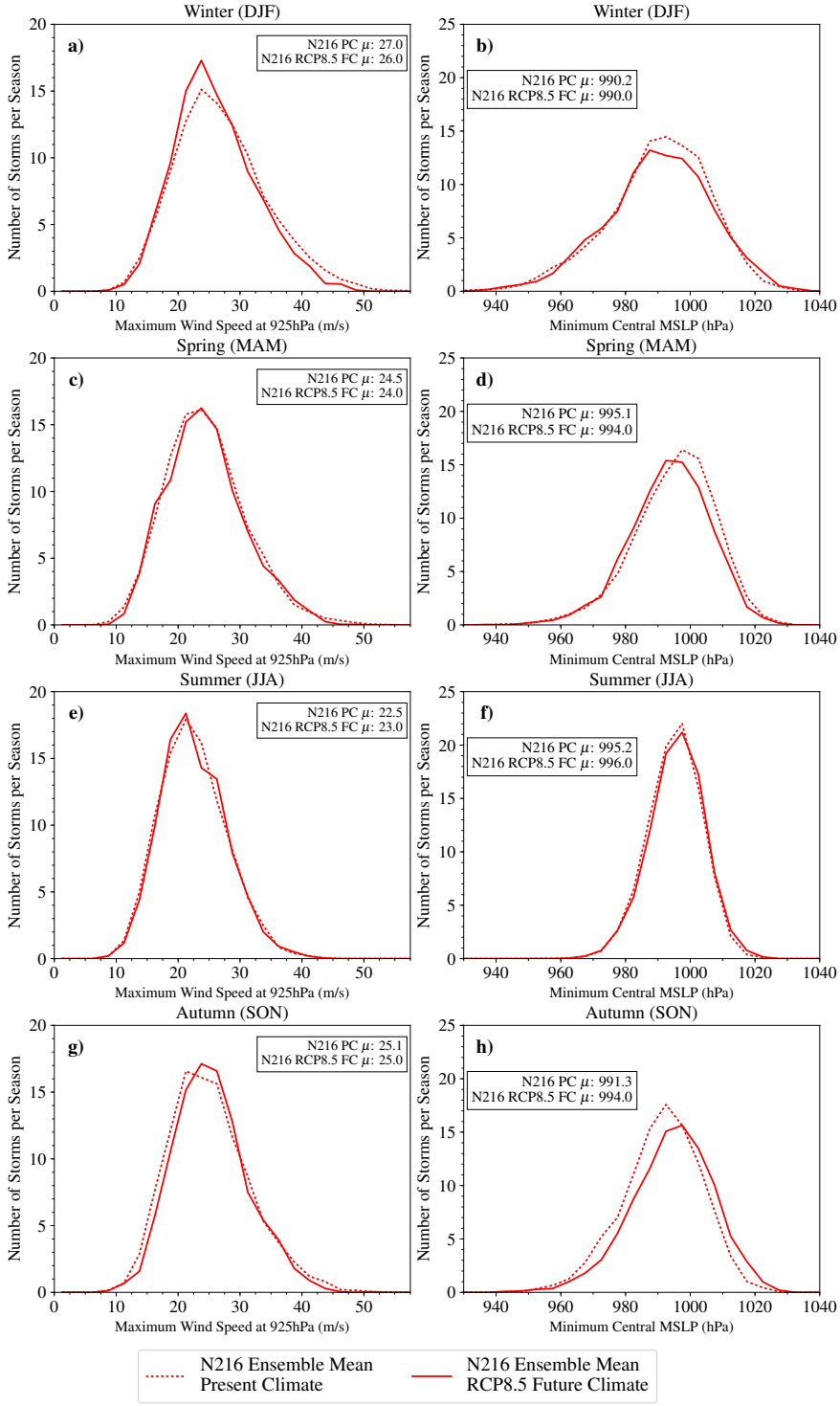

Figure F.11: Description same as Figure **F.10**, but for the HadGEM3-GA3.0 N216 simulations.

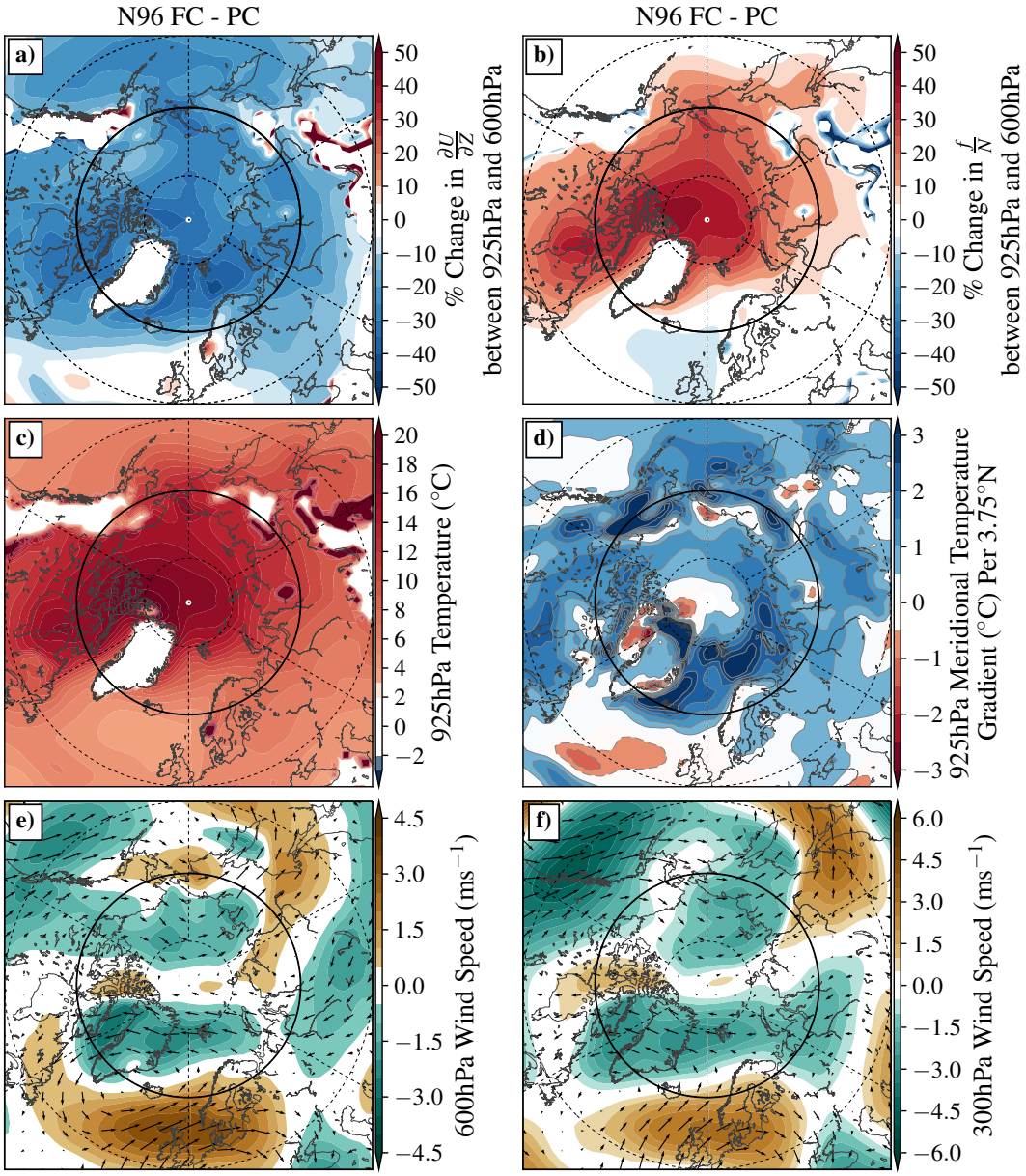

Figure F.12: Changes in the large scale environment in the winter (DJF) N512 HadGEM3-GA3.0 simulations at a horizontal of N96 (RCP8.5 future climate (2086-2110) (FC) minus present-day climate (1986-2010) (PC) simulations). Percentage change in **a)** wind shear and **b)** Brunt Vaisala frequency divided by the Coriolis force between 925 and 600 hPa. Change in **c)** 925 hPa temperature, **d)** meridional temperature gradient at 925 hPa temperature per 3.75°N, **e)** 600 hPa wind speed and direction, and, **f)** 300 hPa wind speed and direction.

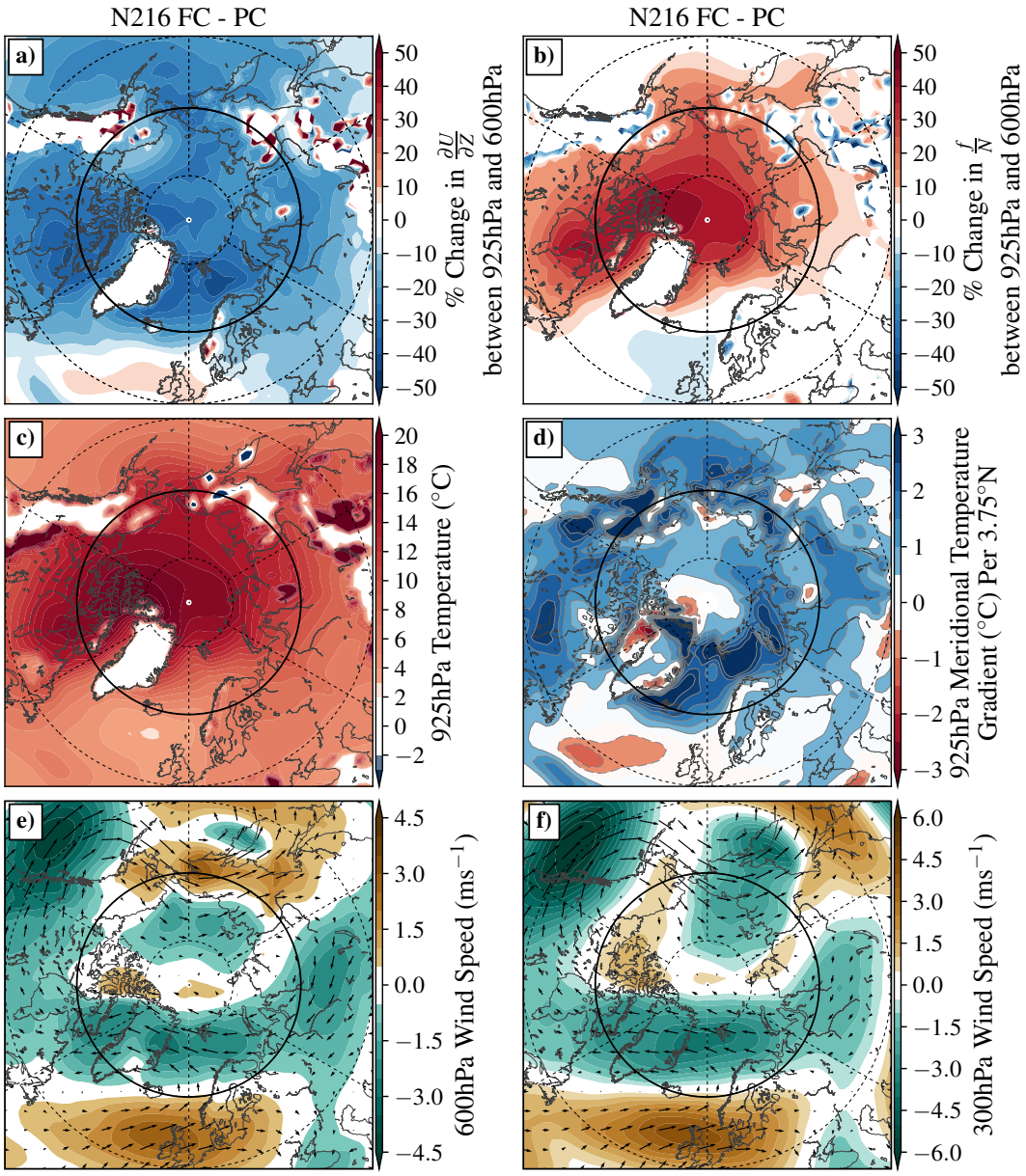

Figure F.13: Description same as Figure **F.10**, but for the HadGEM3-GA3.0 N216 simulations.

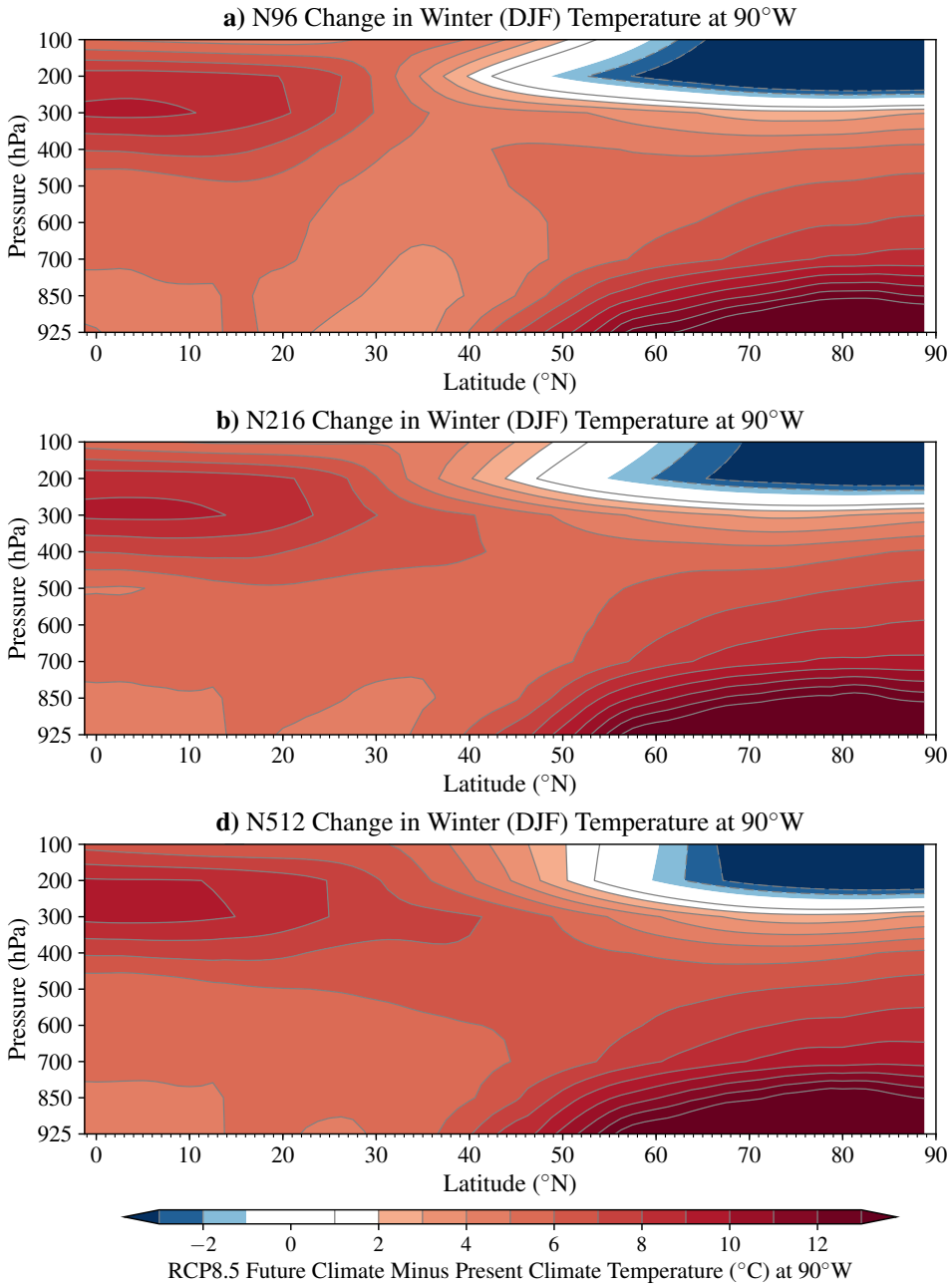

Figure F.14: Vertical cross section at 90°W between 0-90°N of the ensemble mean winter (DJF) RCP8.5 future climate simulations minus present-day climate simulations air temperature from the HadGEM3-GA3.0 climate model at a horizontal resolution of **a)** N96, **b)** N216 and **c)** N512.

Appendix G

Chapter 6 Supplementary Material

G.1 Arctic Shipping

Table G.1: The percentage of all gate crossings by ships in the Arctic in 2019 by type of ship.

General Ship Type	% of 2019 Gate Crossings	All Ship Types	% of 2019 Gate Crossings
Cargo Ship	30.3%	Chemical / Product Tanker	3.4%
		Gas Tanker	4.0%
		Bulk ship	6.8%
		Cargo Ship	13.2%
		Container Ship	1.5%
		Roll-on/Roll-off Ship	0.3%
		Refrigerator/Freezer Ship	1.2%
Oil Ship	2.4%	Crude Oil Tanker	0.0%
		Oil Product Tanker	2.4%
Small Ship	67.3%	Fishing Vessel	59.0%
		Offshore Supply/Service Ship	8.3%

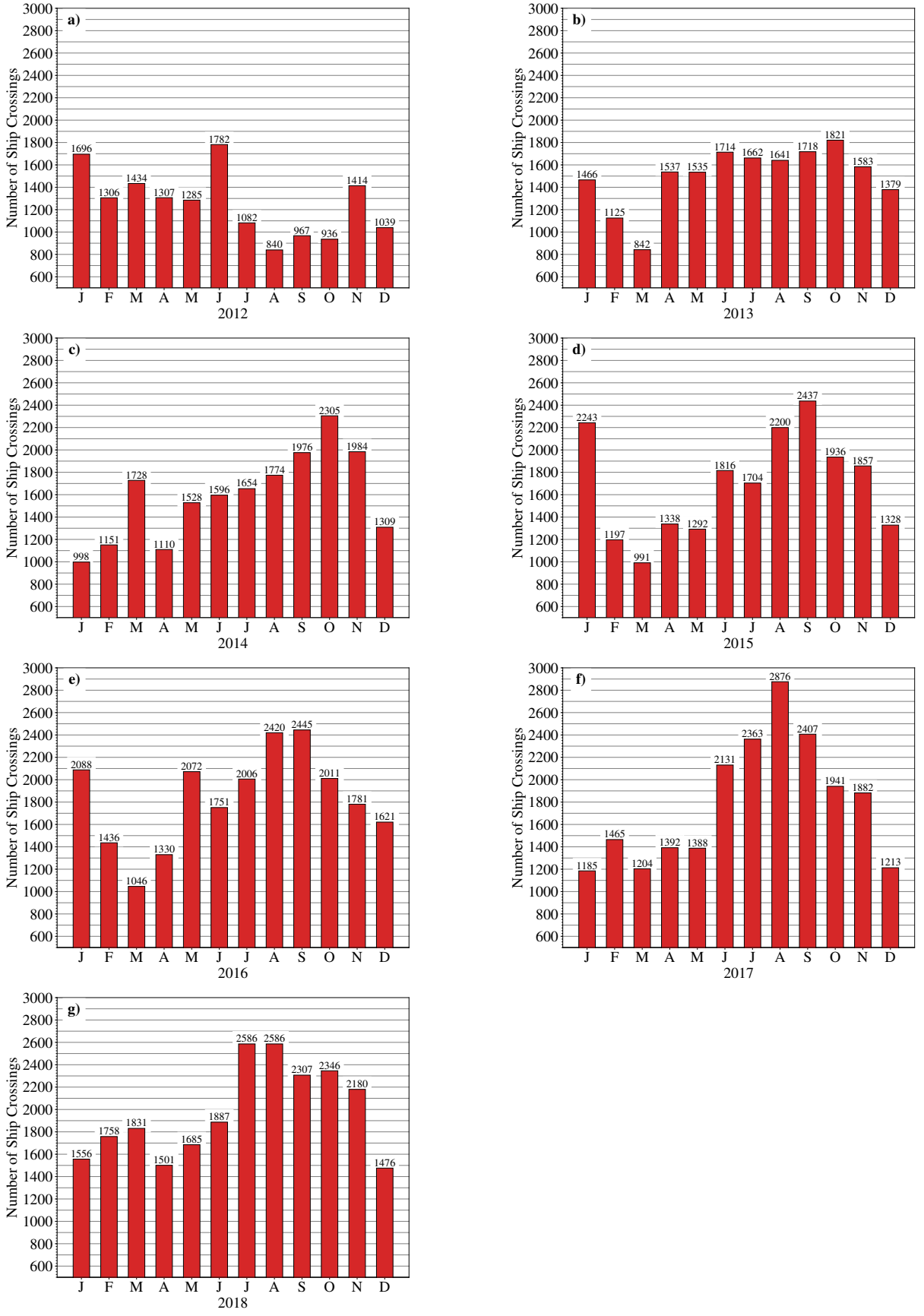

Figure G.1: The total number of gate crossings by ships across all Havbase gates in the Arctic per month in **a)** 2012, **b)** 2013, **c)** 2014, **d)** 2015, **e)** 2016, **f)** 2017 and **g)** 2018.

a) Arctic Ship Crossings: 2012

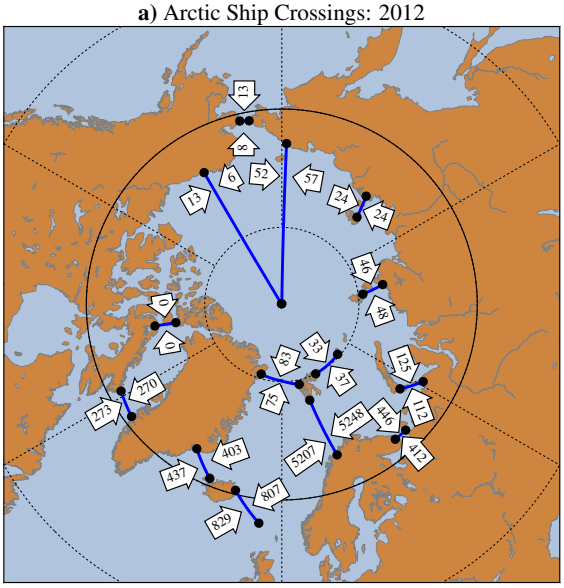

b) Arctic Ship Crossings: 2013

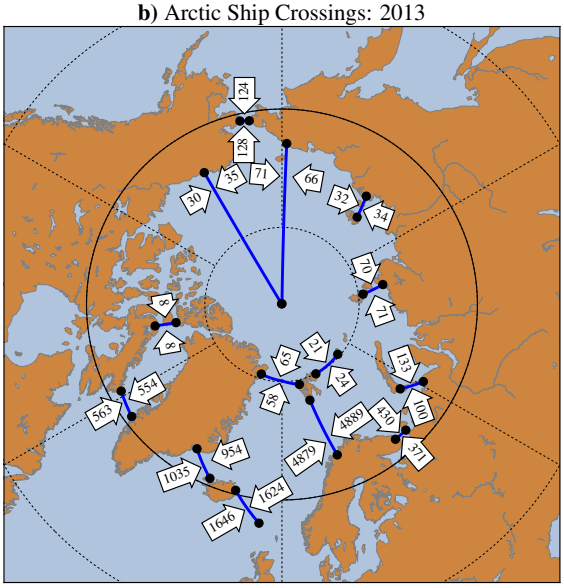

c) Arctic Ship Crossings: 2014

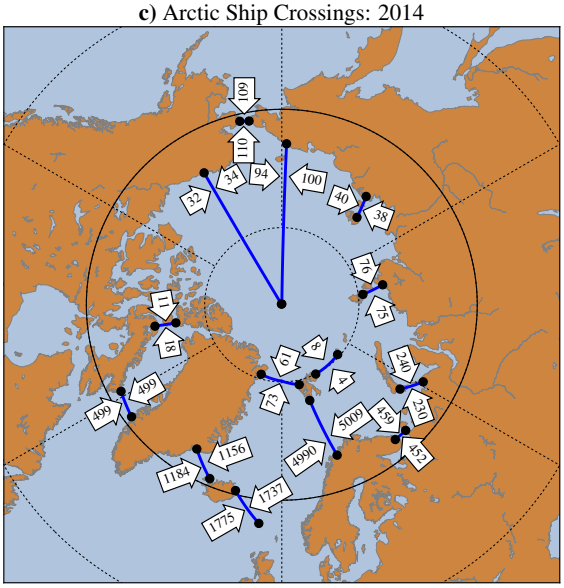

d) Arctic Ship Crossings: 2015

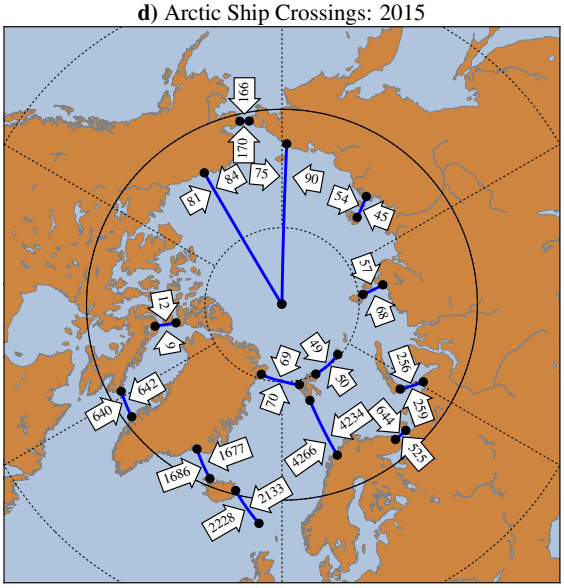

e) Arctic Ship Crossings: 2016

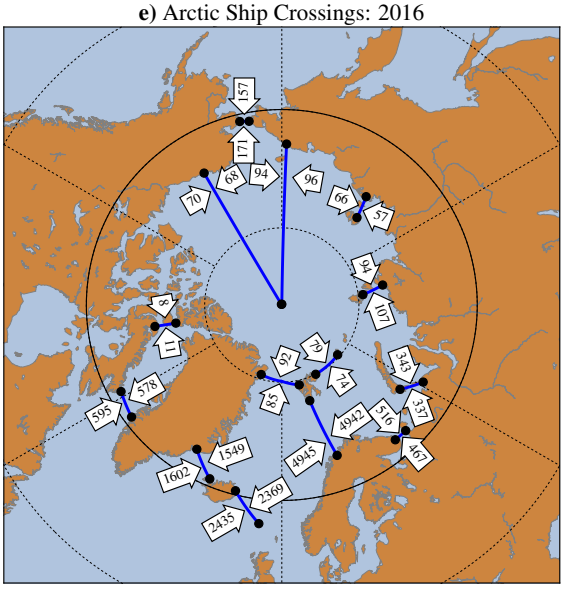

f) Arctic Ship Crossings: 2017

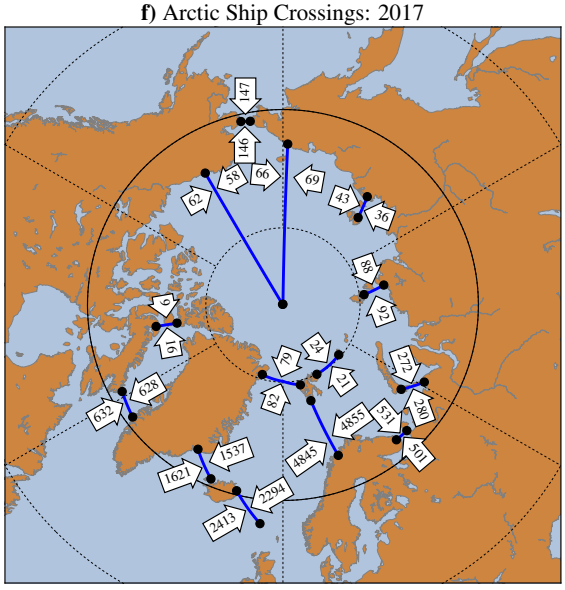

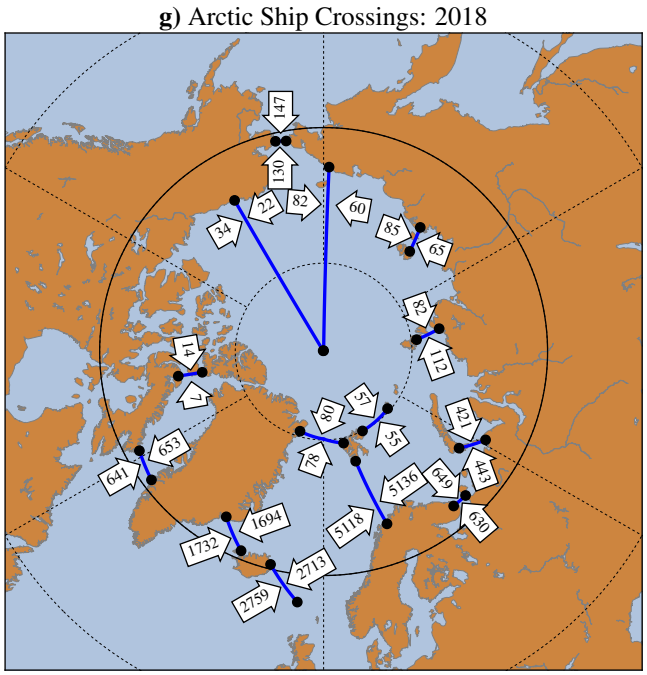

Figure G.2: The number of gate crossings by ships through each gate from the Havbase database across the Arctic. The arrows indicate the direction to which a ship passed through the gate (blue and black dots). **a)** 2012, **b)** 2013, **c)** 2014, **d)** 2015, **e)** 2016, **f)** 2017 and **g)** 2018.

G.2 Arctic Storm and Ship Model Statistics

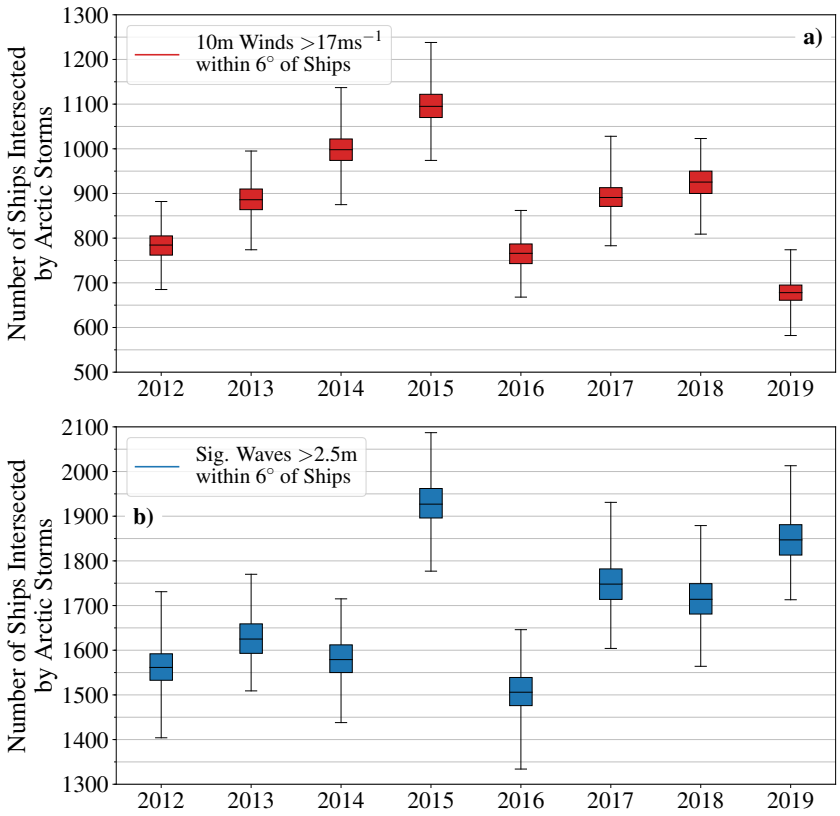

Figure G.3: The number of simulated ships tracks that are intersected (within 2°) by Arctic storms with **a)** 10 m wind speeds > 17 ms^{-1} (Beaufort Scale 8) and **b)** significant wave heights > 2.5 m (Douglas Sea State Scale 5), from 2012 to 2019.

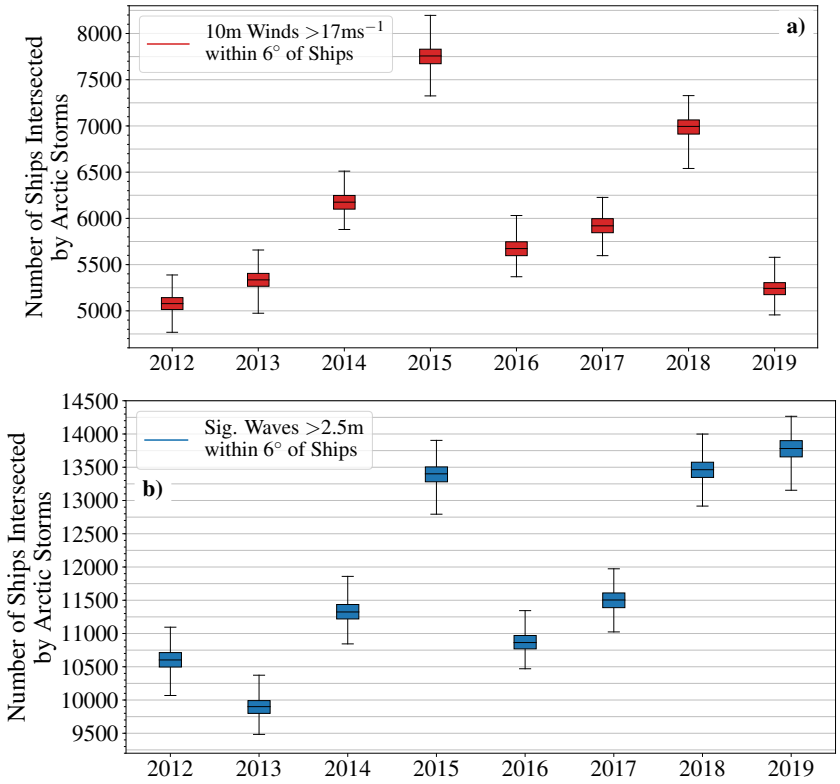

Figure G.4: The number of simulated ships tracks that are intersected (within 6°) by Arctic storms with **a)** 10 m wind speeds > 17 ms^{-1} (Beaufort Scale 8) and **b)** significant wave heights > 2.5 m (Douglas Sea State Scale 5), from 2012 to 2019.

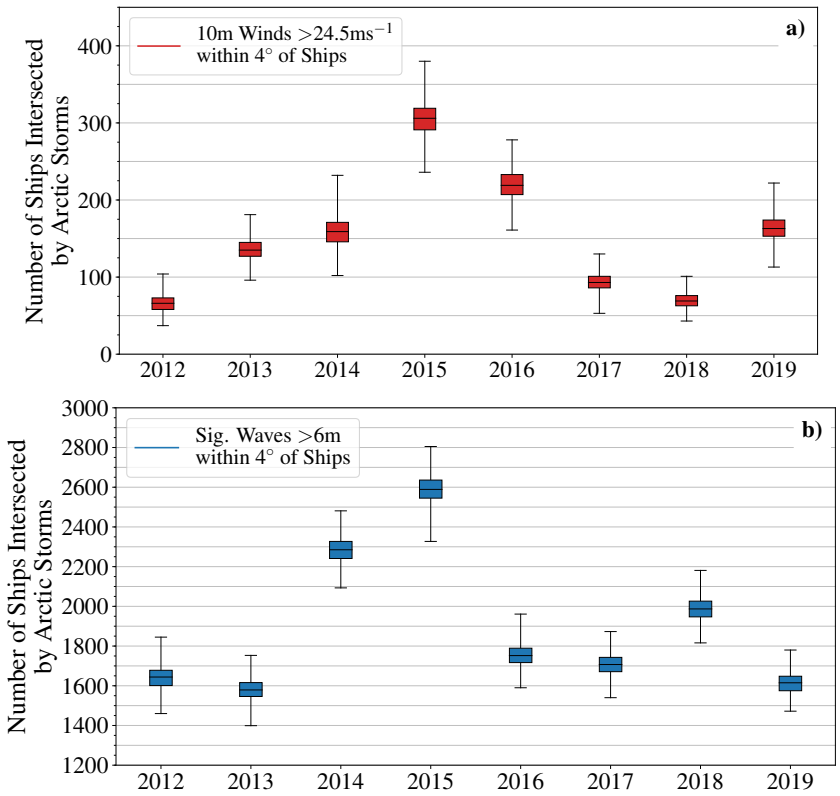

Figure G.5: The number of simulated ships tracks that are intersected (within 4°) by Arctic storms with **a)** 10 m wind speeds > 24.5 ms^{-1} (Beaufort Scale 10) and **b)** significant wave heights > 6.0 m (Douglas Sea State Scale 7), from 2012 to 2019.

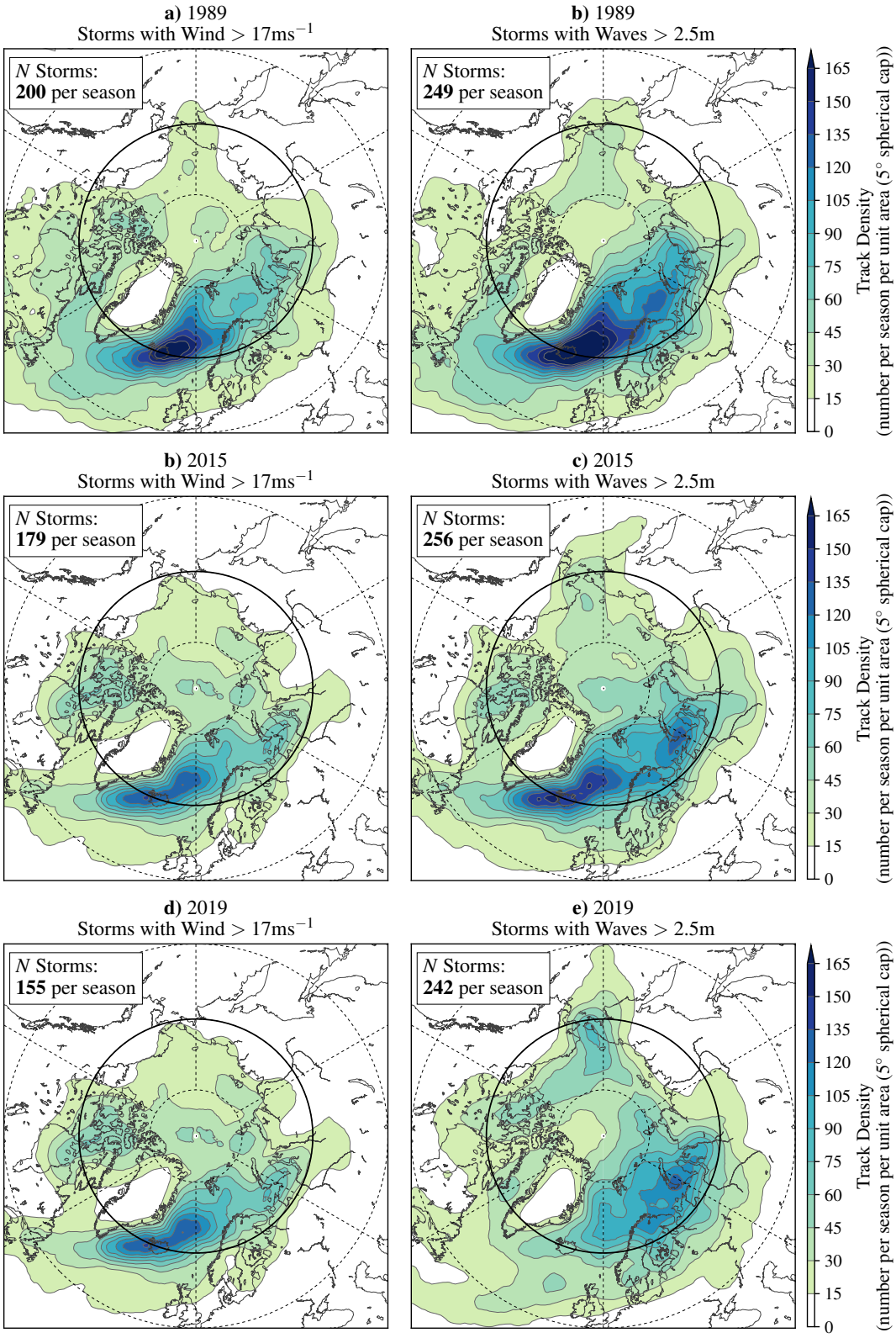

Figure G.6: Track density of Arctic storms in **a) and b)** 1989, **c) and d)** 2015 and **e) and f)** 1989, that have **a), c) and e)** maximum 10 metre (m) wind speeds in the Arctic greater than 17 ms^{-1}, and, **b), d) and f)** significant wave heights in the Arctic greater than 2.5m. Storms are identified in the ERA-5 reanalysis dataset. Densities indicate the number of storms that travel over an area and have units of number per season per unit area (5° spherical cap, $\approx 10^6$ km^2). Longitudes are shown every 60°E, and latitudes are shown at 80°N, 65°N (bold) and 50°N.